Long Term Mechanical Performance of MEMS in Liquid Environments

A DISSERTATION
SUBMITTED TO THE FACULTY OF THE GRADUATE SCHOOL
OF THE UNIVERSITY OF MINNESOTA
BY

Shaikh Mubassar Ali

IN PARTIAL FULFILLMENT OF THE REQUIREMENTS
FOR THE DEGREE OF
DOCTOR OF PHILOSOPHY

Prof. Susan C. Mantell and Prof. Ellen K. Longmire, Advisers

April 2009

Acknowledgements

I wish to express my sincere gratitude for my advisors, Prof. Susan C. Mantell and Prof. Ellen K. Longmire for their support, guidance, and inspiration. I am grateful to them for giving me the opportunity to work on this project.

This study has been funded by the National Science Foundation under grant number NSF/ CMS- 0300125.

I would also like to thank my committee members Prof. Thomas R. Chase and Prof. Tianhong Cui for their comments, suggestions, and kind consideration to serve on my committee.

Thomas P. Kuehn, Brandon J. Murphy, and Michael D. Eggen have worked on several experiments of this study, and their help and support is greatly appreciated. Matthew J. Stegmeir and Chunhui Wu had helped me with designing electrical circuits for my experimental setup.

I am also grateful to the staff of the Nanofabrication Center at the University of Minnesota. Kevin Roberts, Tony Whipple, and Mark Fisher have helped me through the numerous practical challenges to fabricate the MEMS samples. Past staff members Kathy Burkland and Suzanne Miller had helped me develop microfabrication processes for my test specimens. I also appreciate help from John Nelson at the IT Characterization Facility for his help with the scanning electron microscope. I am also grateful to Dave Hultman at the EE Machine Shop for fabricating experimental facilities with great ingenuity and enthusiasm. I would also like to thank the Institute of Rock Magnetism (IRM) at the University of Minnesota for allowing me to use their vibrating

sample magnetometer (VSM). I wish to thank John Gardner for his willingness to help with academic and administrative issues.

I have enjoyed the company of Casey Briscoe, Will Camisa, Kathleen McGill, and Jim Hambleton in the lab. I would like to thank friends and colleagues, Kalyanjit Ghosh, Rajesh Mukherjee, and Jami Hafiz for their support.

Finally, I would like to thank my parents, and wife Shabnam Rahman for their unconditional love, and support.

Dedication

This dissertation is dedicated to my parents, teachers, friends and family who have inspired and supported me over all these years.

Abstract

Micro-electro-mechanical systems (MEMS) are exposed to a variety of liquid environments in applications such as chemical and biological sensors, and microfluidic devices. Environmental interactions between the liquids and micron-sized structures can lead to unpredictable long-term performance of MEMS in liquid environments. The present understanding of long-term mechanical performance of MEMS is based on studies conducted in air or vacuum. The objective of this study was to extend the present understanding of long-term mechanical performance of MEMS to liquid environments. Two broad categories of long-term mechanical failures reported in the literature were experimentally investigated– operational failures and structural fatigue failures. Typically operational failures are observed to occur at low stress levels, while fatigue failures are reported at higher stress levels. In order to investigate these failure modes, two different designs of test specimens and experimental techniques were developed. Low stress level (0-5 MPa) tests to investigate operational failures of MEMS in liquids were performed on microcantilever test specimens. Higher stress level (~ 0.2 GPa) tests were conducted on MEMS tensile specimens for investigating fatigue failures in liquids. Microcantilever specimens were made of silicon and silicon nitride. In addition, performance of silicon microcantilevers coated with common MEMS coating materials such as Titanium and SU-8 was also investigated. Microcantilever specimens were tested in liquids such as de-ionized water, saline, and glucose solution and compared with results in air. The microcantilevers were subjected to long-term cyclic actuation (10^8-10^9 cycles) in liquid filled enclosures. Mechanical performance of the microcantilevers was evaluated by periodically monitoring changes

in resonant frequency. Any unpredictable change in resonant frequency was deemed to constitute an operational failure. Despite low stress levels, mechanical performance of microcantilever test specimens was affected to a varying degree depending on environmental interactions between the structural/ coating material and the liquid environment. The changes in resonant frequency, often to the extent of ~1%, were attributed to factors such as mineral deposition, corrosion fatigue, water absorption, and intrinsic stresses. Tensile-tensile fatigue tests (high stress level) were performed on aluminum MEMS tensile specimens, in air and saline solution. Fatigue life was observed to range between 1.2×10^6 to 2.2×10^6 cycles at mean and alternating stresses of 0.13 GPa. The effect of saline environment on fatigue failures of aluminum tensile specimens was inconclusive from the experiments performed in this study. In conclusion, experimental results indicate subtle operational failures to be a potential critical failure mode for MEMS operating in liquid environments. Long-term mechanical failures in MEMS are expected to depend on the particular combination of material, stress level, and environment.

Table of Contents

List of Tables

List of Figures

Nomenclature

a	Crack length, m
a_i	Initial crack length, m
a_f	Final crack length, m
α	Scale factor for LV
α_l	Coefficient of thermal expansion, m/°C
$\dot{a}_{EAC}$	Crack growth rate for environmentally assisted cracking, m/s
A_2	Area of cross-section of the aluminum tensile specimen, m^2
c	Viscous damping coefficient, m/s
δ_{max}	Displacement amplitude at the tip of a microcantilever, m
E	Elastic modulus, GPa
E_1	Elastic modulus of silicon, GPa
E_2	Elastic modulus of aluminum, GPa
ε	Strain
f, f_0, f_1	Resonant frequency, Hz
f_n, f_r	Resonant frequency of a microcantilever in vacuum, Hz
f_{ra}	Resonant frequency of a microcantilever in air, Hz
f_{nl}	Resonant frequency of a microcantilever in liquid, Hz
F	Gage factor of a strain gage
F_1, F_2, F_3	Forces in the spring elements of the tensile specimen, N
F_{act}	Total force required from the LVPZT for a given strain, N
Δf_{saline}	Change in resonant frequency of Ti coated microcantilevers in saline, Hz
Δf_{air}	Change in resonant frequency of Ti coated cantilevers in air, Hz
γ	Damping factor
I	Moment of inertia, m^4
I_{ctd}	Moment of inertia of a Ti coated microcantilever, m^4
I_{unc}	Moment of inertia of a Ti coated microcantilever after cracking of the entire coating, m^4
k_{eq}	Equivalent stiffness/ spring constant, N/m
k_1, k_2, k_3	Spring constants of microstructures of the tensile specimen, N/m
K, K_0, K_1	Spring constant of a microcantilever, N/m
K	Stress intensity factor, MPa$\sqrt{m}$
l, L	Length of microcantilever, m
l	Length of aluminum tensile specimen, m
L_1, L_3	Length of spring microstructures of the tensile specimen, m
l_P	Length of the Permalloy strip, m
M_c	Initial mass of microcantilever, kg
m, m_0, m_1	Effective mass of a microcantilever, kg
Δm_m	Additional mass of minerals deposited on a microcantilever, kg/m^2
η	Refractive index
N	Number of cycles
N_L	Number of leaf springs

Q	Q-factor
ρ	Density, kg/m^3
ρ_l	Density of liquid, kg/m^3
ρ_{Si}	Density of silicon, kg/m^3
ρ_P	Density of Permalloy, kg/m^3
σ_{max}	Maximum stress during a loading cycle, N/m^2
σ_{min}	Minimum stress during a loading cycle, N/m^2
σ_m	Mean stress during a loading cycle, N/m^2
σ_a	Alternating stress during a loading cycle, N/m^2
σ_{Eq}	Equivalent alternating stress, N/m^2
σ_{th}	Thermal stress, N/m^2
R_g	Resistance of strain gage, Ohm
S	Stress, N/m^2
S_u	Ultimate tensile strength, GPa
t	Thickness of microcantilever, m
t_P	Thickness of Permalloy layer, m
t_{poly}	Thickness of the polysilicon layer, m
t, T	time, sec
T	Total test time, sec
ΔT	Change in temperature, °C
v_0	Velocity amplitude, m/s
w	Width of microcantilever, m
w	Width of aluminum tensile specimen, m
ω	Resonant frequency of a cantilever, rad/s
x_1, x_2, x_3	Displacements at specific points of the tensile specimen, m
X	Resonant amplitude, m

CHAPTER 1

Motivation

Micro-electro-mechanical Systems (MEMS) have witnessed rapid technological advances over the past two decades. Applications such as pressure transducers, accelerometers, digital micro-mirror displays, and inkjet printer heads are among the key commercial successes. As laboratory prototypes continue to evolve into commercial products, the market for MEMS is expected to grow steadily with some studies predicting a multi-billion dollar market for MEMS by 2015 [1, 2]. Significant demand for MEMS is projected from diverse industrial sectors such as biomedical, chemical, pharmaceutical, petrochemical, defense and aerospace [2, 3].

MEMS have received attention from various sectors of the industry due in part to their ability to integrate micron-sized mechanical structures (microstructures), and electronic circuitry in a relatively small device. Further, MEMS offer low unit cost advantages over conventional electromechanical devices since they can be batch-fabricated using semiconductor processing techniques [3, 4]. MEMS are the next logical step for microelectronics: the electronic circuit processes and stores information, while the microstructures can interact with physical environment to sense and modify information. The ability to manipulate microstructures is a key feature of MEMS, and is considered an important tool for the development of nanotechnology.

The techniques for design, fabrication, and testing of microstructures are a relatively recent development compared to established practices for microelectronic circuits. While established design and testing standards exist for microelectronic devices, no

comparable standards have been developed for microstructures. Considering the extremely small length scales of microstructures, mechanical design guidelines and test standards developed for macroscale structures and machinery may not be extended to predict mechanical behavior of microstructures.

There are fundamental differences in material behavior and properties between microstructures and macroscale objects, primarily due to length scale effects. Often, the dimensions of microstructures are of the order of a few micrometers which is comparable to the size of the grains constituting the microstructure as illustrated in Figure 1.1. For microstructures, the typical value of surface area to volume ratio can be 1000 times compared to bulk materials, and as a result surface effects are expected to dominate deformation mechanisms. Viscosity, surface tension, and damping dominate dynamics of microstructures when compared to inertial or gravitational effects.

During the last decade, several researchers have recognized these fundamental differences and have experimentally investigated basic mechanical properties of microstructures such as fracture stresses, hardness, and elastic modulus using microscale test specimens [5-7]. These investigations have revealed several interesting aspects of microscale material behavior which are in contrast to their macroscale counterparts. For example, Haque [8] observed that yield strength values obtained from experiments conducted on microscale aluminum tensile specimens were 33 times smaller compared to bulk values. This behavior was attributed to the increasing volume fraction of disordered grain boundary atoms with extremely small grain sizes (~ 50 nm) characteristic of microstructures. Other studies have reported significant differences in failure mechanisms of microstructures when compared to their macroscale counterparts.

For example, while bulk silicon was not known to exhibit fatigue fracture [9], several investigators have observed fatigue fractures in silicon microstructures after 10^5-10^{11} cycles [10-15]. Silicon microstructures exhibit fatigue due to environmentally assisted stress-corrosion cracking of the ~ 50 nm thick native oxide layer [10]. For bulk silicon, the 50 nm thick native oxide layer is not sufficient to contain the critical crack size [10]. Unpredictable mechanical behavior and failures similar to those described above can lead to subtle changes in mechanical performance, or complete structural failure of microstructures. Any compromise in the mechanical stability or structural integrity of the microstructures can cause performance degradation or failure of microstructural components. Hence, performance and reliability of MEMS are an important concern.

The present understanding of mechanical performance and reliability of MEMS is limited to studies which have been carried out in air or vacuum [6, 8, 11, 12, 14, 15]. As MEMS continue to evolve for deployment in critical applications in aerospace, defense, biological, and petrochemical industries, understanding effects of extreme environmental conditions on the microstructures is important. Several current or potential critical applications such as oilfield chemical sensors [16], implantable biological sensors, drug delivery BioMEMS, lab-on-chip devices, microfluidic devices (e.g. micro-pumps), and optofluidic devices [17] operate in liquid environments. Designing MEMS for reliable operation in liquid environments is more complex compared to air due to coupled effects of microscale liquid-structure dynamics [18], environmental interactions with liquids, and mechanical stresses.

Further, several current and potential applications of MEMS require long-term operation, often over their lifetime spanning several years without replacement or

periodic inspection. For example, MEMS automotive airbag accelerometers are expected to function over several years and still deploy airbags reliably when required. Potential applications such as implantable closed loop drug delivery systems [19], and implantable sensors [20] also require continuous and reliable operation *in vivo* over several years. Hence, understanding the long-term mechanical performance of MEMS in important.

The motivation of this study was to investigate long-term mechanical performance and reliability of MEMS in liquid environments. Performance and reliability of common MEMS materials under coupled effects of cyclic mechanical stresses and liquid environments was experimentally investigated. Under the combined effects of mechanical stresses and liquid environment MEMS may fail due to either structural or operational failures (performance degradation). In this study, microscale test structures and experimental techniques were developed to investigate long-term MEMS failures in liquid environments.

1.1. Objectives

The present understanding of long-term failures of MEMS is limited to air or vacuum as the operating or testing environment. The motivation for this research is to extend the present knowledge of long-term failures of MEMS to include liquid environments. The specific objectives of this research are:

(i) To experimentally investigate long-term failures of MEMS in liquid environments.

(ii) To study the role of mechanical stresses, materials, and liquid environments on the long-term performance of selected MEMS structural materials and coatings.

The primary contribution of this research will be to advance the understanding of failure mechanisms of materials currently used in MEMS operating in liquid environments. This study is comprised of an experimental study of MEMS cantilever specimens (for operational failures) and tensile specimens (for structural failures) tested in liquid environments. The experimental results of this study can be used to develop design guidelines, criteria for material selection, and enhance the performance and reliability of MEMS operating in liquids.

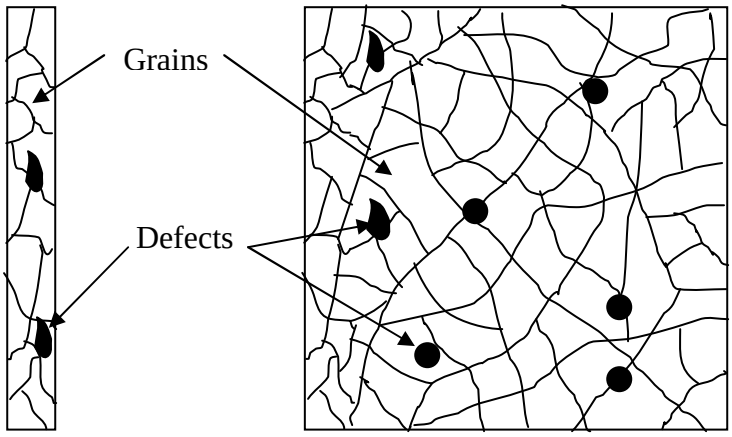

Figure 1.1. Comparison of microstructures to macroscale objects: (a) for microstructures specimen dimensions are of the same order as grain sizes and defects (b) for macroscale objects grain sizes and defects are much smaller compared to specimen dimensions

CHAPTER 2

Literature Review

In this chapter we review the literature for long-term mechanical performance of MEMS with specific attention to the following questions:

(i) What are the typical long-term mechanical performance issues observed in MEMS?

(ii) Which are the typical materials tested?

(iii) What are the typical test conditions?

- mechanical stresses
- environment
- number of cycles

Since mechanical testing of MEMS is still in its early stages, we also focus on the experimental techniques employed in the literature. We first discuss long-term mechanical performance issues of MEMS reported in the literature with specific focus on failure modes, materials, experimental techniques, and test conditions. Next, we discuss the effect of environmental interactions in liquids on mechanical failures and implications for MEMS in section 2.2.

2.1. Long-term mechanical performance of MEMS

MEMS are susceptible to sudden mechanical failure due to overloading, shock, impact, vibration, and stiction (un-intentional adhesion) during handling, storage, or processing [21]. In service, long-term mechanical performance of MEMS is an added concern in addition to these sudden failure modes. Long-term performance of MEMS

can be compromised due to electrical failures, but is outside the scope of this study. A review of the literature reveals that a majority of the researchers studying long-term mechanical performance of MEMS have reported failure modes which can be classified into two broad categories:

(i) Structural fatigue failures

(ii) Operational failures due to shift in mechanical performance.

In the following sections, we review the literature for each of these failure modes. Conclusions based on the literature review are discussed in section 2.1.3.

2.1.1. Structural fatigue failures

Structural fatigue failures in MEMS have been observed when microstructures were subjected to cyclic mechanical stresses. Table 2.1 summarizes selected microscale fatigue testing efforts. Structural fatigue failures in MEMS have been reported in air or vacuum for ceramic and metallic materials, but only at high stress levels close to the tensile strength of the material. For example, fatigue failures in silicon (ceramic) were observed at stress levels of 1-10 GPa, while the tensile strength of silicon is typically 1-4 GPa. Typical fatigue life was 10^5 to 10^{11} cycles for ceramics and 10^3 to 10^7 cycles for metals. Often the cyclic frequencies for the applied alternating stresses were as high as 40 kHz [11]. The objective of this section is to evaluate challenges with microscale fatigue testing and review fatigue testing of MEMS reported in the literature. Further, we focus on critical observations such as microscale specimen design, novel experimental techniques, stress levels, test frequencies, and materials. A review of fatigue failures of metals at the macroscale is included in Appendix A.

(i) Challenges with microscale fatigue testing: Presently microscale fatigue testing in MEMS is in its early stages, and standardized test procedures or specimens have not been developed to date. Macroscale fatigue testing protocols such as ASTM Standard E 466 (developed for stress or strain life (S/N) testing of bulk metallic materials) may not be extended to include microscale specimens. Materials commonly used in MEMS, for example, silicon and silicon nitride are ceramics, hence, conventional test procedures employed for testing ductile metals cannot be directly applied to microscale fatigue testing. Further, a conventional understanding of macroscale ceramic fatigue failures may not apply to MEMS structures in view of their extremely small dimensional features. For example, while Chen and Knapp [9] report that bulk silicon is not susceptible to ductile or brittle fatigue, several studies have observed fatigue failures in silicon MEMS structures [10-15, 22]. Fatigue failures in MEMS are expected to be different from those at macroscale because of extremely small length scales, and higher surface area-to-volume ratios. These observations emphasize the need to develop specialized microscale fatigue testing procedures and understand microscale failure mechanisms.

Apart from the effects of extremely small length scales, variation in crystal structure of MEMS and anisotropy also complicates the understanding of microscale fatigue failures. While conventional understanding of fatigue failures is predominantly based on polycrystalline metals, microstructural features in MEMS range from a single crystal structure in single crystal silicon (SCS), to polycrystalline in polysilicon, and amorphous in silicon oxide. For SCS, material properties such as elastic modulus are dependent on crystallographic directions [13, 23].

Fatigue testing in MEMS presents several practical challenges. Design of test structures, loading, and mounting of specimens is complicated due to the extremely small length scales of MEMS. Identification of fatigue failures, crack propagation rates, and failure mechanisms are yet another challenge at the microscale. For example, conventional fatigue crack propagation testing on a compact notched specimen may involve measuring the crack size periodically by visual examination (or monitoring the change in resistance of the specimen), which is difficult for microscale fatigue testing. The magnitude of microscale fatigue crack growth rates is yet another challenge primarily due to the small length scales. Fatigue crack growth velocities for macroscale specimens have been observed to be greater than 10^{-8} m/s [15]. For microstructures, crack growth rates of the order of 10^{-8} m/s are fast, and would lead to failure within a few minutes of testing [15]. For instance, based on a crack growth velocity of 10^{-8} m/s a 2 μm thick typical surface-micromachined [3] microstructure is expected to fail in only 3.4 minutes. For long-term fatigue failures in MEMS, crack growth velocities of the order of 10^{-12} m/s must be understood to design reliable MEMS devices [15]. In view of these practical challenges and absence of standardized test protocols, different investigators have explored novel specimen designs, and loading mechanisms as described below.

(ii) Microscale fatigue testing efforts: Connally and Brown were among the earliest investigators to report fatigue failures in MEMS [12]. They studied fatigue in boron (B) doped SCS MEMS cantilever test specimens. The electrostatically actuated cantilever specimens were 235 μm long, 150 μm wide, and about 130 μm thick and were pre-cracked using a nano-indenter. Connally and Brown [12] observed a change in

resonant frequency of 130 Hz (1.05 % of initial resonant frequency) after testing for 2 x 10^7 cycles (1600 seconds). Ando et al. [13] have proposed a bulk micromachined SCS test specimen for tensile-mode fatigue testing of SCS thin films. Load was applied to the specimen using an external actuator. They observed that the number of cycles to failure was dependent on the amplitude of applied strains (2 to 6%). Assuming the elastic modulus of silicon to be 160 GPa, the applied stress levels are estimated to range from 3.2 to 9.6 GPa. Sharpe and Bagdahn [14] have developed a tensile fatigue test method using surface micromachined polysilicon test specimens produced by a MUMPs^{TM} process [24] (run 36). The specimen was 3.5 µm thick and separated from the substrate by a 2 µm gap. One end of the specimen is glued to a silicon carbide fiber, while the other end of the fiber is attached to a piezoelectric actuator or loudspeaker, to enable cyclic actuation. They observed fatigue life ranging from 10^4 to 10^9 cycles corresponding to maximum stress of 0.9 to 0.7 GPa. Van Arsdell and Brown [15] have developed a surface micro-machined polysilicon MEMS fatigue test specimen as shown in Figure 2.1. The test specimen is attached to a fan-shaped resonant mass, with identical inter-digitated capacitive transducers (known as comb drives) at either ends. One of these comb drives was used to actuate the resonant mass, while the other was used as a capacitive displacement sensor. Advantages of this structure over other fatigue test specimens are capability of complete stress reversals, and high-frequency testing. Muhlstein et al. [11] used a test specimen similar to that described in [15] and observed fatigue life in silicon increase from 10^5 to 10^{11} cycles as stress amplitudes are decreased from 10 to 4 GPa. Muhlstein et al. [10] proposed that fatigue failures in silicon are observed at the microscale due to stress corrosion cracking of the 50 nm

thick superficial silicon oxide layer. For microstructures, the 50 nm thick silicon oxide is thick enough to contain the critical flaw size for fatigue failure. In contrast, for bulk silicon the thickness of the silicon oxide layer (50 nm) is insufficient to contain the critical flaw size. Kahn et al. [25] contest the simple stress-corrosion cracking mechanism proposed by Muhlstein et al. [10] and suggest that stress-corrosion cracking does not occur in polysilicon without cyclic loading. Kahn et al. [25, 26] have developed their hypothesis based on tests on their polysilicon test structure which is capable of testing at different values of mean and alternating stresses. Most of the studies discussed above have used a stress-based approach to explain their findings and summarized their results using S-N curves.

(iii) Critical observations: Novel design features and experimental and characterization techniques have been employed for microscale fatigue testing. A notable design feature was the extensive use of electrostatic actuation schemes to load the test specimen. Since MEMS are typically low power devices [3], generation of large forces required to attain mechanical stresses that will cause fatigue failures is challenging. Electrostatic actuation has the largest power density in air and is preferred over other actuating schemes. Several studies have employed an external mechanical actuator, but were restricted to testing at lower frequencies (~ 10 Hz) [13]. A common technique employed by several investigators to increase the stress amplitudes was to actuate the test specimen at its resonant frequency [11, 12]. A majority of fatigue studies in MEMS beginning with the first investigation by Connally and Brown [12] to date have employed some configuration of a vibrating cantilever beam test specimen. The

resulting stress-state for the test structures was either completely reversed or fluctuating bending stresses.

The extremely small feature sizes of MEMS have also led to the use of advanced experimental and characterization techniques such as atomic force microscopy (AFM), scanning electron microscopy (SEM), transmission electron microscopy (TEM), and electron dispersive spectroscopy (EDS). For example, Allameh et al. [22] have used the AFM for *in-situ* AFM observations while actuating their specimens at resonance in order to characterize failure. They observed changes in surface morphology with cyclic actuation, and an increase in surface roughness of the specimen, which are more pronounced near the notch-tip. Muhlstein et al. [10] have observed oxide thickening and cracks near the notch tip of their MEMS fatigue test specimens using high voltage TEM (HVTEM). SEM imaging for examination of the fractured surfaces is common practice in the literature. Several investigators have used the change in stiffness of the MEMS test specimen over time as an indicator of fatigue crack growth. The resonant frequency of the specimen in air is recorded after every few cycles in order to track the change in stiffness, or increase in crack length. Muhlstein et al. [11] had observed the resonant frequency to decrease by 24 Hz for an initial resonant frequency of 40 kHz, which translates to 0.06 %. Hence, we conclude that extremely small frequency changes could also be indicative of mechanical failures in MEMS.

A majority of fatigue failures in silicon MEMS have been observed at high stress amplitudes ranging from 0.85 to 4 GPa, which is comparable to the tensile strength of silicon (~1-3 GPa) [11]. However, these stress levels are much higher that that experienced by several MEMS applications such as resonators, sensors, and AFM tips.

Long-term performance of MEMS subjected to comparatively smaller stress levels has been reported in the literature and discussed in the following section.

2.1.2. Operational failures due to instability in mechanical performance

The test specimens discussed in the previous section were designed to study microscale fatigue failures, and were subjected to stress levels comparable to the ultimate tensile strength of the material (e.g 1-3 GPa for silicon). For a complete understanding of long-term mechanical performance of MEMS, investigating mechanical stability of practical microstructure designs subjected to typical operational stresses is also important. Due to the extremely small length scales, different mechanical properties, and relatively defect-free structures, long-term failures in MEMS may be characterized differently than complete structural fatigue failure. Long-term failures in MEMS may assume a subtle form such as degradation in rated performance, mechanical stability, and accuracy. These unpredictable deviations from expected mechanical performance can lead to operational failures [27] in MEMS. In this section, we discuss the significance of operational failures in MEMS, and review the literature for operational failures reported in MEMS.

Operational failures are an important concern due in part to typical operational characteristics of MEMS [27]. Several important applications of MEMS, such as embedded sensors and resonators, subject the microstructures to high-frequency vibrations (1-100 kHz), and harsh environments during the service life of the device. Due to high-frequency vibrations, MEMS accumulate a large number of cycles in a relatively short time period. For example, a MEMS resonator operating at 30 kHz will experience about 10 billion cycles during 1000 hours of service, and the number of

cycles is substantially higher than a macroscale turbine would experience rotating at few thousand RPM [28]. Tapping mode AFM tips with a typical operating frequency of 10 kHz will experience 6x 10^6 cycles during a single scan typically lasting 10 minutes. Thus, effects of cyclic stresses on mechanical performance are an important concern for such high-frequency applications. Further, several MEMS devices are frequently exposed to harsh environmental conditions when used as embedded sensors or actuators such as accelerometers, chemical and biological sensors, and drug delivery applications. Harsh environmental conditions may result from extremes in temperature and humidity, chemical corrosion, vibration, and shock. Thus environmental conditions may cause operational failures by affecting the mechanical performance of MEMS.

Several instances of operational failures that have been reported in the literature are summarized in Table 2.2. Sparks et al. [28] had observed performance change in an electroplated nickel angular rate MEMS sensor at stress levels as low as 22-24 MPa, but without structural failure. The predicted endurance limit for electroplated nickel using macroscale approach should range between 98.3 to 242 MPa. While stresses in the range of 22-24 MPa should not induce fatigue failure, a shift in performance indicated by a shift in operational parameter (BLFO, balance loop filter output) is experimentally observed. These findings suggest that changes in mechanical performance can occur at low stress values. Frederick and Fedder [29] have investigated mechanical effects of fatigue on CMOS MEMS, by cyclically actuating polysilicon test specimens similar to Van Arsdell and Brown [15], but at much lower stresses. They observed that while peak cyclic stresses of 70 MPa did not result in mechanical fracture after 5 billion cycles, resonant frequency decreased indicating a change in stiffness. These findings

indicate that at low stress levels, failures at the microscale may assume the form of a subtle shift in mechanical performance instead of complete structural failure.

Environmental effects have been reported to affect the long-term mechanical performance of MEMS. Ono and Esashi [30] have studied the stability of mechanical performance of nanometer-scale silicon microcantilever resonators in ultra high vacuum. They report a change in resonant frequency of the cantilevers with time due to desorption of superficial water or oxygen molecules and resulting change in surface stresses. Ono and Esashi [30] discuss that adsorption of oxygen results in breaking of Si-Si bonds and formation of Si-O-Si bonds leading to a tensile surface stress, which in turn leads to an increase in beam length and resonant frequency. Kazinczi et al. [31] have used a conventional AFM system to study fatigue failure in LPCVD silicon nitride AFM cantilever tips. They observed a gradual increase in resonant frequency from 34 kHz to 34.7 kHz (2 % increase). The authors suggest that a stiffening mechanism due to the oxidation of silicon clusters on the cantilever surface which causes formation of a stiff layer of silicon oxynitride may be responsible for the change in resonant frequency. Resonant frequency was employed as an indicator of stable mechanical performance by several investigators. While structural fatigue failures inevitably led to a decrease in resonant frequency, operational failures were observed to cause either an increase or decrease in resonant frequency. The reported shifts in resonant frequencies are small (~ 0.05 to 2 %); however, such unpredictable changes in stiffness and resonant frequency can lead to false signals in an AFM, or incorrect mass sensing using nano-mechanical sensors [32]. For example, Lavrik and Datskos [32] report a frequency shift of 2 kHz (0.08%) while sensing a mass of 5.5 femto-gram using

nano-mechanical resonators with a resonant frequency of 2.25 MHz. MEMS resonators which are an important application in the wireless communication industry are required to meet a sub ppm/yr quartz stability [1].

Certain environmental interactions reported in the literature indicate potential possibilities of operational failures. For example, polymeric MEMS materials such as SU-8 are known to absorb water [33]. Microstructures made of SU-8 may absorb water or moisture in service leading to performance degradation. Similarly, silicon nitride microcantilevers exhibited an affinity towards calcium ions (Ca^{2+}) in a liquid $CaCl_2$ solution [34]. Hence, unpredictable selective affinities of MEMS materials towards certain chemical species or solvents present in the surrounding environment affect mechanical performance. While no long-term failures have been documented, chemical interactions similar to those discussed above can result in operational failures. In summary, operational failures may constitute a critical failure mode for MEMS.

2.1.3. Conclusions

Long-term performance of MEMS is influenced by three major parameters:

(i) magnitude of mechanical stresses: low or high

(ii) type of material: ceramic, metal, or polymer

(iii) type of environment: inert or aggressive

Table 2.3 shows a summary of expected long-term failure modes for each category of material type based on environment and stress level. From the literature survey we make the following observations:

(i) *Long-term mechanical performance*: Long-term mechanical performance issues in MEMS can be classified into two broad categories: (i) structural fatigue failures,

and (ii) operational failures. In addition to structural fatigue failures which have been known to cause premature and unpredictable failure of macroscale machine components, operational failures are an added concern for microstructures.

(ii) *Materials*: Common MEMS materials tested in the literature are ceramics such as single crystal silicon [11-13, 15], polysilicon [6, 10, 14, 22], and silicon nitride [35]. Thin films of metals and alloys such as nickel [36], titanium [37], silver [38], aluminum [39, 40], nickel-phosphorus alloy [41] have also been studied. As MEMS fabrication processes and techniques continue to grow beyond the traditional boundaries of microelectronics processing to include polymers, mechanical properties of polymer microstructures have also been examined [42]. Fatigue behavior for single crystal silicon and polysilicon is most widely documented among all MEMS materials, as these materials are the most widely used structural materials for MEMS.

(iii) *Test conditions*: Typical mechanical stresses observed for experiments which reported structural fatigue failures in silicon [11] and metals [39] often had stress amplitudes in the range of 80 to 100 % of value of ultimate tensile strength (UTS) of the specimen. Muhlstein et al. [11] had observed fatigue failures in silicon at stress amplitudes of 4-10 GPa. They observed fatigue life to range between 10^5 to 10^{11} cycles. Macroscale fatigue in metals is often observed at much lower stress levels of 35-85 % of the value of UTS [43]. For several studies that report operational failures, the mechanical stresses were not explicitly stated. From calculations based on values of loads and displacements, the expected value of mechanical stresses for these studies is approximately 1-10 MPa for ceramics

(silicon, silicon nitride) which have tensile strength values of the order of 1-3 GPa. Sparks et al. [28] observed operational failure in nickel at stress level of ~10% of the value of UTS. We conclude that high values of cyclic stresses (80-100 % of UTS) lead to structural fatigue failures in microstructures, while operational failures are observed at lower stress levels (smaller than ~10% of UTS).

Both structural and operational failures were observed to cause small changes in resonant frequencies ranging from -0.06 % to + 2 %. Though the magnitude of the change is small, we note that microcantilever sensors are designed to respond to resonant frequency changes as small as 0.08 % to sense, for example, presence of micro-organisms [32]. Hence, we conclude that any unpredictable change in resonant frequencies as small as 0.06 % may indicate degradation in mechanical performance.

The test environment for the majority of the studies discussed in the preceding review was air or vacuum. Mizutani et al. [44] had observed that MEMS cantilever specimens of Ni-P amorphous alloy actuated in air failed after 5×10^5 cycles, while those actuated in NaCl solution withstood only 6×10^3 cycles. While they do not discuss the exact failure mechanisms or stress levels, their findings emphasize the detrimental effect of a liquid environment on MEMS. The effects of liquid environments on long-term failures in MEMS are largely unexplored.

(iv) *Scope of current research*: The primary focus of the current research is to extend the understanding of long-term mechanical performance of MEMS to liquid environments. We investigate long-term mechanical performance of MEMS in liquid environments at both low and high stress levels. Low-stress levels tests are

performed on microcantilever test specimens in liquid filled enclosures, and are expected to advance the present understanding of operational failures to include liquid environments. Silicon and silicon nitride (both ceramics) are chosen as structural materials for low-stress level tests. Performance of titanium (metal) and SU-8 (polymer) are evaluated as coatings on silicon microcantilevers. High-stress level tests are conducted on aluminum (metal) MEMS tensile test specimens in liquids and are intended to study the effect of liquid environments on structural fatigue failures.

In the following section, we review the literature for the effects of liquid environments on mechanical performance of microstructures.

2.2. Environmental interactions in liquids

In the previous section we reviewed the long-term mechanical failures in MEMS, with specific focus on stress levels, materials, and life (number of cycles to failure). We now review the literature to evaluate the role of liquid environments on long-term mechanical failures in MEMS. Liquids can influence the failure of MEMS operating in liquid environments due to both physical and chemical interactions. Liquids influence the dynamics of MEMS operating in liquid environments. Liquid viscosities tend to damp the motion of microstructures and damping effects can be strongly enhanced by small surrounding dimensions often of the order of a few micrometers. Naik et al. [18] in their study of dynamics of a cantilever oscillating close to a surface in liquids reported that the cantilever resonant frequency is affected by the gap height and width of the cantilever. Also, the resonant frequency of the cantilevers was observed to be smaller in liquids compared to air due to the ‘added mass’ effect [18].

Chemical interactions with the liquid environment can result in either adsorption of chemical species or dissolution of microstructure. For example, Cherian et al. [34] have observed that stationary silicon nitride cantilevers chemisorb calcium ions (Ca^{2+}) from surrounding liquid environment ($CaCl_2$ solution). For metallic microstructures, dissolution due to corrosion can result in loss of material. The mechanism of corrosion in metals is an electrochemical process involving transfer of electrons from one chemical species to another. Ceramics are reported to be relatively resistant to corrosion except at high temperatures. Corrosion of ceramics involves simple chemical dissolution without any role for electrochemical processes. Hence, ceramic MEMS structural materials such as silicon are not expected to undergo corrosion in ambient environments. Chemical dissolution of ceramics is a possibility only in liquids which etch or dissolve silicon such as potassium hydroxide (KOH). Deterioration of polymers due to undesirable interactions is specified as degradation rather than corrosion due to differences in failure mechanisms. Polymers exposed to liquids may experience degradation by swelling and dissolution. When polymers are exposed to liquids or solvents, the liquid molecules diffuse into the polymer and are absorbed. The small liquid molecules occupy spaces between the polymer macromolecular chains and gradually force them apart. Increased separation between the macromolecules at the microscopic level leads to swelling of the polymer specimen [45]. Increased separation between the macromolecular chains leads to the polymer becoming softer and ductile. Dissolution of polymers occurs when the polymer is soluble in the liquid.

In the following sections we focus on the effects of corrosive liquid environments on fatigue failures in metals at the macroscale. The objective of the following

discussion is to understand fatigue failures of metallic materials in corrosive liquids since in this study metals such as titanium and aluminum were tested in saline. Corrosive liquid environments such as seawater have been known to accelerate fatigue failures of engineering metals at the macroscale [46]. Environmentally induced mechanisms responsible for corrosion are discussed in section 2.2.1. In section 2.2.2 we compare the individual and combined effects of mechanical stresses and environmental effects on corrosion of metals. A review of environmental effects on small fatigue cracks which may be encountered in MEMS is included in section 2.2.3. Finally, implications for metallic MEMS operating in liquids are discussed in section 2.2.4.

2.2.1. Corrosion fatigue of metals in liquids

Resistance to fatigue failure of engineering metals and alloys is compromised in corrosive gases, liquids and solid [47]. The phenomenon of corrosion of engineering metals and alloys in aqueous solutions under steady mechanical stresses is referred to as stress corrosion cracking [47]. For ductile metals immersed in aqueous media and subjected to either cyclic or monotonic loads, environmentally induced damage involves electrochemical reactions occurring in the vicinity of the crack tip or slip steps. The electrochemical reactions may be driven by two different environmentally induced mechanisms:

(i) Anodic slip dissolution, and

(ii) Hydrogen embrittlement.

Anodic slip dissolution involves repeated formation and rupture of a passivating oxide film over the metal surface. Suresh [47] describes the stepwise mechanism of anodic slip dissolution:

(i) diffusion of active species such as water molecules or halide ions to the vicinity of the crack,

(ii) rupture of the protective oxide film at the slip steps or in the immediate wake of the crack tip,

(iii) dissolution of the freshly exposed metallic surfaces, and

(iv) nucleation and growth of oxide on these bare metallic surfaces.

Under cyclic loads, crack growth rates are determined by the oxide film rupture rate, solution renewal rate, and the passivation rate. Crack growth rates are reported to be strongly influenced by cyclic frequency and load waveform.

The alternative mechanism of environmental damage, termed as hydrogen embrittlement occurs due to incorporation of hydrogen in the metal. Hydrogen is introduced into the metal as atomic hydrogen from dissociated hydrogen molecules or release of hydrogen from metal dissolution, and damages the mechanical response of the metal. Hydrogen embrittlement in aqueous media involves the following critical steps [47]:

(i) diffusion of water molecules or hydrogen ions between crack walls toward the crack tip,

(ii) reduction chemical reactions leading to formation of hydrogen atoms at the crack tip,

(iii) diffusion of adsorbed atoms to preferential sites along the surface, and

(iv) absorption of hydrogen adatoms to a critical location such as a grain boundary or a void.

2.2.2. Crack initiation and crack growth in corrosive aqueous environments

The objective of this section is to study the role of a corrosive environment on crack initiation and crack growth. Fatigue cracks initiate at stress concentration sites such as corrosion pits. Electrochemical effects are pronounced at bare surfaces of fatigued metal where the oxide film has ruptured and plastic deformation is localized. Oxidation of the slip steps leads to slip irreversibility and impedes crack closure effects. Dissolved oxygen in aqueous media is essential for corrosion fatigue to occur in neutral pH solutions. Grain boundary precipitates affect corrosion fatigue of aluminum alloys in aqueous media by affecting hydrogen evolution and altering the chemistry and fracture stress at the crack tip. Corrosion pits can often nucleate along grain boundaries.

Fatigue crack growth rates are enhanced in corrosive liquids for most ductile metals. Fatigue crack growth in a corrosive liquid is due to combined effects of the environment and mechanical stresses. The relative effects and interaction of these two effects can be evaluated by considering crack growth rates under purely mechanical stresses or purely environmental effect of a corrosive liquid. Figure 2.2a shows the variation of fatigue crack growth as a function of stress intensity factor range under cyclic mechanical stresses in an inert environment. The vertical axis represents crack growth rate per cycle. The horizontal axis, ΔK is proportional to the amplitude of the imposed alternating stresses (σ_a) (Appendix A). Crack growth rates are low at small values of ΔK (or σ_a), which increase gradually with increasing ΔK, and experience a steep increase at high values of ΔK. Figure 2.2b shows the typical trend of crack growth rate

(crack velocity) of a metallic material in a corrosive medium at steady mechanical stresses (σ_a=0, $\sigma_m \neq 0$). This phenomenon is known as stress corrosion cracking. The crack growth rate is plotted as a function of applied stress intensity factor on a log-log scale. Since no cyclic stresses are present, crack growth rate per unit time (*da/dt*) is plotted on the vertical axis. Figure 2.2b shows that environment does not affect crack growth rate below a threshold stress intensity factor, K_{Iscc}. For $K_I > K_{Iscc}$, three distinct crack growth regimes can be observed. In region I, a rapid increase in crack growth is observed. The crack growth rate is independent of stress intensity factor in Region II. With further increase in K approaching the fracture toughness (K_c) of the material, a steep increase in crack growth rate is observed. Hence, subcritical crack growth can occur under the effect of a corrosive environment at stress intensity factors much lower than the critical stress intensity factor (K_c).

Depending on the relative effects of cyclic stresses and stress corrosion, three different modes corrosion fatigue can occur: stress corrosion fatigue, true corrosion fatigue, and mixed corrosion fatigue. A simple superposition of mechanical fatigue (Figure 2.2a) and stress corrosion cracking (Figure 2.2b) leads to a crack growth variation shown in Figure 2.3. This phenomenon is termed as stress corrosion fatigue and and occurs when $K_{max} > K_{Iscc}$. Enhanced crack growth rates are observed for $K_{max} > K_{Iscc}$ in a corrosive environment, while crack growth rates are identical for inert and corrosive environments for $K_{max} < K_{Iscc}$. Figure 2.4 compares the variation in crack growth rate with ΔK for a metallic material due to the environment only, with no steady mechanical stresses applied (σ_m= 0, $\sigma_a \neq 0$). It is observed that the crack growth rates are higher in the corrosive liquid compared to an inert environment. This behavior is

termed as true corrosion fatigue. For true corrosion fatigue, the environment acting by itself does not affect crack growth. The environment accelerates the crack growth rate only when cyclic mechanical stresses are applied, even at small values of ΔK (or σ_a). The combination of stress corrosion fatigue and true corrosion fatigue results in a behavior known as mixed corrosion behavior and is schematically depicted in Figure 2.5.

The effect of a corrosive environment on a mechanical material results due to a complex interaction between the environment, microstructure of the material, cyclic frequency, and waveform of the mechanical stresses. From the above discussion we conclude that stress corrosion effects may accelerate crack growth rates even at low mechanical stress levels typical to several MEMS applications such as microcantilever sensors. We expect corrosive liquid environments to accelerate crack growth rates and reduce fatigue life of the *metallic* microstructures. We note that mechanical materials in MEMS include a variety of materials such as metals (e.g. aluminum), ceramics (silicon), and polymers (SU-8). The above discussion is expected to serve as a guideline for metallic microstructures only.

2.2.3. Environmental effects on small fatigue cracks

Corrosion fatigue can lead to anomalous acceleration of crack propagation rates for small fatigue cracks [47]. The phenomenon of corrosion fatigue has been known to strongly depend on the crack size. For example, Gangloff [48] had observed that in the embrittling environment of 3 % NaCl, crack propagation rates for small fatigue cracks ($a \sim 0.1–0.8$ mm) in AISI 4140 steel were two orders of magnitude faster than long cracks ($a \sim 50$ mm). Crack growth rates for short and long cracks were reported to be

similar in a laboratory air environment. The anomalous crack propagation rates in a corrosive environment were observed despite the validity of LEFM (linear elastic fracture mechanics) characterization and absence of crack closure effects. Other investigators have reported chemical effects on short crack growth for ferrous and aluminum alloys fatigued in hydrogen-containing or hydrogen-producing gases or liquids. Environmental effects, particularly of corrosive aqueous media, are severe on short cracks reportedly due to enhanced electrochemical production of hydrogen within small cracks due to lowering of the pH level (increased acidification) and restricted oxygen reduction, which otherwise consumes H^+ [47]. Below a certain critical crack size, the crack surface area to crack solution volume ratio affects the acidity and chemistry of the crack tip environment [47]. The critical crack size is determined by the microstructure, environment, applied stress range, and specimen geometry [46, 47].

2.2.4. Implications for MEMS

Failures in aqueous media are fundamentally different from those in air. Experimental data and observations are necessary to understand liquid-microstructure environmental interactions. However, based on the literature review we conclude:

(i) Stress corrosion fatigue occurs in a liquid environment at stress levels which satisfy $K_{max} > K_{Iscc}$. True corrosion fatigue can occur at K_{max} values that are smaller than K_{Iscc}. At low stress levels typically encountered in MEMS, true corrosion fatigue is more likely to affect crack growth rates in MEMS. Microstructures subjected to larger cyclic stress amplitudes in corrosive environments may experience stress corrosion, true, or mixed corrosion fatigue.

(ii) K_{Iscc} values are specific to the material, environment, and temperature during the experiment [46]. Values of K_{Iscc} are determined from long-term static loading tests. The extent of corrosion fatigue is expected to depend on a particular combination of material type, environment, and test conditions. Corrosion of metallic macroscale objects is attributed to electrochemical reactions [45]. In contrast, environmental factors affect polymers differently involving both physical and chemical phenomena such as swelling and dissolution [45]. Ceramics have been reported to be immune to corrosion in most environments [45].

(iii) Further, considering the extremely small dimensions of MEMS, it is important to understand the interaction of the microstructures and the liquid environment since small cracks of the order of micro-structural features experience increased crack growth rates in corrosive environments. While at the macroscale, typically cracks of the size of 0.1 mm to 1 mm are considered small, at the microscale defects and cracks are expected to be of the order of a few microns or even smaller.

(iv) The nature of processing and testing of MEMS are expected to yield devices with only small cracks and defects of the order of the micro-structural features, which are relatively difficult to detect.

(v) Microstructural features and discontinuities such as grain boundaries, crystal structure and orientation, voids, inclusions, and precipitates may be of a same size scale as small fatigue cracks. These microstructual defects can strongly influence the rate and path of crack propagation for a small fatigue crack. In contrast, fracture behavior of a long fatigue crack is determined by the bulk properties of the material.

(vi) Lack of bulk material surrounding a small fatigue crack can also lead to unpredictable crack growth phenomena. For a long fatigue crack in a bulk material, constraint is imposed by the surrounding elastic material. Microstructures are characterized by planar geometries and possess large surface area to volume ratios, and experience minimal constraint in at least one dimension. Growth mechanisms for small cracks in MEMS may differ from long cracks in bulk materials under identical values of imposed ΔK.

(vii) The physical smallness of small fatigue cracks decreases the probability of closure mechanism competing against crack extension mechanisms, leading to increased crack growth rates. In contrast, long cracks benefit from crack closure effects and crack-wake retardation mechanisms [47].

(viii) For small cracks, which are common to MEMS and often of the order of a few nanometers, poor circulation of reactants and products can also accelerate crack growth rates. We conclude that small fatigue cracks which can occur in MEMS may have anomalously accelerated growth rates from those predicted by valid LEFM characterization.

Table 2.1. Summary of selected structural fatigue failures in MEMS

Material	Type	Stress level (GPa)	Environment	Observations	References
Silicon	Ceramic	1-6 (UTS: 1-4)	Vacuum, Humid air (34-47 % RH)	Fatigue life exceeded 10^8 cycles in vacuum. Ranges 10^4-10^7 cycles in humid air.	[25]
Silicon	Ceramic	4-10 (UTS: 1-4)	Humid Air, 50 % RH	Fatigue life was 10^5-10^{11} cycles.	[11]
Copper	Metal	0.1-0.3 (UTS: 0.3-0.38)	Ambient air	Fatigue life was 10^3 to 10^7 cycles depending on stress level	[49]
SiN	Ceramic	2-9 (UTS: 7-12)	Vacuum	Fatigue life is 10^5 to 10^8 cycles	[50]
Ni-P	Metallic Alloy	-*	NaCl solution	Fatigue life was 5 x 10^5 in air, and 6 x 10^3 cycles in saline.	[44]

* Not reported

Table 2.2. Summary of selected operational failures in MEMS

Material	Type	Stress level (GPa)	Environment	Observations	References
Nickel	Metal	0.022-0.024 (UTS 0.098-0.242)	Air/ vacuum	Change in characteristic voltage output over 500 hours	[28]
CMOS MEMS	Glass (SiO_2) and metal layers	0.070-0.124	Air/ vacuum	Resonant frequency initially 10 kHz, changes to 7 kHz over 0.2 billion cycles	[29]
Silicon	Ceramic	-* (UTS 1-4)	Vacuum	0.003% increase in resonant frequency	[30]
Silicon nitride	Ceramic	-* (UTS 1-4)	Argon, air, humid air	~0.9-2 % change in resonant frequency in 60 hours	[31]

* Not reported

Table 2.3. Expected long-term failure modes in MEMS

Material type	Typical materials	Environment	Expected failure mechanisms	
			Low stress	High Stress
Ceramics	Silicon, Silicon Nitride	Inert	-	Structural: Fracture
		Aggressive (corrosive, humid/ water)	Operational: Non-specific adsorption, chemical interactions	Structural: Fatigue, Fracture, stress corrosion
Metals and alloys	Ni-P, Nickel, Aluminum	Inert	Operational failures due to microscopic interactions	Structural: Fracture, fatigue, creep
		Aggressive (corrosive, humid/ water)	Non-specific absorption, oxidation, corrosion, stress-corrosion	Structural: Fracture, fatigue, stress corrosion, stress-relaxation
Polymers	SU-8, PMMA	Inert	-	Structural: Fracture, fatigue, creep
		Aggressive (corrosive, humid/ water)	Water absorption, stress relaxation, oxidation, stress corrosion, Hydrolysis, Ozonolysis, Chlorine induced attack	Structural: Fracture, fatigue, delamination, creep, oxidation, stress corrosion, Hydrolysis, Ozonolysis, Chlorine induced attack [45]

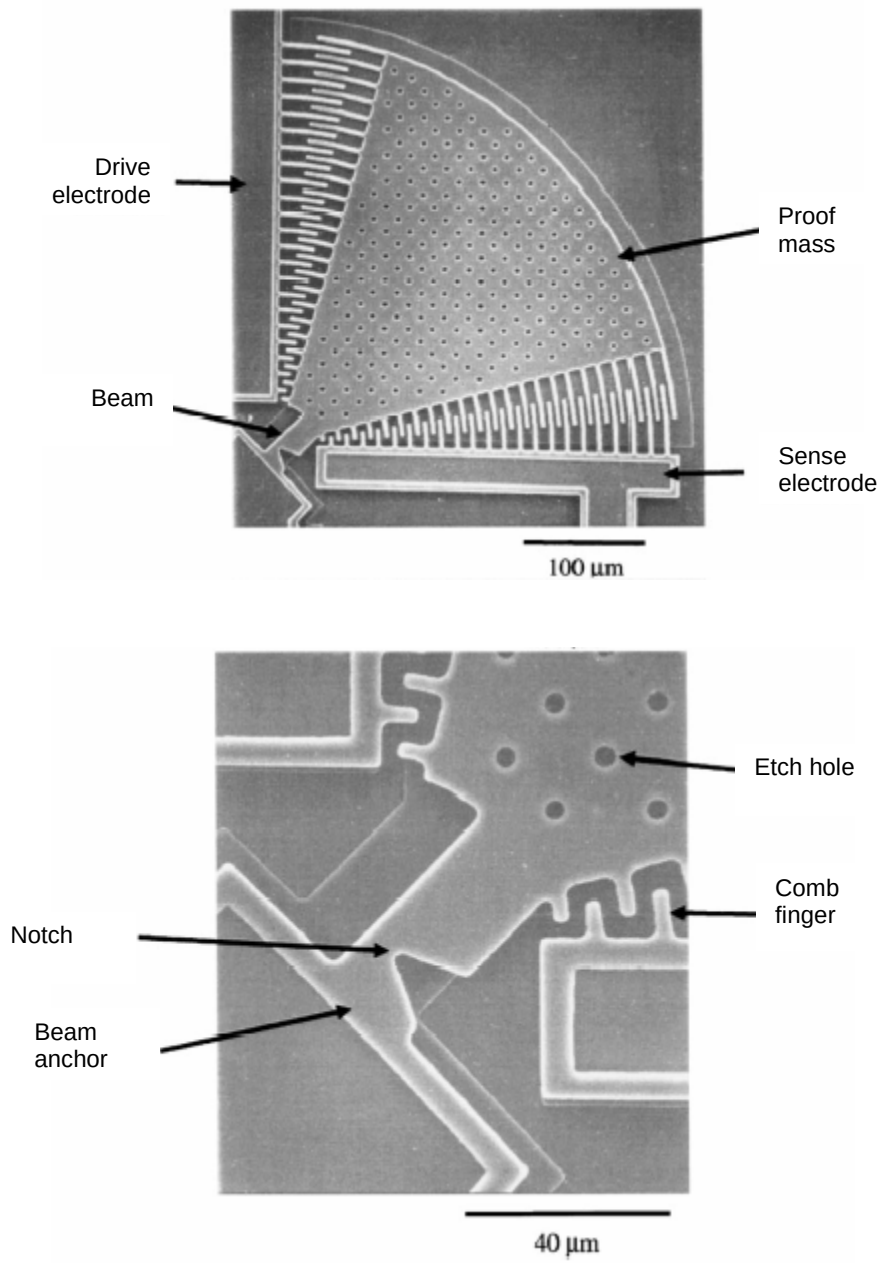

Figure 2.1. Fatigue test specimens developed by Van Arsdell and Brown [15] (a) Specimen (b) close up view of the area near the notch

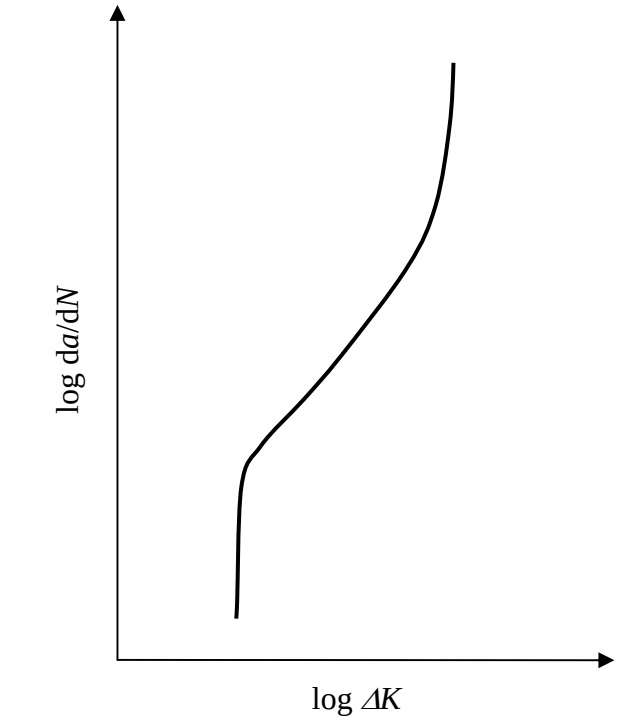

Figure 2.2. Variation of crack growth rates: (a) fatigue crack growth in an inert environment (b) fatigue crack growth in a corrosive environment under steady mechanical stresses, $\sigma_a = 0$, $\sigma_m \neq 0$ (stress corrosion cracking) [47]

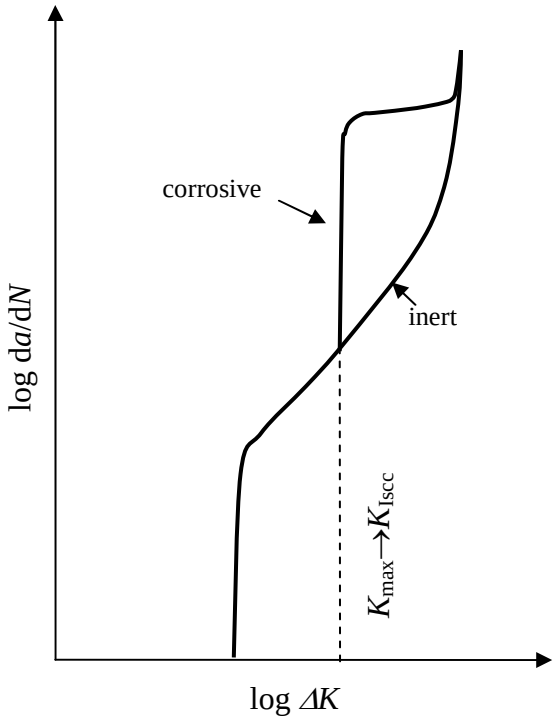

Figure 2.3. Schematic of stress corrosion fatigue behavior: Variation of crack growth due to superposition of mechanical fatigue (Fig 2.9a) and stress corrosion cracking (Fig 2.9b) [47]

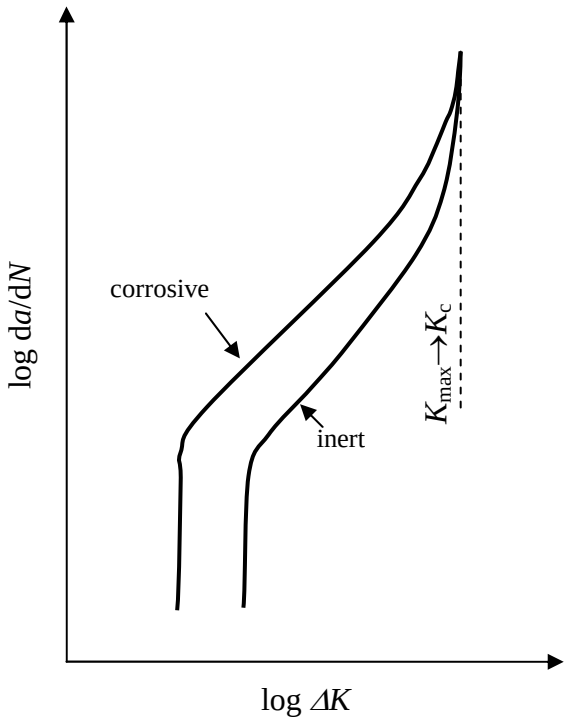

Figure 2.4. True corrosion fatigue: Comparison of crack growth rates of a metallic material in an inert environment with a corrosive environment under cyclic mechanical stresses ($\sigma_a \neq 0$) [47]

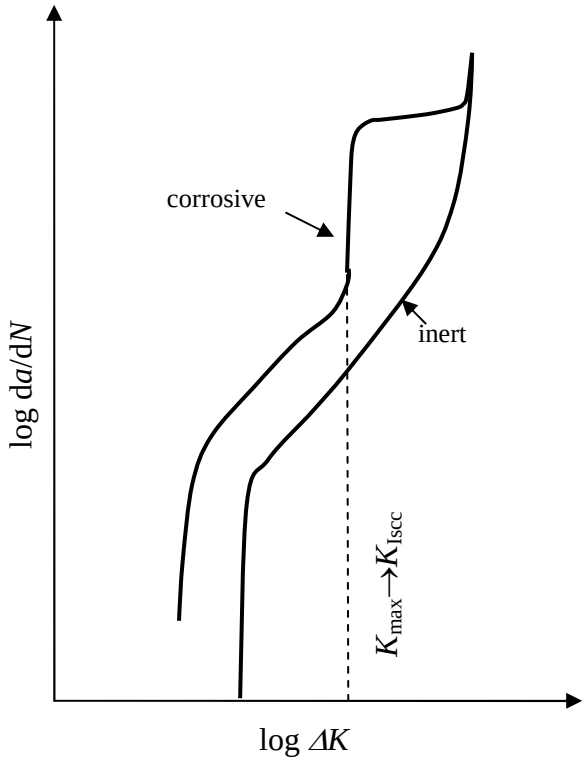

Figure 2.5. Schematic representation of mixed corrosion behavior resulting from a combination of true corrosion fatigue and stress corrosion fatigue

CHAPTER 3

Experimental Framework

An experimental approach is implemented to achieve the objectives of this study. Since microscale fatigue failures are fundamentally different from operational failures, two different experimental techniques were employed to investigate these failure modes. Structural fatigue failures occur at high-stress levels with catastrophic effects, while operational failures occur at low-stress levels with subtle effects. Significant differences in microscale actuation and sensing techniques for test samples designed to study these failure modes necessitated the two different experimental techniques:

(i) Low-stress level tests for operational failures

(ii) High-stress levels tests for structural failures

The methodology and scope of these experimental techniques are outlined below.

3.1. Low-stress level tests for operational failures

MEMS cantilevers (microcantilevers) were designed and fabricated as test specimens for investigating operational failures in liquids. The choice of microcantilevers as test specimens was influenced by practical MEMS applications in liquids, where microcantilevers are often the primary sensing element. Examples of such applications are chemical and biological sensors, AFM tips for imaging in liquids, and microfluidic devices. Physical, chemical, and biological stimuli can affect specific characteristics of microcantilevers, and the resulting change can be measured using electronic, optical or other sensing techniques. Displacements of the order of 10^{-12} to 10^{-6} m can be easily measured with microcantilever sensors in order to sense surface

stresses, forces, charges, heat fluxes, and even IR photons [32]. Microcantilever sensors have been used in two modes of operation– static and resonant mode [32]. In the static mode, the deflection is related to the gradient of mechanical stress generated in the microcantilever. In contrast, resonant mode microcantilevers vibrate at their resonant frequency and any change in the property being measured is indicated as a change in the resonant frequency. Microcantilever sensors are common due to the simplicity of design, and ease of fabrication. Design implications for more complex structures such as valves and diaphragms can be derived from results obtained from tests on simpler test structures.

Microcantilever test samples were fabricated and subjected to long-term experiments, and results are explained with analytical and characterization techniques.

(i) Test materials: The choice of test materials was influenced by practical applications of MEMS and microcantilever sensors in liquid environments. While materials such as silicon and silicon nitride are used for structural load bearing elements, others materials in MEMS are more suited for coatings, encapsulating materials, and surface modification. For example, nano-mechanical silicon resonators fabricated by Lavrik and Datskos [51] were coated with gold to increase optical reflectivity. The test materials chosen in this study were:

(i) Structural materials: Silicon and silicon nitride

(ii) Coating materials: Titanium and SU-8

Silicon and silicon nitride are among the most widely used MEMS materials and constitute micro-structural features in several liquid applications such as valves, pumps, AFM cantilevers, and chemical and biological sensors. Microcantilever

sensors are often made of MEMS materials such as silicon (SCS), polysilicon, silicon nitride and metal. Titanium and SU-8 are evaluated as coatings for microcantilevers with silicon as the structural material. Titanium is an ideal candidate for coatings in liquids in view of its excellent corrosion resistance. Titanium surfaces usually have a thin layer of TiO_2 which is believed to contribute to the excellent biocompatible performance of titanium at molecular and tissue levels [52]. SU-8 (also known as polyimide) was chosen since it is a polymeric epoxy based photoresist and possesses high chemical resistance ideal for harsh liquid environments. SU-8 has been proposed as a biosensor structural material for highly sensitive DNA detection [53]. SU-8 can be used as a coating for rugged encapsulation or biocompatible surface. In this study, we have studied the performance of SU-8 as a coating. The strength and elastic modulus of SU-8 being low (70-120 MPa and 8-15 GPa respectively [23, 42] suggests that a microcantilever with SU-8 as the structural material would possess low stiffness and experience significant damping in liquids. Such a microcantilever will have a broad resonant peak in liquids, and poses sensing and actuation challenges with experimental techniques used in this study.

(ii) Experimental technique: Microcantilever test specimens were subjected to long-term cyclic actuation in liquid-filled enclosures. The cantilevers were actuated at their resonant frequencies in order to maximize values of displacement amplitudes and stresses. The resonant frequencies of the microcantilevers ranged from 400-6000 Hz depending on the material and the test environment. The microcantilever test specimens were subjected to maximum stress levels of

0-5 MPa for 10^8-10^9 cycles. The cyclic stresses and number of stress cycles are approximately similar to conditions microcantilever sensors and AFM tips may experience in operation. The resonant frequency of the microcantilevers is monitored during the tests since environmental factors and mechanical stresses can cause unpredictable changes in resonant frequency. Any change in resonant frequency was deemed to constitute an operational failure. In addition to microcantilever specimens tested by vibrating in liquids, for certain liquid-material combinations, microcantilevers were tested in liquids without continuous vibration (static).

(iii) Test liquids: The three liquid environments chosen in this study were: (i) De-ionized (DI) water, (ii) Dulbecco's phosphate buffered saline (DPBS, 1X, 0.0095 PO_4 with Ca^{2+} and Mg^{2+}, Cambrex Bio Science) and (iii) Glucose solution (20% Glucose solution, sterile, Fisher Scientific). DI water was selected as a test environment since it is a common solvent and is present in several microfluidic applications. Saline solution was chosen since it is a corrosive liquid for metals and is similar to marine and biological environments. For example, DPBS is used to provide a buffer system to maintain cell culture media in the physiological pH range of 7.0 to 7.6 [54]. Similarly, glucose solution is also an important biofluid, and experimental results can be relevant for MEMS-based drug delivery systems. Microcantilever test specimens made of different test materials were exposed to all or a few of these liquid environments. In addition, tests were also conducted in air to enable comparison with results in liquids.

(iv) Analysis and characterization: A combination of experimental data and characterization techniques was used to understand and explain operational failures in the test structures. Characterization techniques such as scanning electron microscopy (SEM), electron dispersive spectroscopy (EDS), and nano-indentation were used to understand and supplement experimental data.

Table 3.1 summarizes the experiment plan showing structural/ coating materials and test environments.

We now discuss possible failure mechanisms for the microcantilevers tested in liquids. Structural failures are not expected to be the predominant failure mode since the microcantilevers are subjected to low stress levels. Both the structural and coating material may affect the mechanical performance of microcantilever specimens. Long-term performance of microcantilevers operating in vibrating mode is more important compared to those operating in static mode. However, environmental interactions for a microcantilever in a dormant state without applied stresses cannot be overlooked. While the coupled effect of applied stresses and environment is expected to be significant, the influence of the environment alone leading to mechanical failures may not be negligible.

3.2. High-stress level tests for structural failures

The objective of these experiments is to extend the present understanding of fatigue failures of MEMS to include liquid environments. Thin-film MEMS test specimens were fabricated, and tensile-tensile fatigue tests were conducted at high cyclic stresses (~ 0.6 UTS). Standardized macroscale fatigue tests are typically carried out at stress levels ranging from 0.35-0.85 UTS [43].

The test material chosen is aluminum, since it is an important material present in several microscale applications such as interconnects and contacts. Microstructures made of aluminum may frequently experience high stresses due to thermal and vibration effects. Fatigue failures in aluminum MEMS have been reported in the literature in air [39, 40], but long-term mechanical performance in liquids have not been investigated. The test specimens are tested in tensile-tensile mode with maximum stress levels (σ_{max}) of 0.30-0.32 MPa and minimum stresses (σ_{min}) of 0 MPa.

Air and saline solution are chosen as the test environments. Saline solution was chosen because it is reported to affect macroscale aluminum test specimens [47]. The test specimens were subjected to long-term cyclic stresses in air and saline solution and cycles to failures were recorded. Test specimens are subjected to identical stress levels in both air and saline. Results were compared to evaluate the effect of liquid environments on fatigue life of the test specimens. Experiments in saline solution are performed at two different cyclic frequencies (300 Hz and 600 Hz) to investigate the effect of frequency on fatigue failures in corrosive liquids at the microscale. Fatigue fractures are reportedly accelerated at lower cyclic frequencies since there is more time per stress cycle for the environment to interact with the crack tip [47].

Table 3.1. Experimental plan for microcantilever specimens

Material	Structural/ coating material	Environment			
		Air	DI water	Saline solution	Glucose
Silicon	Structural	×	×	×, S	×
Titanium	Coating	×		×	
SU-8	Coating	×	×,S		
Silicon nitride	Structural	×		×	

×- Tested
S- Static tests also performed

CHAPTER 4

Experimental Techniques: Long-Term Performance Testing of Microcantilever Test specimens at Low Stress Levels

The design, fabrication, and experimental techniques for microcantilever test specimens are described in this chapter.

4.1. Design and fabrication of microcantilever test specimens

The microcantilever test specimens fabricated in this study have two different designs depending on the structural materials used:

(i) Silicon microcantilevers

(ii) Silicon Nitride (SiN) microcantilevers

The differences in design are primarily due to differences in microfabrication processes used to fabricate microcantilever specimens made of different structural and coating materials. Table 4.1 lists the type of test specimens fabricated in this study, and the actuation and sensing techniques used to generate and sense oscillating motion. Three different types of silicon microcantilevers were fabricated: uncoated silicon, Ti coated silicon, and SU-8 coated silicon. The uncoated silicon and Ti coated silicon were magnetically actuated and had an electroplated magnetic Permalloy layer. The SU-8 coated silicon and silicon nitride microcantilevers were vibrated with an external piezoelectric actuator and did not possess any special actuating layer. Oscillating motion was sensed with a vibrometer for the uncoated and Ti coated specimens, while a laser diode and a position sensing device (PSD) was used for SU-8 coated and silicon nitride microcantilevers.

All the test specimens described in this study were fabricated at the Nanofabrication Center (NFC) at the University of Minnesota. The masks for all microcantilevers were designed using ICED software. Permanent masks were made by the NFC using the pattern generator. Microfabrication processing techniques for photoresists and etching included in Appendix B. The design and fabrication processes of the microcantilever test specimens are described below.

4.1.1. Silicon microcantilevers

The structural material for silicon microcantilevers was single crystal silicon. Three different types of silicon microcantilevers were fabricated: uncoated, Ti coated, and SU-8 coated. Design features and fabrication processes for these silicon microcantilevers are described below.

(i) Uncoated silicon microcantilevers: Figure 4.1 shows an optical image of an uncoated silicon microcantilever test specimen. These microcantilevers are 3 mm long, 20-50 μm thick, and 0.5 or 1 mm wide. The resonant frequencies for the uncoated microcantilevers were in the range of 360-3600 Hz. These uncoated microcantilevers have a thin layer of electroplated Permalloy ($Ni_{80}Fe_{20}$) at the tip to enable magnetic actuation using an external electromagnet. Magnetic actuation was chosen over other actuation methods (e.g electrostatic, integrated piezoelectric) since alternative methods are difficult to implement in liquid environments. Magnetic actuation was selected in view of its capability for high-frequency vibrations, compatibility to liquid environments, and non-contact actuation. High frequency vibrations were desired so as to obtain a large number of cycles required for performance testing in liquids. Figure 4.2 is a schematic showing the different layers of the uncoated silicon

microcantilever specimen. The electroplated magnetic pad is located at the tip of the microcantilever so that the highly stressed root of the cantilever consists of silicon only. This design feature is intended to eliminate the possibility of fatigue failure of the metallic Permalloy at the cantilever root. For sensing vibration, a laser vibrometer (LV) was employed.

The microcantilever dimensions were designed keeping in mind the minimum detectable amplitude of the laser vibrometer used for vibration sensing, and the laser spot size. Since viscous damping in liquid environments results in small amplitudes of vibration, the microcantilevers were designed to be 3 mm long in order to achieve larger tip displacement which could be detected by the laser vibrometer. The minimum width of these microcantilevers was 0.5 mm to enable focusing and proper reflection from the cantilever surface. Two different beam geometries were designed, with widths of 0.5 mm and 1 mm. Typical thickness of the microcantilevers ranged from 20 to 50 µm. The inherent variation in the deep reactive ion etch (DRIE) rate over the surface of a silicon wafer contributed to a range of thickness and resonant frequencies. The thickness of the cantilevers was a compromise between thin beams with low resonant frequencies and thick stiff beams with low deflection amplitudes.

The uncoated silicon microcantilevers were fabricated using a three-mask fabrication process which is summarized in Figure 4.3. The test samples were fabricated from a 500 µm thick double-side-polished (DSP) 4-inch (101.6 mm) p-type (Boron doped) silicon wafer with orientation (100) (Silicon Quest International). First, the backside of the wafer was patterned with photoresist (Microposit SPR-220) and subjected to a timed etched with DRIE. Process parameters for coating and patterning

photoresist SPR-220 and DRIE are included in Appendix B. The DRIE step determined the 30-40 µm thick device layer on the silicon wafer. After removing the photoresist, the wafer was cleaned with a Piranha etch. Next, a Cr-Cu seedlayer for electroplating Permalloy was sputtered on the frontside of the wafer. The seedlayer consists of a 1800 Å thick layer of Cu over a 200 Å thick adhesion layer of Cr. A 38 µm thick layer of photoresist (AZ 9260) was patterned over the seedlayer (frontside) to form a mold for electroplated Permalloy. A Permalloy electroplating bath was developed for electroplating Permalloy on the tips of the microcantilevers and is described in Appendix B. The photoresist mold was subsequently removed and the wafer cleaned with organic solvents. The Cu seedlayer was etched in DI: H_20_2: CH_3COOH (20:1:1) solution. The Cr adhesion layer was etched with Cr etchant (Cyantek CR-12S diluted 1:5 in DI water). Permalloy protects the underlying seedlayer, and hence the unwanted Cr-Cu seedlayer was selectively removed. Next, the front side was patterned with photoresist (Microposit SPR-220), and etched with DRIE to release the test structures. Test specimens were cleaned using successive rinses in acetone, isopropyl alcohol, and DI water, and dried on a hotplate prior to testing.

(ii) Titanium coated silicon microcantilevers: Figure 4.4 shows a schematic of the Ti coated test specimens. The Ti coated test samples are fabricated by DC magnetron sputter deposition (AJA Sputterer, NFC) of 100 nm thick titanium film over both top and bottom surfaces of uncoated silicon microcantilevers. The electroplated Permalloy layer and the silicon microcantilever surface are coated with titanium. Sputtering was chosen over evaporation in order to achieve better step coverage. Figure 4.5 shows the microfabrication process for Ti coated silicon microcantilevers. Uncoated silicon

microcantilevers were first fabricated, and separated from the wafers using a diamond tipped scriber. The individual samples were then affixed to a handle silicon wafer using a Kapton® polyimide adhesive tape. A Ti layer was deposited at 250 W DC power, with argon pressure at 5mtorr, 20 sccm flow rate. The deposition rate was approximately 5 nm/ min. The wafer with the samples was taken out and individual samples were turned over so that the Ti coated surface was adjacent to the handle wafer surface. The samples were again attached to the silicon wafer, and the uncoated microcantilever surface is now coated with Ti in the sputterer. A monitor wafer was included with each deposition run to determine the thickness of the Ti coating. The titanium coating covers the Permalloy magnetic layer and exposed silicon on the top and bottom surfaces of the microcantilever. The sputtered Ti coating had a residual tensile stress of 85 MPa which was measured using a FSM 900 film stress measurement system. The resonant frequencies of the titanium coated specimens were in the range of 750 to 2500 Hz.

(iii) SU-8 coated silicon microcantilevers: Figure 4.6 shows a schematic of the SU-8 coated microcantilevers. They are similar in design and dimensions to the uncoated silicon microcantilevers except for a 16 μm thick SU-8 film at the microcantilevers tip instead of the electroplated Permalloy. The magnetic Permalloy layer was intentionally excluded from the design to obtain a simple test structure with minimum layers. Since the objective is to study the environmental effects of the liquid on the SU-8 coating, only the tip of the microcantilevers are coated with SU-8 (MicroChem SU-8 2010) to ensure that the critical section at the root of the cantilever is free of interfacial effects such as delamination, peeling, or cracking. The SU-8 coated microcantilevers were

fabricated using the same mask set as the uncoated silicon microcantilevers. Figure 4.7 shows the microfabrication process for SU-8 coated silicon microcantilevers. The resonant frequencies of the titanium coated specimens were in the range of 850 to 5700 Hz.

4.1.2. Silicon nitride microcantilevers

The structural material for the silicon nitride (SiN) microcantilevers was LPCVD low-stress silicon nitride deposited at the NFC (SEMY LPCVD system). The SiN microcantilevers were 0.5 mm to 1.0 mm in length, 0.1 or 0.2 mm in width, and 0.9 μm in thickness. Figure 4.8 shows a schematic of a SiN test specimen. The dimensions of these microcantilevers were chosen based upon stiffness, damping, and resonant characteristics in a liquid environment. The resonant frequencies of the titanium coated specimens were in the range of 400 to 3000 Hz.

These test specimens were fabricated using standard microfabrication processes. Figure 4.9 shows the microfabrication process for silicon nitride microcantilevers. First a 0.9 μm thick LPCVD SiN layer was deposited on a double sided polished silicon wafers. Silicon nitride on the front side of the wafer was patterned with photoresist and etched with reactive ion etching (RIE). Next, a back-to-front side align was done, followed by patterning and etching the LPCVD SiN on the backside of the wafer. The wafer was then subjected to a timed etch in a deep reactive ion etcher (DRIE) so as to leave a thin layer of silicon remaining near the front side of the wafer. This remaining silicon layer was removed in a KOH etch bath, and freestanding SiN microcantilevers were obtained.

Stoichiometric LPCVD silicon nitride was not used in view of the large residual stresses after deposition. The low-stress silicon nitride was only 0.9 μm thick and had a residual compressive stresses less than 100 MPa. Since residual stress increases with increasing film thickness, thicker silicon nitride films were not used as structural layers for test specimens. Residual stresses were measured using the film stress measurement system (FSM 900TC, 750 nm laser). Film thicknesses were measured using an ellipsometer (Gaertner Scientific L116A) or a nano-ellipsometer (Nanometrics Nanospec Model 200 film thickness measurement system). Further details on these specimens are discussed in [55].

4.2. Performance measures for microcantilevers

There are three major parameters for microcantilever sensors that are important for sensing applications– resonant frequency, displacement, and *Q*-factor. In this study, only the resonant frequency of the microcantilevers is used to monitor the performance of the microcantilevers.

For a microcantilever, the resonant frequency in flexural mode in vacuum is given by [56]

$$f_n = \frac{\alpha^2}{2\pi l^2}\sqrt{\frac{EI}{m_l}} = \frac{\alpha^2}{2\pi}\sqrt{\frac{Et^2}{12\rho l^4}} \tag{4.1}$$

where α =1.875, E is the modulus of elasticity, I is the moment of inertia, m_l is the mass per unit length, ρ is the mass density, t is the thickness, l is the length of the microcantilever. For negligible viscous effects, the resonant frequency of a rectangular microcantilever in liquid, f_{nl} can be approximated by the expression

$$f_{nl} = \frac{f_n}{\sqrt{\left(1 + \frac{\pi \rho_l w}{4 \rho t}\right)}}, \tag{4.2}$$

where ρ_l is the density of the liquid, w is the width of the cantilever [56]. In general, the resonant frequency decreases from air to liquid as liquid densities are higher than air. Sader [56] discusses that Eq.(4.2) has demonstrated good agreement with experimental measurements when the amplitude of vibration is far smaller than any length scale of the cantilever, and $l>w$. When the amplitude of vibration is small, all nonlinear convective inertial effects in the fluid can be neglected. In the present study, typical amplitudes (~ 2 μm) are small compared to the minimum length scale of the microcantilevers (thickness ~ 35 μm).

It is difficult to obtain an analytical expression for the resonant amplitude if the damping is assumed to be negligible; theoretical calculations show it to be infinite. However, for finite damping and a harmonically excited microcantilever, the system can be approximated as a second-order spring-mass-damper system, and the resonant amplitude is given by

$$X = \frac{\frac{F_0}{k}}{\sqrt{\left(1 - \frac{m\omega^2}{k}\right)^2 + \left(\frac{c\omega}{k}\right)^2}}, \tag{4.3}$$

where F_0 is the amplitude of harmonic forcing function, m is the equivalent mass of the cantilever, ω is the frequency of actuation, c is the viscous damping coefficient, k is stiffness of the cantilever [57]. For microcantilevers operated in the static mode, the deflection of the microcantilever is measured for sensing.

The *Q*-factor, which represents the sharpness of the resonant peak, is also an important parameter. It is given by

$$Q = \frac{f_{nl}}{\gamma}, \tag{4.4}$$

where γ is the damping factor, and for small damping can be approximated by, $\gamma = \Delta f_{nl}$. Δf_{nl} is the resonant bandwidth at which the response amplitude equals 71% of the peak value [57]. The *Q*-factor is a performance measure of viscous dissipation due to external and internal friction. Due to larger viscous dissipation of liquids, the *Q*-factor is much lower in liquids compared to air. For example, in this study typical values of *Q*-factor were 700 to 1200 in air, and between 20 and 25 in liquids.

4.3. Experimental setups

In this study, two different experimental setups were used to obtain data due to different sensing and actuation schemes used for different microcantilever test specimens:

(i) Experimental setup with magnetic actuation

(ii) Experimental setup with piezoelectric actuation

The experimental setup with magnetic actuation is described in the following section. The experimental setup with piezoelectric actuation was developed as part of a different study, and details regarding the setup are described in [58] (Thomas P. Kuehn, Master's thesis University of Minnesota). A brief summary is included in section 4.5.

4.4. Experimental setup with magnetic actuation

The experimental setup with magnetic actuation was used for testing uncoated silicon and titanium coated microcantilevers. The experimental setup is described in section 4.4.1. Section 4.4.2 discusses an automated data acquisition and experiment control scheme used for conducting experiments on this setup. The experimental procedure is described in section 4.4.3, while data analysis is discussed in section 4.4.4.

4.4.1. Description

Figure 4.10 shows a schematic of the experimental setup. The test specimens were mounted in a sealed liquid enclosure shown in Figure 4.11. Detailed drawings for the liquid enclosure are included in Appendix C. Key design requirements for the liquid enclosure were minimal leakage, rigid specimen clamping, ease of mounting specimens, and clear optical path for a laser beam to sense vibration. The liquid enclosure has a transparent glass top cover, a specimen clamp, and two nozzles. The top cover of the liquid enclosure was made of glass to provide a clear optical path for the laser beam from the laser vibrometer (Polytec PI OFV-353 vibrometer, controller model OFV-2601) used for sensing vibration of the microcantilevers. The specimen clamp was used to mount the microcantilever specimens with stainless steel screws. An O-ring was used to seal the liquid. The nozzles on the vertical sides of the enclosure were used to connect tubing to two funnels which maintain a pressure head on the liquid thus preventing the possibility of air-bubbles entering the system (Appendix C). The liquid enclosure was 4 mm in depth, and ~5 ml in volume. The liquid enclosure and specimen clamp were made of delrin and nylon respectively to minimize the possibility of corrosion due to contact with liquids. Further all specimen clamping surfaces and

screws were made of stainless steel to prevent corrosion and clamping losses. Nearest surfaces of the test enclosure were at least 3 mm away from the microcantilever surface to eliminate any 'wall effects' as described in Naik et al. [59].

The laser head of the vibrometer emits a visible He-Ne laser beam of wavelength 633 nm. The laser vibrometer was aimed near the tip of the cantilever. The laser beam was focused and aligned with the microcantilever while it was vibrating to obtain optimal alignment. The laser beam was aimed at the cantilever tip, and the focusing lens on the laser head was manually adjusted so as the get the smallest spot size. When the LED signal level indicator on the vibrometer was lit at least 50%, the laser was considered to be in satisfactory focus. The laser vibrometer has three scale factor settings: 125, 25, and 5 mm/s/V. The choice of the scale factor was influenced by magnitude of the output signal and signal-to-noise ratio. For example, the scale factor of 5 mm/s/V was chosen for sub-micron displacement amplitudes of cantilever motion. For most experiments in this study, displacement amplitudes were ~2-5 μm, and the scale factor of 125 mm/s/V was chosen. A dichroic mirror (CVI Laser, Part # SWP-45-RU633) was used to direct and align the laser beam normal to the cantilever surface. The laser vibrometer outputs the velocity waveform of the vibrating motion of the microcantilever which is monitored by a digital oscilloscope (Tektronix, Model TDS 210). The microcantilevers were actuated with an external electromagnet (McMaster-Carr, Part No. 57025K61), which was powered by a vector signal analyzer (HP 89410A) with a sinusoidal signal. Since the output voltage of the vector analyzer was small, an amplifier was used to increase the voltage supplied to the electromagnet (maximum of 48 V). Communication between LabVIEW and the vector analyzer was

enabled using a GPIB (General Purpose Interface Bus) connection. Analog output (velocity signal) of the laser vibrometer was fed to a low-pass filter (cutoff at 20 kHz) and then to a National Instruments BNC breakout box (BNC-2110).

4.4.2. Automated data acquisition and experiment control

The long-term nature of the experiments required an automated data acquisition and experiment control scheme. An automated experimental scheme was implemented using a custom LabVIEW Virtual Instrument (VI) and the algorithm is summarized in Figure 4.12. (Screen images of the LabVIEW VI are included in Appendix D). First, the vector signal analyzer was used to obtain an estimate of the fundamental resonant frequency from the FFT (Fast Fourier Transform) spectrum of the cantilever motion. A random noise signal (0.5 to 7 kHz, level 0.5 or 1V) was used as the actuating signal. The output of the vibrometer was fed to the vector analyzer (channel 1) to obtain the spectrum and a sample plot is shown in Figure 4.13. Viscous damping in liquids results in a flatter profile for the resonant peak compared to that in air, as depicted in Figure 4.14. The signal peak in Figures 4.13 and 4.14 correspond to the fundamental resonant frequency of the cantilever in the respective medium. Using this estimate of resonant frequency, a coarse frequency sweep (spread ± 40 Hz from the estimate) was executed using LabVIEW VI commands to the vector analyzer. A sinusoidal signal was used for the frequency sweeps. Amplitudes were sampled at frequency intervals of 0.5-2 Hz in air, and 2-4 Hz in liquids.

The filtered analog output signal from the laser vibrometer was analyzed by LabVIEW. LabVIEW has an in-built function which can analyze a waveform input for its frequency and amplitude. During the sweeps, amplitude (in mV) corresponding to

each frequency (Hz) was recorded. A polynomial curve fit was implemented in LabVIEW to fit the recorded amplitude-frequency data to reduce the effect of noise. The order of the polynomial could be chosen in the LabVIEW VI. In air, due to sharp resonant peaks, the curve fit technique was not required. In liquids, a fourth order polynomial was observed to be the best fit for the recorded data. The coarse frequency sweep was designed to give an estimate of the resonant frequency with an accuracy of ±1 Hz (in air) or ± 2 Hz (in liquids). Figure 4.15 shows variation of amplitude with frequency of an uncoated silicon microcantilever tested in saline. The resonant frequency estimate obtained from coarse sweep was further refined with a finer frequency sweep (spread ± 20 Hz from most recent estimate), and the resonant frequency was determined with an accuracy of ± 0.2 Hz (in air) or ± 2 Hz (in liquids). The finer frequency sweep sampled laser vibrometer amplitudes at intervals of 0.2 Hz in air, and 2-3 Hz in liquid environments. In liquids, the resonant peak was flatter due to damping, and the resonant frequency could be determined with an accuracy of ± 2 Hz only. Next, the cantilever was vibrated with a sinusoidal signal at this resonant frequency for 5-9 minutes. The final estimates of resonant frequency for each loop (f_r), and the vibration time (t_f) were both recorded. The above steps were repeated to estimate the resonant frequency again, and frequency of the actuating sinusoidal signal updated to that of the latest resonant frequency.

The following data was acquired using the automated experimental scheme:

(i) Data files containing frequency (in Hz) and vibrometer amplitude data (in mV) for coarse frequency sweep for each loop.

(ii) Data files containing frequency (in Hz) and vibrometer amplitude data (in mV) for fine frequency sweep for each loop.

(iii) One summary data file containing resonant frequency (in Hz), resonant amplitude (in mV), and time at the end of all loops. (The number of cycles was calculated by multiplying the resonant frequency with the vibration time.).

Resonant frequency data obtained from these experiments were plotted against cycles (or time) as shown in Figure 4.16 to examine the long-term mechanical performance of these cantilevers.

4.4.3. Experimental procedure

Figure 4.17 summarizes the experimental procedure in a flowchart. The stepwise procedure for performing the long-term experiments is described below:

(i) *Mounting specimen*: The liquid enclosure including all its components were first cleaned with successive rinses with acetone, isopropyl alcohol, and DI water. The microcantilever specimens were also cleaned following the same procedure and dried on a hotplate. The specimen is secured using the specimen clamp and the screws are tightened.

(ii) *Determination of resonant frequency in air (f_{ra})*: The resonant frequency of the microcantilever specimen is first recorded in air using the automated experimental scheme described above. The resonant frequency in air is used to determine the thickness of the microcantilever specimen (based on Eq.(4.1)), and also to determine the maximum limit for the frequency sweep for estimating the resonant frequency in water. If the test environment is air, the automated data acquisition

and experimental control scheme (section 4.4.2) is continued without executing the following steps.

(iii) *Liquid filling*: For testing in liquid environments, it was important to initially fill the enclosure completely with liquid, and ensure absence of the air pockets. The liquid enclosure was filled using the funnels attached to the enclosure with PVC tubing. Liquid was initially filled so that the both funnels were half-full and at the same vertical height. One of the funnels was raised vertically, so that the liquid enclosure was vertical, and the liquid was emptied into the second funnel. Next, the raised funnel was slowly lowered, and liquid was allowed to flow into the enclosure in a vertical position. The enclosure was carefully rested horizontally, and the funnels were mounted on an elevated holder (test-tube holders) so that the top surface of the liquid in the funnels was approximately 6-10 inches above the glass cover of the liquid enclosure (Appendix C). The pressure of the liquid column minimizes the possibility of air entering the liquid cavity. Next, the funnels were covered with wax paper to minimize evaporation of water which can result in change in concentration of the liquid solution. A change in solution concentration due to evaporation of water will lead to a denser liquid, and lead to unwanted change (decrease) in resonant frequency of the microcantilevers.

(iv) *Matching stress levels*: In order to compare experimental data in water, saline, and air, reliability testing of the silicon microcantilevers was conducted at similar applied stress levels. The stresses in the cantilevers were approximately matched using elastic beam bending theory (Appendix E). The displacement amplitude of the cantilever tip (δ_{max}) necessary to match stresses in the microcantilevers was

calculated. The output voltage of the vector analyzer was adjusted to obtain the required microcantilever displacement. The desired output voltage was then entered in the LabVIEW VI. Typical values of δ_{max} for silicon microcantilevers were 1 to 5 μm depending on the thickness of the microcantilever. Value of δ_{max} for silicon nitride microcantilevers were ~ 1 μm since the thickness and lengths of these microcantilevers were smaller than silicon microcantilevers. Stress levels were maintained between 1 and 5 MPa for vibrating microcantilevers.

(v) *Long-term testing*: Long-term tests (up to 7 days) were conducted using the automated data acquisition algorithm described in section 4.4.2. The LabVIEW VI was programmed to periodically execute auto-calibration functions required for the vector analyzer every 30 minutes. Manual periodic checks were carried out at least every 12 hours to ensure stable operation of the experiment. For example, the nature of the environmental interactions for uncoated silicon specimens in saline solution caused the laser vibrometer to be misaligned during the course of the experiment, and required occasional re-alignment during the course of the experiment (once in ~12 hours).

4.4.4. Data analysis

Velocity signal from the vibrometer was used to obtain velocity amplitude, v_0 and vibration frequency, f. The output voltage of the laser vibrometer is proportional to the velocity of the microcantilever motion. The velocity signal from the laser vibrometer was in Volts, and can be first converted to the velocity amplitude v_0 in meters/ second using the following relation [60]:

$$v_0 = \frac{Velocity\ Amplitude\ (Volts)\ x\ \alpha}{1000\ x\ \eta}\ , \tag{4.5}$$

where η is the refractive index of the test fluid, and α is the scale factor of the vibrometer (α = 125 or 25 or 5 mm/s/V). Refractive indices of 1.0 and 1.33 were used for air and water respectively. Since both the saline and glucose solutions are dilute solutions, an approximate value of $\eta = 1.33$ is used. The displacement amplitude is obtained by integrating the velocity signal. Since the velocity signal was observed to be sinusoidal, the displacement amplitude, δ_{max} in meters was calculated using

$$\delta_{\max} = \frac{v_0}{2\pi f}, \tag{4.6}$$

where *f* is the frequency of vibration in Hz. The calculations were done either after data acquisition or incorporated into the LabVIEW program. An example calculation is illustrated assuming values for LV output amplitude of 240 mV corresponding to a vibration frequency of 2000 Hz, and LV scale factor of 125 mm/s/V in water. The velocity amplitude, v_0 is calculated as follows:

$$v_0 = \frac{0.240\text{V x } 0.125\text{m/s/V}}{1.33} = 0.02255\ \text{m/sec} \tag{4.7}$$

The displacement amplitude is calculated to be

$$\delta_{\max} = \frac{0.02255}{2 \text{ x } 3.14 \text{ x } 2000} = 1.795 \text{ x } 10^{-6}\ \text{m} = 1.795\ \mu\text{m} \tag{4.8}$$

The automated experimental algorithm records the resonant frequency and corresponding time for all loops. Long-term performance of test specimens was studied by examining the normalized resonant frequency of the vibrating cantilever over time or number of cycles. The initial resonant frequency of a particular microcantilever tested

in a specific environment was chosen as the normalizing resonant frequency for that microcantilever. The number of cycles was calculated by summing the product of vibration time with the resonant frequency for each loop:

$$N = \sum t \text{ x } f_r \tag{4.9}$$

4.5. Experimental setup with piezoelectric actuation

This experimental setup was used for performance testing of silicon nitride and SU-8 coated silicon microcantilevers. Since these microcantilevers lacked any integrated actuation capability, an external piezoelectric stack actuator (Physik Instrumente PI-249.2) attached to the microcantilever mount was used for actuation. Figure 4.18 shows a schematic of this experimental setup and is based on a similar apparatus described in Ghatkesar et al. [61]. Figure 4.19 shows an optical image of the experimental setup. The sinusoidal input to the actuator was generated by a frequency generator (Agilent 33220A), and amplified using a 100 W stereo amplifier. An optical sensing scheme consisting of a photosensitive position sensing device (PSD) and a diode laser (Edmund Optics P57-098 635 nm, 0.9 mW) was used to sense microcantilever motion. A circular neutral density filter (Edmund Optics, P54-080) was mounted in the path of the laser to control the spot size on the cantilever surface. Deflection of the microcantilevers causes a movement of the reflected laser spot on the PSD (SiTek S2-0171 SPC-PSD), which generates an output signal proportional to the movement of the laser spot. The output signal of the PSD can then be used to calculate the deflection of the microcantilever using trigonometry. The resonant frequency of the microcantilever was extracted from the PSD signal. Data acquisition and automated

test scheme were implemented in LabVIEW and was similar to that described for the magnetic actuation setup. Further details on this experimental setup are discussed in Kuehn et al. [58].

4.5. Interpretation of experimental data

In this section, we discuss the interpretation of data recorded during the experiments. Any change in resonant frequency over cycles (and time) is indicative of operational failure and degraded mechanical performance. Specifically, assuming liquid properties to remain constant, any change in resonant frequency is indicative of a change in either the spring constant or effective mass or both. The resonant frequency of the microcantilevers in a liquid can be determined using Eq.(4.2):

$$f_{nl} = \frac{f_n}{\sqrt{\left(1 + \frac{\pi \rho_l w}{4 \rho t}\right)}}. \tag{4.2}$$

Assuming material and liquid densities, ρ and ρ_l remain constant, any change in resonant frequency in liquid, f_{nl} is due to change in resonant frequency in vacuum, f_n. Changes in resonant frequency in vacuum, f_n can be due to

(i) a change in effective spring constant (K), or

(ii) a change in effective mass of the cantilever (m), as can be inferred from

$$f_n = \frac{1}{2\pi}\sqrt{\frac{K \pm \Delta K}{m \pm \Delta m}} \tag{4.10}$$

where ΔK is the change in spring constant and Δm is the change in effective mass of the cantilever. Consider the case of a cantilever with initial resonant frequency of f_0, stiffness K_0, and effective mass, m_0. Let final values of resonant frequency, stiffness,

and effective mass be f_1, K_1, and m_1 respectively. Using Eq.(4.1) we get the following expression,

$$\frac{f_1^{\,2} - f_0^{\,2}}{f_0^{\,2}} = \left(\frac{\frac{K_1}{m_1} - \frac{K_0}{m_0}}{\frac{K_0}{m_0}} \right) \tag{4.11}$$

where the term of the left hand side of the above equation accounts for both a change in mass and stiffness. For the case when stiffness remains unchanged, $K_0 = K_1$ we get,

$$\begin{aligned} \frac{f_1^{\,2} - f_0^{\,2}}{f_0^{\,2}} &= \left(\frac{m_0 - m_1}{m_1} \right) \\ f_1 &= f_0 \sqrt{\frac{m_0}{m_1}} \end{aligned} \tag{4.12}$$

For no change in effective mass, $m_1 = m_0$, we get

$$\begin{aligned} \frac{f_1^{\,2} - f_0^{\,2}}{f_0^{\,2}} &= \left(\frac{K_1 - K_0}{K_0} \right) \\ f_1 &= f_0 \sqrt{\frac{K_1}{K_0}} \end{aligned} \tag{4.13}$$

An increase in the effective mass of the cantilever or a decrease in spring constant can be responsible for a decrease in resonant frequency. Similarly, an increase in resonant frequency can be due to either an increase in spring constant or a decrease in effective mass. We also note that effective stiffness and mass can change in a manner causing the numerator on the right hand side of Eq.(4.11) to be zero. In such a case, no change in resonant frequency will be observed despite changes in both effective stiffness and mass. The spring constant of a microcantilever may be affected by physical phenomena such as crack growth, stress relaxation, absorption stresses, and oxidation. The

effective mass of the microcantilevers may change due to corrosion, or mass absorption/ adsorption. We conclude that any change in resonant frequency is indicative of operational failure of the microcantilever specimens.

4.6. Experimental uncertainties

(i) *Resonant frequency*: Resonant frequencies were determined experimentally, as discussed in the preceding sections. Experimental uncertainties for resonant frequency were ± 0.2 Hz in air, and ± 2 Hz in liquids. These uncertainties are determined by the frequency step size programmed in the LabVIEW VI's and exceed any uncertainties due to the signal analyzer, or sampling limits of the data acquisition card. For the typical resonant frequencies of the microcantilevers (~ 2 kHz) in this study, the experimental uncertainties are 0.01 % in air, and 0.1 % in liquids. In liquids, due to a damped resonant peak, the amplitudes of vibration for a 4 Hz range in the vicinity of the resonant peak were similar to within noise levels (Figure 4.15).

(ii) *Number of cycles* (*N*): Uncertainties in measuring time and frequency were combined using methods described in [62] to determine the uncertainty in number of cycles, which is of the order of 0.14%. The uncertainty in time (Δt) is 1 ms and uncertainty in frequency (Δf_r) is 0.1 %. The uncertainty in number of cycles (ΔN) can be calculated using

$$\frac{\Delta N}{N} = \sqrt{\left(\frac{\Delta t}{t}\right)^2 + \left(\frac{\Delta f_r}{f_r}\right)^2} \cong 0.0014 \text{ or } 0.14\ \%. \qquad (4.14)$$

Table 4.1. Microcantilever specimens: design, actuation, and sensing

Specimen designation	Structural Material	Coating	Actuation Technique	Sensing
Uncoated silicon	Si	None	Magnetic*	Laser Vibrometer
Ti coated	Si	Ti	Magnetic*	Laser Vibrometer
SU-8 coated	Si	SU-8	HVPZT	Laser diode-PSD
Silicon nitride	SiN	None	HVPZT	Laser diode-PSD

* These specimens have an electroplated Permalloy for magnetic actuation

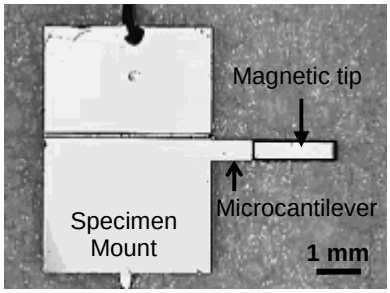

Figure 4.1. Optical image of an uncoated silicon microcantilever

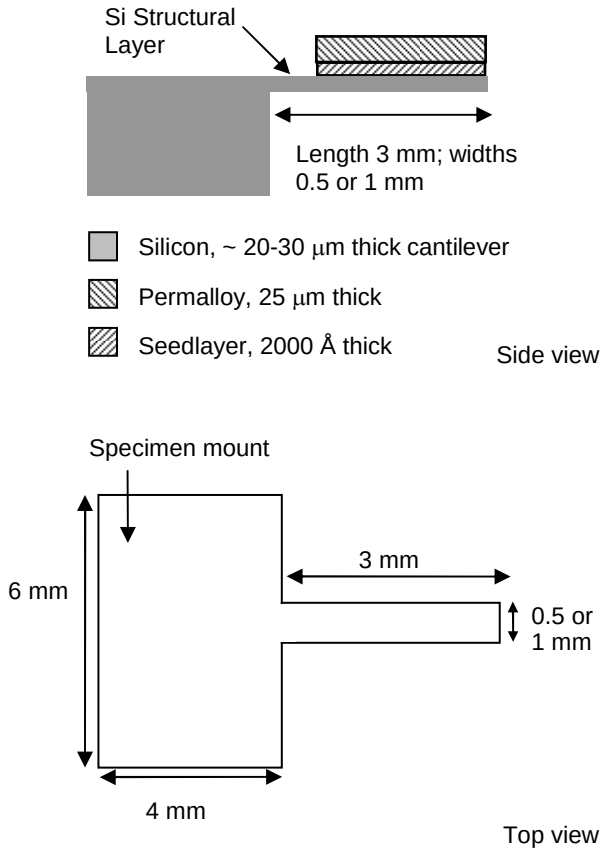

Figure 4.2. Schematic of an uncoated silicon microcantilever

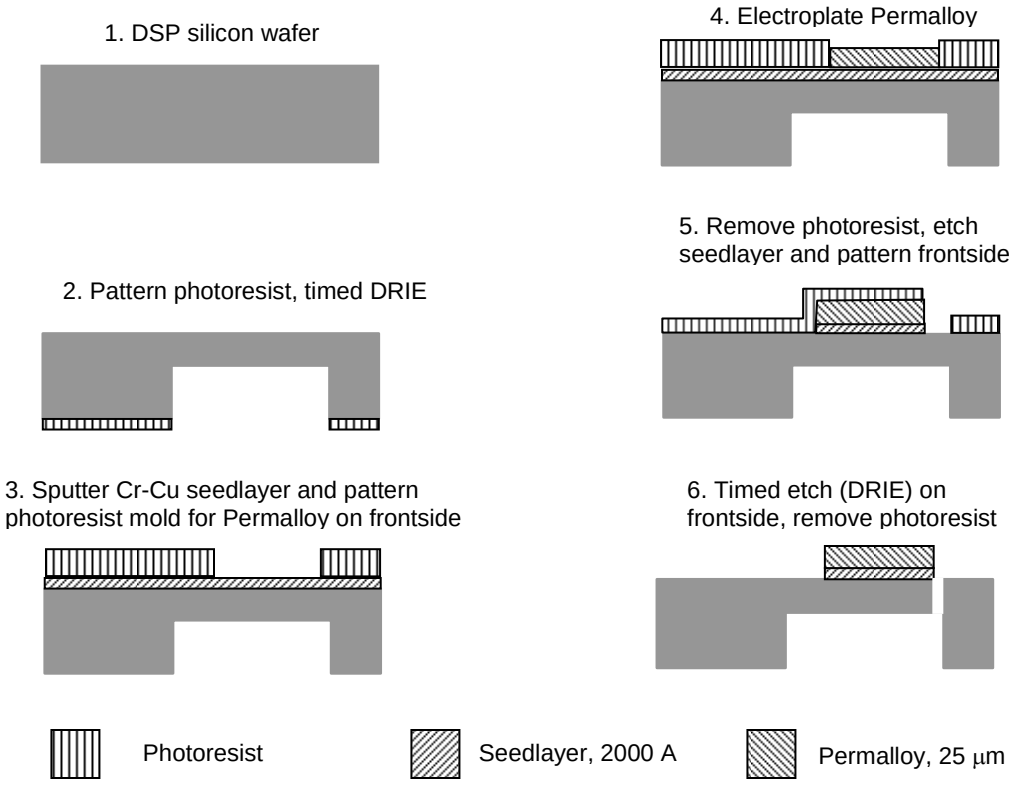

Figure 4.3. Fabrication process for uncoated silicon microcantilever test specimens

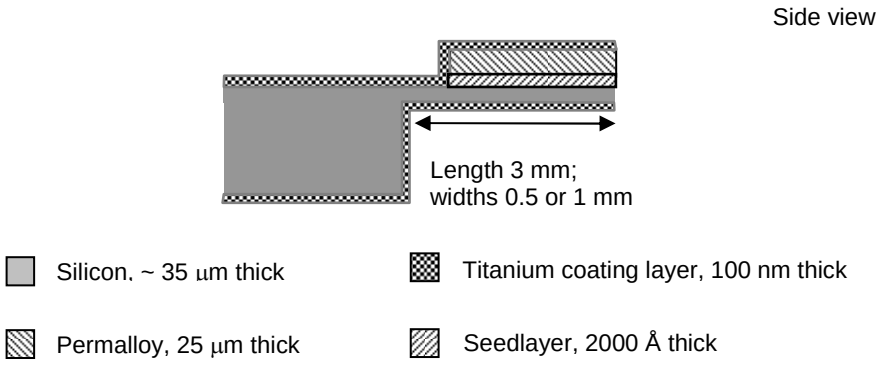

Figure 4.4. Schematic showing different layers of Ti coated silicon microcantilevers

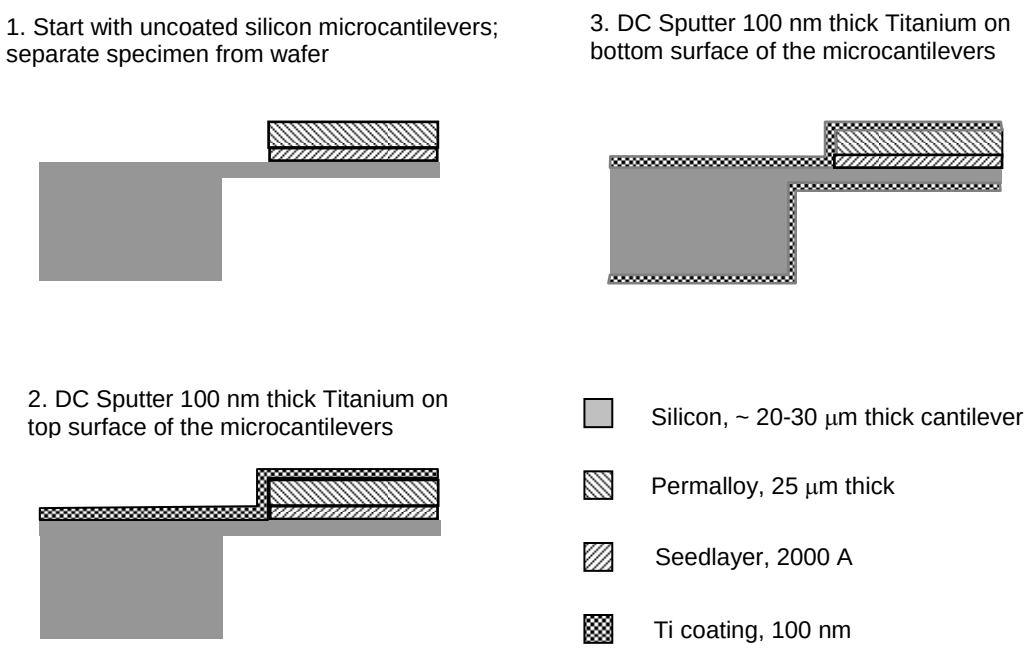

Figure 4.5. Fabrication process for Ti coated silicon microcantilever specimens

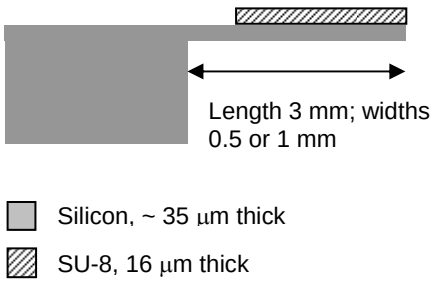

Figure 4.6. Schematic showing different layers of SU-8 coated silicon microcantilever

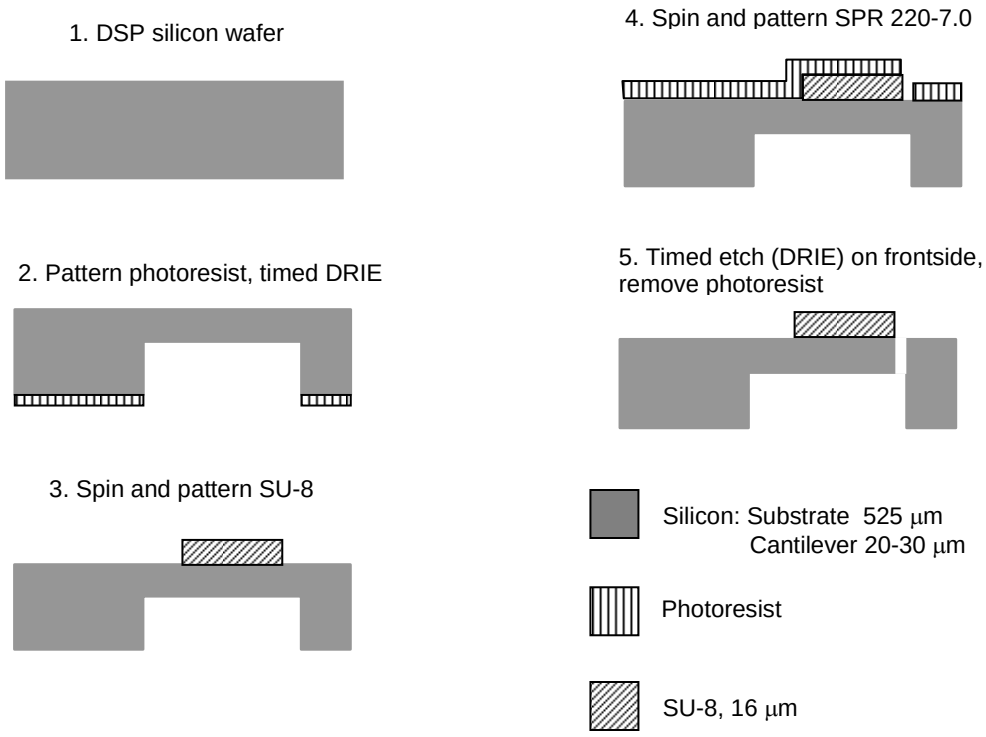

Figure 4.7. Fabrication process for SU-8 coated silicon microcantilevers

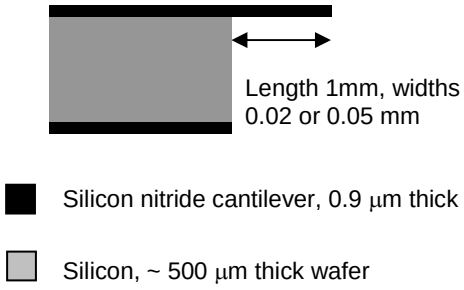

Figure 4.8. Schematic showing different layers of a silicon nitride microcantilever

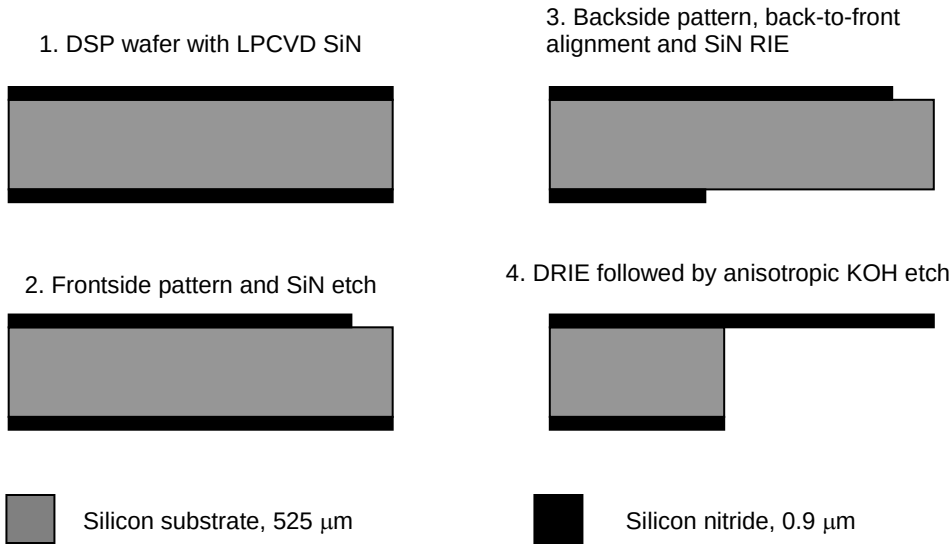

Figure 4.9. Fabrication process for silicon nitride microcantilever test specimens

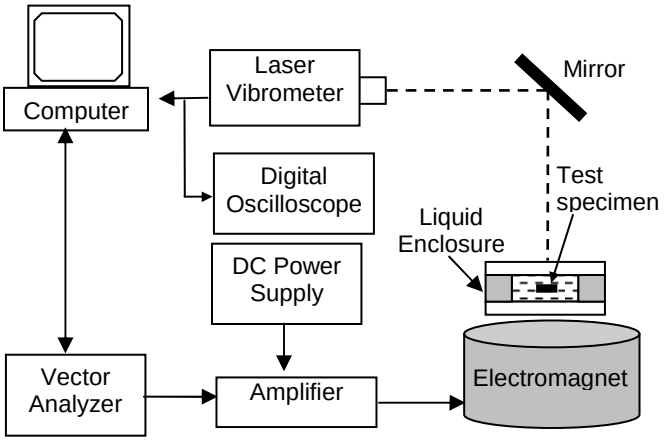

Figure 4.10. Schematic of the experimental setup with magnetic actuation

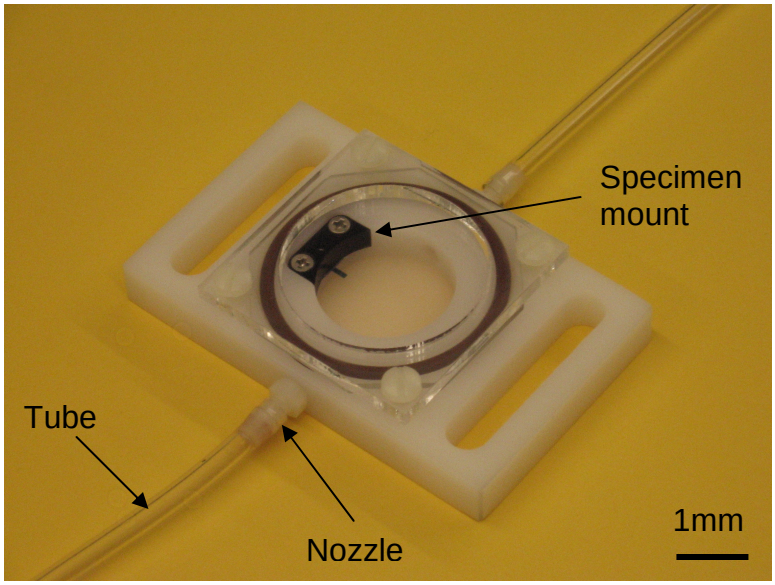

Figure 4.11. Liquid enclosure and specimen mount used for testing uncoated silicon and Ti coated silicon microcantilevers in the experimental setup with magnetic actuation

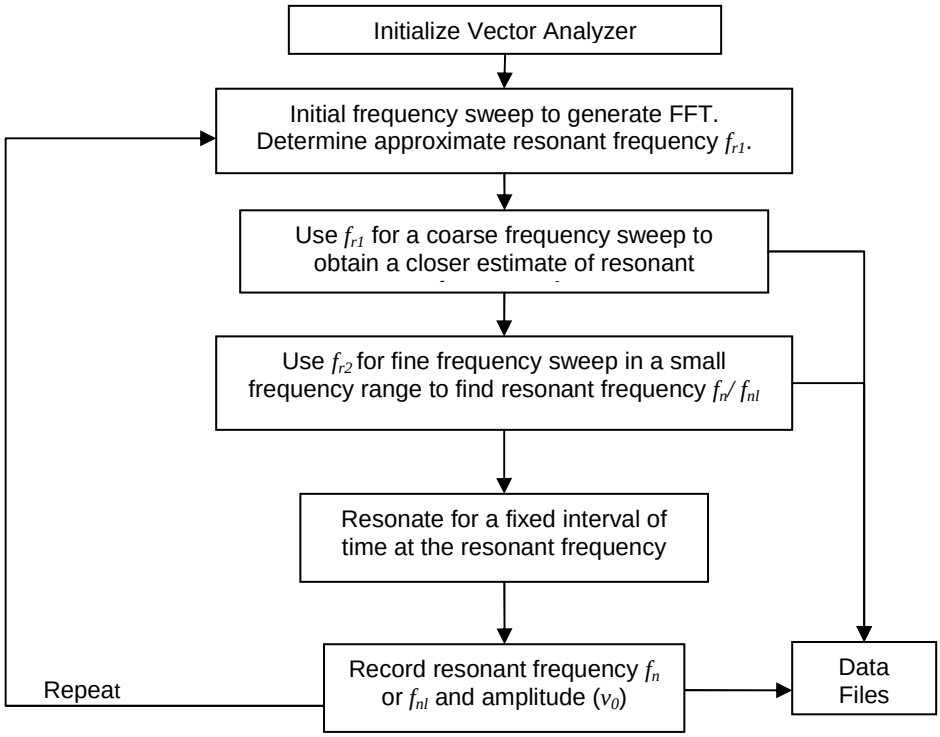

Figure 4.12. Automated experimental scheme for long-term performance testing of microcantilever test specimens

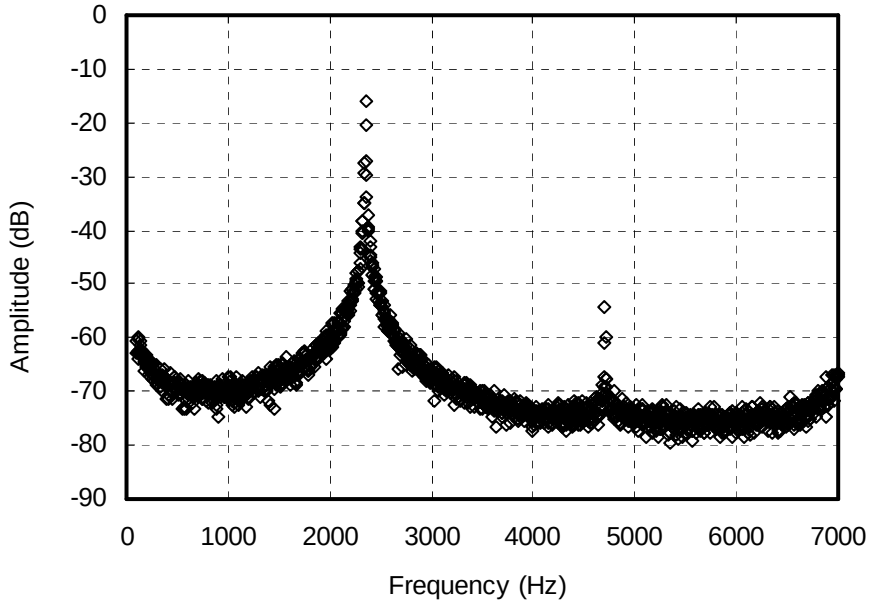

Figure 4.13. FFT of an uncoated silicon microcantilever magnetically actuated in air

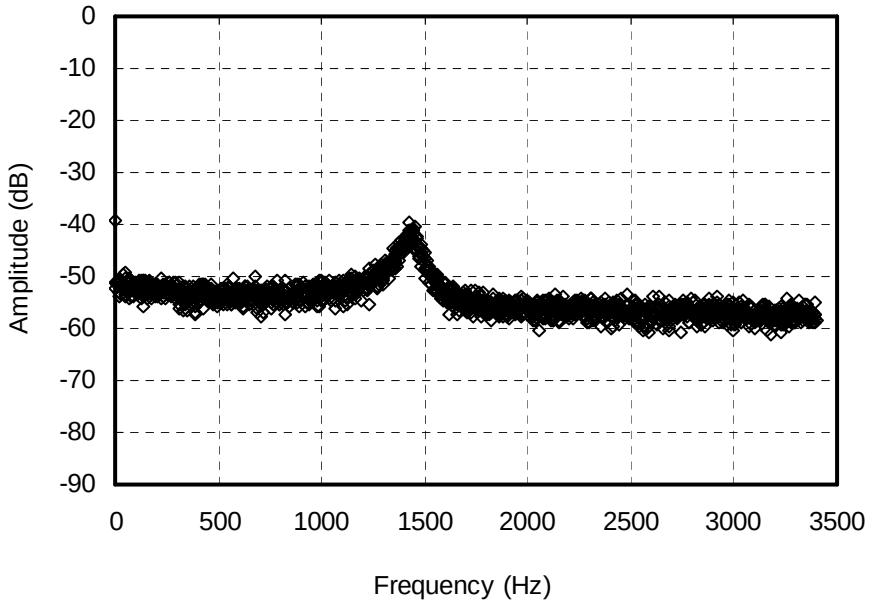

Figure 4.14. FFT of an uncoated silicon microcantilever magnetically actuated in water

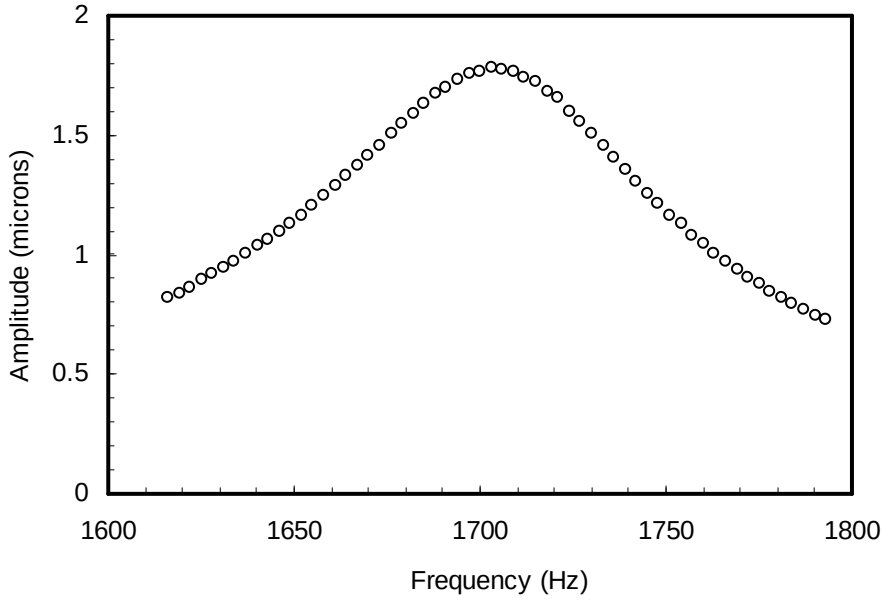

Figure 4.15. Plot showing variation of amplitude with frequency of an uncoated silicon microcantilever in saline

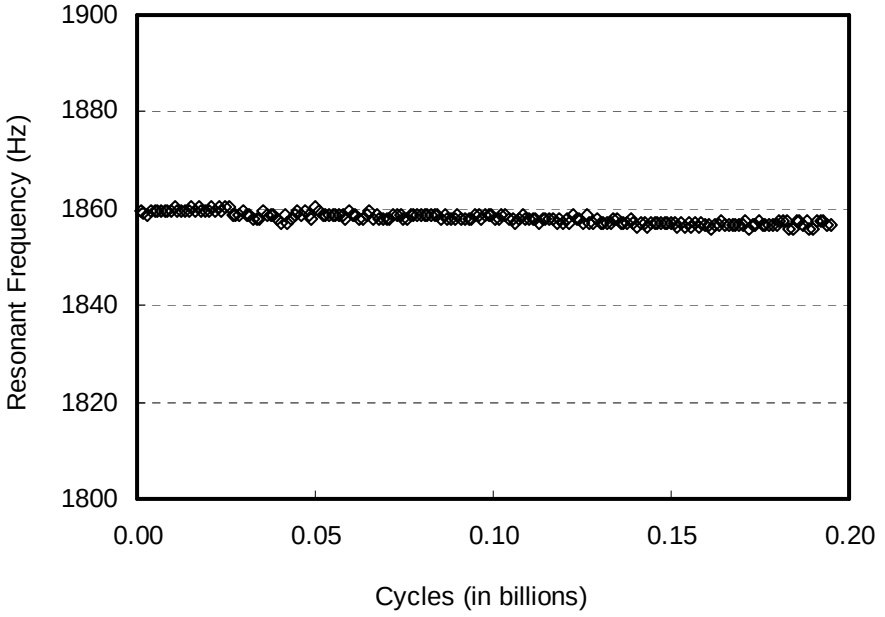

Figure 4.16. Variation of resonant frequency with cycles for a Ti coated silicon microcantilever tested in saline

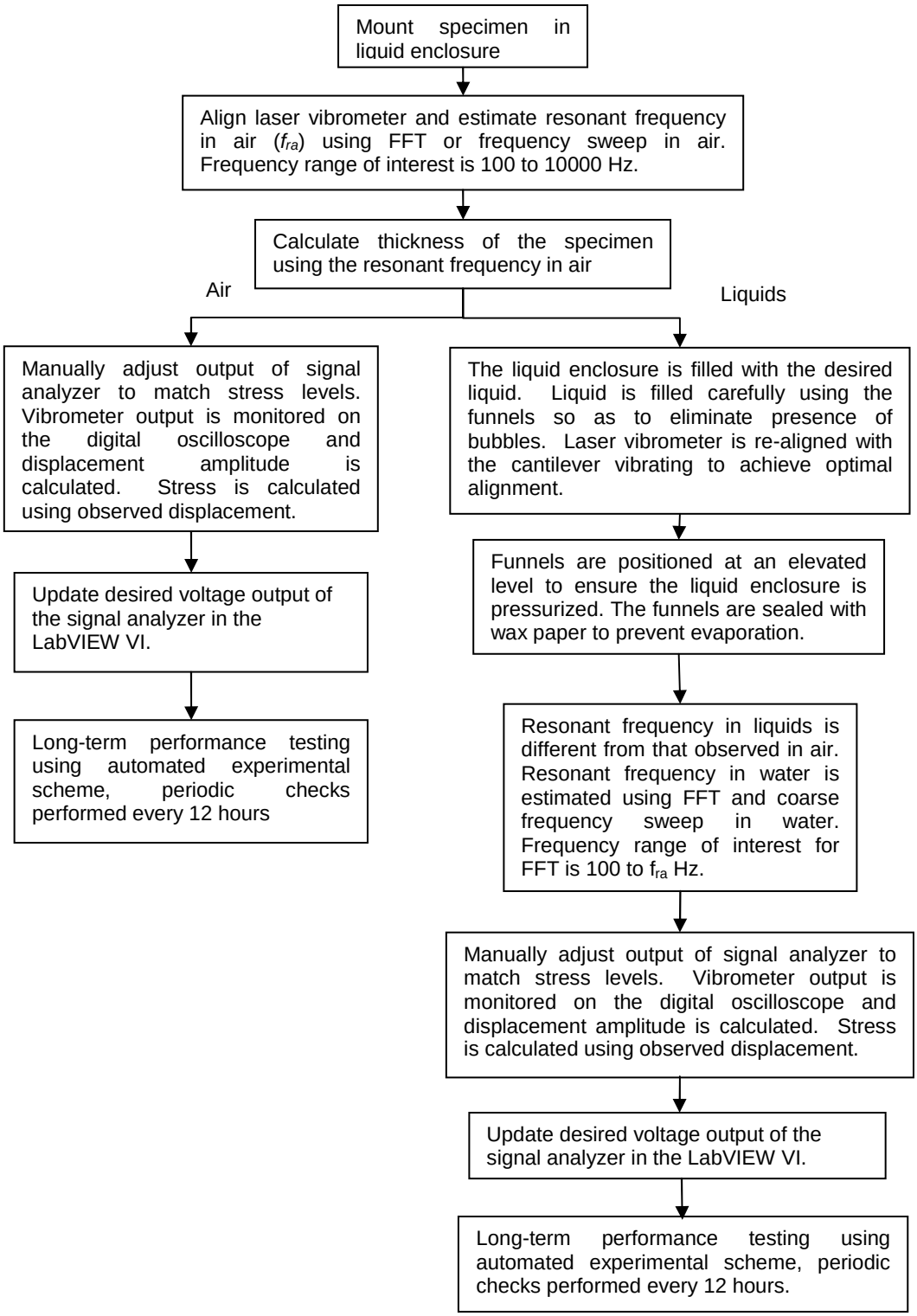

Figure 4.17. Flowchart showing experimental procedure

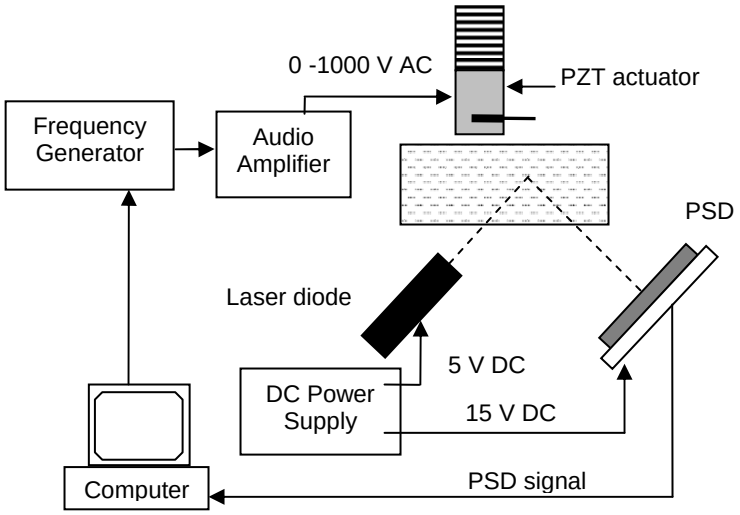

Figure 4.18. Schematic of the experimental setup with piezoelectric actuation: used for long-term performance testing of silicon nitride and SU-8 coated silicon microcantilevers

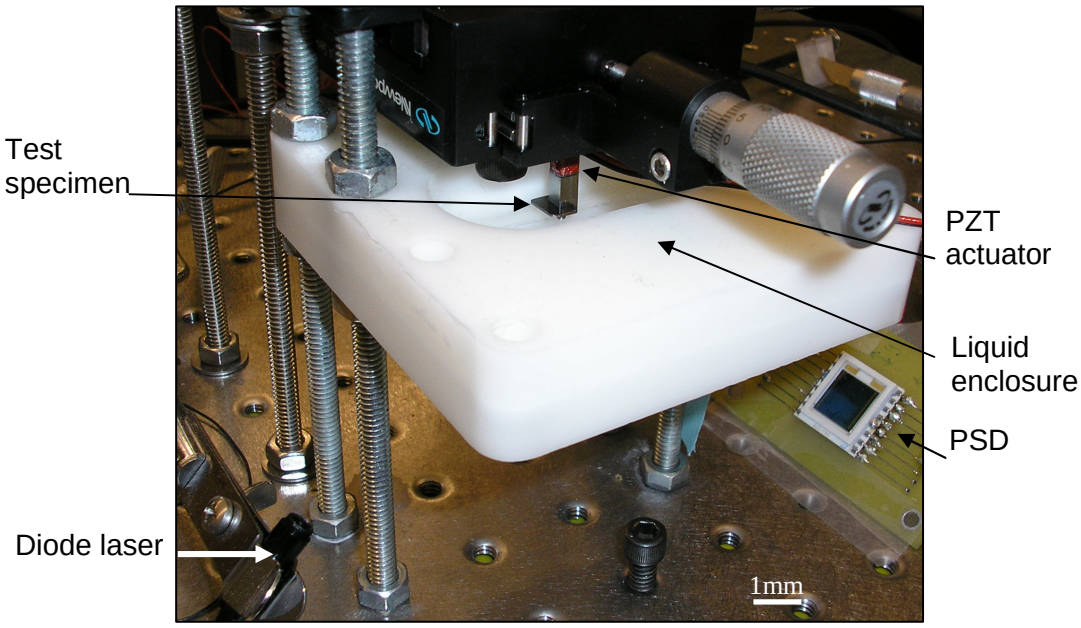

Figure 4.19. Optical image of experimental setup with PZT actuation

CHAPTER 5

Experimental Results: Performance Testing of Microcantilevers

The survey of the literature indicates that long-term mechanical performance of MEMS is influenced by three major factors: mechanical stresses, environment, and material. The microcantilever specimens were tested at low stress levels (0-5 MPa) with the objective of studying subtle long-term operational failures. Complete structural fatigue failure of the microcantilevers was neither expected nor observed. Long-term mechanical performance of the microcantilevers is expected to depend on the particular combination of material (structural/ coating) and environment. Long-term mechanical performance was evaluated by studying the variation of normalized resonant frequency of microcantilevers against number of cycles (or time, in some cases). Results are discussed in the following sections according to the particular microcantilever structural or coating material: (a) Uncoated silicon, (b) Ti coated silicon, (c) SU-8 coated silicon, and (d) Silicon nitride. The specimens are designated using 3 alphabetical letters as follows:

(i) The first letter indicates the type of specimen: Uncoated silicon (S), Titanium coated silicon (T), SU-8 coated silicon (P), or Silicon nitride (N).

(ii) The second letter indicates type of liquid environment: Air (A), Water (W), Saline (S), or Glucose (G).

(iii) The third letter indicates whether microcantilever was vibrating (V) or static (S) during the test.

For example, a sample designated as SSV stands for silicon, tested in saline by vibrating.

5.1. Performance of uncoated silicon microcantilevers

5.1.1. Results

Uncoated silicon microcantilevers were tested in air, water, saline, and glucose solution and experimental results are summarized in Table 5.1. The stress levels were approximately 5 MPa for the vibrating samples. For static samples, the stress levels were zero. Table 5.1 lists the initial and final resonant frequency (f_r) for each test, the number of cycles, and the actual test duration. The microcantilevers tested by vibrating in air and liquids were subjected to at least ~ 10^8 cycles. The change in resonant frequency (in %) of all uncoated silicon microcantilevers is compared after 2 x 10^8 cycles and is tabulated in Table 5.1. Resonant frequency changes at the end of each test performed in saline are tabulated in Table 5.2 to enable comparison of results for static samples (tested in saline only). The static samples experience no cycles since they were not vibrated for long-term testing. Further details on static samples are discussed in section 5.1.2.

Changes in resonant frequency of microcantilevers actuated in air (designated SAV), water (designated SWV), and glucose (designated SGV) were negligible to within the limits of experimental accuracy (Figure 5.1). Small changes in resonant frequency of ± 1-2 Hz are within the limits of experimental uncertainty. The resonant frequency of microcantilevers tested by vibrating in saline, however, was observed to decrease gradually and finally stabilize as shown in Figure 5.2. These samples are designated as SSV 1-4 in Table 5.1, Table 5.2 and Figure 5.2. The resonant

frequency of these microcantilevers was observed to decrease to the extent of ~1 % after 2 x 10^8 cycles, and is comparable to changes in frequency reported in the literature due to long-term failures. The magnitude of this shift in resonant frequency exceeds the stringent frequency stability requirements expected for MEMS cantilevers sensors (~ 0.08 %) and resonators (sub ppm) discussed in the literature review. We also note that the experimental setups are only capable of detecting resonant frequency changes exceeding ~0.01 % in air, and ~0.1 % in liquids. We conclude that uncoated silicon microcantilevers perform reliably in air, water, and glucose but experience a long-term performance failure in saline.

5.1.2. Discussion

Changes in resonant frequency of the microcantilevers may be caused by a change in spring constant of the cantilever or a change in effective mass or both as discussed previously in section 4.4. Changes in density of air and liquids can also lead to changes in resonant frequency, but fluid properties were not expected to change significantly during the experiments. We now focus on the experimental results obtained from tests performed in air, water, and glucose. The stability of resonant frequency of uncoated silicon microcantilevers in air, water, and glucose indicate no or minimal chemical interaction between the silicon surface and the environment (air or liquid). Silicon surfaces exposed to ambient, humid, or oxidizing environments are prone to oxidation, and have a ~50 nm thick superficial layer of silicon oxide (SiO_2). Silicon oxide which is similar to silica or sand is one of the most inert materials indicated by the abundance of sand in the earth's crust. The chemical inertness of silicon oxide can be evaluated by comparing bond dissociation energies of Si–O (798 kJ/ mol at 298 K) with that of Si-Si

(327 kJ/ mol at 298 K) [63]. Higher bond dissociation energy indicates higher chemical inertness. We expect the surfaces of the uncoated silicon microcantilevers to have been covered by a thin superficial layer of SiO_2 prior to long-term testing. The low stress levels imposed on the microcantilevers (0-5 MPa) do not lead to crack growth or fracture in the silicon oxide layer since the ultimate tensile strength of silicon oxide is significantly higher (0.6-1.9 GPa). SEM imaging of the microcantilevers did not provide any evidence of presence of cracks or mechanical damage. Minimal chemical interaction is expected between the inert superficial SiO_2 layer and air, water, or glucose solution.

Next, we focus on the decrease in resonant frequency in saline solution. As discussed in section 4.4.4, a decrease in resonant frequency can be due to either a decrease in spring constant or an increase in effective mass. Surface characterization of the tested microcantilevers indicated that the resonant frequency decreased in saline due to deposition of minerals from the saline solution. Scanning electron microscope (SEM) images of the test specimen surfaces showed the presence of particles on the silicon surfaces on the cantilever (Figure 5.3). Figure 5.4 shows magnified SEM images of the particles on the silicon surfaces of the microcantilever. Figure 5.5 shows electron dispersive spectroscopy (EDS) results of the surfaces of these test specimens, which revealed the presence of minerals (Na and Cl) from the saline solution. These results suggest that the additional mass of minerals from saline solution causes the decrease in resonant frequency. Prior to SEM/ EDS examination, these microcantilevers had been cleaned with successive solvent rinses, and dried, so as to displace any traces of saline solution remaining on the microcantilever. Figure 5.6

shows EDS results of the uncoated microcantilever surface after fabrication prior to any long-term testing which shows that the minerals Na and Cl were absent before testing in saline. Further, no cracks were observed on the microcantilever surface under the SEM, thus ruling out the possibility of decreased spring constant affecting the resonant frequency. In addition, a comparison of load-displacement curves of the microcantilevers obtained using a nano-indenter, showed negligible changes in spring constant before and after the vibrating tests (Figure 5.7).

Assuming no change in stiffness, the additional mass of minerals per unit surface area of the microcantilevers (kg/m^2) can be approximately calculated from the shift in resonant frequency using

$$\Delta m_m = \left(\frac{f_2^{\,2} - f_1^{\,2}}{f_1^{\,2}} \right) \left(\frac{M_c}{2wL} \right), \tag{5.1}$$

where f_1 and f_2 are the initial and final resonant frequencies in Hz, M_c is the initial mass of the cantilever in kg, and L and w are length and width of the cantilever respectively in meters. M_c is estimated by multiplying the volumes of the silicon cantilever and the Permalloy tip with their respective densities:

$$M_c = w(\rho_{Si} Lt + \rho_P l_P t_P) \tag{5.2}$$

where t and t_p are thicknesses of the silicon and Permalloy respectively in meters, l_P is the length of the Permalloy strip in meters, and ρ_{Si} and ρ_P are densities of silicon and Permalloy assumed 2330 kg/m^3 and 8900 kg/m^3 respectively. The surface area of the vertical sidewalls of the cantilever being comparatively small is neglected in calculating Δm_m. Using these equations, Figure 5.8 plots the additional mass of minerals per unit area as a function of time. It is observed that data from all microcantilevers vibrated in

saline collapse in Figure 5.8 to indicate a consistent trend compared to Figure 5.2. The additional mass of minerals deposited per unit surface area is observed to increase gradually, and then stabilize after 2-2.5 days. This trend indicates that mass deposition is a function of exposure time (to saline) and not number of cycles. Since resonant frequencies, thickness, and widths of the microcantilevers are different, comparing additional mass per unit area is a better way of comparing data from different microcantilevers for this particular effect. The surfaces of the static and vibrating samples appear to saturate after approximately 2 and 2.5 days respectively (Figure 5.8 and Table 5.1). From the above discussion, we conclude that the decrease in resonant frequency of the microcantilevers is entirely due to the increased effective cantilever mass.

Possible causes for deposition of minerals from saline are chemical interactions between the microcantilever surface and saline solution. Cherian et al. [34] have reported a similar phenomenon where calcium ions (Ca^{2+}) were observed to adsorb on stationary silicon nitride cantilevers immersed in $CaCl_2$ solution. They observed that the resonant frequency of the silicon nitride microcantilevers decreased from 13.7 kHz to 13.35 kHz (2.5 % decrease) as concentration of $CaCl_2$ solution was increased from 0 to 80 mM. Thus the magnitude of the decrease in resonant frequency caused by chemisorption of ionic species may be dependent on the concentration. In the present study, deposition of minerals on the surfaces of the microcantilevers from the saline solution may be caused by surface contamination and fluoro-polymer passivation deposits on the silicon microcantilevers introduced during DRIE step. From the results of EDS examination of the uncoated microcantilever surface (Figure 5.6) after

fabrication prior to any long-term testing, presence of elements such as carbon, oxygen, and aluminum is observed in addition to silicon on the microcantilever surface. While presence of carbon and oxygen can be traced to the ambient environment, aluminum may have been introduced during DRIE since the etch chamber is made of aluminum. These contaminants on the surface of the microcantilever may be responsible for attraction and deposition of ionic species from the saline solution. Particles observed in Figure 5.4 can comprise contaminants, and minerals from the saline solution.

The mechanical performance of these microcantilevers could have been affected by the environment or vibration, or a combination of both. In order to investigate the effect of the saline environment alone, uncoupled from effects of cyclic actuation, several microcantilever test specimens were immersed in saline for a particular time period, but not vibrated during the test interval (designated SSS in Table 5.1). The test intervals ranged from a minimum of 1 day to a maximum of 8 days. These microcantilevers were vibrated only before and after the test interval to monitor any change in resonant frequencies. The vibration time for interrogation of resonant frequency was minimized, since longer vibration periods were observed to affect the results. The resonant frequencies of the static samples were observed to decrease to the extent of 0.17 to 1.11 % (Table 5.2) corresponding to additional mass of minerals ranging from 0.0005 to 0.0013 kg/m^2. Figure 5.8 indicates that the static samples adsorb smaller additional mass of minerals compared to vibrating samples. Mass adsorption for the static samples (excluding SSS 5 and 6) stabilizes at a lower level (~0.0013 kg/m^2) compared to vibrating specimens (~0.004 kg/m^2). Samples SSS 5 and SSS 6 experienced comparatively higher mass adsorption due to longer vibration

times (~ 3 hours) while measuring the resonant frequencies. Typically, resonant frequencies for the static samples were measured within 15 minutes. SEM images for static test samples showed significantly fewer particles compared to vibrating samples. The static samples exhibit an increasing trend for mass adsorption with increasing immersion time in saline. Interpolating data points for static samples in Figure 5.8 the additional mass of minerals adsorbed by the static samples stabilizes at approximately 2.5 days.

In the present study, the deposition of minerals stabilizes with time possibly due to saturation of the interacting species or contaminants on the surface of the microcantilevers. Minerals deposited on the vibrating samples were observed to attain a higher equilibrium mass compared to the static samples. This result could be caused by increased mineral mass transport caused by vibrating motion of the microcantilevers. Deposition of minerals on the microcantilever surfaces leads to a decrease in mineral concentration of the saline solution surrounding the microcantilevers. In absence of any motion, mass transport of minerals for the case of static samples is diffusion dominated. For vibrating samples, the oscillating motion of the microcantilevers can promote mass transport due to vibration-induced flows caused by phenomena such as acoustic streaming [64, 65].

The possibility of degradation of the Permalloy layer was also considered. The effect of the liquid environments and long-term cyclic actuation on the Permalloy magnetic layer had been evaluated in additional experiments (Appendix B). The saturation magnetization of the Permalloy tip of the cantilevers (measured using a vibrating sample magnetometer) remained unchanged after long-term stress cycling, or

immersion in saline for a week. No evidence of corrosion or deposition was observed after immersion in saline for a week.

5.2. Performance of titanium coated silicon microcantilevers

5.2.1. Results

Titanium coated specimens were tested in air and saline solution. Experimental results for Ti coated silicon microcantilevers are summarized in Figure 5.9 and Table 5.3. Changes in resonant frequencies of samples tested in air (designated TAV) are negligible to within the limits of experimental accuracy. Resonant frequency of microcantilever samples tested in saline was observed to decrease to the extent of 0.06-0.58 % after testing for at least 10^8 cycles. The actual test time varied between 1 and 3 days. Figures 5.10 and 5.11 show the variation in resonant frequency of Ti coated microcantilevers tested in saline with cycles and time respectively. The resonant frequency of the Ti coated microcantilevers was observed to decrease with time/ cycles after an initial period of relative stability for 5×10^7 cycles (about 12 hours). Resonant frequencies of samples TSV 1 (2040.7 Hz) and TSV 2 (1859.5 Hz) differ by only ~190 Hz in saline, and follow a similar trend in variation of resonant frequencies with time. Sample TSV 3 has a low resonant frequency of 756 Hz and experiences a faster decrease in resonant frequency with increasing number of cycles. The rates of decrease of the resonant frequency of samples TSV 1, 2, and 3 were 0.11 %, 0.07 %, and 0.62 % per 10^8 cycles respectively, once the initial stable range of 5×10^7 cycles had been exceeded. Figure 5.11 indicates that the variations in resonant frequency for all Ti coated samples tested in saline follow a similar trend with respect to time. The rates of decrease of the resonant frequency of samples TSV 1, 2, and 3 were 0.17 %, 0.1 %,

and 0.32 % per day respectively. In summary, Ti coated microcantilevers suffered long-term performance failure in saline solution, while performing reliably in air.

5.2.2. Discussion

We now focus on the relative instability in mechanical performance exhibited by the Ti coated microcantilevers in saline. To investigate whether a decrease in stiffness or an increase in mass was responsible for the decrease in resonant frequency, surfaces of the tested microcantilevers were examined under a SEM. SEM images showed negligible mineral deposition; however, several cracks were observed in the vicinity of the root region of the microcantilever (Figure 5.12). For these microcantilevers, the location of the maximum stress is at the root of the microcantilevers. Samples tested in air were not observed to have any cracks. The decrease in resonant frequency of Ti coated microcantilevers can be caused by a decrease in spring constant caused by cracking of the Ti coating.

Cracking of the Ti coating may have been caused due to combined effects of cyclic stresses and the saline environment leading to corrosion fatigue. The applied cyclic stress levels of ~ 5 MPa were small compared to the ultimate tensile strength of titanium (0.95 ± 0.15 GPa) [23]. Residual stresses in the sputtered titanium layer were measured to be 85 MPa (tensile). The maximum stress σ_{max}, resulting from imposed and residual stresses is 0.09 GPa which is less than 10 % of the tensile strength of titanium. In view of low stress levels, structural fatigue or fracture under the sole effect of mechanical stresses is not expected for the range of cycles (~ 10^9) in this study. We recall that Ti coated specimens tested in air did not experience any cracking when subjected to similar stress levels and cycles. This indicates that the saline environment could have

led to accelerated crack growth rates causing corrosion fatigue of the Ti coating. For Ti coated microcantilevers tested in air, the combination of low mechanical stresses and a non-aggressive environment did not influence the resonant frequency stability. Since titanium is a non-ferrous metal, it is not expected to have an endurance limit. In air, low stress levels may result in fatigue failures occurring at cycles several orders of magnitude higher than the 10^9 cycles tested in this study. Papakyriacou et al. [66] in their investigation of high cycle corrosion fatigue of macroscale titanium-based metallic implants have reported fatigue life of 10^5 cycles at 0.4 GPa stress in ambient air, and ~10^8 cycles at 0.35 GPa in corrosive fluid.

Next, we focus on crack growth in the Ti coating. Assuming that the decrease in resonant frequency of Ti coated microcantilevers in saline is entirely due to cracking of the Ti coating, the extent of the crack growth in the Ti coating can be calculated using Eq.(4.1), and detailed calculations are described in Appendix F. The crack lengths in one surface of the Ti coating for specimens TSV 1, 2, and 3 are estimated to be 80 nm, 30 nm, 60 nm respectively. The variation in the estimated crack length may be due to different test frequencies and test times for the microcantilevers or could be random due to variation in the exact moment of crack initiation. Average crack growth rates in Ti coated specimens can be calculated with cycles or test time. The average crack growth rate with time expressed in meters per second can be calculated using

$$Average\ crack\ growth\ rate\ with\ time = \frac{a}{T} \tag{5.3}$$

where a is the crack length, and T is the total test time. The average crack growth rate with cycles, expressed in meters per cycle can be calculated using

$$Average\ crack\ growth\ rate\ with\ cycles = \frac{a}{N} \tag{5.4}$$

where N is the total number of cycles experienced by the sample during the test. Note that these average crack growth rates are different from instantaneous crack growth rates (*da/dt* or *da/dN*). Average crack growth rates are summarized in Table 5.4. We observe that all Ti coated samples have comparable average crack growth rates with time, and range from ~ 2.4 x 10^{-13} to 2.9 x 10^{-13} m/s. Sample TSV 3 experiences higher average crack growth rate with cycles (5 x 10^{-16} m/ cycle) compared to samples TSV 1 and 2 (1.78 and 1.58 x 10^{-16} m/ cycle). Higher average crack growth rate per cycle for TSV 3 may be due to lower resonant frequency of TSV 3. Sample TSV 3 is vibrated at frequencies of 752-756 Hz corresponding to its resonant frequency in saline. As discussed previously in Chapter 2, lower vibration frequencies allow the environment more time per cycle to interact with the crack tip, thus accelerating instantaneous crack growth rates per cycle, *da/dN*.

We also note that the average crack growth rates with time are of the order of 10^{-13} m/s. Van Arsdell and Brown discuss that crack growth rates of the order of 10^{-12} m/s must be understood to design MEMS devices against sub-critical crack growth [15]. These results also demonstrate that small crack growth rates per cycle can lead to performance degradation of high frequency MEMS since these MEMS devices have extremely small dimensions, and can accumulate large number of cycles over a short time period compared to macroscale objects. These results demonstrate that long-term mechanical performance of MEMS can be affected by extremely small crack growth rates.

The dotted lines in Figure 5.10 indicate the expected resonant frequency of the microcantilevers without any Ti coating based on calculations described in Appendix F. The normalized resonant frequencies of samples TSV 1, 2, and 3 if the Ti coating had cracked through its entire thickness were calculated to be 0.995 , 0.994, and 0.991 respectively. The decreasing trend in resonant frequency of the Ti coated specimens tested in saline was within the minimum limits showed using dotted lines in Figure 5.10. This indicates that the titanium coating was not cracked through its entire 100 nm thickness. The decreasing trend of the resonant frequency is expected to stabilize once the Ti coating had cracked through its entire thickness. In this study, resonant frequency is not observed to stabilize in Figures 5.10 and 5.11 since the Ti coated specimens were not tested long enough to achieve cracking of the Ti coating through its thickness. In summary, while the Ti coated microcantilevers did not experience operational failures on account of mineral deposition in saline solution, they exhibited corrosion fatigue in a corrosive liquid. The exact type of corrosion fatigue: stress-corrosion, true, or mixed, cannot be concluded from these experiments.

5.3. Performance of SU-8 coated microcantilevers

5.3.1. Results

SU-8 coated silicon microcantilevers were tested in two environments: air, and DI water. Experimental results are summarized in Figure 5.13 and Table 5.5. For SU-8 coated microcantilevers tested in air, only the initial and final normalized resonant frequencies are shown in Figure 5.13, and the variation in resonant frequencies is linear between these points. Trends in variation in resonant frequencies of SU-8 samples tested in water with cycles are shown in Figure 5.13 by plotting only a few data points

collected during the experiments. The resonant frequency of microcantilevers tested in air did not change beyond the limits of experimental uncertainty after testing for more than 10^8 cycles. In contrast, resonant frequency of microcantilevers tested by vibrating in water was observed to decrease gradually to an extent of 0.18-1.4 % after testing for 0.6×10^8 to 4.5×10^8 cycles. Since performance of uncoated silicon microcantilevers was observed to be unaffected in water, we conclude that the change in resonant frequency of SU-8 coated microcantilevers is due to the SU-8 coating only. Unlike uncoated silicon microcantilevers tested in saline, the resonant frequency of SU-8 coated samples was not observed to stabilize during the experiments performed in water. From Figure 5.13 we observe that the variation in resonant frequency of vibrating SU-8 coated specimens displays a consistent trend only below 10^8 cycles and then diverges with increasing number of cycles.

5.3.2. Discussion

The decrease in resonant frequency in water must be due to one or a combination of the following factors: (i) an increase in effective mass of the cantilever due to water absorption or (ii) a decrease in the spring constant due to change in intrinsic stress of the SU-8 coating. Changes in intrinsic stresses of the SU-8 coating may be caused by absorption stresses or stress cycling. Typically, water absorption for polymeric materials is known to range between 0.3 and 3 %, at the end of 24 hours [67]. Since water absorption could be a function of time, variation of resonant frequency for vibrating samples in water (PWV 1-5) is examined as a function of time in Figure 5.14. The two horizontal lines in Figure 5.14 represent the limits of resonant frequency after 24 hours, assuming the frequency decrease is entirely due to increased effective mass

with water absorption rates of 0.3 % and 3 %. The horizontal lines represent normalized resonant frequencies of 0.999 and 0.996 corresponding to 0.3 % and 3 % absorbency respectively. For SU-8 used in this study, manufacturer specifications indicate water absorption of 0.65 % at 85° C and 85 RH [33]. The magnitude of the decrease in resonant frequency is observed to exceed the maximum limit corresponding to 3 % water absorption at the end of 24 hours. Hence, in addition to increased effective mass, changes in intrinsic stresses may be responsible for the gradual decrease in resonant frequency of SU-8 coated silicon microcantilevers. Test times for the vibrating SU-8 samples ranged between 20 and 90 hours. Figure 5.14 also includes results from experiments performed on static SU-8 coated microcantilevers (PWS 1-4). In order to investigate the relative effects of the water absorption and cyclic stresses, several SU-8 coated test samples were immersed in water, but not vibrated. We observe that the static samples experience smaller decreases in resonant frequency compared to vibrating microcantilevers. Further, the resonant frequency of the static SU-8 coated microcantilevers was observed to be confined within the horizontal lines in Figure 5.14 corresponding to 0.3 % and 3 % water absorption. These experimental results indicate that other factors in addition to water absorption lead to a decrease in resonant frequency of the vibrating SU-8 coated specimens tested in water.

Detailed experimental results for the static SU-8 coated specimens tested in water are summarized in Table 5.6 and Figure 5.15. In addition to monitoring the resonant frequency in water at 1 day intervals, effect of drying the specimens tested in water was also investigated. The resonant frequencies of these specimens were recorded in air before and after immersion in water, and are plotted in Figure 5.15 (corresponding to air

pre test and air post test). Prior to testing the resonant frequency in air, the static test specimens were dried on a 115 °C hotplate for 15 minutes. Next, these specimens were immersed in water and the resonant frequencies were recorded at intervals of 1 day for 3 days (plotted in Figure 5.15). The initial resonant frequency in air was chosen as the normalizing frequency for all data points. The decrease in resonant frequencies of static samples shown in Figure 5.15 from air to water is primarily due to damping and viscous effects in water. We note that the difference in resonant frequencies of static samples measured in air before and after immersion in water was negligible. Further, no significant changes in resonant frequencies of the static test specimens were observed between immersion in water for 24 hours to 72 hours. This result indicates the decrease in resonant frequencies of SU-8 coated static samples was entirely due to water absorption effects and is reversible.

In order to examine whether the resonant frequency decrease for vibrating samples in water was reversible, resonant frequencies were compared in air before and after cyclic actuation for 0.5×10^8 to 1.0×10^8 cycles in water. The recovery of initial resonant frequency in air follows an inconsistent trend, and is inconclusive (Figure 5.16).

Based on the above discussion, the change in resonant frequency of SU-8 microcantilevers tested by vibrating in water may be caused by two separate effects:

i) Mass increase due to water absorption

ii) Changes is stiffness due to (a) cyclic stresses (b) absorption induced stresses

Increase in mass of the microcantilevers due to water absorption was indicated by the static samples. The change in stiffness is due partly to cyclic stresses which must be a function of cycles, and in part to absorption induced stresses.

5.4. Performance of silicon nitride microcantilevers

Silicon nitride microcantilevers[†] were tested in the following environments: air, DI water, and saline. Sample experimental results are shown in Figure 5.17 and summarized in Table 5.7. Changes in resonant frequencies of silicon nitride microcantilevers tested in air, DI water, and saline ranged between 0.007 % and 0.36 % after testing for approximately 10^8 cycles. These small changes in resonant frequency were insignificant to within the limits of experimental uncertainty. Silicon nitride exhibited no change in mechanical performance since silicon nitride is relatively inert compared to other materials tested in this study. The bond dissociation energy for the Si–N bond is 439 kJ/ mol indicating higher chemical stability and inertness [63]. Silicon nitride is widely used as an isolation or passivation layer in microelectronics due to its excellent chemical inertness and stability. In addition, the KOH wet etching used to fabricate silicon nitride cantilevers leads to a relatively cleaner surface compared to a silicon surface etched with DRIE.

5.5. Practical implications

The practical significance of this study can be illustrated by considering the case of MEMS cantilever sensors used for chemical and biological sensing such as detecting bio-molecules (DNA or glucose) from liquid media. These sensors may have

[†] The silicon nitride microcantilevers were fabricated as a part of this study. Experiments were performed by Thomas P. Kuehn and results are discussed in detail in [58. T. P. Kuehn, "*Testing Reliability of MEMS in Liquids*," MSME Thesis, Department of Mechanical Engineering, University of Minnesota, 2007.

bio-recognition molecules (antibody or DNA) immobilized on the surface of a silicon or silicon nitride microcantilever which selectively binds to a bio-molecule suspended in a liquid medium causing an increased static deflection or a decreased resonant frequency. The performance of these biosensors can be influenced by non-specific or unintended adsorption of chemical species from solution. For example, Figure 5.18 illustrates the problem of non-specific adsorption for microcantilever sensors immersed in liquid environments. The microcantilever has a triangular bio-recognition molecule (labeled A) on the surface which is designed to selectively attract the circular analyte (labeled B). The accuracy of the microcantilever sensor depends on the selective affinity of the bio-recognition molecule towards the analyte in the liquid medium. Non-specific adsorption of other liquid constituents (labeled C) on the microcantilever surface may lead to incorrect sensing. Performance degradation of uncoated silicon samples in saline indicates that undesirable non-specific interactions between microcantilever surfaces and chemical species present in the liquid media can compromise the accuracy of the microcantilever sensors. Typically, microcantilever sensors are designed to detect masses as small as 10^{-15} grams and the corresponding decrease in resonant frequency maybe much smaller than 0.1% [32, 51]. In this study, the change in resonant frequency of microcantilevers vibrated in saline was observed to be as high as 1%. Hence, environmentally induced changes in resonant frequency can destroy the sensing ability and undermine the accuracy of MEMS cantilever sensors for chemical and biological sensing.

Long-term *in vivo* sensing is expected to play a critical role in future closed-loop drug delivery or monitoring systems [19]. For implanted biological sensors

biocompatibility and biofouling are important concerns to prevent undesirable response similar to the mineral deposition observed for uncoated microcantilevers in saline. Bio-fouling of typical MEMS surfaces are a concern since silicon, silicon nitride, and SU-8 have also been reported to cause platelet adhesion [68], and may not be compatible with human blood. The results of this study demonstrate the requirement of biosensors to interface reliably with complex biological samples and fluids.

Materials such as titanium are expected to complement and replace silicon based MEMS in the future [69]. Titanium is a relatively inert material which can be used as a coating to eliminate undesirable chemical interactions. This is indicated by negligible mineral deposition on the surface of the Ti coated microcantilevers tested in saline. However, metallic coatings such as titanium may be susceptible to corrosion fatigue in liquid environments under coupled effects of corrosive liquids and cyclic stresses. Crack growth rates in MEMS may be extremely small, of the order of 10^{-12} to 10^{-13} m/s, which can result in unpredictable long-term mechanical performance of MEMS applications such as implanted biosensors or on-board automotive sensors. For macroscale objects, crack growth rates of 10^{-12} m/s are not fast enough to cause failure during its service lifetime. For example, assuming an average crack growth rate of 10^{-12} m/s a macroscale shaft 1 cm in diameter will fail in 10^{10} seconds or 317 years. In contrast, an average crack growth rate of 10^{-12} m/s will cause a 2 μm thick microstructure to fail after 23 days. Macroscale objects have relatively larger dimensions and are designed to be less sensitive compared to MEMS, hence they do not experience performance degradation caused by extremely slow crack growth rates

during their service life. The extreme sensitivities of MEMS provide an opportunity to study material behavior at extremely slow crack growth rates.

Calleja et al. [53] have developed highly sensitive SU-8 cantilever sensors for DNA detection. However, results of this study indicate that polymeric materials such as SU-8 may experience time-dependent water absorption and changes in intrinsic stresses, which can lead to performance degradation.

The difference in response of vibrating and stationary test specimens suggests that environmental effects on reliability of biosensors may depend on their mode of operation: resonating or static. Vibrating motion of microcantilevers in liquids may influence mass transport, intrinsic stresses, or crack growth leading to loss of sensor accuracy and performance. Microcantilevers operated in the resonant mode may cause vibration-induced flows and fundamentally influence the sensing process.

In addition to predicting microcantilever performance, techniques and results of this study can be used to select particular combinations of structural or coating materials and liquid environments to achieve reliable performance. Applications include oilfield sensors [16], automotive sensors, harsh environment microtechnologies [70], micropumps [71], liquid lenses and optofluidics [17]. For example, Feng et al. [71] have developed a micropump which uses a diaphragm vibrating at 0.318 to 91 kHz for pumping liquids at the microscale. Reliability of vibrating microstructures such as diaphragms may be compromised by issues similar to microcantilever specimens in this study.

Table 5.1. Experimental results: Uncoated silicon microcantilevers

Sample	Width (mm)	Stress (MPa)	Initial f_r (Hz)	Final f_r (Hz)	Cycles	Total test time (Days)	% Change in f_r at 2 x 10^8 cycles
Ambient Air (SAV)							
SAV 1	0.5	5.3	2824.5 ± 0.2	2825.5 ± 0.2	8 x 10^8	5.9	+ 8.85 x 10^{-3}
SAV 2	1	5.1	3162.9 ± 0.2	3161.2 ± 0.2	4.5 x 10^8	4.8	- 3.16 x 10^{-3}
DI Water (SWV)							
SWV 1	0.5	4.9	1427.7 ± 3	1429.9 ± 1.4	4.0 x 10^8	7.2	+ 0.13
SWV 2	1	5.0	2010.1 ± 1.8	2009.0 ± 1.5	2.0 x 10^8	2.1	- 0.05
SWV 3	0.5	4.9	1207.2 ± 0.7	1210.1 ± 1.7	2.5 x 10^8	5.8	+ 0.28
SWV 4	1	4.9	2360.6 ± 0.4	2358.6 ± 0.2	9.7 x 10^8	4.1	- 0.09
Glucose solution (SGV)							
SGV 1	0.5	4.9	2670.0 ± 0.5	2670.0 ± 1.0	3.9 x 10^8	1.9	- 0.026
SGV 2	1	4.8	1192.5 ± 0.2	1192.4 ± 1.0	1.69 x 10^8	1.5	-
Saline: Vibrating (SSV)							
SSV 1	0.5	4.5	1709.4 ± 2.1	1686.6 ± 1.9	5.0 x 10^8	4.2	-1.04
SSV 2	1	4.8	1368.2 ± 0.6	1354.4 ± 1.0	3.9 x 10^8	4.2	-0.79
SSV 3	0.5	4.5	2592.7 ± 1.2	2577.4 ± 1.3	7.8 x 10^8	4.2	-0.34
SSV 4	1	4.5	1953.1 ± 0.5	1932.5 ± 0.8	5.3 x 10^8	4.2	- 0.87
Saline: Stationary (SSS)							
SSS 1	1	0	1730 ± 1.5	1727.3 ± 1.5	0	1	Not vibrating
SSS 2	1	0	572.4 ± 1.5	569.5 ± 1.5	0	2	Not vibrating
SSS 3	1	0	3255.1 ± 1.5	3247.0 ± 1.5	0	2	Not vibrating
SSS 4	1	0	3631.2 ± 1.5	3622.0 ± 1.5	0	4	Not vibrating
SSS 5	1	0	568.8 ± 1.5	563.8 ± 1.5	0	4	Not vibrating
SSS 6	1	0	359.6 ± 1.5	355.5 ± 1.5	0	4	Not vibrating
SSS 7	1	0	761.2 ± 1.5	758.0 ± 1.5	0	8	Not vibrating
SSS 8	1	0	1575.1 ± 1.5	1568.0 ± 1.5	0	8	Not vibrating

Table 5.2. Results for uncoated Si microcantilevers tested in saline

Sample	Width (mm)	Stress (MPa)	Initial f_r (Hz)	Final f_r (Hz)	Cycles	Total test time (Days)	% Change in f_r at end of test
SSV 1	0.5	4.5	1709.4 ± 2.1	1686.6 ± 1.9	5.0 x 10^8	4.2	-1.33
SSV 2	1	4.8	1368.2 ± 0.6	1354.4 ± 1.0	3.9 x 10^8	4.2	-1.01
SSV 3	0.5	4.5	2592.7 ± 1.2	2577.4 ± 1.3	7.8 x 10^8	4.2	-0.59
SSV 4	1	4.5	1953.1 ± 0.5	1932.5 ± 0.8	5.3 x 10^8	4.2	-1.05
SSS 1	1	0	1730 ± 1.5	1727.3 ± 1.5	0	1	-0.17
SSS 2	1	0	572.4 ± 1.5	569.5 ± 1.5	0	2	-0.52
SSS 3	1	0	3255.1 ± 1.5	3247.0 ± 1.5	0	2	-0.24
SSS 4	1	0	3631.2 ± 1.5	3622.0 ± 1.5	0	4	-0.24
SSS 5	1	0	568.8 ± 1.5	563.8 ± 1.5	0	4	-0.80
SSS 6	1	0	359.6 ± 1.5	355.5 ± 1.5	0	4	-1.11
SSS 7	1	0	761.2 ± 1.5	758.0 ± 1.5	0	8	-0.39
SSS 8	1	0	1575.1 ± 1.5	1568.0 ± 1.5	0	8	-0.45

Table 5.3. Experimental results: Ti coated microcantilevers

Sample	Width (mm)	Stress (MPa)	Initial f_r (Hz)	Final f_r (Hz)	Cycles	Total test time (Days)	% Change in f_r at 2×10^8 cycles/ end
Ambient Air (TAV)							
TAV 1	0.5	4.7	1915.8 ± 0.0	1916. 3 ± 0.0	3.6×10^8	2.0	+ 0.027
TAV 2	1	4.5	2554.8 ± 0.1	2554. 8 ± 0.0	5.2×10^8	2.1	0
Saline: Vibrating (TSV)							
TSV 1	0.5	4.7	2040.7 ± 0.3	2032.0 ± 1.3	4.5×10^8	3.1	- 0.06
TSV 2	0.5	4.6	1859.5 ± 0.0	1856.9 ± 0.4	1.9×10^8	1.4	-0.14
TSV 3	0.5	4.9	756.6 ± 0.3	752.2 ± 0.0	1.2×10^8	2.4	- 0.58

Table 5.4. Average crack growth rates for Ti coated specimens in saline

Sample	Initial f_r (Hz)	Calculated crack growth, a (nm)	Cycles, N	Total test time, T (Days)	Average crack growth rate with time, (a/T) (meters/ second)	Average crack growth rate with cycles, (a/N) (meters/ cycle)
TSV 1	2040.7 ± 0.3	80	4.5×10^8	3.1	2.98×10^{-13}	1.78×10^{-16}
TSV 2	1859.5 ± 0.0	30	1.9×10^8	1.4	2.48×10^{-13}	1.58×10^{-16}
TSV 3	756.6 ± 0.3	60	1.2×10^8	2.4	2.89×10^{-13}	5.00×10^{-16}

Table 5.5. Experimental results: SU-8 coated microcantilevers

Sample	Width (mm)	Initial f_r (Hz)	Final f_r (Hz)	Cycles	Total test time (Days)	Change in f_r at end (%)
Ambient Air (PAV)						
PAV 1	0.5	2243.6 ± 0.1	2243.2 ± 0.1	1.5×10^8	0.8	- 0.02
PAV 2	1	5566.6 ± 0.0	5565.9 ± 0.1	6.5×10^8	0.4	- 0.01
DI Water (PWV)						
PWV 1	1	852.3 ± 0.3	850.7 ± 0.2	0.6×10^8	1.0	-0.18
PWV 2	0.5	2022.8 ± 0.8	2012.6 ± 0.8	1.4×10^8	1.0	- 0.50
PWV 3	0.5	2021.6 ± 0.4	1998.7 ± 1.4	4.5×10^8	2.0	- 1.13
PWV 4	0.5	2024.8 ± 0.1	2012.8 ± 0.5	1.3×10^8	0.8	- 0.59
PWV 5	0.5	982.3 ± 1.8	968.5 ± 0.4	3.5×10^8	3.8	- 1.4

Table 5.6. SU-8 static samples in water

Sample	Width (mm)	Initial f_r in air (Hz)	Resonant Frequency in water at				Final f_r in air (Hz)	% change in water at 1 day	% change in water at end
			0 day	1 day	2 days	3 days			
PWS 1	1	2130	654	652	652	652	2130	-0.30	-0.30
PWS 2	1	4757	2169	2165	2165	2165	4758	-0.18	-0.18
PWS 3	1	5689	2565	2562	2564	2558	5688	-0.11	-0.27
PWS 4	1	2388	777	775	775	775	2387	0.25	-0.25

Table 5.7. Experimental results: SiN microcantilevers

Sample	Width (mm)	Initial f_r (Hz)	Final f_r (Hz)	Cycles	Total test time (Days)	Change in f_r (%)
Ambient Air (NAV)						
NAV 1	0.1	2941.0 ± 0.5	2940.8 ± 0.7	2.5×10^8	1.0	-0.007
NAV 2	0.2	1127.3 ± 0.4	1127.7 ± 1.0	1.2×10^8	1.0	+ 0.035
DI Water (NWV)						
NWV 1	0.1	1125.9 ± 1.2	1127.4 ± 0.7	0.8×10^8	1.0	+ 0.133
NWV 2	0.2	471.1 ± 1.5	472.8 ± 0.9	0.9×10^8	1.0	+ 0.360
Saline: Vibrating (NSV)						
NSV 1	0.1	1716.9 ± 2.1	1718.7 ± 1.0	0.8×10^8	1.0	+ 0.105
NSV 2	0.2	1708.8 ± 1.0	1710.8 ± 1.2	1.2×10^8	1.0	+ 0.117

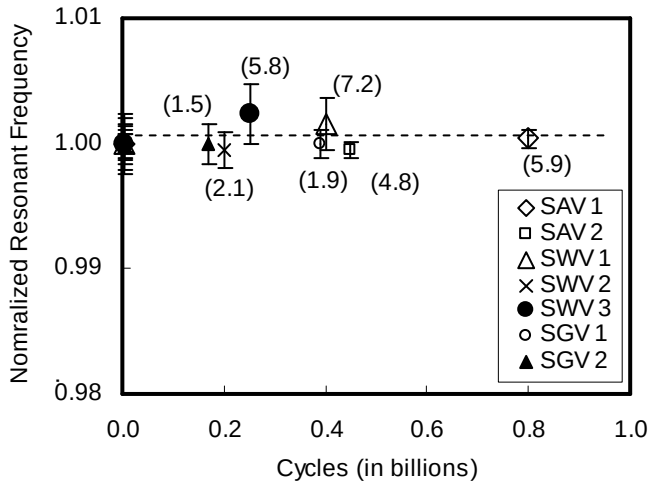

Figure 5.1. Plot of normalized resonant frequency of uncoated silicon microcantilevers tested in air, water, and glucose with increasing number of cycles. Numbers in brackets indicate actual test time in days

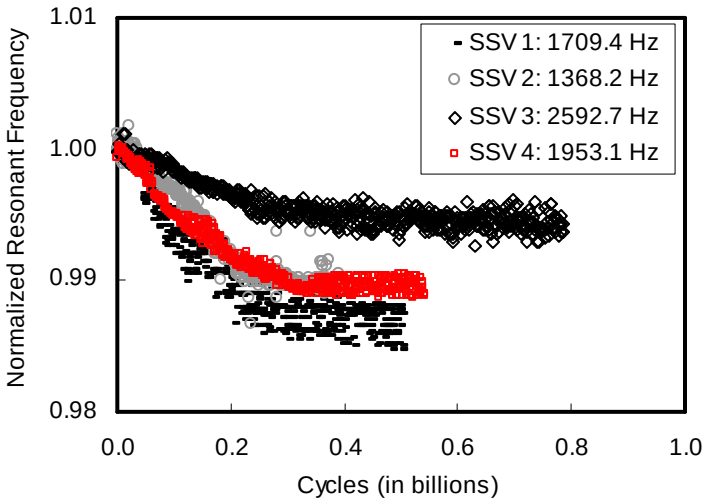

Figure 5.2. Plot of normalized resonant frequency of uncoated silicon microcantilevers SSV 1, SSV 2, SSV 3, and SSV 4 tested in saline decreases with increasing number of cycles

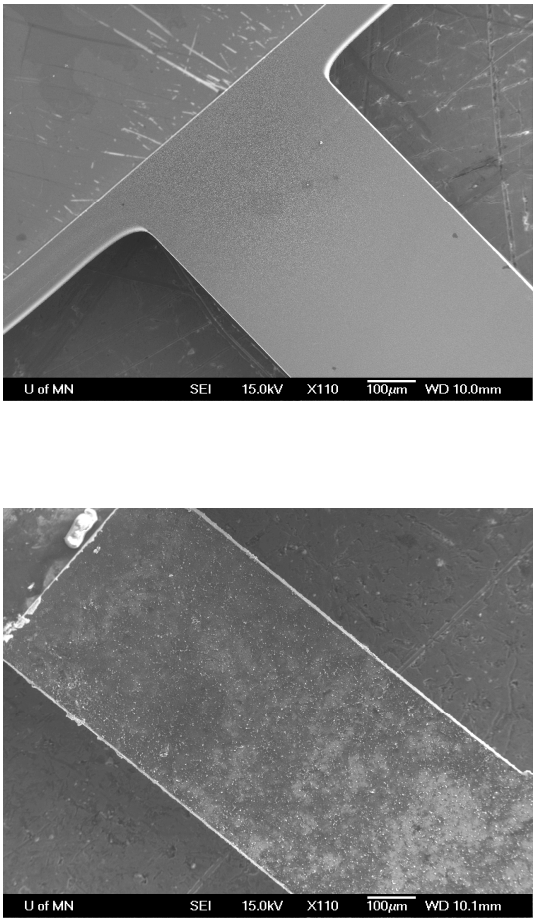

Figure 5.3. Scanning electron microscope images of uncoated silicon samples: (a) a microcantilever before testing shows a clean surface (b) a microcantilever after long-term testing in saline shows presence of particles

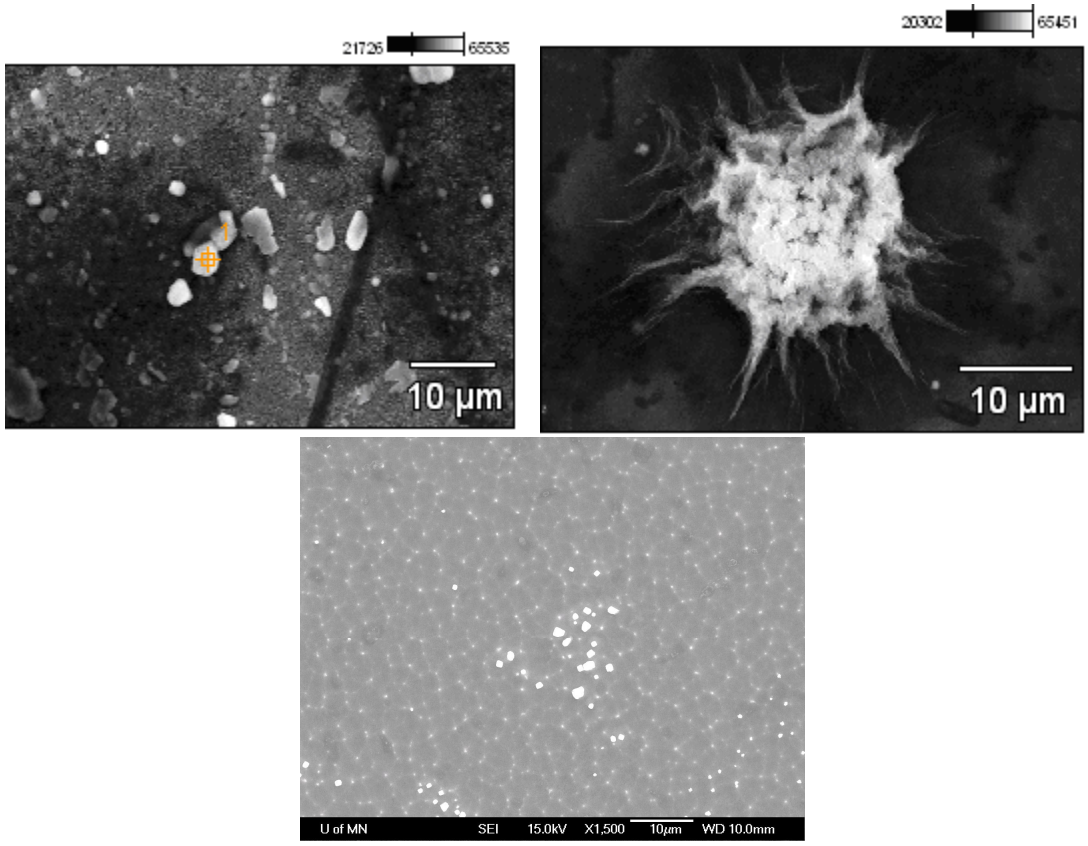

Figure 5.4. Magnified SEM images showing presence of particles on the surface of an uncoated silicon microcantilever after testing by vibrating in saline

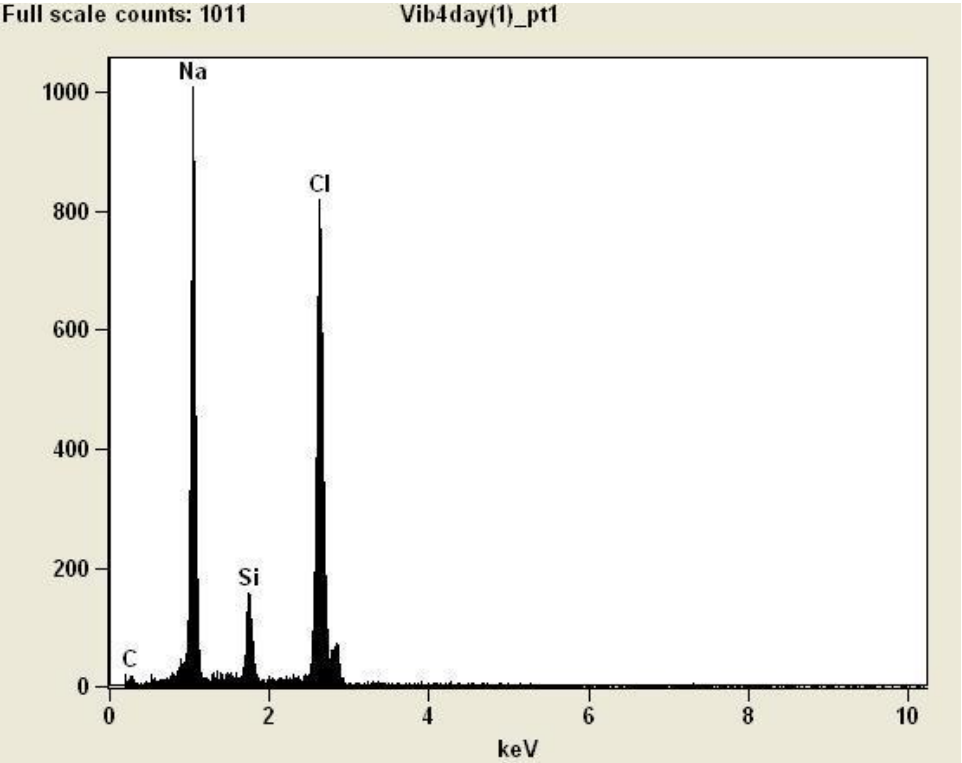

Figure 5.5. Energy dispersive spectroscopy (EDS) analysis for uncoated silicon samples indicates the presence of minerals from saline solution

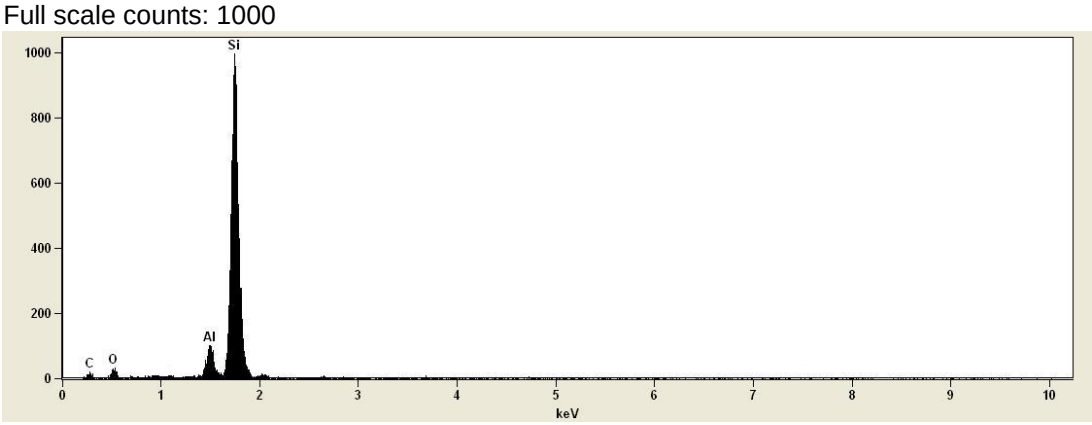

Figure 5.6. Energy dispersive spectroscopy (EDS) analysis for uncoated silicon samples after fabrication indicates presence of carbon, oxygen, and aluminum in addition to silicon

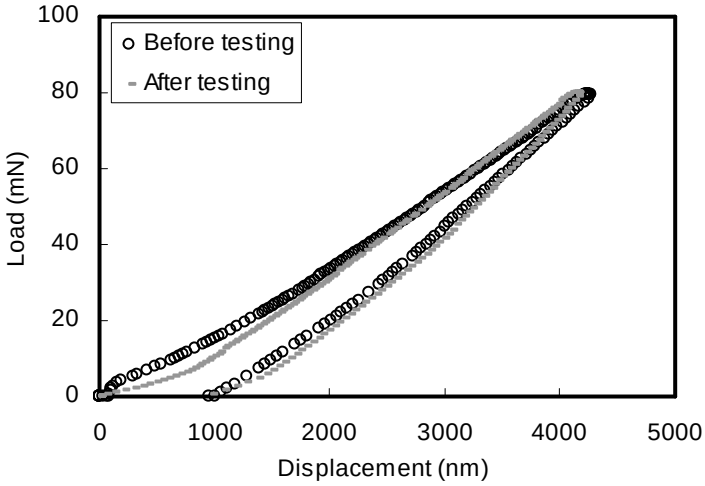

Figure 5.7. Load-deflection curve of an uncoated silicon microcantilever before and after long-term cyclic actuation in saline

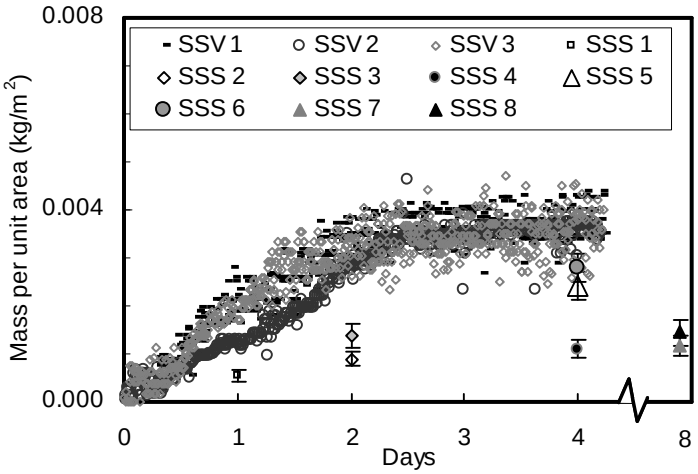

Figure 5.8. Additional mass of minerals adsorbed per unit area for uncoated silicon microcantilever samples tested in saline

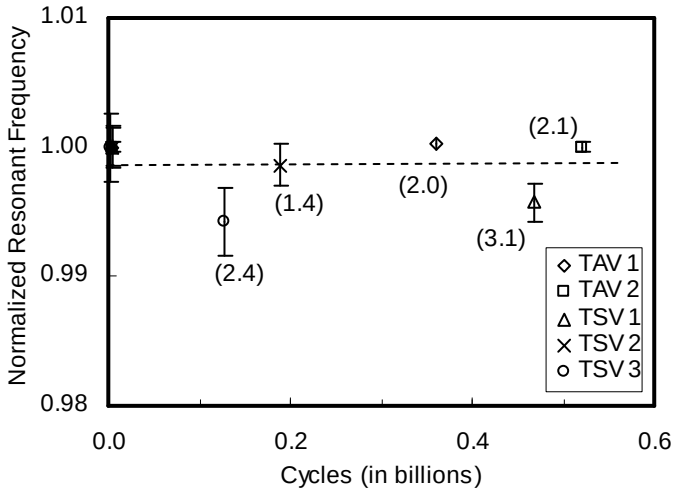

Figure 5.9. Plot of normalized resonant frequency of Ti coated microcantilevers tested in air, water, and saline with increasing number of cycles

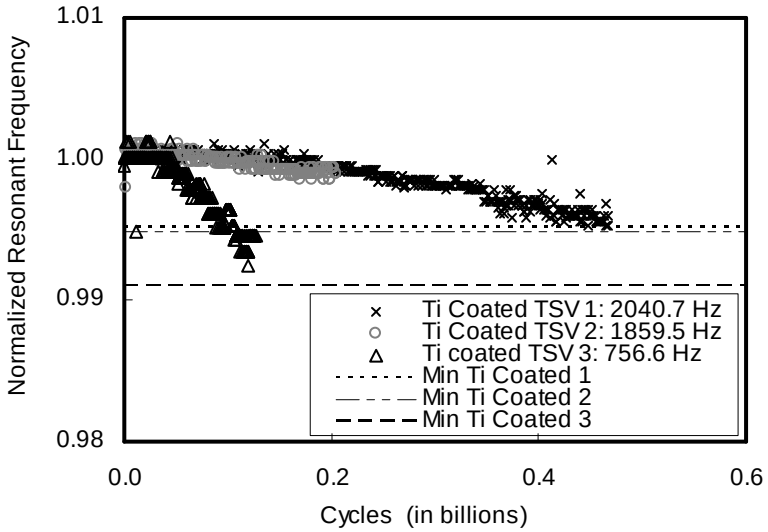

Figure 5.10. Plot of normalized resonant frequency of Ti coated microcantilevers in saline versus cycles

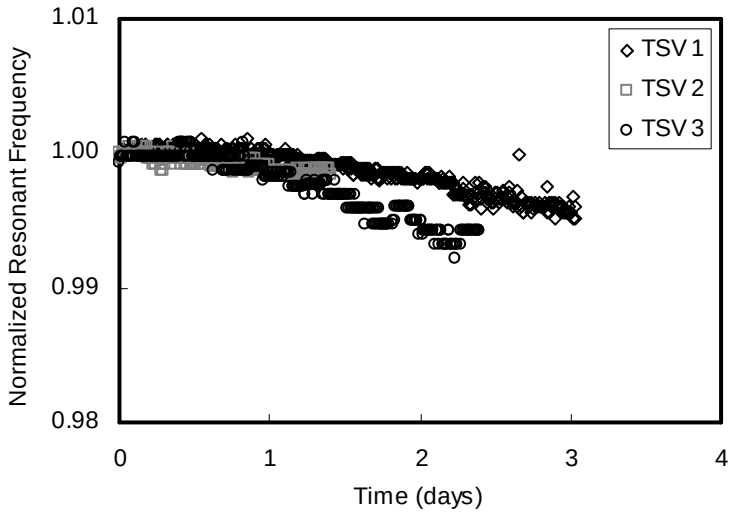

Figure 5.11. Plot of normalized resonant frequency of Ti coated microcantilevers in saline versus time

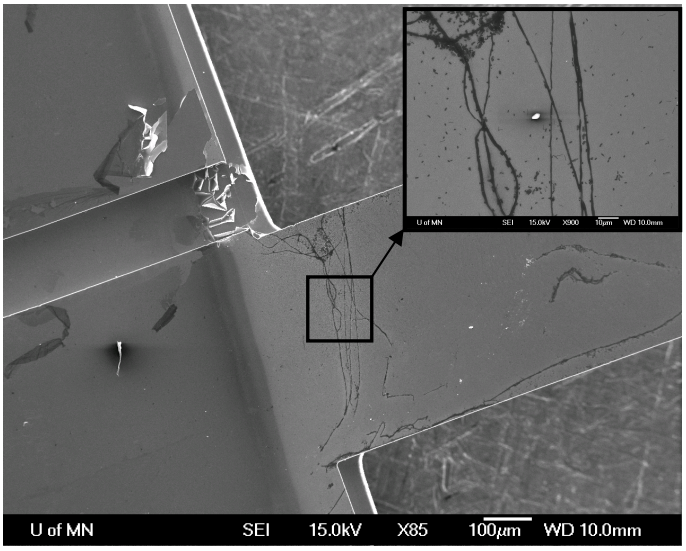

Figure 5.12. SEM image showing cracks in Ti coated microcantilever tested in saline

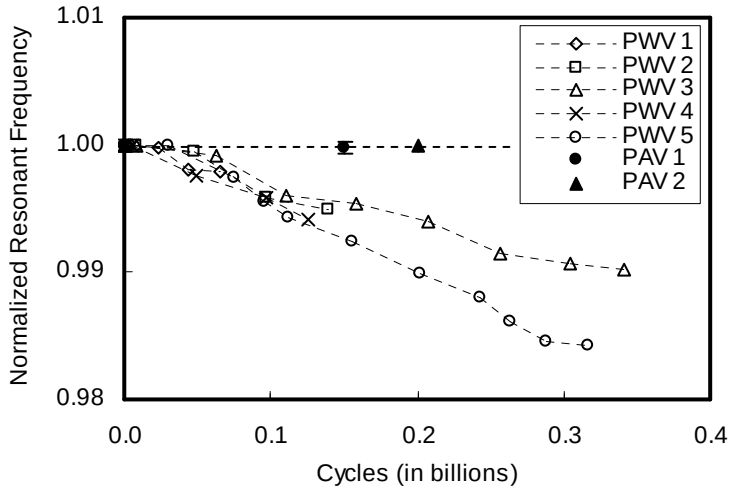

Figure 5.13. Plot of normalized resonant frequency of SU-8 coated microcantilevers tested in air and water with increasing number of cycles

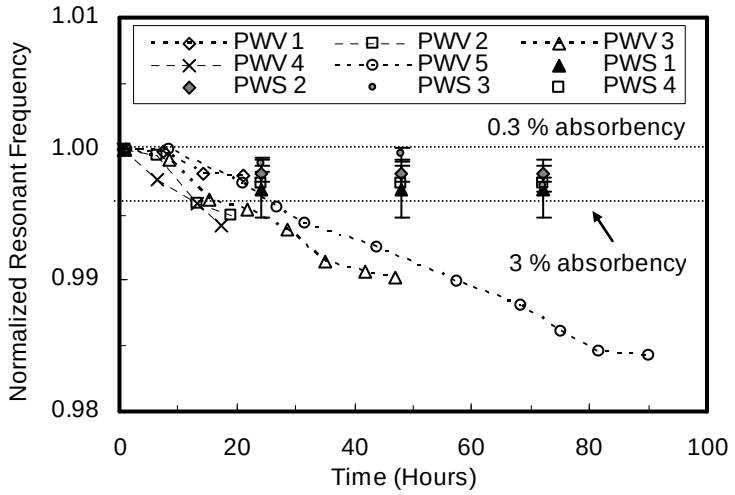

Figure 5.14. Plot of normalized resonant frequency of SU-8 coated microcantilevers tested in air and water with time

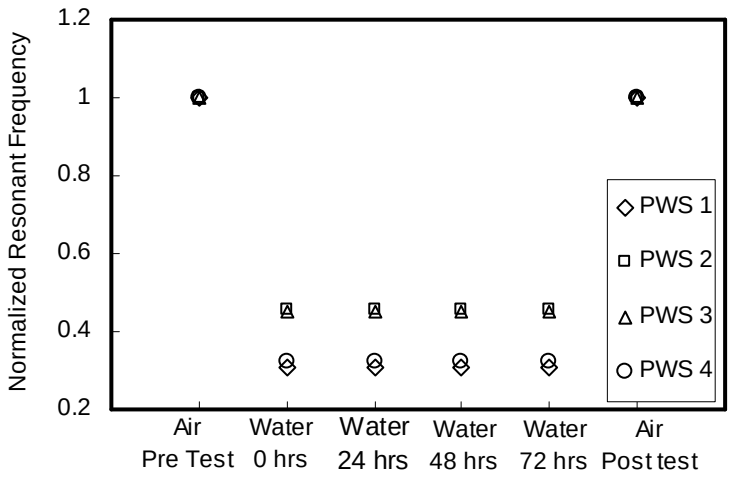

Figure 5.15. Plot of normalized resonant frequency of static SU-8 coated samples tested in water

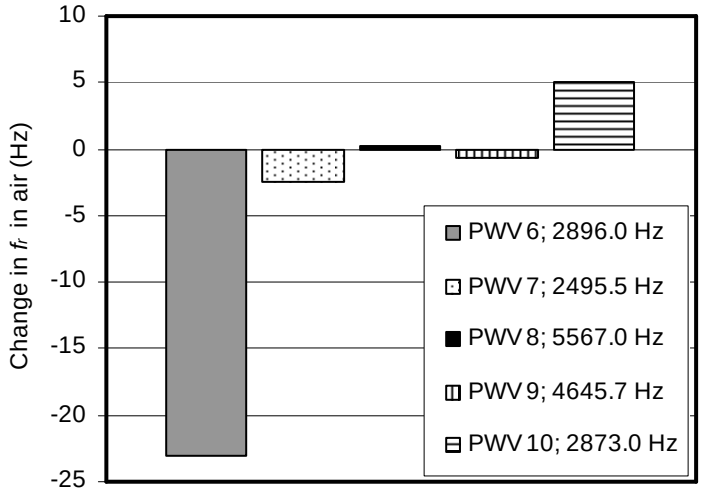

Figure 5.16. Change in resonant frequencies in air for SU-8 samples vibrated in water

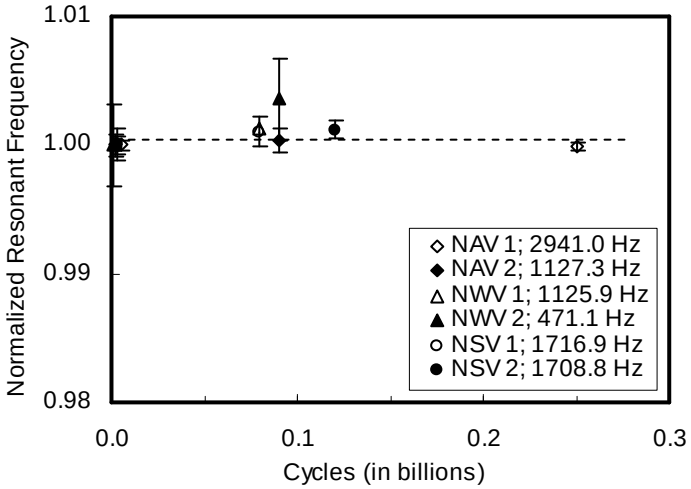

Figure 5.17. Plot of normalized resonant frequency of silicon nitride coated microcantilevers tested in air, water, and saline with increasing number of cycles

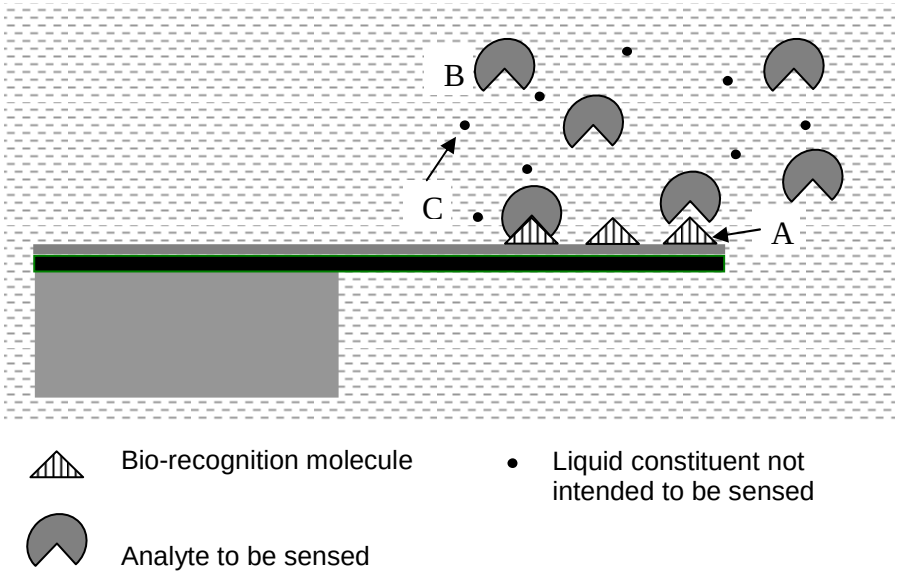

Figure 5.18. Schematic illustrating the issue of non-specific adsorption for a microcantilever sensor immersed in a liquid

CHAPTER 6

Tensile Fatigue of MEMS in Liquids

6.1. Introduction

MEMS tensile specimens were designed to investigate structural fatigue failures of MEMS in liquids. Structural fatigue failures in MEMS have been observed by several investigators and have been discussed in detail in section 2.1.1. Experiments performed on the tensile specimens were conducted at higher stress levels (~ 0.3 GPa) compared to microcantilever specimens (~ 5 MPa). Aluminum was chosen as the test material, and experiments were performed in air and saline solution. Design, fabrication, testing, and experimental results of the tensile specimens are described in detail in the following sections.

6.2. Tensile specimen design

Studying fatigue failures of MEMS in liquids presents practical challenges with specimen design, loading and gripping specimens, and measurement of loads and displacements. Design considerations that were important for test specimens intended for studying structural fatigue of MEMS in liquids are summarized below:

(i) Uniformity of stress state, ease of stress and strain measurement, and a relatively simple design are important requirements. Tensile specimens are common test structures that possess these features.

(ii) Complete contact between the liquid and the test specimen is desirable. Extremely small surrounding dimensions, characteristic of surface micro-machined MEMS may prevent full contact between the test specimen and the liquid environment in

view of capillary forces and surface tension. In contrast, bulk-micromachined MEMS test specimens without the underlying substrate will enable the test specimen to be enveloped by the liquid environment.

(iii) The specimen must allow for testing at different stress levels and testing different materials.

(iv) The ability to test across a range of frequencies is important to evaluate the effect of frequency on fatigue failures in a corrosive environment.

In this study, we have chosen a bulk-micromachined MEMS tensile test structure for fatigue testing in liquids as shown in Figure 6.1. This design is based on a test specimen developed by Haque and Saif [8] for tensile testing of microscale thin films of metals (Al, Au etc.). Certain key design features of the MEMS tensile specimens used in the present study are summarized below:

(i) The MEMS tensile specimens have the gripping fixture integrated with the aluminum specimen on a single MEMS chip. An enlarged image of the aluminum specimen is shown in Figure 6.2.

(ii) The specimen was mounted on the experimental setup using areas A and B labeled in Figure 6.1. Tensile loads were applied on the tensile specimen at specimen grip A, while grips B remained fixed. Microstructures labeled C and D in Figure 6.1 act as springs designed to accommodate small misalignments of the load axis with the specimen axis. These structures ensure that the tensile specimen was subjected to uniaxial loads for small misalignments. Microstructures labeled E are force-sensing leaf springs and support the other end of the tensile specimen and a shuttle labeled F. The shuttle was designed for measurement of displacement using

a laser vibrometer focused on the vertical edge of the shuttle. The aluminum tensile specimen is labeled G.

(iii) Specimen grip A was actuated with a piezoelectric actuator to apply cyclic loads. The load was transmitted to the specimen through the spring supporting structures. Any applied load causes deformation of the spring structures C and D, elongation of the tensile specimen G, and deformation of the spring structures E. The deflection of the force-sensing microstructures E was caused by the load transmitted by the aluminum specimen. The analysis of forces and displacements can be simplified by representing the microstructures with equivalent springs. Figure 6.3 shows the equivalent representation of the tensile specimen with microstructures replaced by three springs with equivalent spring constants k_1, k_2 and k_3. The corresponding elongations of the springs are x_1, Δl, and x_3 respectively and are shown in Figure 6.4. The microstructures C are represented by a single spring with constant k_1. The spring constant k_1 is given by

$$k_1 = N_L\left(\frac{12E_1I_1}{{L_1}^3}\right) \tag{6.1}$$

where N_L is the total number of leaf springs C (N_L = 6), E_1 is the elastic modulus of silicon (160 GPa), I_1 is the moment of inertia, and L_1 is the length of each spring. The aluminum specimen is substituted with a spring constant k_2 given by

$$k_2 = \frac{A_2E_2}{l} \tag{6.2}$$

where A_2 is the area of cross-section of the aluminum specimen, E_2 is the elastic modulus of aluminum (96 GPa), and l is the length of the aluminum specimen. The force-sensing springs E, are represented by a spring with a constant k_3 given by

$$k_3 = 2\left(\frac{12E_3I_3}{{L_3}^3}\right) \tag{6.3}$$

where E_3 is the elastic modulus of silicon (160 GPa), I_3 is the moment of inertia and L_3 is the length of the springs E. The springs representing the aluminum specimen and the force-sensing springs E are in series, and the combination is in parallel with the spring representing microstructures C. The equivalent spring constant for the system, k_{eq} is given by

$$k_{eq} = k_1 + \frac{k_2k_3}{k_2 + k_3} \tag{6.4}$$

The elongation of the springs is related by the following equation:

$$x_1 = \Delta l + x_3 \tag{6.5}$$

Let F_1, F_2, and F_3 be the forces in the springs 1, 2, and 3. The forces in the springs are given by

$$F_1 = k_1x_1. \tag{6.6}$$

$$F_2 = k_2\Delta l. \tag{6.7}$$

$$F_3 = k_3x_3. \tag{6.8}$$

Since springs 2 and 3 are in series, $F_2=F_3$. The total force required from the actuator for a given specimen strain ($\Delta l/l$) can be estimated as

$$F_{act} = F_1 + F_2. \tag{6.9}$$

The calculations discussed above were used to design the microstructures and also to estimate force requirements for the PZT actuator. Stiffness of the microstructures D (U-springs) were neglected since their stiffness was small compared to k_1. Dimensions of the spring supporting structures and specimen grips are included in Appendix C.

(iv) The elongation of the specimen *(Δl)* is related to the displacement of the specimen grip A (x_1) and the shuttle (x_3) along direction of the specimen axis:

$$\Delta l = x_1 - x_3 \tag{6.10}$$

The strain in the specimen is given by

$$\varepsilon = \frac{\Delta l}{l} \tag{6.11}$$

where l is the length of the aluminum specimen. All displacements are expressed in meters in the above calculations. The spring constant of the microstructures E (k_3) can be used to determine the load F experienced by the tensile specimen in Newtons, using

$$F = 2\left(\frac{12E_3I_3}{L_3^{\,3}}\right)x_3 \tag{6.12}$$

where E_3 is elastic modulus in N/m^2, I_3 is the moment of inertia in m^4, and L_3 is length of spring E in meters. The spring structures E are assumed to act as cantilevers with one end fixed, and the shuttle end free but with fixed zero slope. The stress experienced by the aluminum specimen in N/m^2 can be calculated using

$$\sigma_s = \frac{F}{A_2} = \left(\frac{24E_3I_3}{L_3^{\,3}}\right).\frac{x_3}{wt} \tag{6.13}$$

where A_2 is the cross-sectional area of the specimen in m^2, w is the width, and t is the thickness of the aluminum specimen, both in meters. Values of elastic modulus, dimensions and moment of inertia for spring component E used in Eq.(6.13) are listed in Table 6.1. Note that the thickness dimension of the silicon spring lies in the plane of the paper as shown in Figure 6.2. Final fracture of the specimen results in no force being transmitted by the specimen to the force sensing springs E, and is indicated by decrease in value of x_3 to zero ($x_3 \approx 0$).

(v) The spring supporting structures (C, D, and E), specimen grips (A, B), and shuttle (F) were etched from the substrate material, single crystal silicon. The tensile specimen (G) is 99.9 % pure sputtered aluminum.

(vi) The aluminum tensile specimen (G) is 250 μm long, 30 μm wide, and 0.2 μm thick. The length and width dimensions were defined by photolithography, and uncertainties in these values were estimated to be within 1 μm. The thickness of the aluminum specimens was determined for each run with an accuracy of 10 nm.

The MEMS tensile specimens fabricated in this study were designed for testing in liquid environments and differ in a few aspects from the test specimen developed by Haque and Saif [8] . Haque and Saif [8] had conducted uniaxial tensile tests inside a SEM, and used high resolution, high-magnification SEM images for measuring displacements. The liquid environment in the present experiments excludes the deployment of a SEM for measurement or sensing, since operation of an SEM requires high vacuum. In this study, the laser vibrometer discussed previously in Chapter 4 was used for sensing displacements. The shuttle end of the specimen and specimen grips B were modified to allow a clear optical access for the laser vibrometer to the shuttle end.

In addition, the dimensions of the spring elements C, D and E and the specimen are uniquely selected for compatibility with the PZT actuator used in the current study.

6.3. Fabrication of MEMS tensile specimens

The fabrication process for the tensile test specimens is summarized in Figure 6.5. The test samples were fabricated from a 300 ± 20 μm thick double-side-polished (DSP) 4-inch p-type (Boron doped) silicon wafer with orientation (100) (Montco Silicon Technologies, Inc.). The 4-mask fabrication process is described below:

(i) A 0.8 μm thick PECVD SiO_2 was first deposited at 340°C in the PlasmaTherm PECVD deposition system using the SiO2340 recipe (Nanofabrication Center, Univ. of Minnesota). This SiO_2 layer deposited at relatively high temperature was intended to serve as an etch mask for the final release step using DRIE.

(ii) Next, the backside etch mask was patterned over the PECVD oxide layer using SPR-220-7.0 photoresist. The wafer was subjected to an O_2 plasma cleaning step (30-60 seconds) followed by oxide etch step in the STS etcher. For oxide etching, a $CF_4 + O_2$ plasma (STS Etcher, NIT3 or NIT1 recipe, Nanofabrication Center) was used until the oxide layer was completely removed. A nano-ellipsometer (Nanometrics Nanospec AFT, Model 200 Film thickness measurement system) was used to monitor the thickness of the PECVD oxide, and ensure its complete removal. After the etch step, the wafer was cleaned using successive solvent rinses and dried.

(iii) The area under the aluminum specimen was etched during this step. These areas were patterned using photolithography and features were aligned to those obtained in the previous step. SPR-220-7 was used as the masking photoresist for etching

the trenches in the DRIE. Timing the etch step and depth measurement with HS-200P confocal microscope were employed to ensure that these trenches were 100-120 μm deep.

(iv) After removing photoresist and cleaning the wafer, SPR-220-7.0 was spin coated on the backside of the wafer. The wafer was now subjected to a buffered oxide etch to ensure removal of any silicon oxide on the frontside of the wafer. Presence of oxide residue from the PECVD step will act as an etch stop during the final release, leading to the formation of a bilayer with aluminum specimen.

(v) Next, the aluminum tensile specimen (G) was patterned on the frontside of the wafer using the lift-off process (Appendix B). The frontside of the wafer was patterned using the photoresist S1813 (Shipley Company). The mask features were aligned using the MABA 6 back-to-front aligner. The aluminum layer was deposited by sputtering (AJA International sputterer). Prior to the actual sputtering process a 10 min deposition was carried out for cleaning the aluminum source targets, followed by another 25 min test deposition for deposition rate determination. Typically, a 200 nm thick aluminum layer was obtained for a 25 min deposition at 235 W with DC magnetron sputtering. After deposition, the wafer was immersed in acetone until complete lift-off. Scratching the wafer surface with a cotton swab or ultrasonic agitation expedites lift-off. The wafers were then cleaned with successive solvent rinses, and dried. The residual stresses were small, and were measured to be 29 MPa (compressive) using the FSM 900 film stress measurement system.

(vi) Next, the supporting structures and springs were defined using the frontside etch mask patterned with SPR-220-7.0. The mask features were aligned using the MA/BA 6 back-to-front aligner. The frontside was etched to a depth of 100-120 μm. Etch depth was periodically monitored with Dektak 3030 surface profiler and a dial gage.

(vii) The backside was subjected to DRIE using the PECVD oxide as the etch mask. In order to etch the backside, the wafer would have to be rested on the frontside over the deep trench etcher chuck. Since the frontside has deep features, bonding of a backing wafer was necessary to increase heat transfer and prevent triggering alarms (Helium compliance alarm) in the deep trench etcher. Cool Grease® CGR 7016 (AI Technology) was used to bond the wafer to a backing wafer using the process described in Appendix B. The wafer was subjected to a timed etch and periodic visual inspection under the microscope to ensure that silicon was completely etched away under the aluminum specimen. The number of MEMS tensile specimens fabricated on one wafer is 32. The number of functional specimens was usually less than 16 due to low yield. Finally, individual specimens were separated from the wafer by gently breaking the tethers (labeled H in Figure 6.1) with a diamond-tipped scriber.

6.4. Experimental setup

Figure 6.6 shows a schematic of the experimental setup. A precision specimen mount was used for specimen gripping and loading. Design of the specimen mount was critical to ensure proper alignment and loading. Figure 6.7 shows an optical image of the specimen mount used in this study which was designed for testing the MEMS

tensile specimens. Additional drawings and details are included in Appendix C. The test specimens were glued to the expendable polyester spacers, which in turn were screwed to the rigid stainless steel members as shown in Figure 6.8. The spacers prevent damage to the machined flat stainless steel surfaces due to repeated use of glue (Loctite Superglue 01-21309). A commercially available LVPZT (Low Voltage Pb (Lead) Zirconia Titanate) piezoelectric stack actuator (Physik Instrumente, PI 820.20) was used to apply cyclic loads on the MEMS tensile specimens. The L-mount shown in Figure 6.7 was magnetically clamped to the PZT actuator which allows easy removal, installation, and alignment adjustments. The vertical height of the L-mount was designed to keep the PZT actuator away from the liquid surface while the specimen can be actuated immersed in liquid. The PVC bracket was designed to freely suspend the L-mount, the C-mount, and the specimen in the Plexiglas liquid enclosure. Any force or constraint on the mounts can lead to destruction of the tensile specimen. The specimen mount was securely fixed to the Plexiglas enclosure with adhesive tape. A separate Plexiglas bracket was fabricated as shown in Figure 6.9 to allow easier manipulation during mounting, aligning, and gluing the test specimen to the specimen mount. The Plexiglas bracket allows the specimen mount to be suspended, preventing unintended loads on the L or C mounts.

A Plexiglas enclosure was designed to hold the liquid, and has overflow ports to prevent any liquid contacting the LVPZT and cause failure. The enclosure has glass covered windows for the laser, since glass was observed to possess better optical transmission for the laser beam (from the laser vibrometer) compared to Plexiglas. The

Plexiglas enclosure was mounted on an XY stage in order to align the specimen shuttle to the laser beam.

The PZT actuator was used to apply cyclic loads, and the laser vibrometer was used to sense motion. The choice of the PZT actuator was influenced by factors such as maximum displacement/ strain, power requirements, blocking force, heat generation, and unloaded resonant frequency. For example, the unloaded LVPZT resonant frequency was 15 kHz, which was intended to be significantly higher than the desired test frequencies of 300-600 Hz. Since the PZT was not preloaded, it was designed to withstand compressive forces only. The specimen mount consisting of the PZT, L-mount, and C-mount was designed so that tensile loads were applied on the specimen, but the PZT actuator was in compression. The PZT was powered by an amplifier (Physik Instrumente PI E-610.00), which was used to amplify sinusoidal signals generated by the vector signal analyzer (HP 89410A).

The laser vibrometer was focused on the shuttle of the test specimen to sense vibration. The output of the laser vibrometer was observed on an oscilloscope (Tektronix TDS 2010) and also connected to a data acquisition card for monitoring with LabVIEW. Digital images of the specimen were observed during the fatigue test for monitoring the specimen. A CCD camera (Panasonic CCTV camera, WV-BP 330) coupled with a Navitar 6.5x zoom lens (Part No. 1-60135), and 0.67 X adapter (Navitar 1-6020) was positioned above the specimen for imaging. The CCD camera was used to record images of the tensile specimen before and after the test. The CCD camera was also used to visually monitor the appearance of cracks during the experiment. The frame rate of the CCD camera (30 frames/ second) is smaller than the actuation

frequencies (300 to 600 Hz), and no high speed videos were recorded. Figure 6.10 shows an optical image of the experimental setup showing the Plexiglas enclosure, the XY stage, and the CCD camera.

6.5. Experimental techniques

The tensile fatigue tests in this study were carried out at maximum stress level of 0.24-0.26 GPa (σ_{max}) and minimum stress level (σ_{min}) of ~ 0 GPa. The stress-levels were identical for samples tested in air and saline. Limitations of the LVPZT and the experimental setup limit the value of σ_{min} to greater than or equal to zero. The value of the maximum stress σ_{max} can be controlled by the output of the PZT amplifier, which in turn was determined by the input to the amplifier from the HP 89410 signal analyzer. The output of the PZT amplifier was limited to 30 V (peak-to-peak) at test frequencies ranging from 300 to 600 Hz due to heat generation considerations. In the following sections, we discuss the procedure for performing the structural fatigue experiments and data analysis.

6.5.1. Procedure

The steps involved in the testing of tensile specimens are described below:

(i) *Specimen mounting and preparation*: The L-mount was clamped to the PZT actuator and visually aligned so that the machined top surfaces of the L-mount and the C-mounts were on the same horizontal plane. An optical microscope (NFC) and a magnifying glass were used as visual aids during alignment. A knife edge was used to ensure that the top surfaces of the spacers were aligned since the specimen rests on the top surface of the spacers. Next, the polyester spacers were

screwed to the mounts. The burrs on the edges of the spacers were removed with sandpaper. A new set of spaces was used for each experiment to ensure that the grips of the MEMS tensile specimen were resting over the smooth surface of the spacers. The specimen mount was then suspended on the Plexiglas bracket. At this point, the MEMS tensile specimen was placed over the spacers and aligned visually. A few drops of superglue were put over and around the specimen grips, and excess glue was absorbed with blotting paper. No pressure was applied on the specimen. The glue was allowed to dry for at least 5-6 hours before testing. The specimen mount was transferred to the Plexiglas enclosure and fixed with tape. When testing in saline solution, a squirt bottle was used to fill the Plexiglas enclosure with saline to a level below the overflow port.

(ii) *Laser vibrometer alignment*: The laser beam from the vibrometer was aligned with the vertical edge of the shuttle. The PZT was actuated with a low-voltage sinusoidal signal (10-20 V peak-to-peak), and the vibrometer signal was monitored on the oscilloscope. The low voltage signal was used for aid during alignment while ensuring minimal impact on the fatigue life of the specimen during test preparation.

(iii) *Setting of stress levels and frequency*: After mounting and alignment, the actual test was ready to be run. The peak-to-peak output voltage on the vector analyzer was set so as to obtain a higher output voltage (26 to 30 V) from the PZT amplifier to obtain the desired stress level. The output voltage of the PZT amplifier then cycles between 0 and 26-30 V. The test start time was recorded. The frequency of the sinusoidal signal was set to 300 or 600 Hz as required. The laser beam from

the vibrometer was briefly pointed at any point on the specimen mount to record the amplitude of any vibration generated motion (x_c). This value of x_c was subtracted from any experimentally determined values of x_1 and x_3 to obtain corrected values. To determine the value of the displacement x_1, the laser vibrometer could be briefly focused at the vertical sidewall of specimen grip A. Since only one vibrometer was used, only one displacement could be measured at a time. Displacement x_3 was the most important as it indicated final fracture; hence, the laser beam was focused back on the shuttle.

(iv) *Fatigue testing*: The frequency and amplitude of the laser vibrometer output signal was monitored on the oscilloscope and LabVIEW every 15 seconds. A decrease in amplitude of the vibrometer signal indicated final fracture of the tensile specimen. The test stop time was recorded.

6.5.2. Data analysis

(i) Displacements: Displacement x_3 was required to calculate the stress level in the test specimen. Since the laser vibrometer records the velocity signal, x_3 was calculated from the shuttle velocity amplitude using

$$x_3 = \frac{v_3 \alpha}{2\eta\pi f} \tag{6.14}$$

where x_3 is the shuttle displacement amplitude in m, v_3 is the velocity amplitude in Volts, α is the scale factor setting of the vibrometer (125 or 25 or 5 mm/s/V), η is the refractive index of the test environment (1 for air, 1.33 for saline), and f is the vibration frequency in Hz. In order to measure x_1, the vibrometer was focused

separately at the vertical sidewall of specimen grip A. Eq.(6.14) can be used to calculate the value of x_1 by substituting the appropriate value of the velocity signal.

(ii) Mean and alternating stresses: All fatigue tests in this study were performed at similar maximum and minimum tensile stresses of $\sigma_{max} \cong 0.26$ GPa, and $\sigma_{min} = 0$ GPa respectively. The mean tensile stress (σ_m) and alternating stress (σ_a) were calculated using

$$\sigma_m = \frac{\sigma_{\max} + \sigma_{\min}}{2}, \tag{6.15}$$

$$\sigma_a = \frac{\sigma_{\max} - \sigma_{\min}}{2}. \tag{6.16}$$

For $\sigma_{min} = 0$, $\sigma_m = \sigma_a = \sigma_{max}/2$. Since σ_m is non-zero, we can approximately determine the equivalent value of alternating stress (σ_{ea}) with $\sigma_m = 0$ using the constant-life fatigue diagram technique described in [72]. The load line for the tensile specimens is shown by $\sigma_m = \sigma_a$ in Figure 6.11. For microscale aluminum specimens, the tensile strength S_u, reported in the literature ranges from 0.03 to 0.31 GPa [23]. Assuming S_u = 0.31 GPa, we can calculate the equivalent alternating stress (σ_{ea}) using

$$\sigma_{ea} = \frac{S_u \sigma_a}{S_u - \sigma_m} \tag{6.17}$$

For the experiments discussed in this chapter $\sigma_{ea} \cong 0.22$ GPa for $\sigma_m = 0.13$ GPa, $\sigma_a = 0.13$ GPa.

(iii) The number of cycles to failure was calculated by multiplying time to failure with the cyclic frequency of the load (300 or 600 Hz).

6.6. Results and discussion

The MEMS tensile specimens experienced structural fatigue failure in both air and saline solution after testing for 10^6 cycles or more. The actual test duration varied from 1 to 2 hours. Experimental results are summarized in Figure 6.12 which shows the variation in the number of cycles to failure with the maximum stress (σ_{max}) and equivalent alternating stress (σ_{ea}) for the tensile samples tested in air, and saline. An optical image of a tensile specimen which experienced fatigue failure in saline solution after 1.65×10^6 cycles is shown in Figure 6.13. In air, the two tensile specimens were observed to fail after 1.9×10^6 and 2.2×10^6 cycles. The frequency of the cyclic stress was 600 Hz. The fatigue life of tensile specimens tested in saline solution was marginally smaller than that for samples tested in air. The fatigue life of tensile specimens tested in saline was observed to range from 1.2×10^6 to 1.8×10^6 cycles. The effect of frequency of cyclic stress on the fatigue life of the tensile specimens was inconclusive. Test specimens tested at 300 and 600 Hz did not exhibit any marked differences in fatigue life.

The difference in fatigue life for the two specimens tested in air is attributed to the large statistical scatter typical for fatigue failures. The failure of the MEMS tensile specimens is likely to be due to fatigue since the applied cyclic stresses (σ_m= 0.13 GPa, σ_a = 0.13 GPa) are lower than the fracture strength of aluminum (~ 0.31 GPa). The fatigue life of typical macroscale aluminum alloy specimens are reported to be less than 10^5 cycles under applied reversed bending stresses of 0.3 GPa [72]. Barbosa et al. [39] had observed fatigue failure in microscale aluminum tensile specimens in excess of 10^5 cycles. The authors did not report the stress levels, but report their results in terms of

strains. Based on the magnitude of the strains, the applied stresses, estimated to be $\sigma_{m,}$= 0.16 GPa, σ_a = 0.1 GPa, resulted in fatigue life of ~ 5 x 10^7 cycles. Figure 6.14 shows a comparison of fatigue life of MEMS aluminum tensile samples tested in the present study with values reported in the literature for microscale and macroscale aluminum. These published fatigue data are likely to have been determined from tests conducted in a laboratory air environment. The fatigue life of the MEMS tensile specimens tested in the current study in air are within the range of fatigue life (10^5-10^7 cycles) reported in the literature. Differences in fatigue life between various studies are expected due to sample design, material composition, stress levels, manufacturing process, and cyclic frequencies. For example, the experimental setup developed by Barbosa et al. [39] was capable of generating cyclic stresses at a maximum frequency of 100 Hz.

The differences in fatigue life of the tensile samples tested in saline and air are within the range of statistical scatter in fatigue life typically observed in fatigue experiments. The effect of the saline environment on fatigue failures of aluminum MEMS tensile specimens was inconclusive from the experiments performed in this study.

We recall from the literature review that the environmental attack in a corrosive liquid environment is more intense at lower frequencies [47]. For example, Suresh [47] reports that crack growth rate of Ti-8Al-1Mo-1V alloy in 3.5 % NaCl at frequencies 5, 15, and 50 Hz were ~ 10^{-3}, 6 x 10^{-4}, and 2 x10^{-4} mm/ cycle respectively with imposed ΔK= 15 MPa$\sqrt{m}$. Fatigue crack growth rate in argon, an inert environment, were observed to be much slower at 10^{-5} mm/ cycle. Smaller crack growth rates lead to

longer fatigue life. The negligible environmental effect of the saline solution observed in this study may be attributed to the relatively high frequencies of applied cyclic stresses. Based on the literature survey, shorter fatigue life is expected at significantly smaller test frequencies, such as 5 Hz. Limitations of the present experiment setup constrain the minimum test frequencies to above 200 Hz. Typically, MEMS applications such as accelerometers, micro-pumps, and AFM tips contain microstructures made of ceramics and are characterized by high resonant frequencies (> 5 kHz). The relatively high frequency of operation of MEMS may reduce the impact of a corrosive environment on fatigue life. Microstructures which operate at lower cyclic frequencies (1-50 Hz) in a corrosive environment may be more susceptible to corrosion fatigue.

6.7. Features, limitations and suggested improvements for the experimental technique

The primary focus of this study of tensile samples was to develop an experimental technique for fatigue testing of MEMS in liquids and investigate whether liquid environments influence fatigue failures in MEMS. Several key features and potential applications of the experimental technique are listed below:

(i) Different materials can be substituted for aluminum by modifying the microfabrication process. A wide range of metals, ceramics, and dielectrics can be sputtered to substitute aluminum. The LVPZT used in this experimental setup may need to be upgraded to test ceramics due to the relatively higher fracture strengths of ceramics. Testing of biomaterials in physiological or biological fluids can also be performed with the experimental technique developed in this study.

For example, implantable microstructures made of titanium based alloys can be studied in liquids such as saline, glucose, and blood plasma. Performance of typical MEMS materials can be evaluated in liquid chemical environments. For example, use of titanium microstructures can be characterized for oilfield applications.

(ii) The experimental technique can be used to evaluate the effect of a variety of liquid environments on fatigue failures of MEMS. The use of relatively inert materials in the specimen mount and test enclosure was intended to reduce interactions with various liquids.

(iii) The LVPZT was designed to allow testing across a range of stress levels independent of the resonant frequency. The experimental technique does not rely on testing at the resonant frequency for achieving maximum stresses. Stress levels can be set by controlling the displacement of the LVPZT which in turn was determined by the voltage input to the LVPZT.

(iv) The experimental technique can be used to study the effect of frequency on fatigue failures in MEMS. The actuation and sensing techniques employed in the experimental setup are expected to perform satisfactorily in the frequency range of 200 Hz to 1000 Hz. Frequencies lower than 200 Hz are not detected optimally by the laser vibrometer, while frequencies larger than 1000 Hz result in higher dynamic loads which cannot be supported by the LVPZT.

The major limitations of the experimental technique are:

(i) Specimen handling and mounting was particularly challenging due to the fragile nature of the specimen. About one-half of the fabricated specimens were damaged during handling and mounting.

(ii) The MEMS tensile specimen fabricated in this study was limited to tensile-tensile fatigue testing. Completely reversed bending fatigue tests cannot be performed with this specimen design.

(iii) Liquid environments must be transparent to the laser beam. Opaque liquids cannot be tested with this experimental setup.

(iv) The LVPZT has been evaluated by the manufacturer for satisfactory performance up to 10^9 cycles. Testing in excess of 10^9 cycles may cause eventual failure of the LVPZT. Prolonged exposure to liquid environments may cause electrical failure of the LVPZT.

(v) Strains in the specimens cannot be measured during the experiment. The laser vibrometer was used to measure only the oscillating motion of the shuttle (x_3) during the experiment. Simultaneous measurement of both x_1 and x_3 was necessary to calculate the instantaneous strain in the specimen.

Suggested improvements for the experimental technique are discussed below:

(i) The present experimental setup employs one laser vibrometer for sensing displacements at the shuttle. While the laser vibrometer can detect vibrating motion, it is not designed to sense static displacements. Use of a laser diode-PSD scheme for sensing motion similar to that described in section 4.5 will enable measurement of static displacements. Using two laser-diode-PSD setups with one

laser focused at the shuttle and the other laser at specimen grip A, the experimental technique can be extended to include tensile/ creep testing of MEMS in liquids in addition to fatigue testing. Use of two sensing setups will enable simultaneous measurement of x_1 and x_3, both of which are necessary to determine the instantaneous value of strain.

(ii) Measurement of instantaneous strains will enable determination of crack growth rates. The lens and camera could be upgraded to enable digital image correlation (DIC) techniques for determination of crack propagation rates.

(iii) Experiments could be performed at low frequencies such as 5 Hz with the use of a laser diode-PSD setup.

Table 6.1. Properties and dimensions of spring component E

Property/ Dimension	Symbol	Value
Elastic modulus of silicon springs E	E_3	160 GPa
Length of silicon springs E	L_3	1350 μm
Width of the silicon springs E	w_3	120 μm
Thickness of silicon springs E	t_3	30 μm
Moment of inertia of silicon springs E	I_3	2.7×10^{-19} m^4

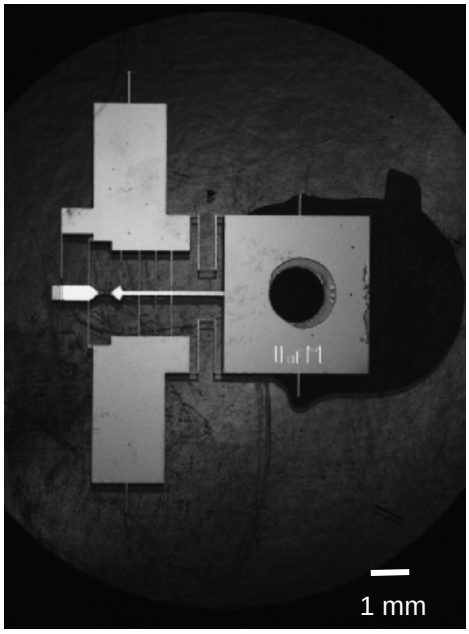

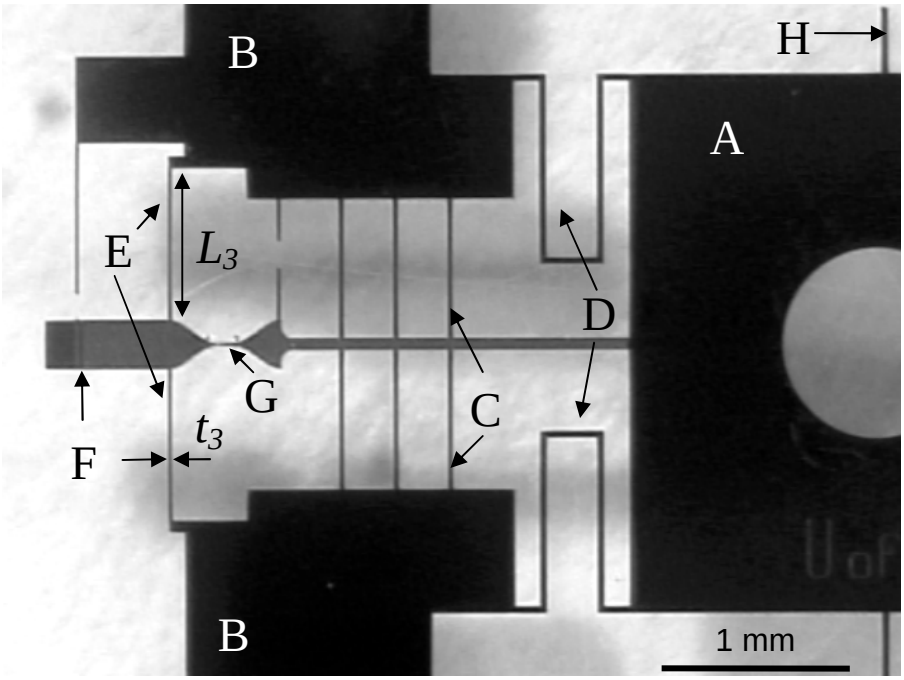

Figure 6.1. Optical images of the MEMS tensile test specimen. Key components are labeled as: (A) Moving specimen grip; (B) Fixed specimen grips; (C) Leaf springs; (D) U-shaped springs; (E) Force sensing leaf springs; (F) Shuttle; (G) Aluminum specimen; and (H) Tethers

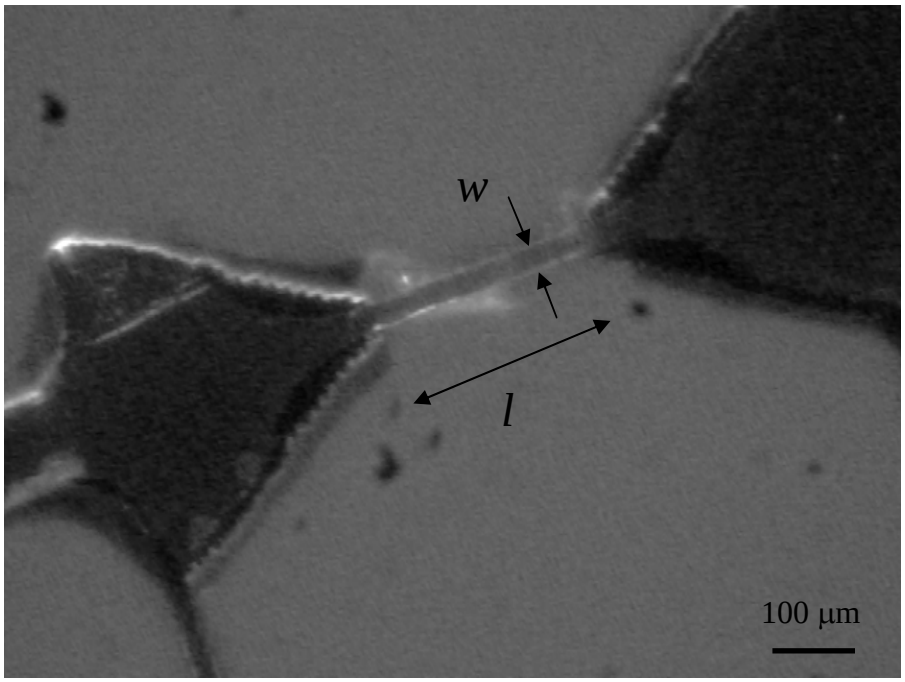

Figure 6.2. Optical image of the actual aluminum tensile specimen: specimen dimensions are l =250 μm, w = 30 μm, t = 0.2 μm (into the plane of the paper)

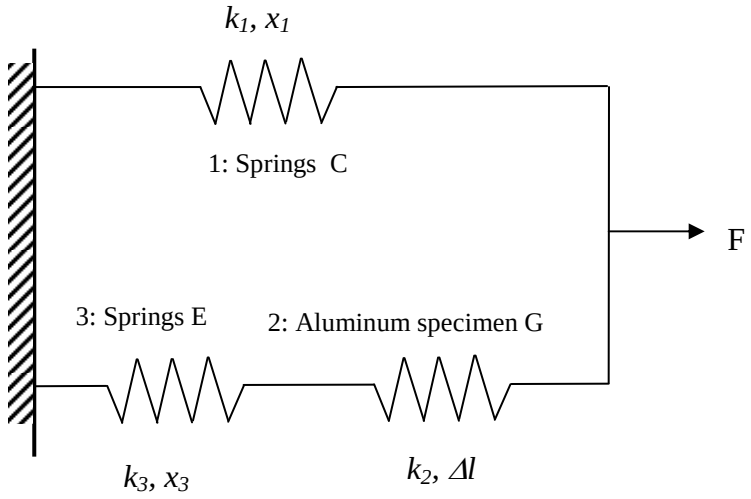

Figure 6.3. Simplified representation of the MEMS tensile specimen with equivalent springs

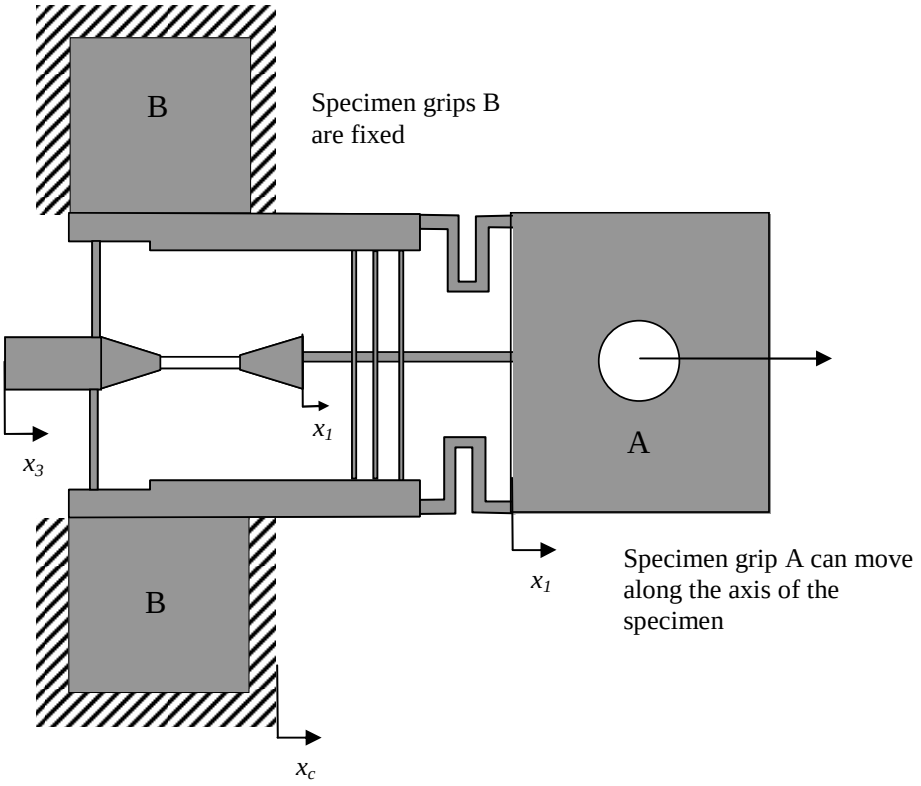

Figure 6.4. Illustration of the MEMS tensile specimen showing displacements

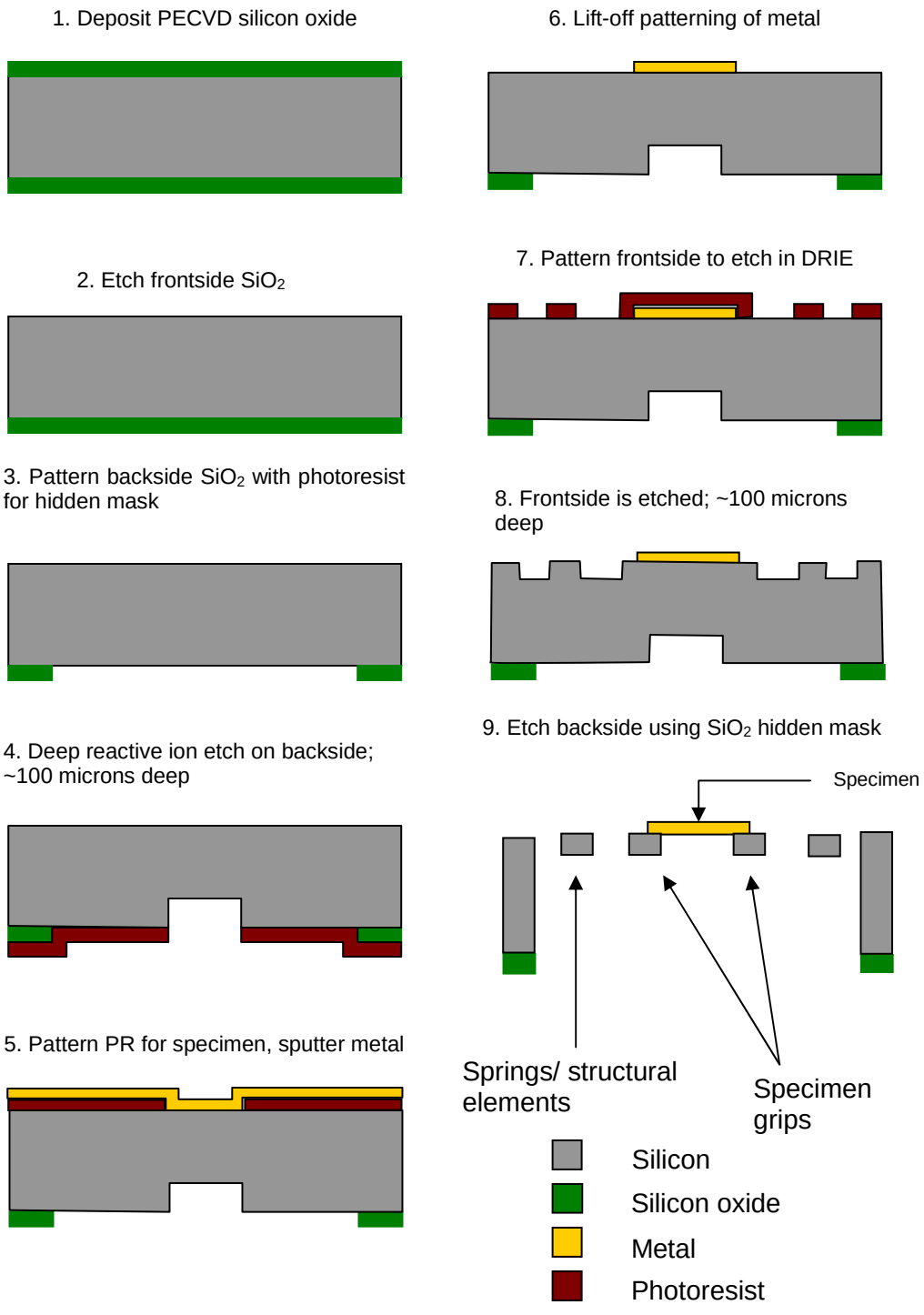

Figure 6.5. Microfabrication process for MEMS tensile specimens

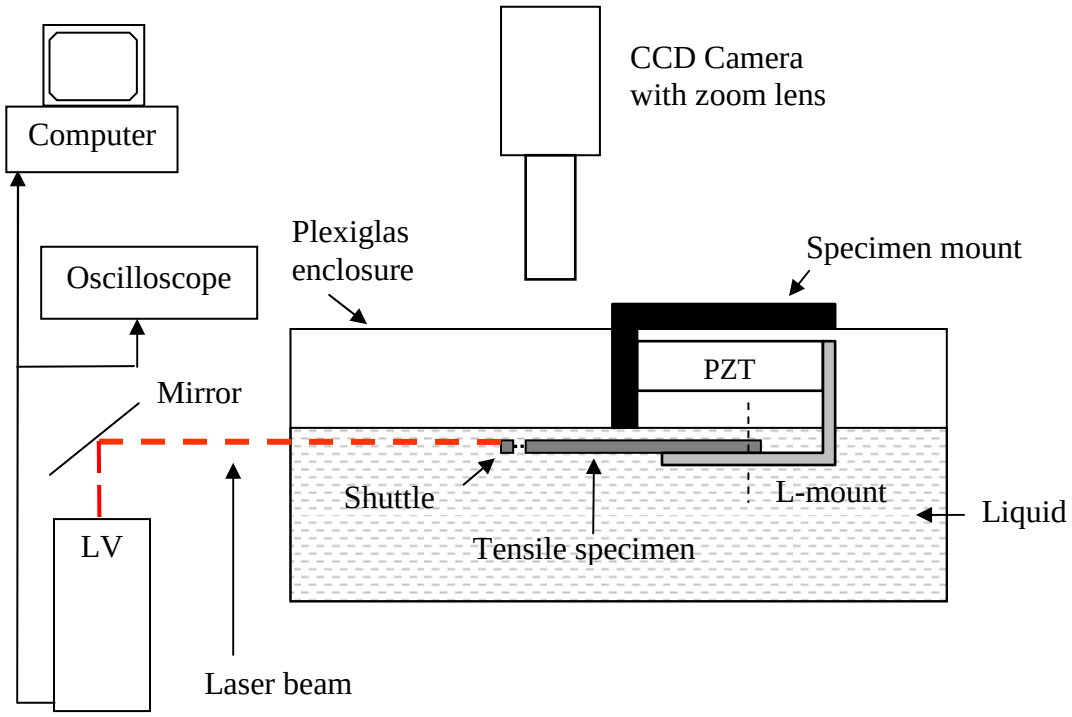

Figure 6.6. Schematic of the experimental setup for fatigue testing of MEMS tensile specimens in liquid environments

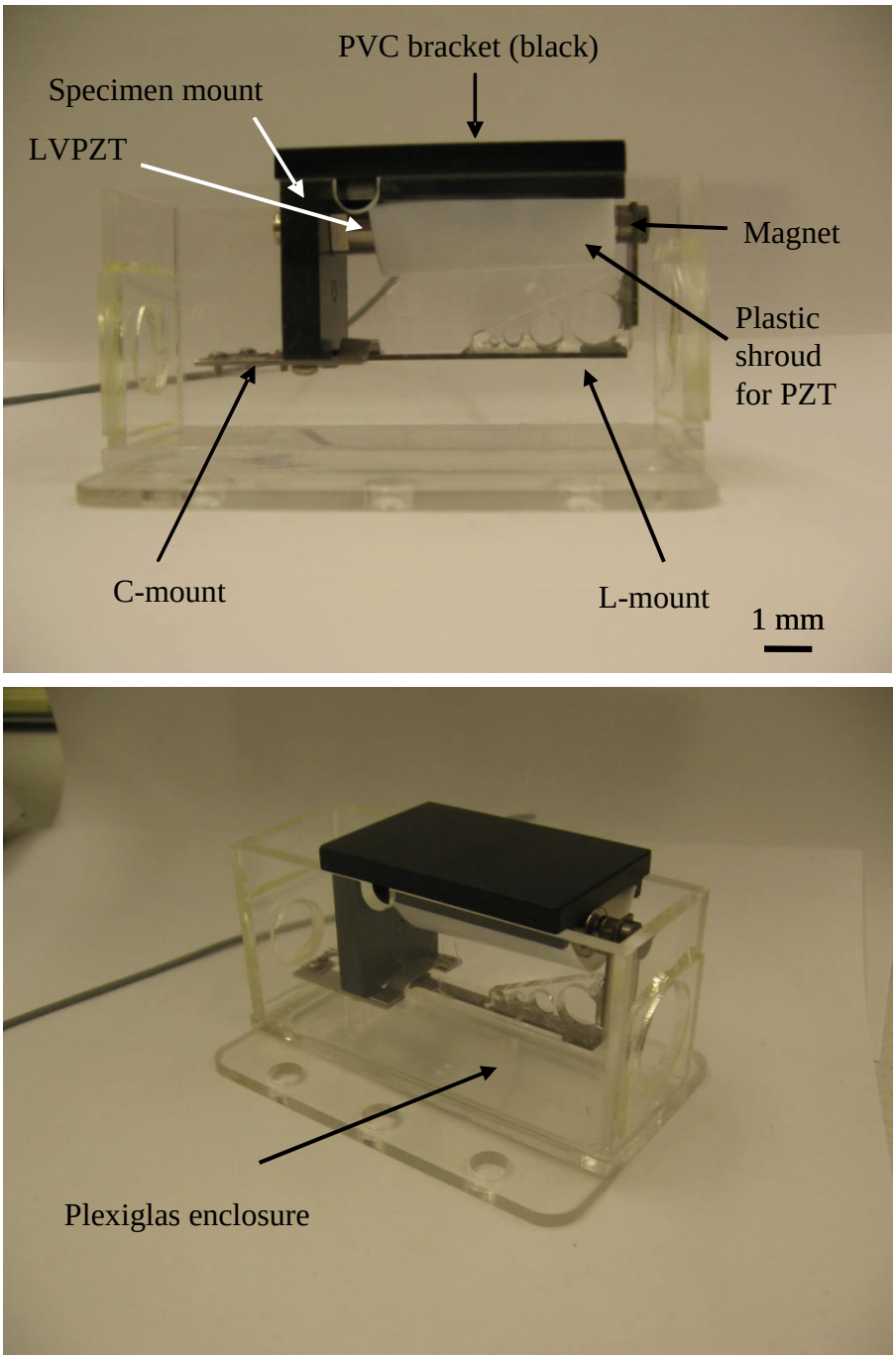

Figure 6.7. Optical images of specimen mount with the Plexiglas enclosure

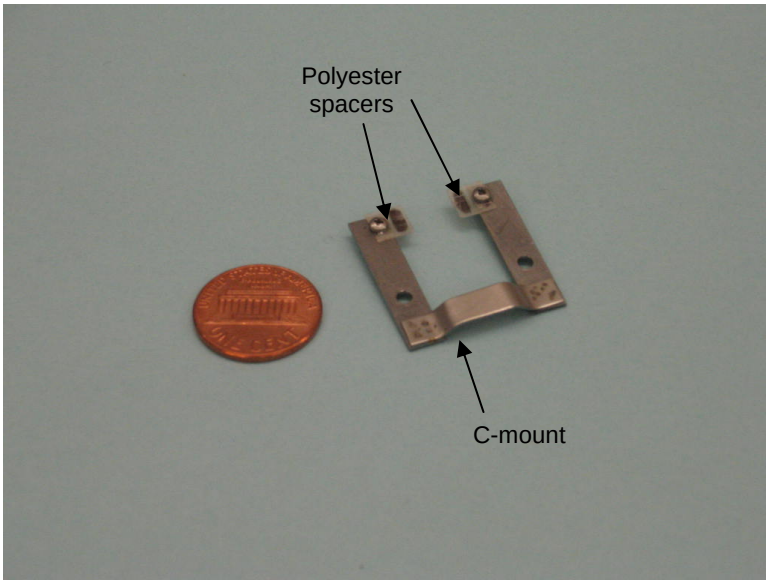

Figure 6.8. Optical image of the C-mount

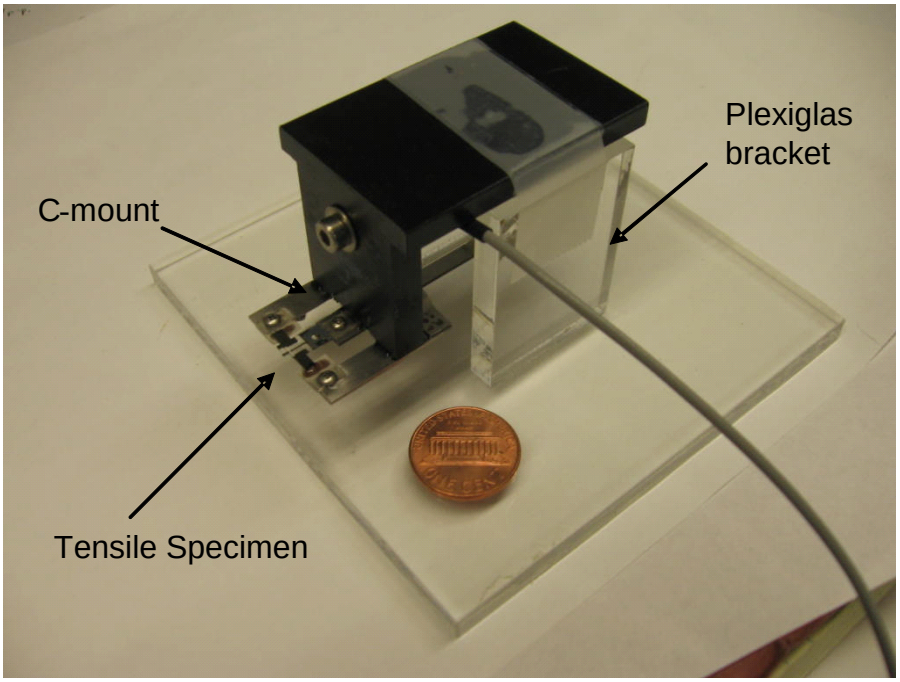

Figure 6.9. Optical image of the Plexiglas bracket

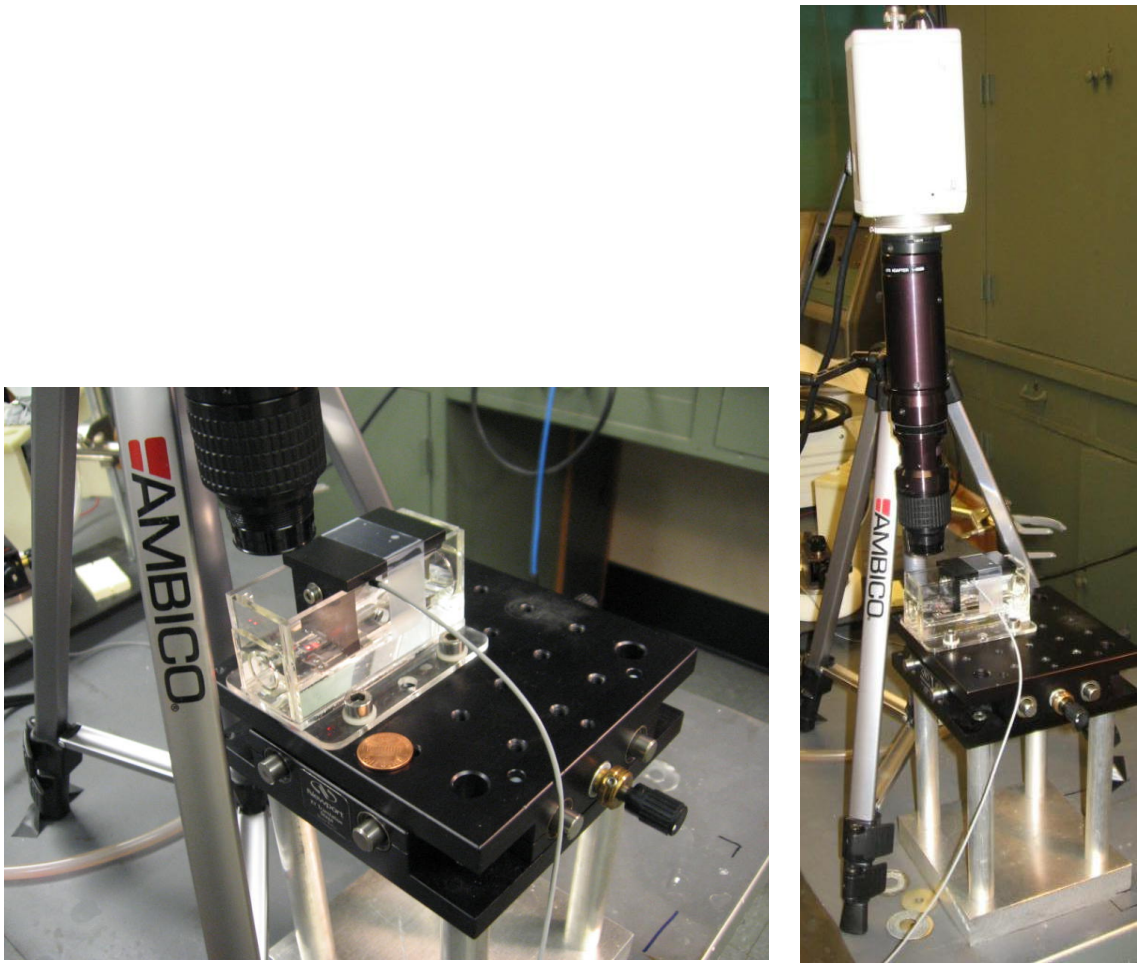

Figure 6.10. Optical image of the experimental setup used for testing MEMS tensile specimens

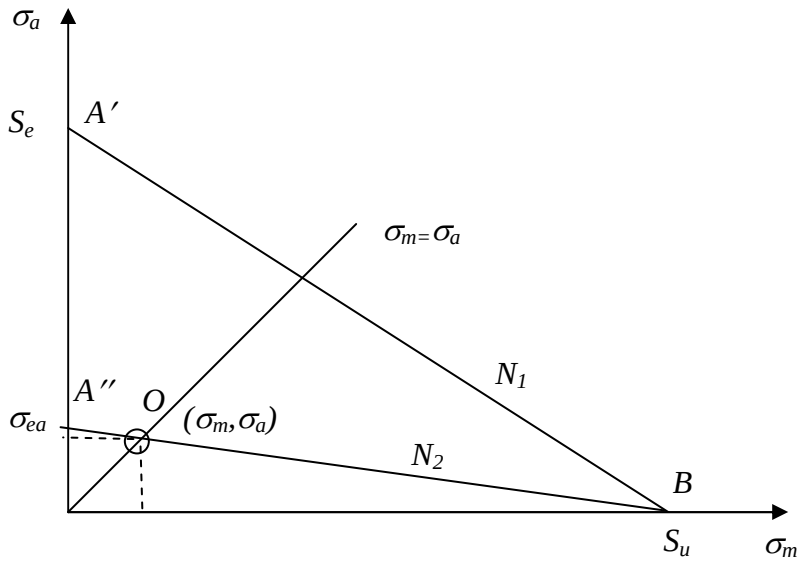

Figure 6.11. Illustration showing constant-life fatigue diagram: *A'B* and *A"B* are lines of constant fatigue life for *N1* and *N2* cycles respectively. Line connecting point B to operating point O is extended to intersect the vertical axis at σ_{ea}

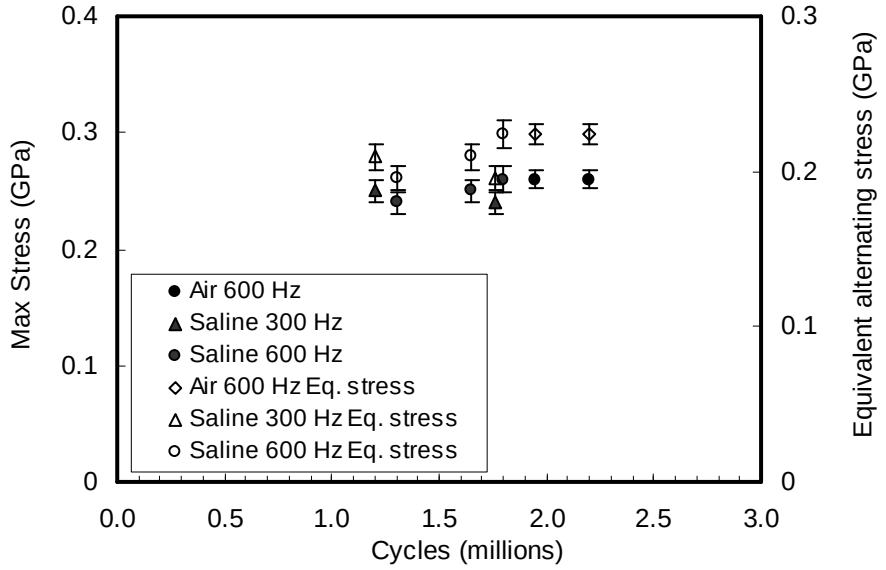

Figure 6.12. Plot of maximum stress (σ_{max}) and equivalent alternating stress (σ_{ea}; σ_m= 0) versus number of cycles to failure for aluminum MEMS tensile samples tested in air and saline solution

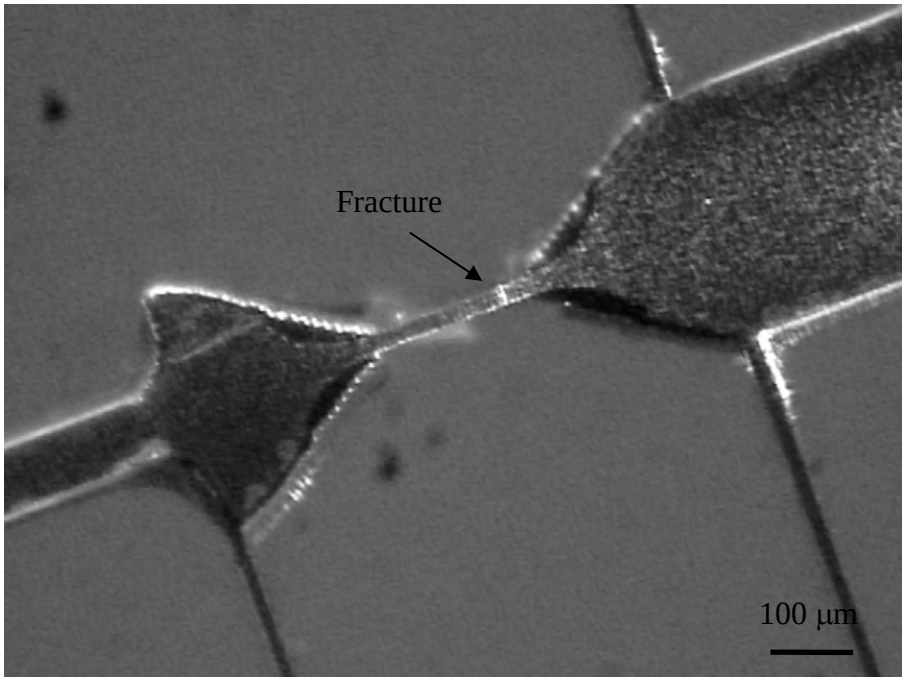

Figure 6.13. Optical image of failed aluminum tensile specimen after testing for 1.65×10^6 cycles in saline solution

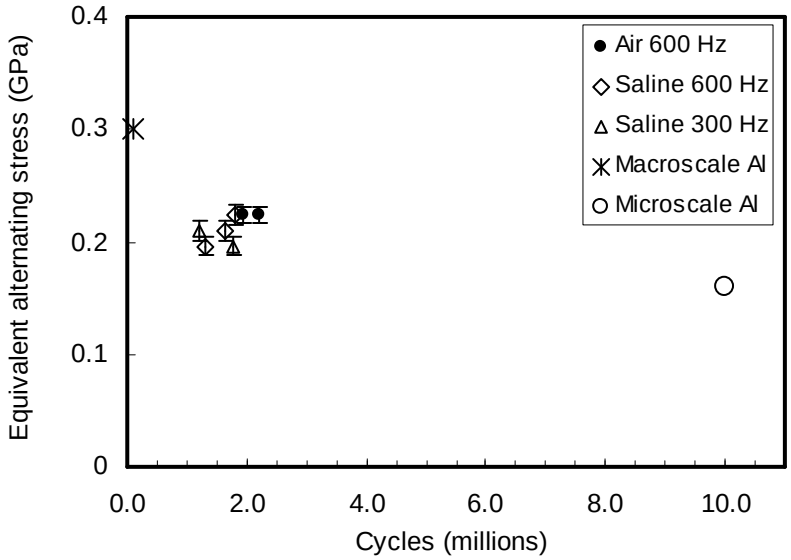

Figure 6.14. Comparison of fatigue life of MEMS aluminum tensile samples tested in the present study with values reported in the literature (macroscale Al [72], microscale Al [39])

CHAPTER 7

Conclusions and Future Work

In this study, long-term mechanical performance of MEMS was experimentally investigated in liquid environments. Based on the literature review, long-term mechanical failures of MEMS observed in air or vacuum can be classified into two broad failure mechanisms: operational failures, and structural fatigue failures. The primary objective of this study was to extend the present understanding of long-term performance of MEMS to liquid environments. Two different types of MEMS test specimens were fabricated to study each of the two failure mechanisms: microcantilever specimens (for operational failures), and tensile specimens (for structural failures). Microcantilever test specimens were designed for testing at low stress levels (0-5 MPa) with the intention to investigate operational failures of MEMS in liquid environments. Operational failures in the present study were indicated by unpredictable changes in resonant frequency of the microcantilevers. MEMS tensile specimens were designed and fabricated with the objective of fatigue testing in liquids at comparatively higher stress levels (~ 0.2 GPa) compared to the microcantilever specimens.

7.1. Conclusions

Long-term mechanical failures in MEMS were influenced by three major factors: stress levels, type of material, and environment. For instance, low stress levels (tests on microcantilevers) resulted in operational failures, while higher stress levels (uniaxial tensile fatigue tests) resulted in structural fatigue failures. Metallic materials such as titanium and aluminum were observed to be more susceptible to corrosion fatigue

failures compared to ceramics such as silicon or silicon nitride. Corrosive environments such as saline solution result in corrosion fatigue while relatively inert environments such as air did not affect the long-term mechanical performance of metals. Results of this study demonstrate that subtle operational failure modes in liquid environments are a long-term reliability concern in addition to fatigue failures. Table 7.1 summarizes the results of long-term performance testing of the different materials evaluated in this study. Table 7.2 summarizes the type of failures observed in this study.

We now focus on results of the experiments performed at low-stress levels on microcantilever specimens to study operational failures in MEMS. Structural fatigue failures were not observed in silicon (both uncoated and coated) and silicon nitride microcantilevers after long-term cycling in air and liquids. Mechanical performance of all microcantilever specimens was unaffected in air, while changes in resonant frequency of microcantilevers were observed depending on the particular combination of structural/ coating material and the liquid environment. Resonant frequency of uncoated silicon microcantilevers was observed to decrease in saline solution due to mineral absorption. Mechanical performance was found to depend on the mode of operation of the microcantilevers, static or vibrating, which could be critical for sensors operating in deflection or resonant mode in liquids. Vibrating uncoated silicon microcantilevers experienced a gradual decrease in resonant frequency to the extent of ~1% over 4 days or 4×10^8 to 8×10^8 cycles. The static samples experience a smaller decrease in resonant frequency ranging from 0.17-0.52 % after exposure to saline solution ranging from 1 to 8 days. The vibrating samples experience higher mass deposition in saline compared to static samples.

Both coating materials Ti and SU-8 exhibited long-term performance degradation. Ti coated microcantilevers showed negligible mineral adsorption from the saline solution. However, Ti coated silicon microcantilevers experienced a gradual decrease in resonant frequency in saline solution due to crack growth in the Ti coating. The average crack growth rates in the Ti coating were determined to be of the order of 10^{-13} m/s. Despite extremely small crack growth rates and low stress levels, possible factors causing performance degradation of the Ti coated specimens are:

(i) High frequency vibrations cause accumulation of a large number of cycles in a relatively short time period,

(ii) Crack growth rates per cycle are accelerated in saline solution

(iii) Dimensions of the microstructures and coatings (particularly thickness) are extremely small.

We note that while the Ti coating was effective in preventing mineral deposition in saline solution, an alternative failure mechanism of corrosion fatigue in a corrosive liquid environment (e.g. saline) caused performance degradation.

SU-8 coated silicon microcantilevers also experience a gradual decrease in resonant frequency in water, due to water absorption and possibly stress relaxation. The resonant frequency of the vibrating SU-8 coated specimens tested in water decreased by 0.18-1.4% (after testing for 0.6×10^8 to 4.5×10^8 cycles), and was not observed to stabilize over the duration of the tests ranging between 20 and 90 hours. In contrast, the resonant frequency of static SU-8 coated specimens decreased to a smaller extent (0.18-0.3%), and stabilized after immersion for 2 days in water. Silicon nitride was found to be the most reliable material for operation in liquids. Change in resonant

frequency of the silicon nitride microcantilevers was negligible to within the limits of experimental certainty. These results demonstrate that both structural and coating materials may affect reliability of microcantilever sensors operating in liquids.

Results of the present study demonstrate that reliable operation of microcantilever sensors is important for both short-term and long-term applications. We note that microcantilever specimens tested in the present study experienced changes in resonant frequency to the extent of ~1 % over a time period ranging from a few hours to several days (1-8 days). While reliability of long-term applications such as implanted biological sensors is an important concern, accuracy of relatively short-term applications such as oilfield chemical sensors could be compromised within the desired service life often lasting only a few days or weeks.

Next, we focus on structural fatigue failures observed in aluminum MEMS tensile specimens tested in air and saline solution. An experimental technique was developed for fatigue testing of MEMS in liquids. These test specimens were tested at significantly higher stress levels of ~ 0.2 GPa (assuming tensile strength of aluminum is ~0.31 GPa). Fatigue life in air was only marginally higher compared to fatigue life observed in saline. The effect of saline solution on accelerating fatigue failures of aluminum was inconclusive possibly due to the high test frequencies (300 Hz and 600 Hz) used for testing.

Based on the results of this study, design guidelines could be developed for MEMS cantilever sensors operating in liquid environments. Errors introduced by undesired or non-specific adsorption could be minimized by choosing structural and coating materials compatible with the liquid environment to reduce liquid-material interactions.

We have observed that aggressive liquid environments could lead to corrosion fatigue despite low stress levels. To design microstructures against corrosion fatigue, crack growth rates for specific material-liquid combinations must be determined for desired life and particular application. Polymeric biocompatible coating for MEMS sensors should compensate for any errors introduced by water absorption and intrinsic stresses. The extent of the effects of cyclic stresses and vibration induced flow on operation of resonating microcantilevers should be evaluated as part of the design and development process to ensure reliable sensing.

7.2. Future work

In this study, long-term mechanical failures were investigated for a several materials tested in liquid filled enclosures at low or high stress levels. Future directions are summarized below:

(i) Additional material-liquid combinations could be tested using the experimental techniques described in this study. Materials could be evaluated either as structural layers or as coatings. Mechanical performance of a material for use in MEMS operating in a biological or chemical environment could be determined from tests similar to that described in this study. It is important to evaluate the effect of frequency on mechanical failures of MEMS functioning in corrosive liquids.

(ii) Reliability of microcantilevers operated in the static and resonant mode could be evaluated and compared in liquids. Microcantilever sensors could be optimized to operate in the static or resonating mode depending on the specific application, and combination of liquid environment and coating/ structural material.

(iii) Long-term mechanical performance of MEMS was investigated in liquid-filled enclosures with microcantilever specimens. Mechanical performance of MEMS in flowing liquids and two phase flows could be investigated to explore the possibility of subtle failure mechanisms. A MEMS cantilever test structure for studying heterogeneous liquids flows has been designed and fabricated, and details are described in Appendix G. Phenomena such as acoustic streaming in conjunction with operational failures may affect the long-term mechanical performance of MEMS.

(iv) A majority of experiments used in this study have used a laser vibrometer to detect vibrating motion. Replacing the vibrometer with a laser diode-PSD setup will enable measurements of static deflection in addition to vibrating motion.

(v) The experimental technique developed in this study for tensile fatigue testing of aluminum thin films in liquids could be used to study mechanical performance of typical MEMS materials and biological materials in liquid environments.

Table 7.1. Evaluation of reliable performance for different materials tested in this study

Material	Structural/ coating material	Environment			
		Air	DI water	Saline solution	Glucose
Silicon	Structural	Yes	Yes	No	Yes
Titanium	Coating	Yes	×	No	×
SU-8	Coating	Yes	No	×	×
Silicon nitride	Structural	Yes	×	Yes	×
Aluminum	Structural	No	×	No	×

×- Not tested

Table 7.2. Failure mechanisms observed in this study

Material	Stress level (MPa)	Environment	Failure type	Failure mechanism/ Results
Silicon	0-5	Saline	Operational	Non-specific adsorption of minerals from saline
Titanium	90	Saline	Operational, Corrosion fatigue	Corrosion fatigue due to cyclic stresses and corrosive environment
SU-8	0-5	DI Water	Operational	Water absorption, and possibly change in intrinsic stresses
Aluminum	200	Air, saline	Structural fatigue	Fatigue failures in air and saline. Corrosion fatigue in saline inconclusive

REFERENCES

1. J. Bryzek, S. Roundy, B. Bircumshaw, C. Chung, K. Castellino, J. R. Stetter, and M. Vestel, "Marvelous MEMS," *IEEE Circuits & Devices Magazine*, 2006, **March/ April 2006**, pp. 8-28.
2. www.smalltimes.com. *Global MEMS/Microsystems markets and opportunities*.
3. M. J. Madou, *Fundamentals of Microfabrication: The Science of Miniaturization, 2nd Edition*, CRC Press, 2002.
4. N. Maluf and K. Williams, *An Introduction to Microelectromechanical Systems Engineering, 2nd Edition*, Artech House, Inc., 2004.
5. H. D. Espinosa, B. C. Prorok, and M. Fischer, "A Methodology for Determining Mechanical Properties of Freestanding Thin Films and MEMS Materials," *Journal of the Mechanics and Physics of Solids*, 2002, **51**, pp. 47-67.
6. W. N. Sharpe Jr., K. M. Jackson, K. J. Hemker, and Z. Xie, "Effect of Specimen Size on Young's Modulus and Fracture Strength of Polysilicon," *Journal of Microelectromechanical Systems*, 2001, **10**(3), pp. 317-326.
7. X. Li, B. Bhusan, K. Takashima, C-W. Baek, and Y.-K. Kim, "Mechanical Characterization of Micro/ Nanoscale Structures for MEMS/ NEMS Applications using Nanoindentation Techniques," *Ultramicroscopy*, 2003, **97**, pp. 481-494.
8. M. A. Haque and M. T. A Saif, "A Review of MEMS-Based Microscale and Nanoscale Tensile and Bending Testing," *Experimental Mechanics*, 2003, **43**(3), pp. 248-255.
9. T. Chen and W. Knapp, "The Fracture of Single-crystal Silicon under Several Liquid Environments," *Journal of American Ceramic Society*, 1980, **Mar/Apr. 1980**, pp. 225-226.
10. C. L. Muhlstein, E. A Stach, and R. O. Ritchie, "A Reaction-layer Mechanism for the Delayed Failure of Micron scale Polycrystalline Silicon Structural Films subjected to High-cycle Fatigue Loading," *Acta Materialia*, 2002, **50**, pp. 3579-3595.
11. C. L. Muhlstein, S. B. Brown, and R.O. Ritchie, "High cycle Fatigue of Single-Crystal Silicon Thin Films," *Journal of Microelectromechanical Systems*, 2001, **10**(4), pp. 593-600.
12. J. A. Connally and S. B. Brown, "Slow Crack Growth in Single-Crystal Silicon," *Science*, 1992, **256**, pp. 1537-1539.
13. T. Ando, M. Shikida, and K. Sato, "Tensile-mode Fatigue Testing of Silicon Films as Structural Materials for MEMS," *Sensors and Actuators A*, 2001, **93**, pp. 70-75.
14. W. N. Sharpe Jr. and J. Bagdahn, "Fatigue Testing of Polysilicon- a Review," *Mechanics of Materials*, 2004, **36**, pp. 3-11.
15. W. W. Van Arsdell and S. B. Brown, "Sub-critical Crack Growth in Silicon MEMS," *Journal of Microelectromechanical Systems*, 1999, **8**(3), pp. 319-327.
16. C. Harrison, S. Ryu, A. Goodwin, K. Hsu, E. Donzier, F. Marty, and B. Mercier, "A MEMS Sensor for the Measurement of Density-Viscosity for Oilfield

Applications," *Reliability, Packaging, Testing, and Characterization of MEMS/ MOEMS V,* 2006. San Jose, CA: SPIE pp. 61110D.
17. S. Bains, "Going with the Flow," *IEE Review*, 2006, **March 2006**, pp. 42-45.
18. T. Naik, E. K. Longmire, and S. C. Mantell, "Dynamic Response of a Cantilever in Liquid near a Solid Wall," *Sensors and Actuators A*, 2003, **102**(3), pp. 240-254.
19. A. C. R. Grayson, R. S. Shawgoo, A. M. Johnson, N. T. Flynn, Y. Li, M. J. Cima, and R. Langer, "A BioMEMS Review: MEMS Technology for Physiologically Integrated Devices," *Biomedical Applications for MEMS and Microfluidics, Proceedings of IEEE*, 2004, **92**(1), pp. 6-21.
20. R. A. M. Receveur, F. W. Lindermans, and N. F. de Rooij, "Microsystem Technologies for Implantable Applications," *Journal of Micromechanics and Microengineering*, 2007, **17**, pp. R50-R80.
21. S. M. Spearing, "Materials Issues in Microelectromechanical Systems," *Acta Materialia*, 2000, **48**(1), pp. 179-196.
22. S. M. Allameh, P. Shrotriya, A. Butterwick, S. B. Brown, and W.O. Sobojeyo, "Surface Topography Evolution and Fatigue Fracture in Polysilicon MEMS Structures," *Journal of Microelectromechanical Systems*, 2003, **12**(3), pp. 313-324.
23. M. Gad el Hak, *The MEMS Handbook*, CRC Press, 2002.
24. www.memscap.com.
25. H. Kahn, R. Ballarini, J. J. Bellante, and A.H. Heuer, "Fatigue Failure in Polysilicon Not Due to Simple Stress Corrosion Cracking," *Science*, 2002, **298**, pp. 1215-1218.
26. H. Kahn, R. Ballarini, and A. H. Heuer, "Surface Oxide Effects on Static Fatigue of Polysilicon MEMS," *Materials Research Society Symposium Proceedings*, 2003, pp. 41-46.
27. J. A. Walraven, "Failure Mechanisms in MEMS," *Proceedings of IEEE International Test Conference,* 2003, pp. 828-833.
28. D. R. Sparks, M. I. Chia, and G. Q. Jiang, "Cyclic Failure and Creep of Electroformed Micromachines," *Sensors and Actuators A*, 2001, **95**, pp. 61-68.
29. K. M. Frederick and G. K. Fedder, "Mechanical Effects of Fatigue and Change on CMOS MEMS," *MEMS Reliability for Critical Applications, Proceedings of SPIE* 2000, pp. 108 116.
30. T. Ono and M. Esashi, "Ultimate Sensing with an Ultrathin Single Crystalline Silicon Resonator," *Proceedings of IEEE, IEEE Sensors* 2002, pp. 916-921.
31. R. Kazinczi, J. R. Mollinger, and A. Bossche, "Environment-induced Failure Modes of Thin Film Resonators," *Journal of Microlithography, Microfabrication, and Microsystems*, 2002, **1**(1), pp. 63-69.
32. N. V. Lavrik, M. J. Sepaniak, and P. G. Datskos, "Cantilever Transducers as a Platform for Chemical and Biological Sensors," *Review of Scientific Instruments*, 2004, **75**(7), pp. 2229 2253.
33. Microchem, "SU-8 2000 Process Datasheet."

34. S. Cherian, A. Mehta, and T. Thundat, "Investigating the Mechanical Effects of Adsorption of Ca^{2+} Ions on a Silicon Nitride Microcantilever Surface," *Langmuir*, 2002, **18**, pp. 6935-6939.
35. W-H Chuang, R. K. Fettig, and R. Ghodssi, "An Electrostatic Actuator for Fatigue Testing of Low-stress LPCVD Silicon Nitride Thin Films," *Sensors and Actuators A*, 2005, **121**, pp. 557-565.
36. S. M. Allameh, J. Lou, F. Kavishe, T. Buchheit, and W. O. Soboyejo, "An Investigation of Fatigue in LIGA Ni MEMS Thin Films," *Materials Science and Engineering A*, 2004, **371**, pp. 256-266.
37. T. Tsuchiya, M. Hirata, and N. Chiba, "Young's Modulus, Fracture Strain, and Tensile Strength of Sputtered Titanium Thin Films," *Thin Solid Films*, 2005, **484**, pp. 245-250.
38. R. Schwaiger and O. Kraft, "High Cycle Fatigue of Thin Silver Films Investigated by Dynamic Microbeam Deflection," *Scripta Materialia*, 1999, **41**(8), pp. 823-829.
39. N. Barbosa, P. El-Deiry, and R. P. Vinci, "Monotonic Testing and Tension-Tension Fatigue Testing of Free-standing Al Microtensile Beams," *Materials Research Society Symposium Proceedings*, 2004, pp. U11.39.1-6.
40. G. Cornella, R. P. Vinci, R. S. Iyer, R. H. Dauskardt, and J. C. Bravman, "Observations of Low Cycle Fatigue of Al Thin Films for MEMS Applications," *Materials Research Symposium Proceedings*, 1998, pp. 81-86.
41. K. Takashima and Y. Higo, "Fatigue and Fracture of Ni-P amorphours Alloy Thin film on the Micrometer Scale," *Fatigue Fracture of Engineering Materials and Structures*, 2005, **28**, pp. 703-710.
42. M. Hopcroft, T. Kramer, G. Kim, K. Takashima, Y. Higo, D. Moore, and J. Brugger., "Micromechanical Testing of SU-8 Cantilevers," *Fatigue Fracture of Engineering Materials and Structures*, 2005, **28**, pp. 735-742.
43. J. E. Shigley, *Mechanical Engineering Design*, McGraw Hill, 1986.
44. Y. Mizutani, Y. Higo, Y. Ichikawa, A. Morita, K. Takashima, and M. V. Swain, "Corrosion Fatigue of Micro sized Specimens," *Materials Research Society Symposium Proceedings*, 2001, pp. EE5.11.1-6.
45. W. J. Callister, *Materials Science and Engineering: An Introduction*, John Wiley, 2003.
46. N. E. Dowling, *Mechanical Behavior of Materials*, Prentice-Hall, 1999.
47. S. Suresh, *Fatigue of Materials, 2nd Edition*, Cambridge University Press, 1998.
48. R. P. Gangloff, "The Criticality of Crack Size in Aqueous Corrosion Fatigue," *Res Mechanica Letters*, 1981, **1**, pp. 299-306.
49. M-T. Lin, C-J. Tong, and K.-S. Shiu, "Monotonic and Fatigue Testing of Freestanding Submicron Thin Beams Application for MEMS," *Microsystems Technologies*, 2007, **14**(7), pp. 1041-1048.
50. W-H Chuang, R. K. Fettig, and R. Ghodssi, "Nano-scale Fatigue Study of LPCVD Silicon Nitride Thin Films using a Mechanical-Amplifier Actuator," *Journal of Micromechanics and Microengineering*, 2007, **17**, pp. 938-944.

51. N. V. Lavrik and P. G. Datskos, "Femtogram Mass Detection using Photothermally Actuated Nanomechanical Resonators," *Applied Physics Letters*, 2003, **82**(16), pp. 2697-2699.
52. *An Introduction to Materials in Medicine*, Academic Press, 1996.
53. M. Calleja, M. Nordstrom, M. Alvarez, J. Tamayo, L. M. Lechuga, and A. Biosen, "Highly Sensitive Polymer based Cantilever sensors for DNA Detection," *Ultramicroscopy*, 2005, **105**, pp. 215-222.
54. Technical information from Cambrex Corporation.
55. T. P. Kuehn, S. M. Ali, S. C. Mantell, and E. K. Longmire, "Testing Reliability of MEMS Materials in Liquids," *Proceedings of SPIE, Reliability, Packaging, Testing, and Characterization of MEMS/MOEMS VI*, 2007. San Jose, CA, pp. 64630L.
56. J. E. Sader, "Frequency Response of Cantilever Beams Immersed in Viscous Fluids with Applications to the Atomic Force Microscope," *Journal of Applied Physics*, 1998, **84**(1), pp. 64-76.
57. W. T. Thomson and M. D. Dahleh, *Theory of Vibration with Applications*, Pearson Education, 1998.
58. T. P. Kuehn, "*Testing Reliability of MEMS in Liquids*," MSME Thesis, Department of Mechanical Engineering, University of Minnesota, 2007.
59. T. Naik, "*Fluid-Structure Interactions of Resonant Cantilevers in Liquids and Liquid-Solid Suspensions Near a Solid Wall*," PhD Thesis, Aerospace Engineering & Mechanics, University of Minnesota-Twin Cities, 2003.
60. *http://www.polytec.com/usa/default.asp*.
61. M. K. Ghatkesar, V. Barwich, T. Braun, A. H. Bredekamp, U. Drechsler, M. Despont, H. P. Lang, M. Hegner, and C. Gerber, "Real-time Mass Sensing by Nanomechanical Resonators in Fluid," *Proceedings of IEEE, Sensors 2004*, 2004.
62. T. M. Beckwith, N. L. Buck, and R. D. Marangoni, *Mechanical Measurements, 3rd Edition*, Addison-Wesley, 1982.
63. *Lange's Handbook of Chemistry*, ed. J.A. Dean, McGraw-Hill, 1999.
64. W. L. Nyborg, "Acoustic Streaming Near a Boundary," *The Journal of the Acoustical Society of America*, 1958, **30**(4), pp. 329-339.
65. L. A. Kuznetsova and W. T. Coakley, "Applications of Ultrasound Streaming and Radiation Force in Biosensors," *Biosensors and Bioelectronics*, 2007, **22**, pp. 1567-1577.
66. M. Papakyriacou, H. Mayer, C. Pypen, H. Plenk Jr, and S. Stanzl-Tschegg, "Effects of Surface Treatments of High Cycle Corrosion Fatigue of Mettalic Implant Materials," *International Journal of Fatigue*, 2000, **22**, pp. 873-886.
67. Technical information from former website of GE Plastics (presently Sabic Innovative Plastics).
68. B. A. Weisenberg and D. L. Mooradian, "Hemocompatibility of Materials Used in Microelectromechanical Systems: Platelet Adhesion and Morphology in vitro," *Journal of Biomedical Materials Research*, 2002, **60**(2), pp. 283-291.
69. "Beyond Silicon,"*Mechanical Engineering*, 2005(July 2005), pp. 30-33.

70. T. George, K. A. Son, R. A. Powers, L. Y. Del Castillo, and R. Okojie, "Harsh Environment Microtechnologies for NASA and Terrestrial Applications," *IEEE Sensors 2005*, 2005, pp. 1253-1258.
71. G-H Feng and E.S. Kim, "Piezoelectrically Actuated Dome-Shaped Diaphragm Micropump," *Journal of Microelectromechanical Systems*, 2005, **14**(2), pp. 192-199.
72. R. C. Juvinall and K. M. Marshek, *Fundamentals of Machine Component Design*, John Wiley and Sons, 2000.
73. Webpage of Microfabrication Laboratory, University of California at Berkeley.
74. J. Y. Park and M. G. Allen, "Development of Magnetic Materials and Processing," *Journal of Micromechanics and Microengineering*, 1998, **8**(4), pp. 307-316.
75. R. C. O'Handley, *Modern Magnetic Materials*, John Wiley & Sons, 2000.
76. G. H. Ryder, *Strength of Materials, 3rd Edition*, ELBS & Macmillan, 1983.
77. P. Marmottant and S. Hilgenfeldt, "A Bubble-driven Microfluidic Transport Element for Bioengineering," *Proceedings of the National Academy of Sciences*, 2004, **101**(26), pp. 9523-9527.
78. P. Marmottant, J. P. Raven, H. Gardeniers, J. G. Bomer, and S. Hilgenfeldt, "Microfluidics with Ultrasound-driven Bubbles," *Journal of Fluid Mechanics*, 2006, **568**, pp. 109-118.
79. M. Stegmeir, E. K. Longmire, and S. C. Mantell, "Parametric Effects of Bubble-microcantilever Impacts in a Confined Channel," *Physics of Fluids*, 2008, **20**(6), pp. 062103.
80. G. T. A. Kovacs, *Micromachined Transducers Sourcebook*, WCB McGraw-Hill, 1998.
81. L. Cao, T. S. Kim, S. C. Mantell, and D. L. Polla, "Simulation and Fabrication of Piezoresistive Membrane type MEMS Strain Sensors," *Sensors and Actuators A*, 2000, **80**, pp. 273-279.

APPENDIX A

Review of Fatigue Failures

Fatigue is defined as a form of failure that occurs in structures subjected to dynamic or fluctuating stresses [45]. Common structures like bridges, aircraft, and machine components are prone to fatigue failures. Under cyclic stresses, failures occur at stress levels considerably lower than the tensile or yield strength for a static load. Fatigue failures occur after the structures have been subjected to an extended period of repeated stresses or strain cycling. Fatigue failures have been recognized in engineering practice for around 175 years. The term fatigue was used as early as 1839 in a mechanics book by J. V. Poncelet of France. Fatigue failures continue to be a major concern in engineering design, as different classes of engineering materials like metals, polymers, and ceramics (except glasses) are susceptible to fatigue failures. Fatigue is reported to be the single largest cause of failure in metals, accounting for 90 % of all metallic failures [46]. Though fatigue failures are sudden, and catastrophic, the process involves successive steps of crack initiation, propagation, stable crack growth and final cleavage. In this appendix, we review the present understanding of fatigue failures at the macroscale.

A. 1. Cyclic stresses

The applied cyclic stresses may be axial, bending, or torsional, and all these three modes contribute to fatigue failures. Fluctuating stresses can have three different modes– reversed, repeated, and random. The cyclic stresses can range from a maximum value σ_{max} and a minimum value σ_{min}, with a mean zero stresses level, as in

Figure A.1. This type of fluctuating stress is known as reversed stress cycle, with equal maximum tensile and compressive stresses. Figure A.2 shows cyclic stresses which are similar to Figure A.1, except that the mean stress is not zero. The maximum tensile stress and the maximum compressive stress are not equal in this case; this is referred to as a repeated stress cycle. Figure A.3 shows cyclic stress which varies randomly with time and frequency and is termed as random stress cycle. Parameters used to describe cyclic stresses are, mean stresses (σ_m), range of stress (σ_r), alternating stress (σ_a) and stress ratio (R). The mean stress σ_m is defined as the average of the maximum and minimum stresses in a cycle,

$$\sigma_m = \frac{\sigma_{\max} + \sigma_{\min}}{2} \tag{A.1}$$

The range of stress σ_r is the difference between the maximum and minimum stresses in a cycle, and is defined as

$$\sigma_r = \sigma_{\max} - \sigma_{\min} \tag{A.2}$$

The alternating stress σ_a is deviation of the maximum or minimum stress from the mean stress, and is defined as

$$\sigma_a = \frac{\sigma_r}{2} = \frac{\sigma_{\max} - \sigma_{\min}}{2} \tag{A.3}$$

Finally, the stress ratio, R, is defined as the ratio of the maximum and minimum stress

$$R = \frac{\sigma_{\min}}{\sigma_{\max}} \tag{A.4}$$

For the above definition, tensile stresses are taken as positive and compressive stresses are negative. Hence, for a reversed stress cycle, σ_{max} and σ_{min} are equal in magnitude

but of opposite signs, and $R = -1$. For $R = 0$, stresses range from zero to a maximum tensile (or compressive) stresses and are termed as tension-tension cycles.

A. 2. Stress versus life (S-N) curves

Similar to other mechanical tests, laboratory tests for fatigue are conducted to study material behavior. If the test specimen or an engineering component is subjected to a sufficiently large number of cyclic stresses it might lead to fatigue damage, and complete structural failure. If the same test is repeated at a higher stress level, the specimen will fail sooner, at a lower number of cycles. If a series of such fatigue failure tests are conducted, and stress levels (S) are plotted against number of cycles to failure (N), as shown in Figure A.4, a *stress-life curve* or S-N curve is obtained.

Two distinct types of S-N curves are observed in common engineering materials and shown in Figure A.4. For some ferrous and titanium alloys, the S-N curve becomes flat at higher values of N, which suggest that below a certain limiting value of stress, fatigue failures do not occur (Figure A.4). This value of limiting stress is termed as fatigue limit or endurance limit. In contrast, for several non-ferrous alloys, such as aluminum, copper, and magnesium, the S-N curve shows a downward trend at increasing values of N (Figure A.5). For these classes of materials, fatigue failures will occur regardless of the applied stresses. Hence, fatigue strength is defined for these materials as the stress level for a certain specified number of cycles.

Experimental fatigue data show considerable scatter due to differences in specimen fabrication, preparation, micro-structural details, composition, specimen alignment and fixturing, mean stress, and test frequency. Hence, several statistical techniques have been developed to specify fatigue life and endurance limit in probabilistic terms.

Other terms associated with S-N curves are *high-cycle fatigue* and *low-cycle fatigue*. High-cycle fatigue is associated with lower stress levels, and minimal yielding effects, and typically occurs above 10^4 to 10^5 cycles to failure [46]. Low-cycle fatigue is characterized by yielding, and plastic deformation, due to higher stress levels, and failures occur below 10^4 to 10^5 cycles [45].

A. 3. Crack initiation and propagation

The process of fatigue failure is characterized by three distinct stages: (i) crack initiation (ii) crack propagation, and (iii) final failure [45, 46]. Crack initiation occurs when a small crack is formed, usually on the surface, at points of stress concentration such as scratches, dents or sharp fillets. As the specimen undergoes stress cycling, the crack propagates into the material. The crack grows in a plane generally normal to an applied tensile stress until it causes failure. Curved lines concentric about the crack origin, called beach marks, can be observed on fractured surfaces, and mark the progress of crack at various stages. After substantial crack growth, the remaining cross-sectional area is no longer able to support the stresses and final fracture occurs. Beach marks and striations will not appear in the region that rapid failure occurs.

The stress intensity factor, *K*, in fracture mechanics characterizes the severity of a crack situation due to the combined effect of crack size, stress, and geometry. For a crack length *a*, nominal stress *S*, the stress intensity factor is given by

$$K = FS\sqrt{\pi a} \tag{A.5}$$

where *F* is a dimensionless function of geometry. The rate of fatigue crack growth depends on *K*. Fatigue crack growth depends on crack size, stress level, and on the

geometrical factor *F*. If we consider a crack which increases in length by Δa, due to application of ΔN number of cycles, the fatigue crack growth rate can be characterized by the derivative *da/dN* for small intervals. When the crack growth rate is plotted against *K*, on a log-log plot, often a straight line relationship has been observed of the form

$$\frac{da}{dN} = C(\Delta K)^m \tag{A.6}$$

where *C* is a constant, and *m* is the slope of the log-log plot [46]. This equation was suggested by P. C. Paris, who first used it to apply fracture mechanics to fatigue failures [46]. Standard methods for conducting fatigue crack growth tests have been developed by ASTM (such as Standard No. E647).

A. 4. Factors affecting fatigue life

Some factors that affect fatigue life are mean stress levels, geometrical features, surface finishes and treatments, and variable amplitude and frequency of applied stresses. Both stress amplitudes and mean stresses affect fatigue life as shown in Figure A.6. With an increase in mean stress levels, the fatigue life or number of cycles to failure (*N)* decreases. Surface effects play an important role as most loading situations such as bending or torsion lead to maximum stresses at the surface. Most cracks leading to fatigue failure originate at the surface, especially at stress concentration sites. Additionally surface treatments like case hardening tend to enhance fatigue life by introducing residual compressive stresses and increasing the hardness. On the other hand, residual tensile stresses introduced by surface finishes such as electroplating cause a decrease in fatigue life.

A. 5. Environmental effects: thermal and corrosion fatigue

At elevated temperatures, fluctuating thermal stresses may cause thermal fatigue. These thermal stresses originate from mechanical constraints that prevent thermal expansion and contraction. The magnitude of the thermal stresses are given by

$$\sigma_{th} = \alpha_l E \Delta T \tag{A.7}$$

where α_l is the coefficient of thermal expansion, E is the Young's modulus, and ΔT is the temperature change.

Fatigue failures that occur under the simultaneous action of cyclic stresses and hostile chemical environments are termed as *environmentally assisted cracking* (EAC) [46]. One such failure mechanism is *stress corrosion cracking*, in which material is removed by corrosion in water, salt water, or any other corrosive liquid which assists crack growth. Corrosive environments thus lead to shorter fatigue life. Small pits due to chemical reactions often lead to formation of stress concentration and crack initiation sites. Additionally, the crack propagation rate is enhanced by the corrosive environment. Often a stress intensity factor for environmentally assisted cracking, K_{Iscc} is used to find associated crack growth rate, $\dot{a}_{EAC}$. Life estimates, t_{if} are then given by

$$t_{if} = \frac{a_f - a_i}{\dot{a}_{EAC}} \tag{A.8}$$

where a_f and a_i are initial and final crack sizes. Protective coatings, and use of corrosion-resistant materials and use of non-corrosive environments are steps taken to enhance fatigue life.

A. 6. Different approaches to fatigue

There are two major approaches to studying fatigue of materials: total-life approaches and defect-tolerant approach. Total-life approaches attempt to determine the number of cycles of stress or strain required to induce fatigue failure in an initially un-cracked laboratory specimen subjected to controlled amplitudes of cyclic stresses or strains. These classical approaches to fatigue design involve characterization of total fatigue life to failure in terms of cyclic stress range (as in *S*-*N* curves) or strain range (plastic or total). Since crack initiation phase constitutes the major component of the total fatigue life, total-life methods represent design against fatigue crack initiation. Components or specimens subjected to low stresses deform primarily elastically and experience high cycle fatigue. Hence, traditionally high cycle fatigue has been characterized in terms of the stress range. In contrast, low cycle fatigue is associated with high stress levels and significant plastic deformation prior to failure. Thus low cycle fatigue is usually characterized in terms of strain range. The strain-based approach to fatigue takes into account the plastic deformation that may occur in localized regions like stress raisers where fatigue cracks usually begin. Stresses and strains in these regions are analyzed and used for life estimation purposes, while the stress-based approach uses the nominal/ average stresses. While the stress-based approach employs a nominal stress versus life (*S*-*N*) curve, the strain-based approach employs the cyclic stress-strain curve and strain versus life curve. Since the strain-based approach is also valid for small plasticity at long lives, it is a more comprehensive approach over the stress-based approach.

On the other hand, the defect-tolerant approach analyzes fatigue failures from a fracture mechanics standpoint. In this approach the useful fatigue life is defined as the number of cycles or time to propagate the dominant crack in the specimen from a certain initial size to some critical dimension. This critical dimension or fatigue crack size is determined by the fracture toughness of the specimen, allowable strain or compliance change, or the maximum load. The prediction of crack propagation life using the defect-tolerant approach involves crack growth laws based on fracture mechanics. This method is valid for small-scale yielding conditions, where the crack-tip plastic zone is small compared to the characteristic dimensions of the cracked component, and predominantly elastic conditions prevail. The defect-tolerant approach is design against fatigue crack propagation. Hence, an optimum analysis for fatigue failure may require a trade-off between the recommendations of the two approaches to attain improved resistance to both crack initiation and crack growth.

The defect-tolerant approach to fatigue failure has been widely applied to fatigue-critical situations where catastrophic failures would cause loss of human life, for example in aerospace and nuclear applications. For ductile metals, with low fatigue life as in machines, vehicles and structures, with plastic strains, the strain-based approach is employed. The stress-based approach is used for smooth specimens with elastic strains and long fatigue life. For the MEMS tensile specimens used in the present study, the stress-based approach to fatigue is used.

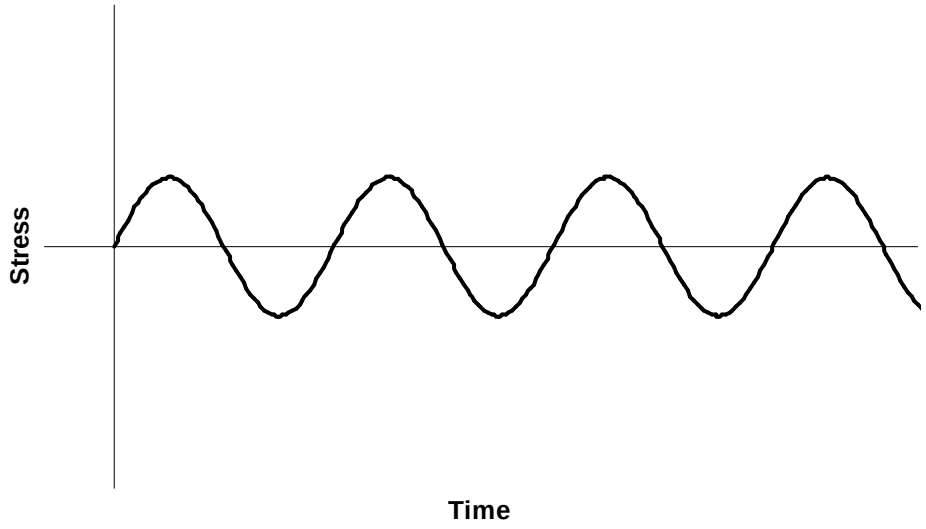

Figure A.1. Reversed stress cycle

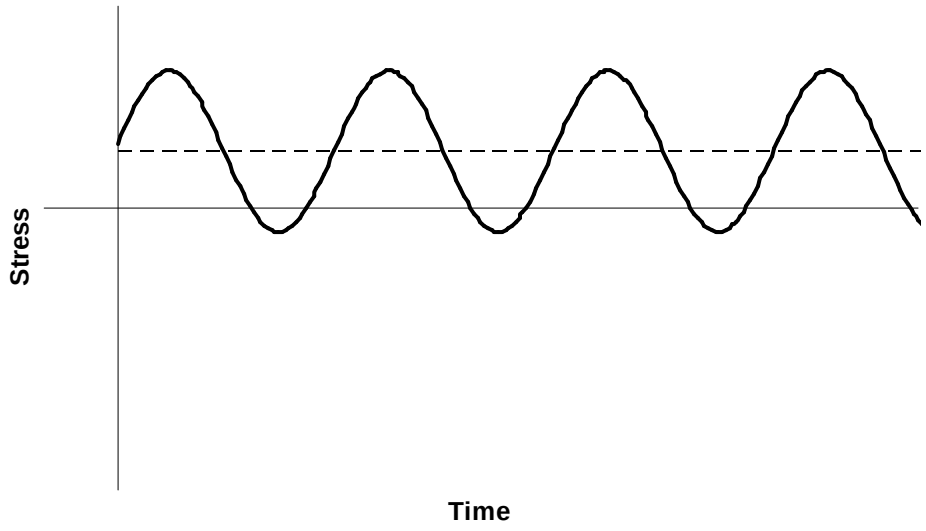

Figure A.2. Repeated stress cycle

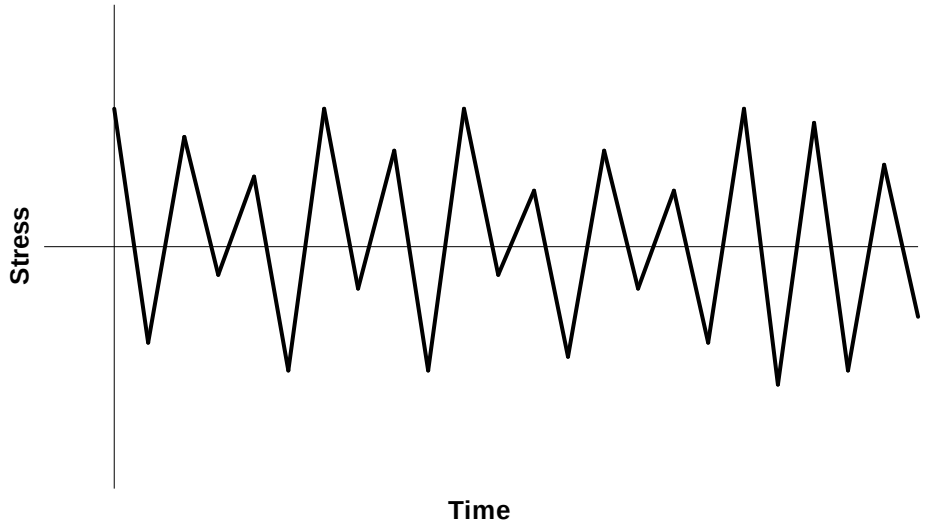

Figure A.3. Random stress cycle

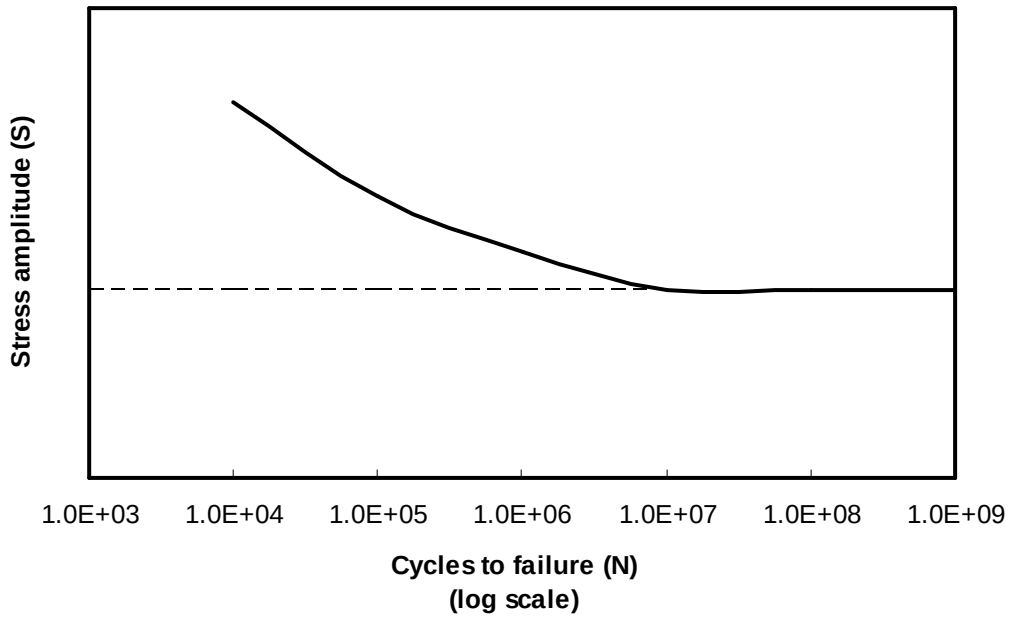

Figure A.4. Typical S-N curve with an endurance limit

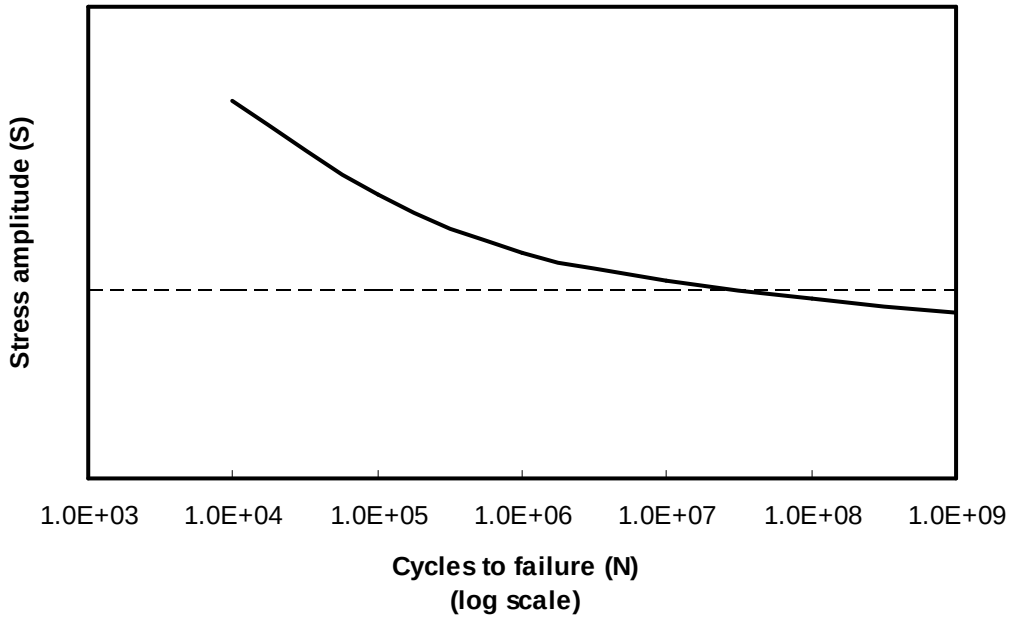

Figure A.5. Typical S-N curve without an endurance limit

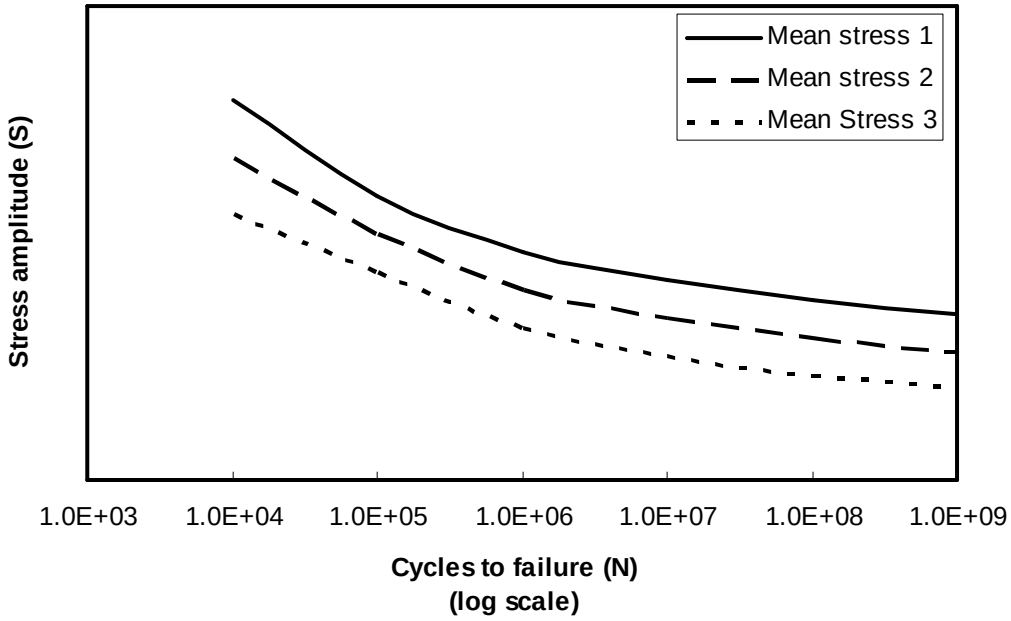

Mean stress 1< Mean stress 2< Mean stress 3

Figure A.6. Effect of mean stresses on S-N curve.

APPENDIX B

Microfabrication Techniques

In this appendix, microfabrication processes used to fabricate the MEMS specimens are discussed. Techniques for processing photoresists and wafer bonding are discussed in section B.1. Process parameters for etching techniques are summarized in section B.2. The Permalloy electroplating process is described in detail in section B.3.

B.1. Photoresist processes

1. SPR-220-7.0 process

(i) Prebake at 120° C for 1-2 min.

(ii) Spin HMDS at 2500 rpm.

(iii) Spin photoresist (2000 rpm: 10 micron, 3000 rpm: 8 micron. Usual: 2500 rpm).

(iv) 115° C Softbake for 1 min 35 sec.

(v) Expose 25-50 sec exposure. Usual 50 sec.

(vi) Develop in MF-CD-26 for 40-45 sec, longer for older developer. Straight MF-CD-26, do not dilute with DI water.

2. SU-8 process

(i) Prebake at 120° C for 1-2 min.

(ii) Optional HMDS spin 2000/2500 rpm

(iii) Dispense SU-8 2010 on wafer. 1 ml of SU-8 for each inch of substrate diameter i.e about 4 ml.

(iv) Spin velocity setting on CEE-1 spinner: Vel1: 500 rpm, 5 secs, Ramp: 100 rpm/s. Spin at 500 rpm for 5-10 seconds.

(v) Vel 2: 1600 rpm for 30s; Ramp: 300 rpm/s

(vi) Soft bake: About 3 minutes at 95 °C.

(vii) Exposure: Intensity 12 W/cm^2. Time: 12 seconds or more.

(viii) Post Exposure Bake: 3-4 minutes at 95°C.

(ix) Develop: PM Acetate, about 2-3 minutes.

(x) Rinse and Dry: IPA wash should not leave white residue, additional time in developer or agitation to improve development.

(xi) Hard Bake (Optional): 150°C- 250°C for 5-30 minutes. 2 minutes at 150° C recommended for all thicknesses.

3. AZ 9260 process for electroplating

(i) Wafers were pre-baked at 120°C on hotplate.

(ii) HMDS (dynamic) spin @ 2000 RPM for 30 seconds.

(iii) AZ 9260 is dispensed on the wafer. Spin at 300 rpm 5 seconds to distribute the puddle of photoresist.

(iv) Wafer was spun at 900 RPM (acceleration 1500 rps).

(v) Wait for 1 minute.

(vi) Bake on hotplate @ 90°C for 1 minute.

(vii) Bake on hotplate @ 110°C for 4 minutes.

(viii) For double coat of thickness 38 μm, repeat step (iii) and then go to step (ix).

(ix) Wait for 1 minute.

(x) Bake on hotplate @ 90°C for 1 minute.

(xi) Bake on hotplate @ 110°C for 8 minutes.

(xii) 1 hour wait prior to exposing.

(xiii) Expose for 90 seconds at MA/BA 6 aligner.

(xiv) Develop for 8 minutes in AZ 400K: DI (1:4).

4. **Lift-off process**

(i) HMDS (dynamic) spin @ 2000 RPM for 30 seconds.

(ii) Spin coat Microposit 1813 photoresist at 3000 rpm for 30 seconds.

(iii) Softbake on a hotplate at 100°C for 90 seconds.

(iv) Chlorobenzene soak for 10 minutes. Allow to dry in air, or blow dry with a nitrogen gun.

(v) Expose for 12-14 seconds in MA/BA6 aligner.

(vi) Develop in 5:1 H_20:351 developer for approximately 60 seconds.

(vii) Deposit metal (Ti or Al) with AJA Sputterer.

(viii) Soak in acetone until complete lift-off. Petri dish with acetone may be placed in ultrasonic agitator for accelerating lift-off. Touch wafer surface gently with a cotton swab to accelerate lift-off.

5. Bonding backing wafer for etching in DRIE

5.1. Bonding with Cool Grease® (CGR 7016, AI Technology)

Adapted from Microfabrication Laboratory, University of California at Berkeley [73].

(i) Piranha clean backing wafer for 10 minutes.

(ii) Rinse and dry the wafer.

(iii) Deposition of oxide layer or LTO on the backing wafer is preferable, but not required.

(iv) Place backing wafer onto a hotplate with temperature of 50ºC. This will soften the cool grease and make it easier to apply evenly across the backing wafer surface.

(v) Use wafer tweezers, razor blade or, cotton swabs to spread Cool Grease on the wafer. The ideal thickness of the Cool Grease after spreading should be about 500 µm to 1000 µm.

(vi) Take the backing wafer off the hotplate. The device wafer was swiftly aligned with the backing wafer and bonded together. The wafers are firmly pressed together using clean-room wipes to contact the wafers.

(vii) Allow the wafers to cool. Return to hotplate at 50ºC for 10 minutes

(viii) Inspect the bonded pair; remove any excess cool grease near the edge with clean room wipes, cotton swabs, or razor blade.

(ix) The photoresist coated device wafer was subjected to a brief (1 minute) etch in O_2 plasma in the STS etcher. This ensures removal or any undeveloped photoresist residue, as well as expulsion of any bubbles entrapped in the Cool Grease layer.

(x) After DRIE, for de-bonding, place the bonded pair in acetone to separate the device wafer from the backing wafer.

5.2. Bonding with a photoresist

(This process was suitable for only short etches)

(i) Photoresists with low viscosity such as Shipley 1813 or 1818 are suitable for bonding with a photoresist.

(ii) A few drops of photoresist are dispensed on the edges of the backing wafer and spread evenly across with a cotton swab or razor blade.

(iii) The device wafer is aligned to the backing wafer, pressed gently, and then placed on a hotplate for 30-60 seconds. In case photoresist is present on the device wafer as a etch mask, time on the hotplate is adjusted so as not to exceed recommended curing time. The bonding photoresist was cured on the hotplate for at least 30-60 seconds to ensure removal of solvents which may otherwise affect the etching process in the deep trench etcher.

(iv) For debonding, the wafers were immersed in acetone. This process removes any photoresist in the bond and the device wafer.

B.2. Etching processes

1. Seed-layer etch for electroplating

(i) Etch Cu with DI: H_20_2: Acetic acid at 20:1:1, rate is 1400 Å/ min

(ii) Etch Cr with HCl: H_20 at 1:10. Touch Cr with some Al foil to start etching.

(iii) Dip in DI water bath for 2 minutes to remove all acid from the wafer.

2. Deep reactive ion etching (DRIE)

Bosch silicon etch (recipe:bosch.rcp):

(i) Passivation step:

Gases: C_4F_8: 70 sccm; SF_6: 0.5 sccm; Ar: 40 sccm

Duration: 5 seconds

RF Power: 825 W

(ii) Etch step:

C_4F_8: 0.5 sccm; SF_6: 100 sccm; Ar: 40 sccm

Duration: 6 seconds

RF Power: 825 W

Other parameters: Process pressure: 23 mTorr;

Cooling He flow: 5.52 sccm; He pressure: 6.0 Torr.

3. STS etcher process

NIT3 Process

Gas flow rates: CF_4: 40 sccm; O_2: 4 sccm.

Process pressure: 100 mtorr

RF Forward power: 25 W.

B.3. Permalloy electroplating process

A Permalloy electroplating bath was developed for electroplating Permalloy on the tips of the microcantilevers. The electroplating process is based on the electroplating technique described by Park and Allen [74].

Figure B.1 shows a schematic of the electroplating setup. A high density polyethylene tank (Nalgene heavy duty rectangular HDPE tank with cover, Cat. No: 14-511-85) was used as the electroplating bath. The HDPE tank was chosen because of excellent chemical resistance and ease of cleaning. A custom made electroplating holder (Sweet Chemical Services) was used to clamp the 4 inch silicon wafers during electroplating (Figure B.2). A 0.787 mm thick strip of 99.5 % pure Ni foil (Alfa Aesar)

was used as the anode. This nickel anode is slowly consumed during the electroplating process. The electroplating holder and the nickel strip are connected to the negative and positive terminal of the DC Power supply, respectively. The HDPE tank was positioned over a stirrer-hotplate and a magnetic stirrer was used to promote mixing and homogeneity.

Electroplating techniques

(i) *Electrolyte preparation*: The HDPE tank was first cleaned with a cleaning powder (Alconox) and DI water. Deposits of Fe_3O_4 (brown color), if present were removed with scrubbing, or rinsing with a dilute sulfuric acid solution. Next, the tank was successively rinsed with acetone, isopropyl alcohol, and water. The tank was filled with 6 liters of DI water. Next, chemicals needed to prepare the electroplating solution are weighed with digital weight balance and added to the DI water in the HDPE tank. The chemicals and the quantities used for preparing the electroplating solution are listed in Table B.1. The magnetic stirrer was turned on, and the pH of the solution was monitored with a pH meter. The pH of the electroplating bath was maintained at 2.7-2.8 by adding a few drops of acetic acid (CH_3COOH) as needed.

(ii) *Electroplating*: At this point, the wafer to be electroplated has a photoresist (AZ 9260) mold over a Cr-Cu seedlayer. The wafer was placed in the electroplating bath for 10 minutes to remove the thin superficial layer of copper oxide. Next, the DC power supply was turned on (constant voltage, CV mode), and the maximum current is set so as to result in a current density of 8-12 mA/cm^2. The current density is calculated by dividing the total current by the area exposed for electroplating. Both the wafer and the nickel anode should be completely immersed in the electroplating solution. The DC

power supply was increased to a voltage level required to attain the desired current density. After 5 minutes, the power supply was switched off, and the electroplating holder was withdrawn from the electroplating solution for visual inspection. Electroplated areas should have metallic silver colored deposits of Permalloy; electroplated areas which are black in color indicate improper electroplating process parameters (e.g. pH, current density). Further, the thickness of the electroplated layer was determined with Dektak III surface profiler for calculating the deposition rate. The electroplating holder was returned to the electroplating bath, and the DC power supply was switched on. The electroplating process was continued to obtain the desired thickness.

The electrochemical reactions taking place near the cathode (wafer) lead to evolution of hydrogen bubbles which can get incorporated in the electroplated Permalloy. To reduce these gas inclusions, the power supply was switched off and the electroplating holder was withdrawn from the solution every 10 minutes. The entire electroplating process to achieve 25 μm thickness took about 2 hours.

(iii) *Characterization*: The thickness of the final electroplated layer was measured using a dial-gage or Dektak III surface profiler. The effect of long-term cyclic actuation and immersion in a saline environment on the magnetic characteristics [75] of the Permalloy layer was measured using a vibrating sample magnetometer at the Institute of Rock Magnetism at the University of Minnesota. Uncoated silicon microcantilevers were subjected to long-term cyclic actuation in air, and the magnetic hysteresis curve was compared before and after long-term actuation in air for 6 days. Results shown in Figure B.3 show negligible effect of long-term cyclic actuation on the magnetic

characteristics of Permalloy. A separate set of samples was immersed in saline and the magnetic characteristics were compared before and after immersion. Immersion in a saline environment for 7 days was not observed to have any detrimental effect in the magnetic properties of electroplated Permalloy (Figure B.4).

Table B.1. Chemicals used for Permalloy electroplating

Chemical	Chemical formula	Item No.	Weight* (g)	Purpose
Nickel (II) Sulfate Hexahydrate, 99%	$NiSO_4.6H_20$	Sigma-Aldrich 227676	97.8	Electrolyte
Nickel (II) Chloride Hexahydrate	$NiCl_2.6H_20$	Sigma-Aldrich 223387	216	Electrolyte
Iron (II) sulfate Heptahydrate, 99%	$FeSO_4.6H_20$	Sigma-Aldrich 310077	8.4	Electrolyte
Boric Acid	H_3BO_4	Fisher A74-1	150	
Saccharin sodium salt hydrate, min 98%	$C_7H_4NNaO_3S.xH_20$	Sigma S1002	9	Adjust stress
Sodium Chloride	NaCl	Mallinckrodt CAS #: 7647-14-5	150	Electrolyte

* For 6 liters of DI water

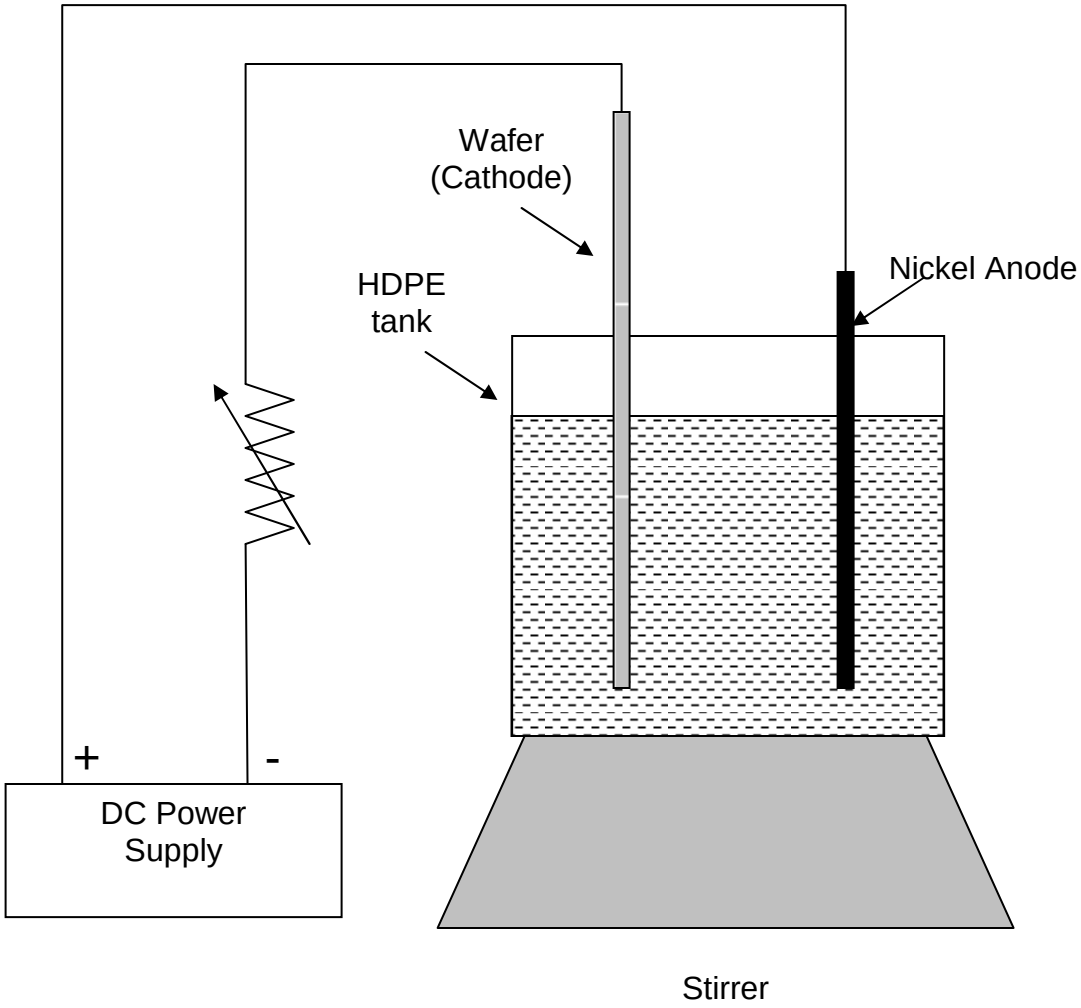

Figure B.1. Schematic of the electroplating setup

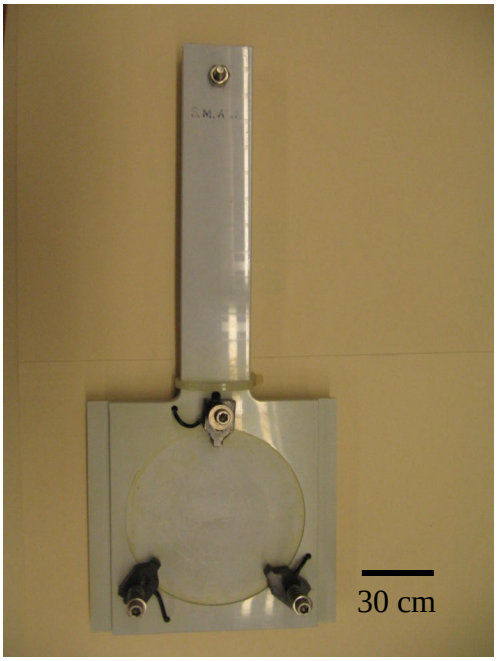

Figure B.2. Optical image of wafer holder (cathode) for electroplating

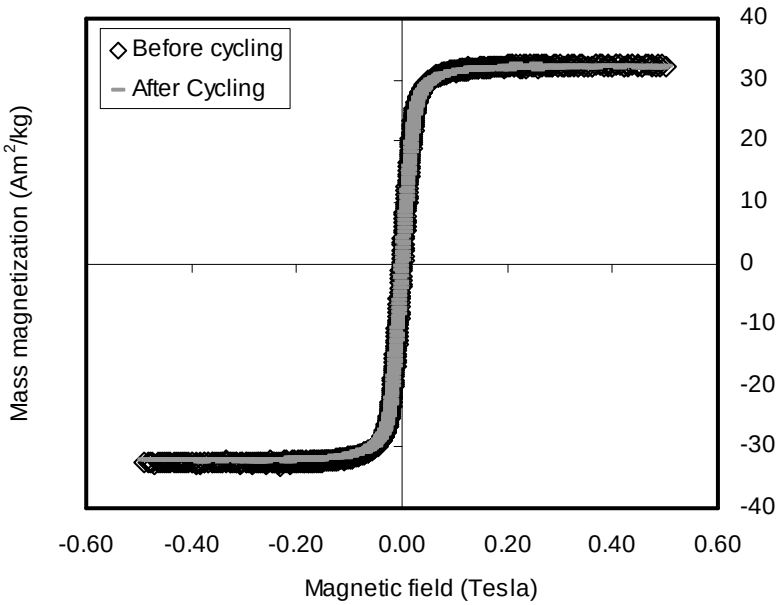

Figure B.3. Effect of long-term cyclic actuation with an electromagnet. (applied magnetic field: 283 gauss, 3.63×10^9 cycles in air over 6 days, Resonant Frequency: 6046.5 Hz)

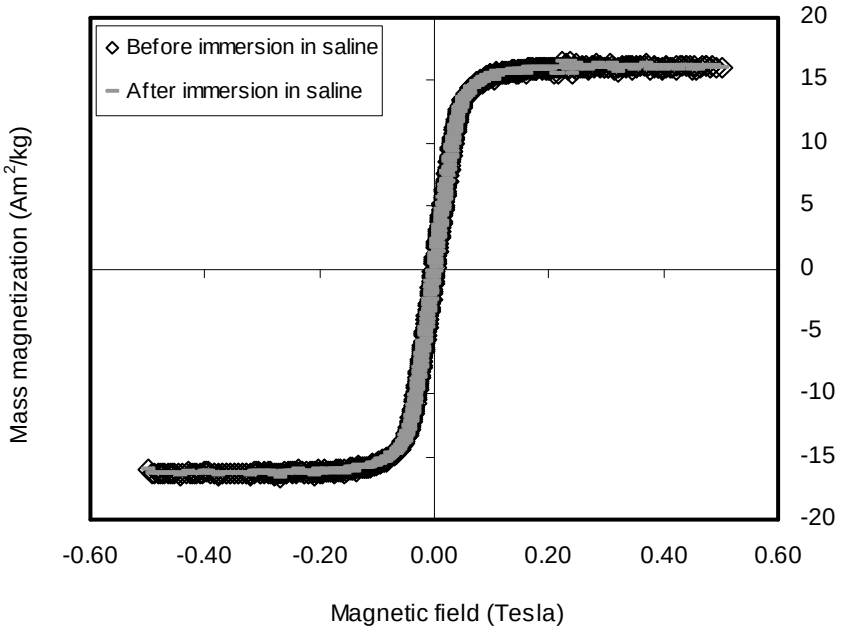

Figure B.4. Comparison of magnetic hysteresis curve before and after immersion in saline for 6 days.

APPENDIX C

Detailed Drawings and Designs of Experimental Setups

Detailed drawings and designs for the experimental setups are included in this appendix. Figure C.1, C.2, C.3, and C.4 show drawings for the liquid enclosure for testing long-term mechanical performance of uncoated silicon, and Ti coated silicon microcantilevers in liquid environments. Figure C.5 shows an optical image of the liquid enclosure with its components. Figure C.6 shows the steps to mount the microcantilevers (uncoated and Ti coated) specimens in the liquid enclosure. Figure C.7 shows the steps involved in preparing the liquid enclosure for testing in liquid environments.

Detailed drawing for the Plexiglas enclosure for tensile fatigue testing of MEMS in liquids (chapter 6) is shown in Figure C.8. Figures C.9 and C.10 show optical images of the specimen mount for the tensile fatigue test and steps involved in mounting the MEMS tensile specimen respectively. Selected dimensions of the tensile specimen are summarized in Figures C.11 and C.12.

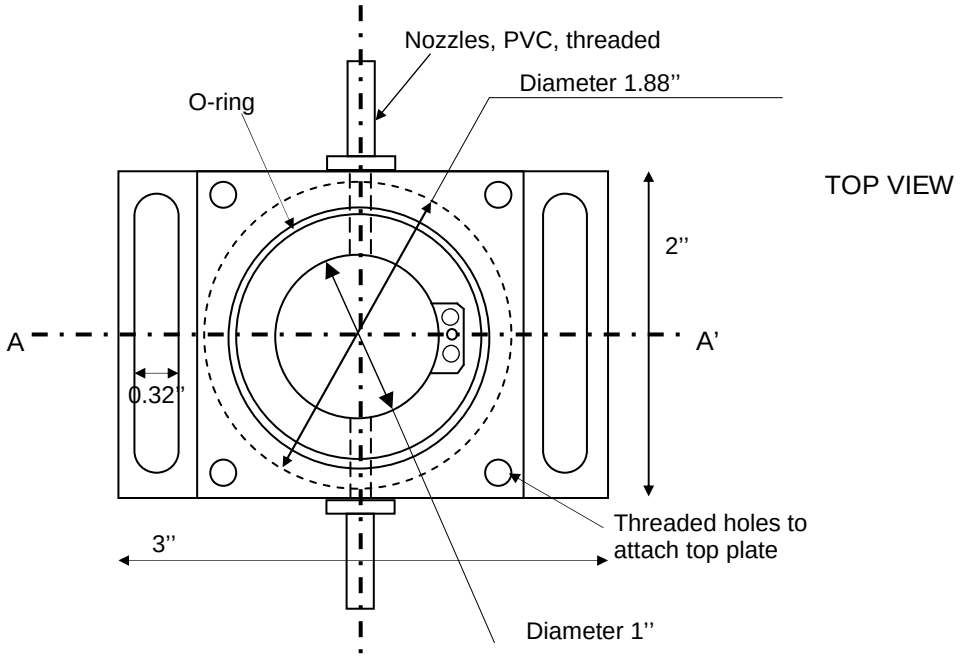

Figure C.1. Top view of the liquid enclosure for testing microcantilevers

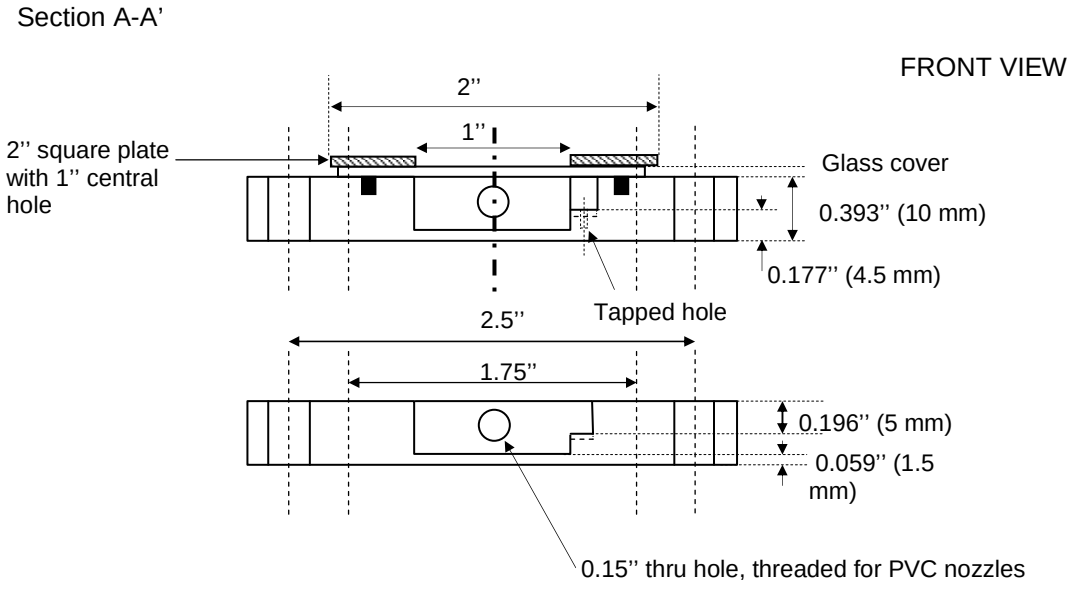

Figure C.2. Front view of the liquid enclosure for testing microcantilevers

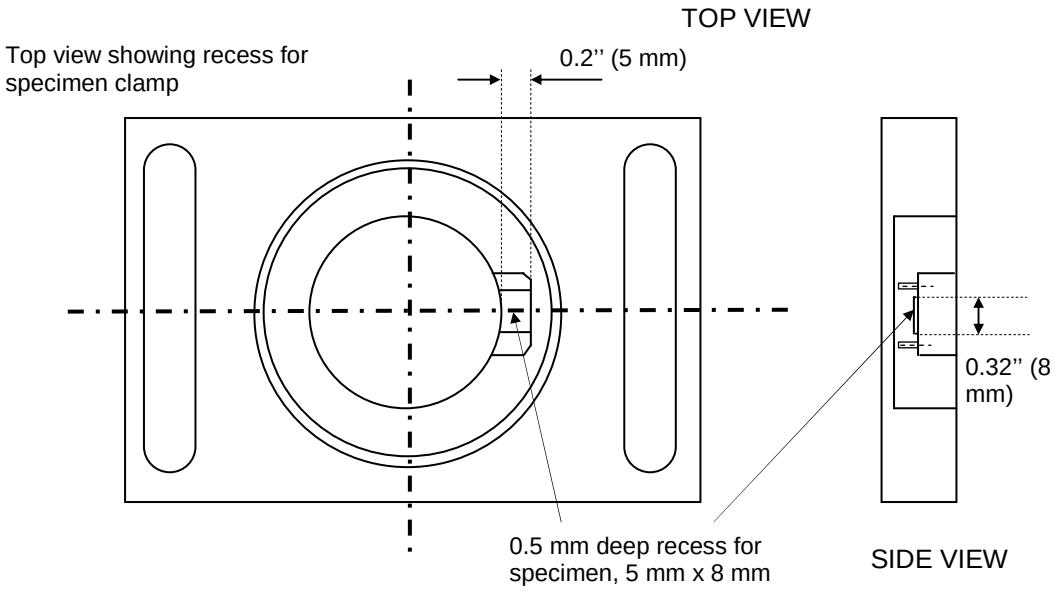

Figure C.3. Additional detail drawing for the liquid enclosure

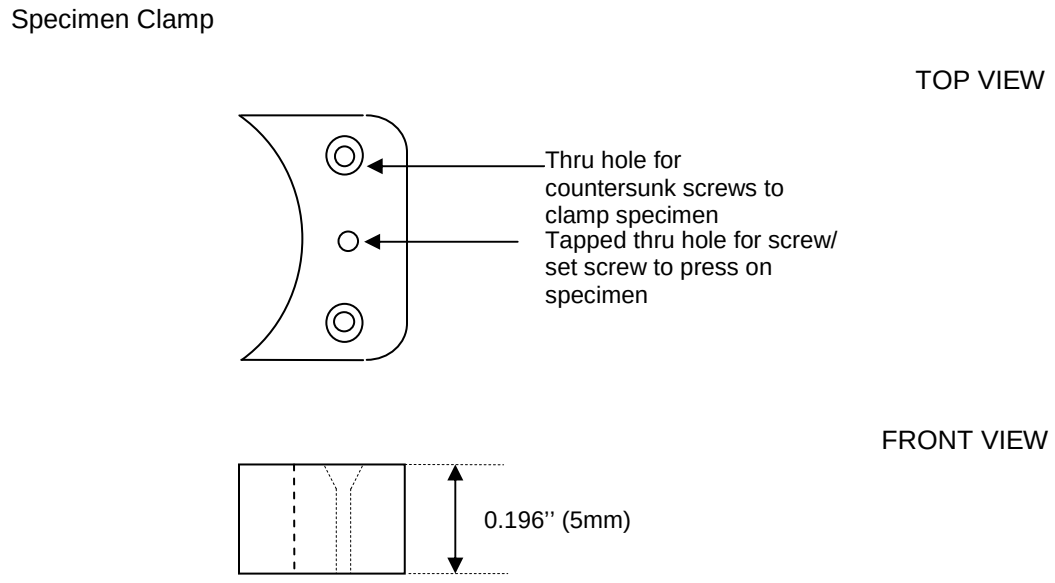

Figure C.4. Top and front view of the specimen clamp for the liquid enclosure

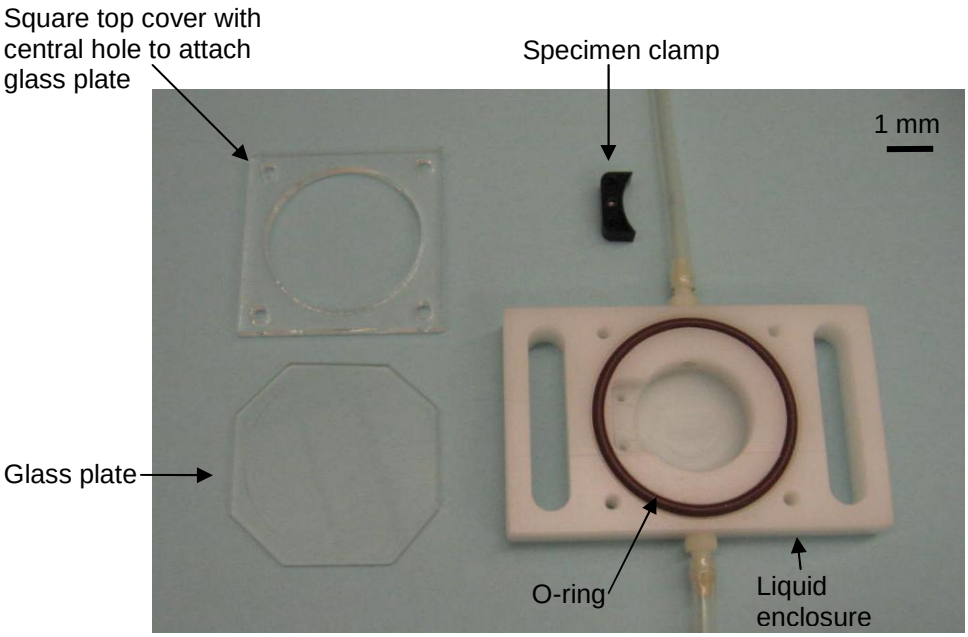

Figure C.5. Optical image of liquid enclosure and its components

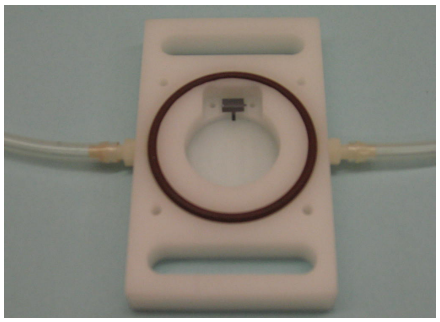

1. Position and align specimen in liquid enclosure

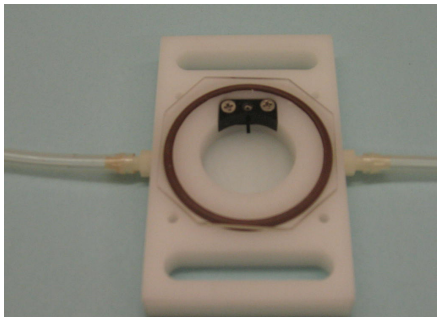

2. Position and attach specimen clamp; position glass cover

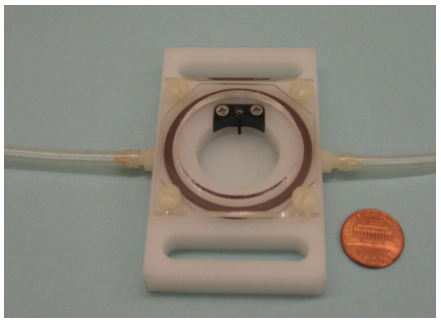

3. Attach acrylic top cover

Figure C.6. Steps showing mounting procedure for uncoated and Ti coated silicon microcantilevers in liquid enclosure

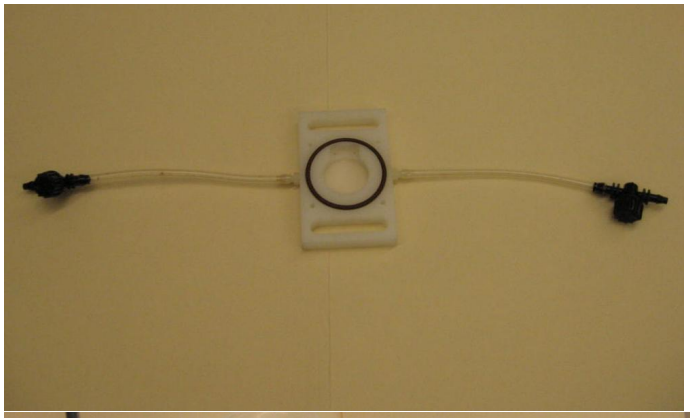

1. Liquid enclosure with attached tubing and nozzles

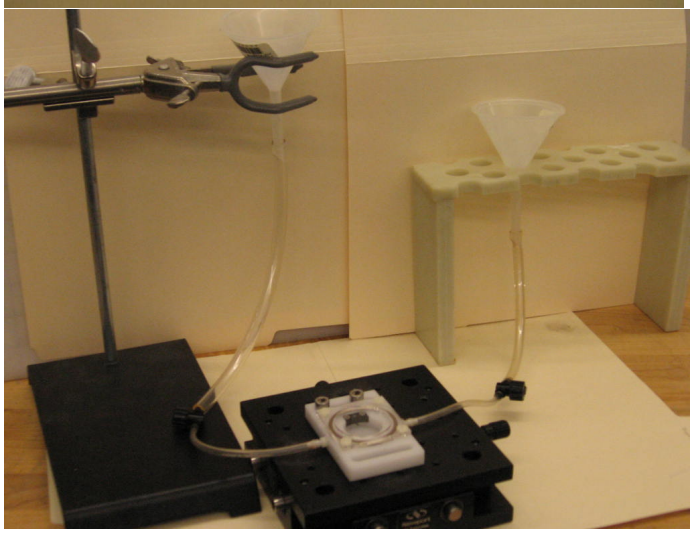

2. Mount specimen; liquid enclosure was attached to funnels with tubes for pressure head of liquid column to keep out bubbles

3. Funnels were covered with wax-paper to prevent evaporation

Figure C.7. Preparation of liquid enclosure for testing microcantilevers in liquid environments

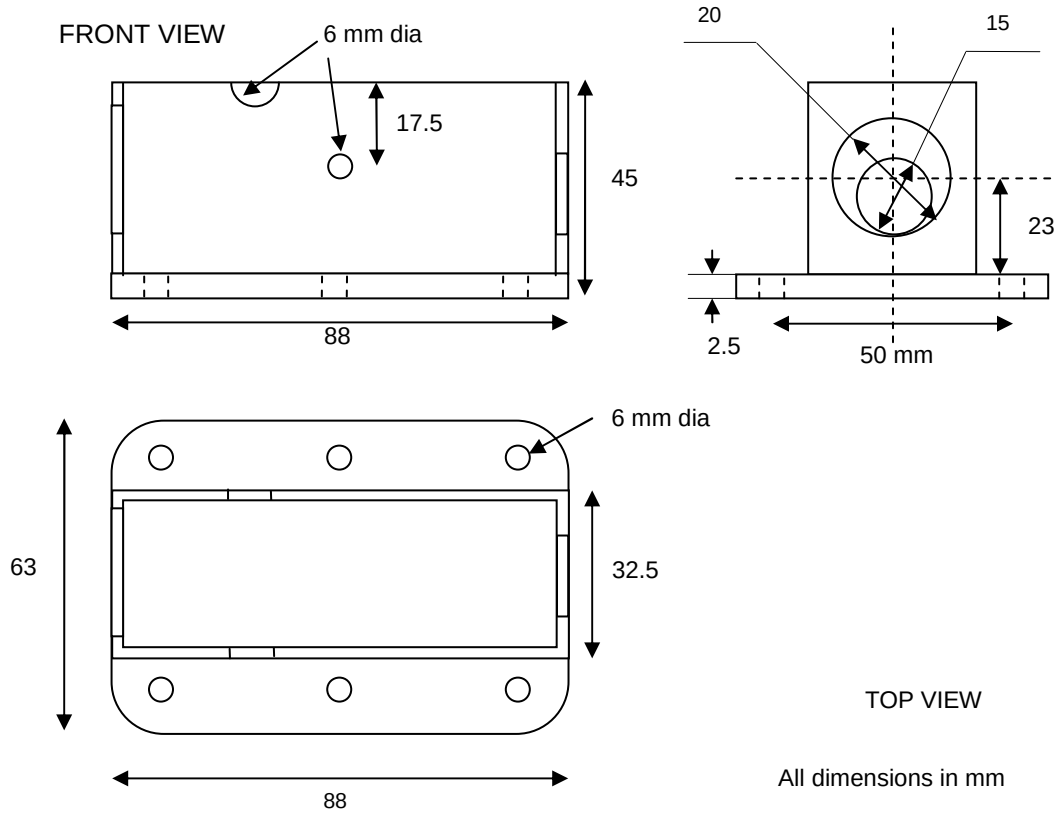

Figure C.8. Detailed sketch of Plexiglas enclosure for tensile fatigue testing of MEMS in liquids

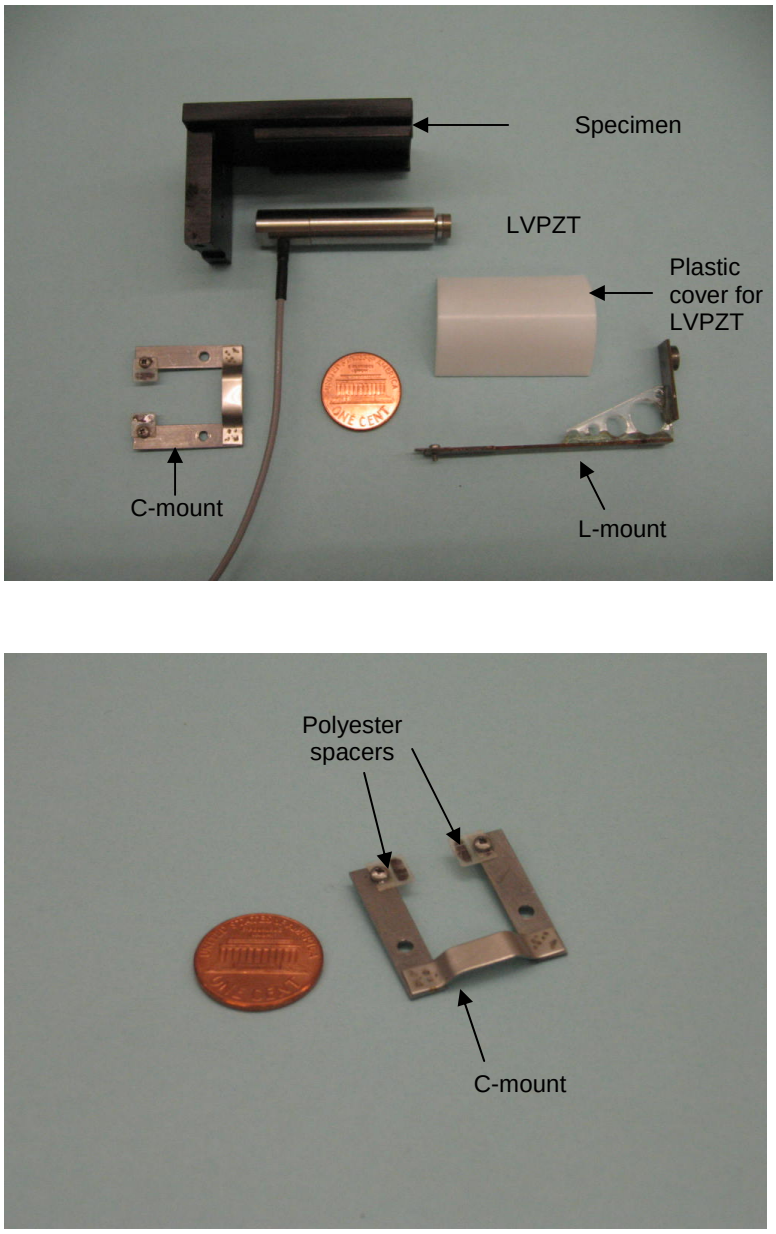

Figure C.9. Optical image showing components of the specimen mount used for fatigue testing of MEMS tensile specimens in liquids

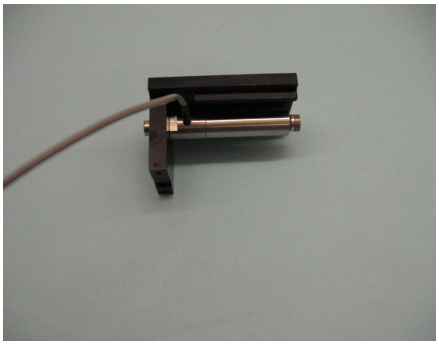

1. LVPZT is attached to specimen mount

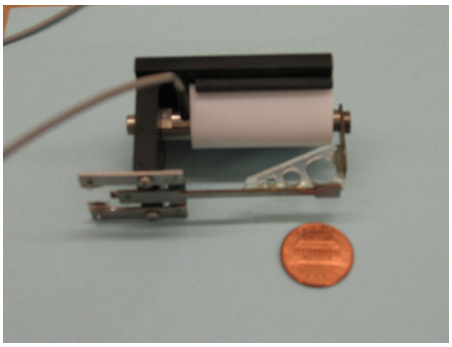

4. L-clamp is attached to specimen mount

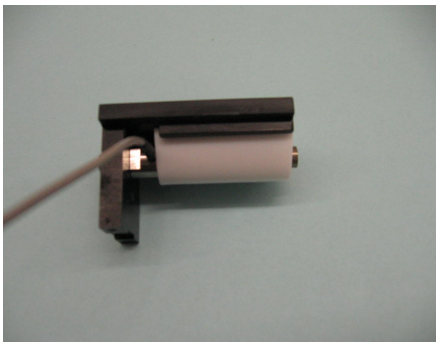

2. Plastic cover for LVPZT is attached (to prevent liquid contact)

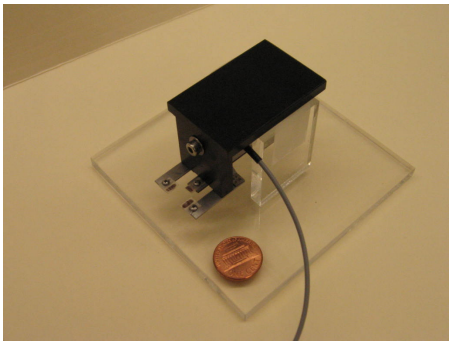

5. Specimen mount is suspended on PVC bracket and tensile specimen is aligned and attached with superglue

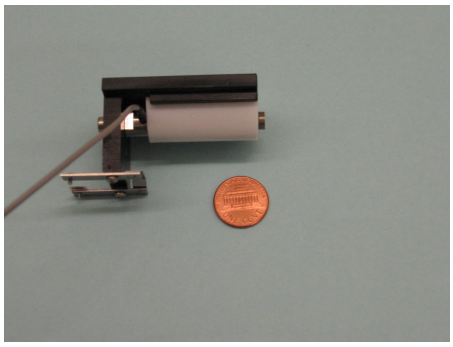

3. C-clamp is attached to specimen mount

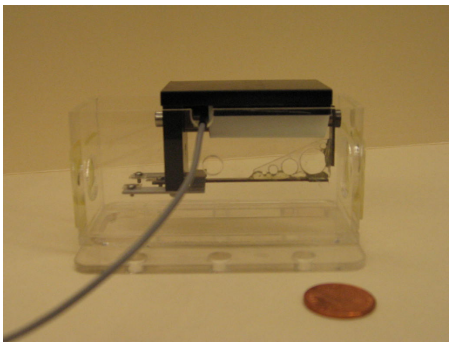

6. Specimen mount is transferred to Plexiglas enclosure

Figure C.10. Assembly sequence for specimen mounting for MEMS tensile specimens

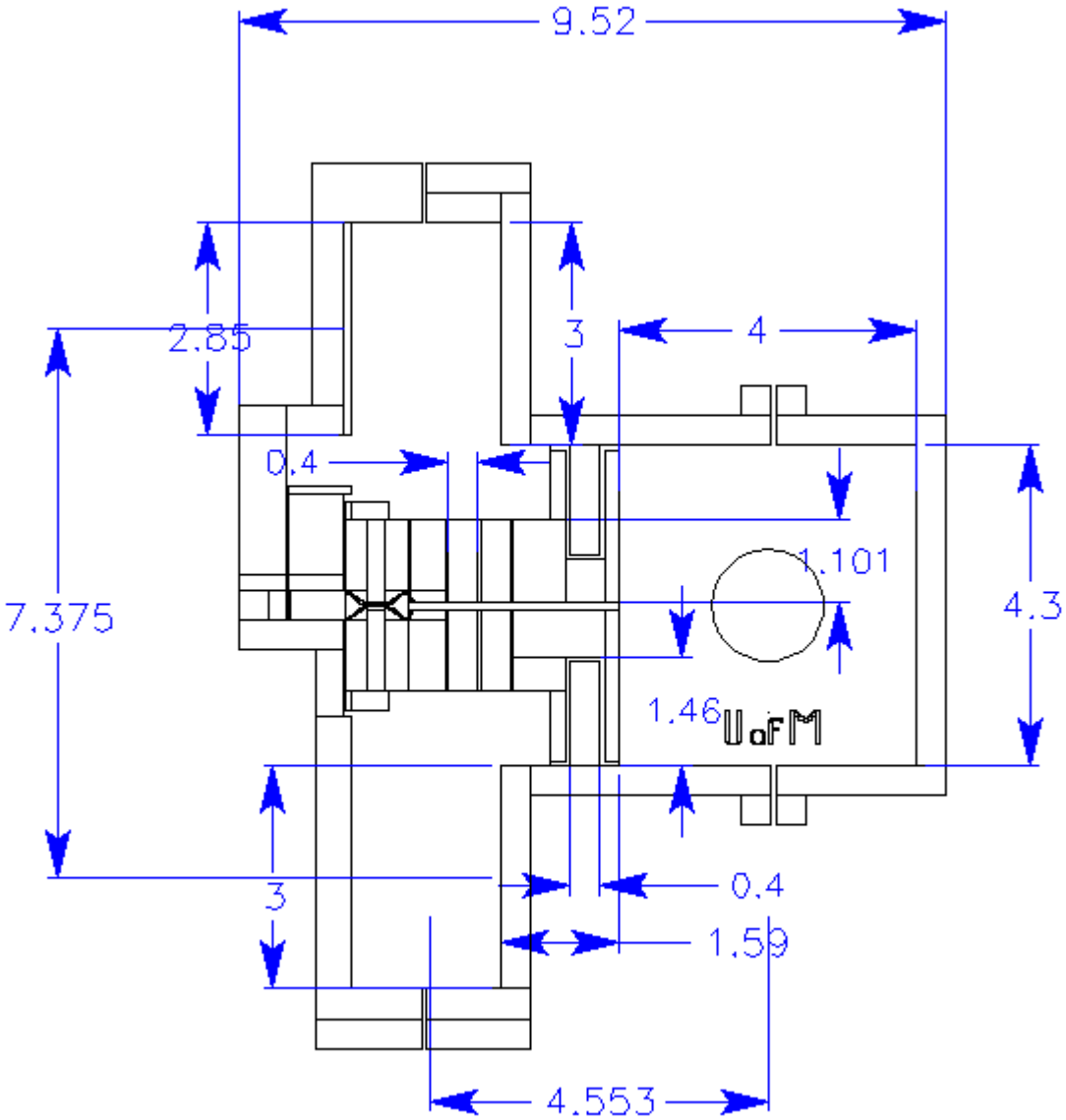

All dimensions are in mm

Figure C.11. Selected dimensions of the MEMS tensile specimen

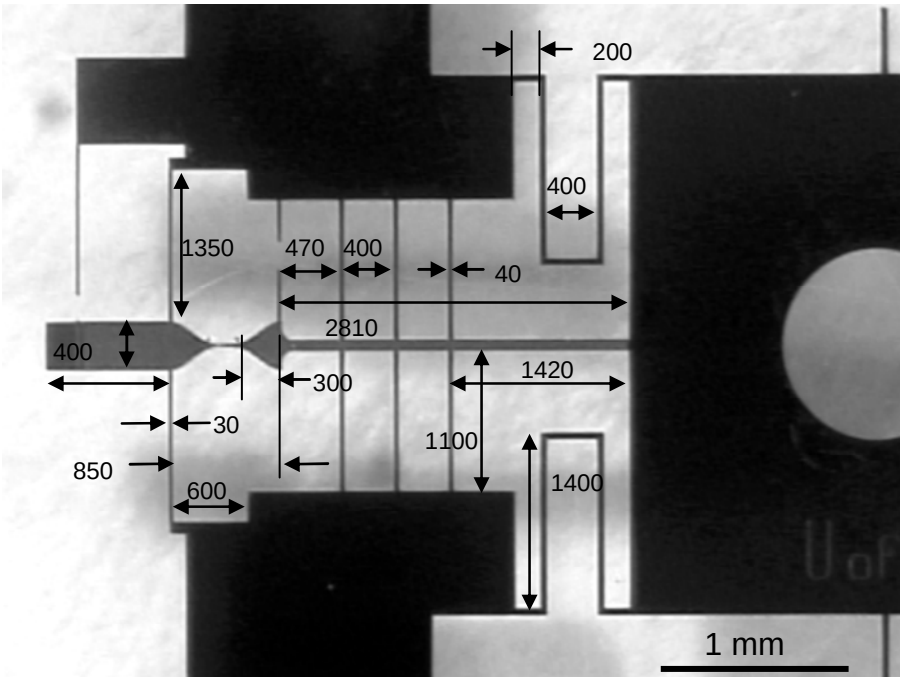

Figure C.12. Dimensions of selected microstructures of the MEMS tensile specimen (in micrometers)

Table C.1. Dimensions of spring components C (see Fig. 6.1)

Dimension	Symbol	Value
Length of silicon springs C	L_1	1100 μm
Width of the silicon springs C	w_1	120 μm
Thickness of silicon springs C	t_1	30 μm
Spacing between silicon springs C	-	400 μm

Table C.2. Thicknesses of microstructures* (see Fig. 6.1)

Microstructure	Thickness (μm)
Specimen grips A, B (silicon)	310-320
Springs C, D, and E (silicon)	120
Shuttle F (silicon)	310-320
Specimen G (aluminum)	0.2

* Dimension perpendicular the plane of the paper

APPENDIX D

LabVIEW Schematics

In this appendix, screenshots of the LabVIEW VIs (Virtual Instruments) used in the present study are included.

D.1. LabVIEW VIs for testing of uncoated and titanium coated microcantilevers in liquids

Screen image of the complete VI

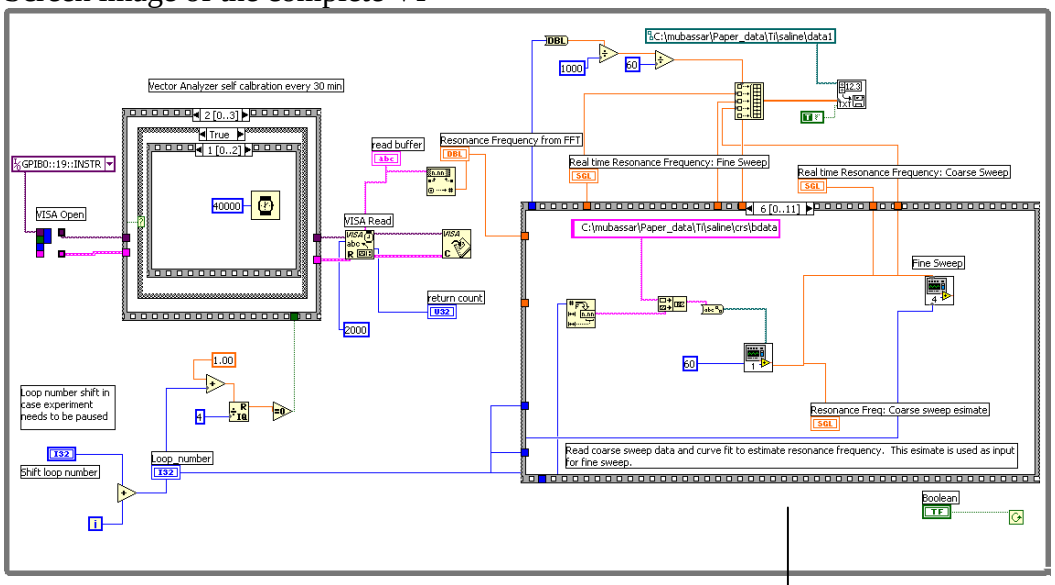

Individual frames in the sequence

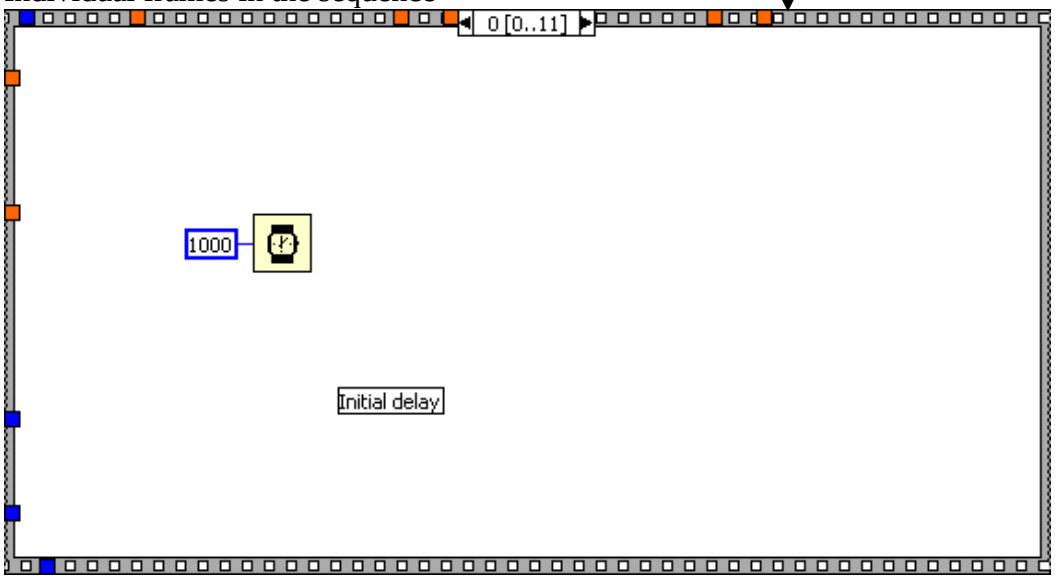

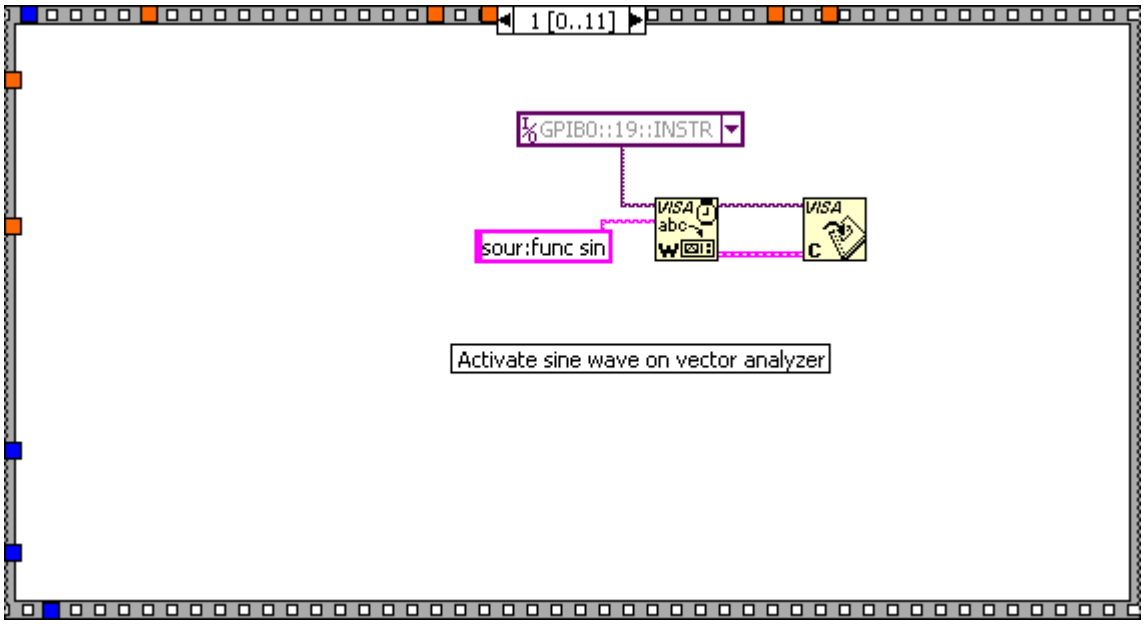
1 [0..11]
GPIB0::19::INSTR
VISA
abc
VISA
sour:func sin
Activate sine wave on vector analyzer

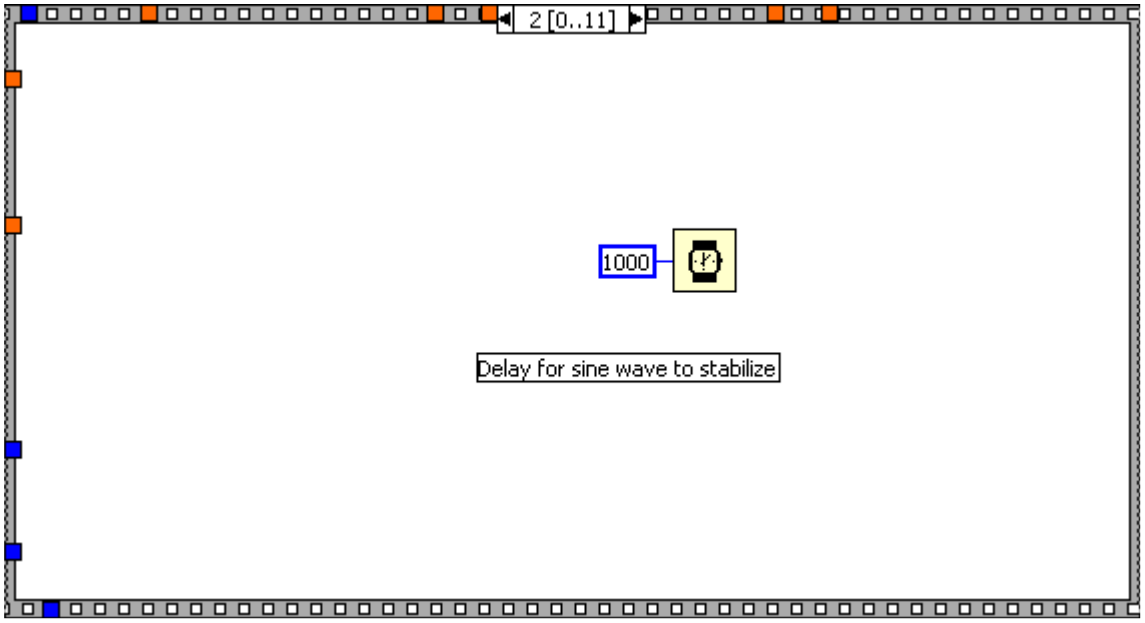
2 [0..11]
1000
Delay for sine wave to stabilize

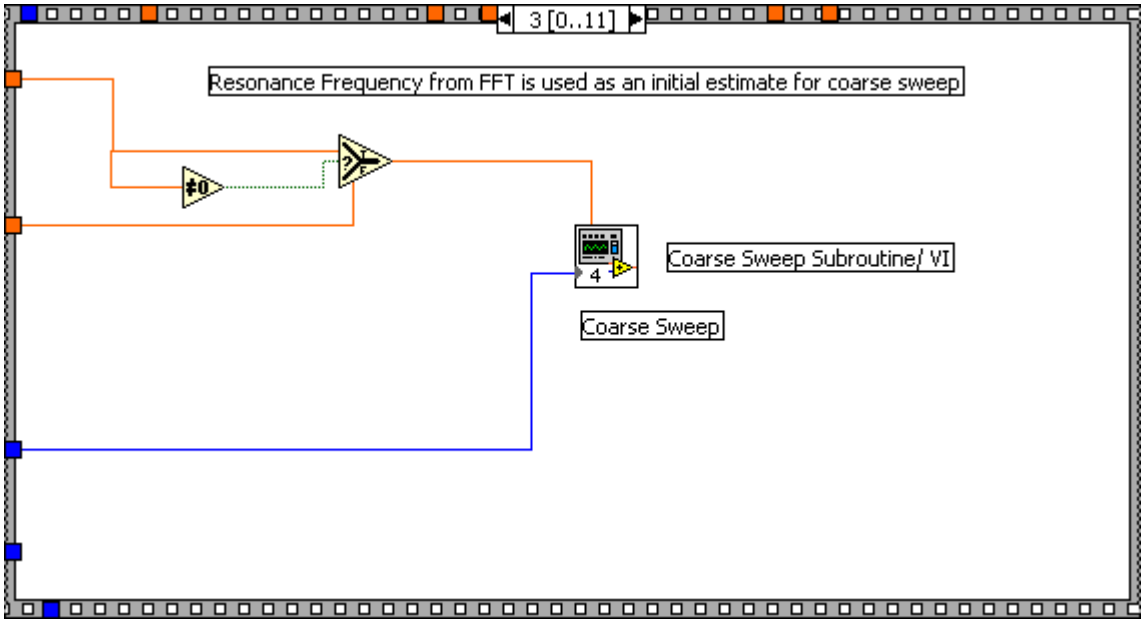
3 [0..11]
Resonance Frequency from FFT is used as an initial estimate for coarse sweep
≠0
4
Coarse Sweep Subroutine/ VI
Coarse Sweep

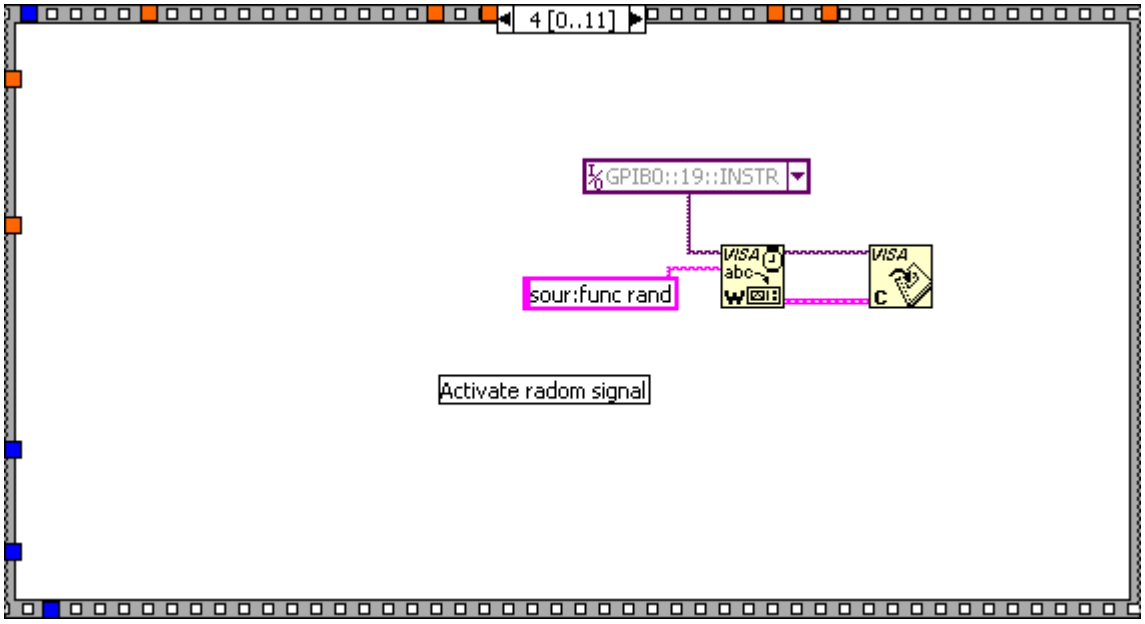
4 [0..11]
GPIB0::19::INSTR
VISA
abc
VISA
sour:func rand
Activate radom signal

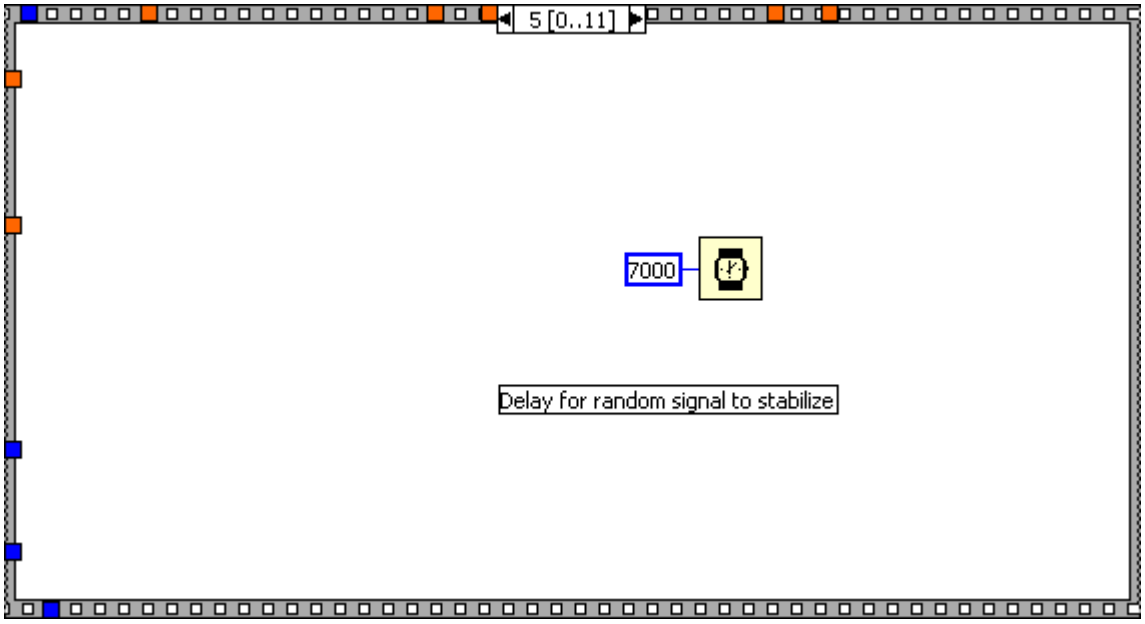
5 [0..11]
7000
Delay for random signal to stabilize

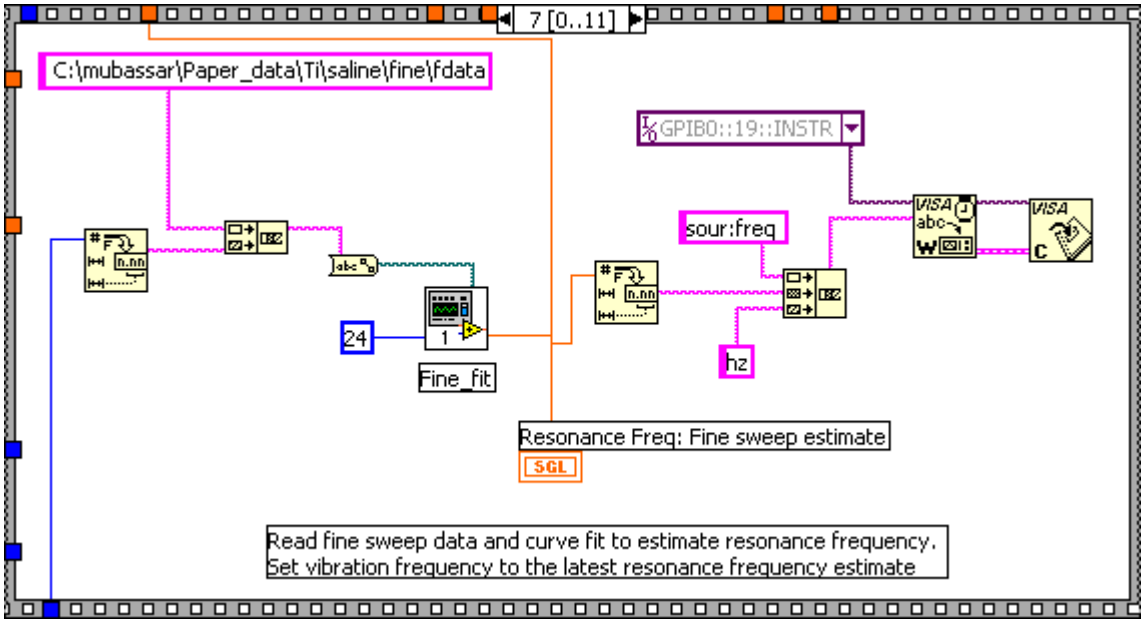
7 [0..11]
C:\mubassar\Paper_data\Ti\saline\fine\fdata
GPIB0::19::INSTR
sour:freq
VISA
VISA
24
1
Fine_fit
hz
Resonance Freq: Fine sweep estimate
SGL
Read fine sweep data and curve fit to estimate resonance frequency.
Set vibration frequency to the latest resonance frequency estimate

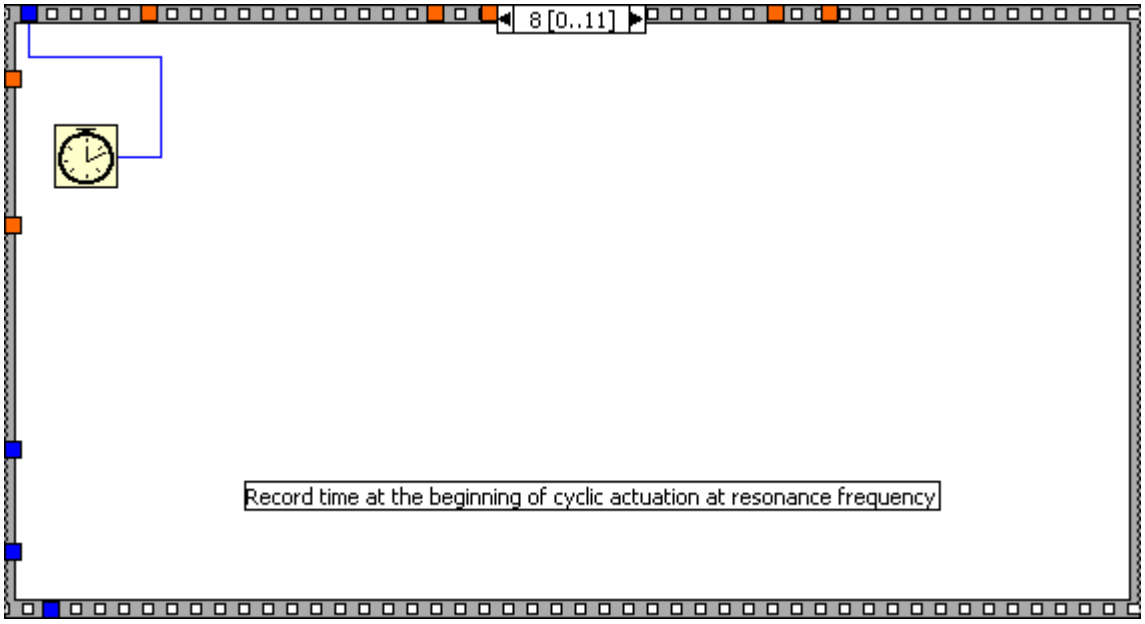
8 [0..11]
Record time at the beginning of cyclic actuation at resonance frequency

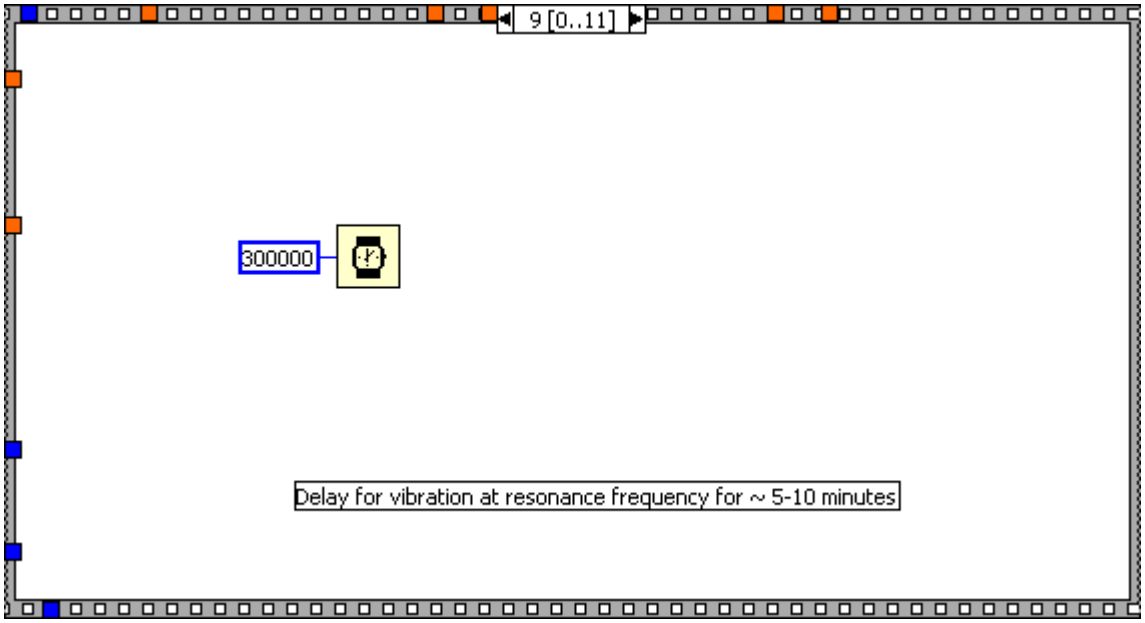
9 [0..11]
300000
Delay for vibration at resonance frequency for ~ 5-10 minutes

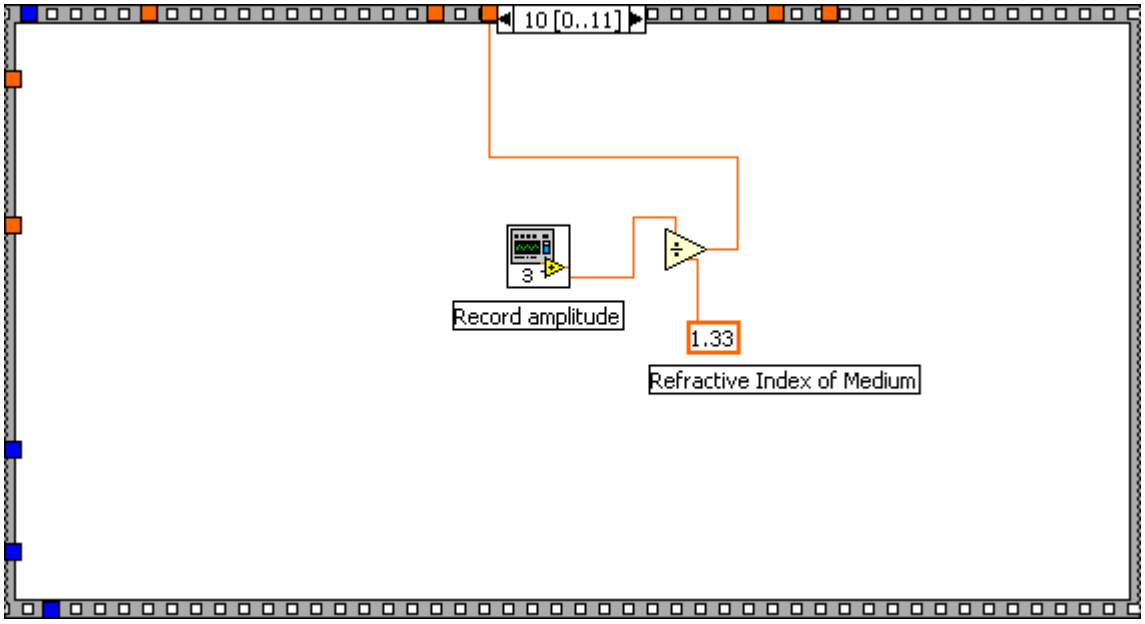
10 [0..11]
3
Record amplitude
1.33
Refractive Index of Medium

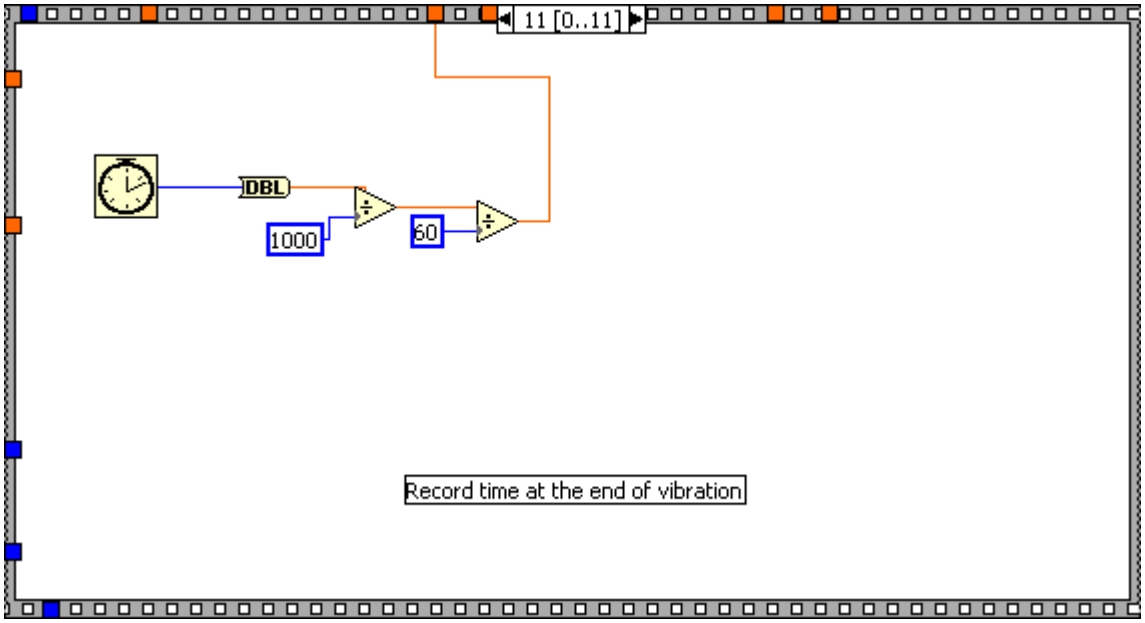
11 [0..11]
DBL
1000
60
Record time at the end of vibration

Individual frames for calibration of the vector analyzer

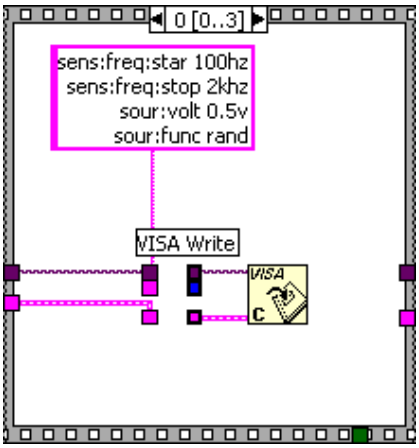

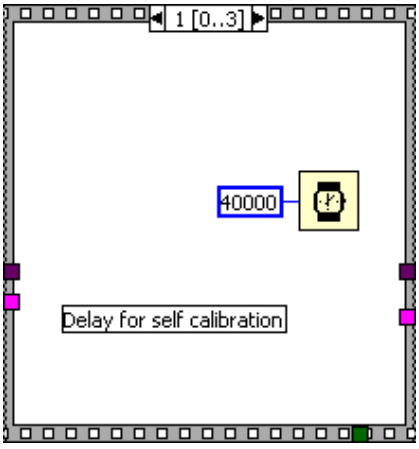

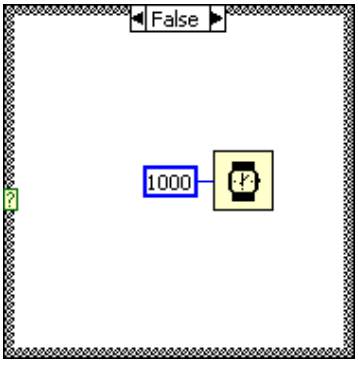

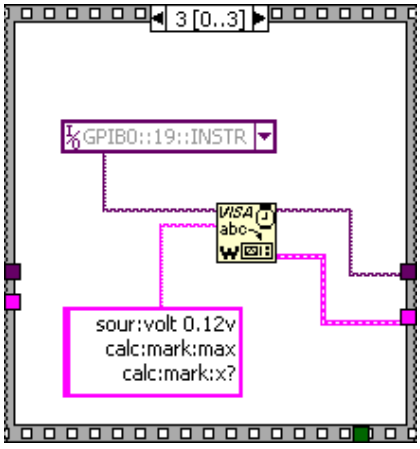

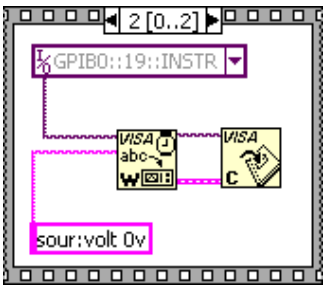

Instrument panel

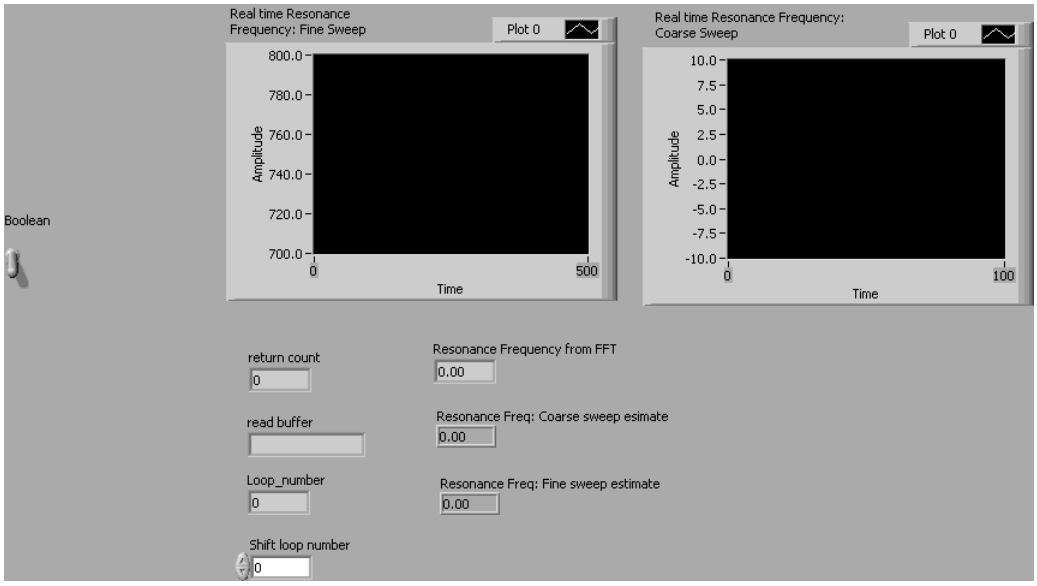

D.2. Coarse/ Fine sweep VI

Screen image of the complete VI

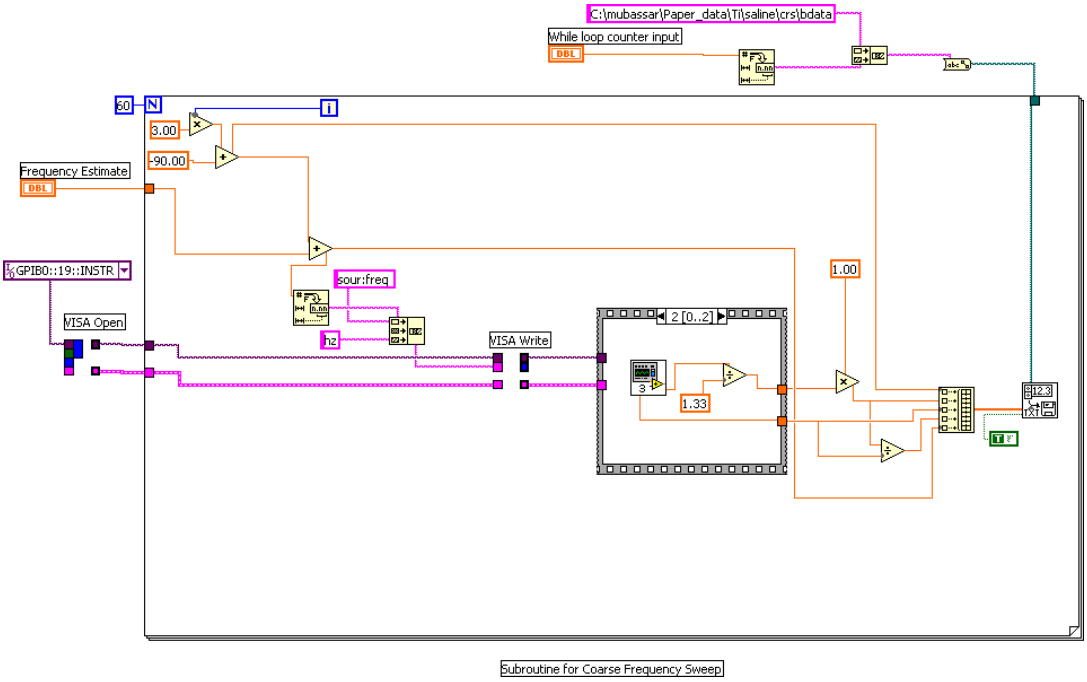

Screen image of sequence structure for measurement of frequency and amplitude

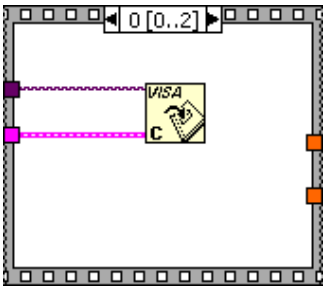

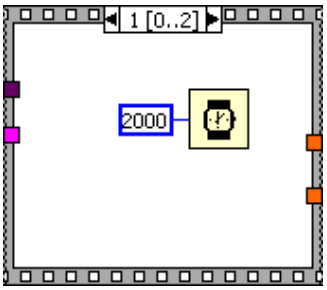

D.3. Amplitude and frequency measurement VI subroutine

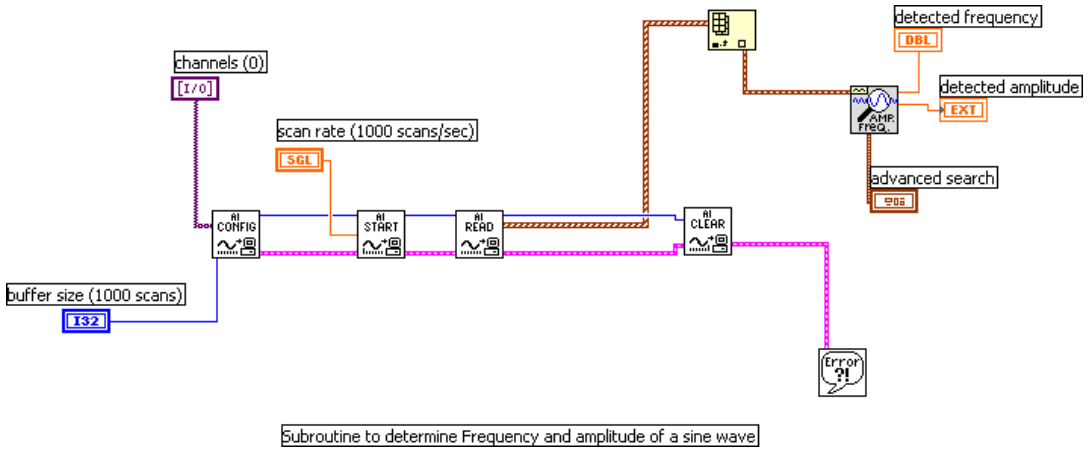

D.4. Tensile test VI for data acquisition

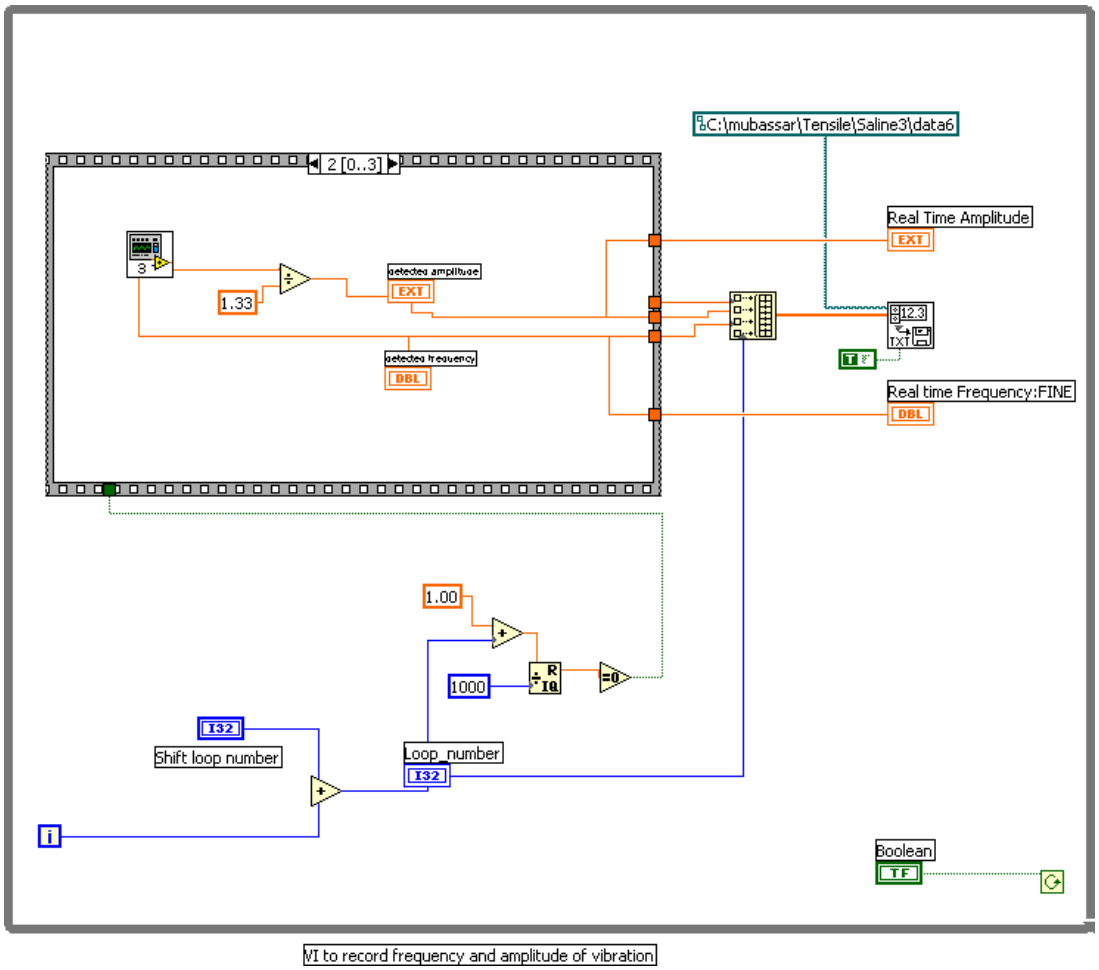

Individual frames from sequence structure for measuring frequency and amplitude

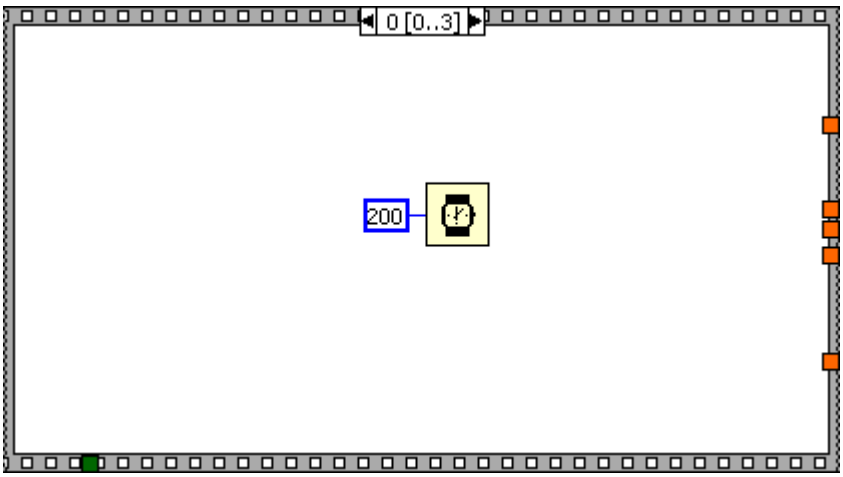

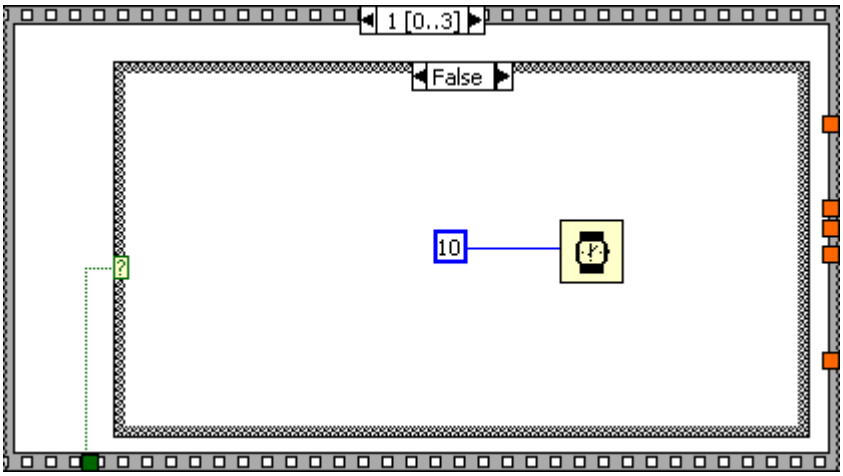

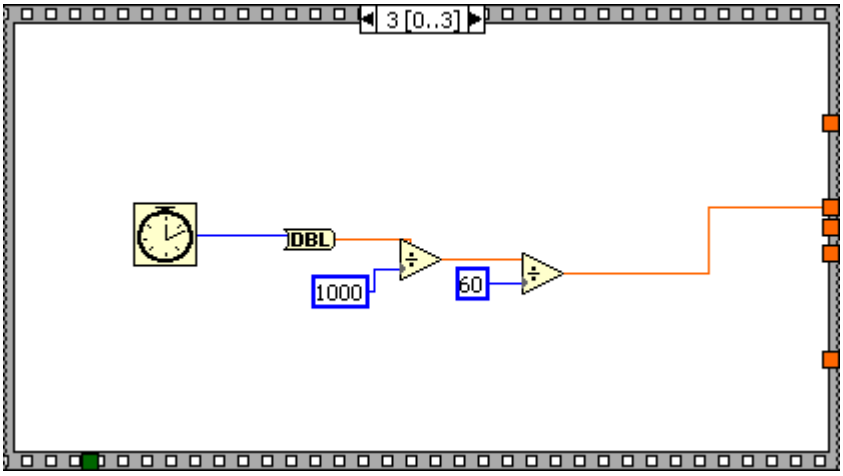

Individual frames from sequence structure to calibrate vector analyzer

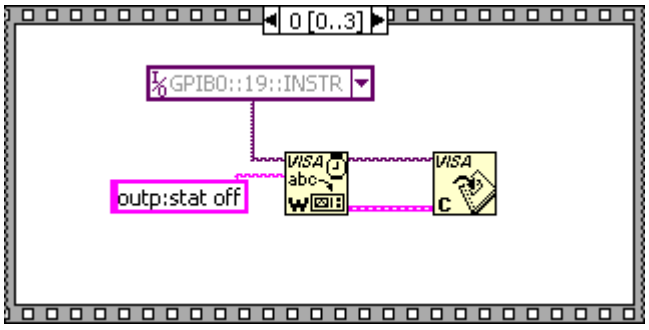

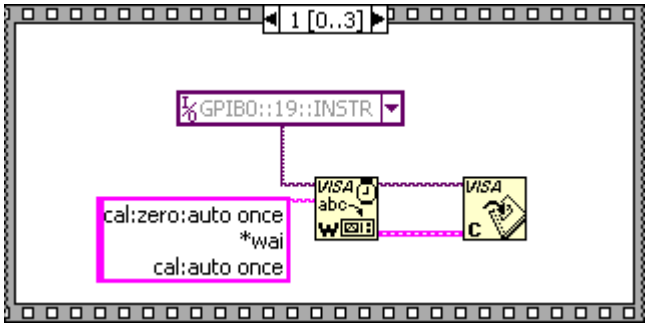

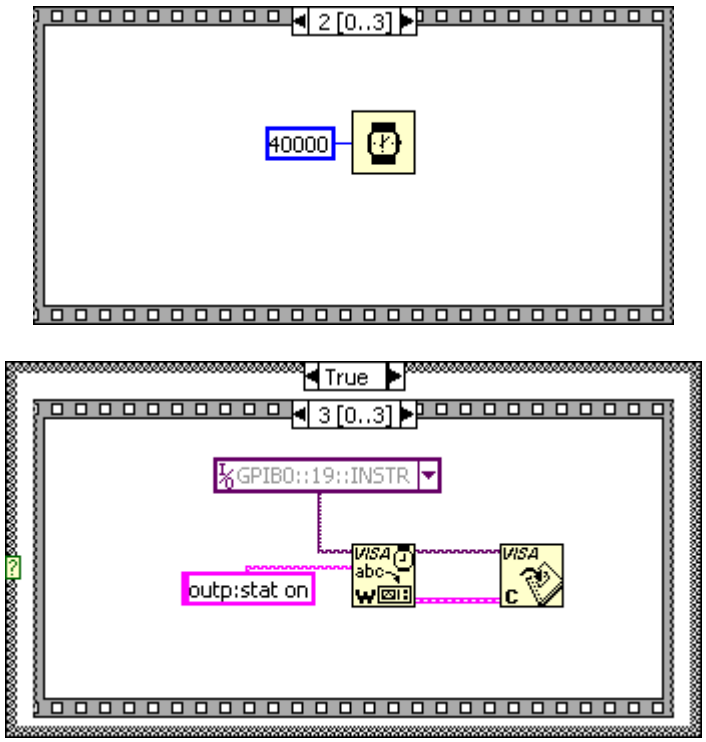

Instrument panel

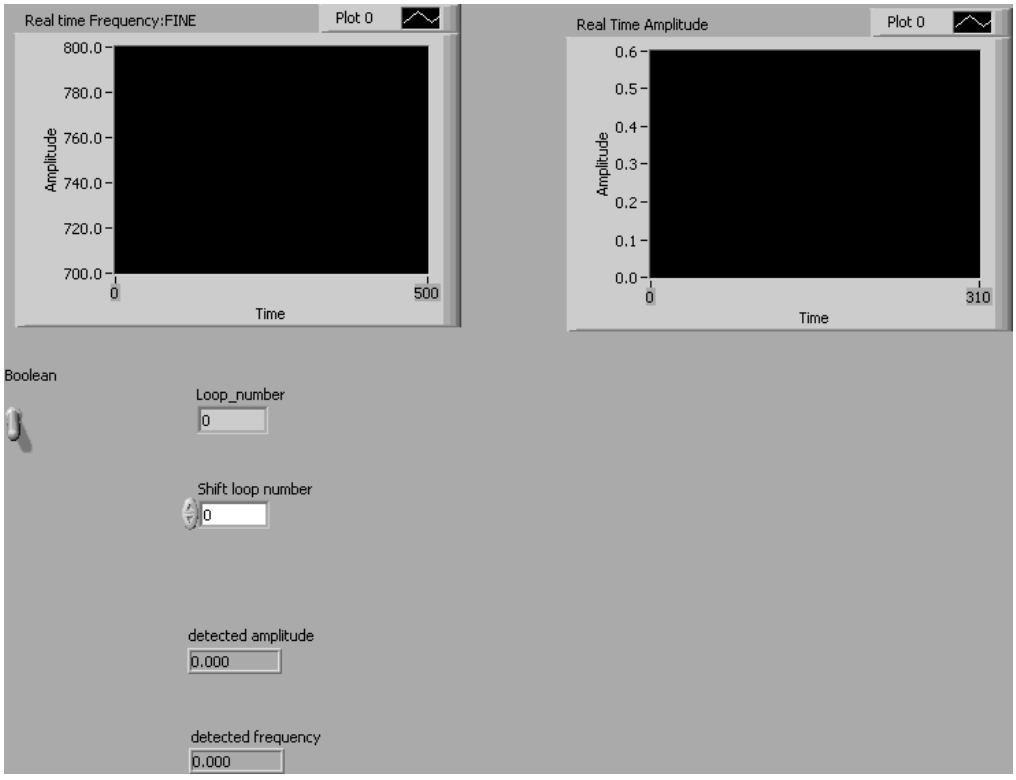

APPENDIX E

Method for Matching Stresses for Microcantilevers

This appendix describes an approximate method for matching stresses for the microcantilever specimens tested in this study in air and liquids. The bending moment for a cantilever is related to its deflection profile according to the following relationship:

$$M = EI\left(\frac{\partial^2 \delta}{\partial x^2}\right) \tag{E.1}$$

where E is the modulus of elasticity, and δ is the deflection perpendicular to the length of the cantilever [76]. Bending stresses in a cantilever result from bending moments which are calculated using [72]

$$\sigma = \frac{M_{net} y}{I} \tag{E.2}$$

where σ is the bending stress, M_{net} is net bending moment acting on the beam, y is the distance of the maximum stress from the neutral axis (assumed to be one-half the thickness), and I is the moment of inertia. Due to the nature of the microfabrication processes, y and I are different for each microcantilever. Further, the value of M_{net} will vary with the environment primarily due added mass and viscous effects in liquids. The method for matching stresses for experiments performed on microcantilevers samples has two objectives:

(i) To ensure that microcantilevers with different thickness are subjected to the same stress level; and

(ii) To ensure that microcantilevers are subjected to the similar stress level in air and liquids.

For uncoated silicon microcantilevers tested in air, the applied bending moment acting (M_{net}) on the cantilever is primarily due to the magnetic field of the electromagnet. Contributions from damping due to the silicon material and air, and inertia of the cantilever motion are neglected. The oscillating magnetic field of the electromagnet generates a time-varying bending moment, which causes vibration of the microcantilever. The location of maximum stress occurs at the root of the microcantilever. Assuming the deflection of the microcantilever is due to a point load *P*, acting at the center of the Permalloy strip, the maximum stress (σ_{max}) during a cycle results at maximum tip deflection, δ_{max} from its horizontal position. The maximum tip deflection is related to the point load, *P* by [72]

$$\delta_{\max} = \frac{Pa^2(3l-a)}{6EI} = \frac{28Pl^2}{162EI} \tag{E.3}$$

where l is the length of the microcantilever, a is the distance of the center of the permalloy strip from the root of the microcantilever ($a = 2l/3$), and E is the elastic modulus of silicon. Using (E.2) and (E.3) the maximum stress is given by

$$\sigma_{\max} = \frac{Pay}{I} = \frac{162EI\delta_{\max}}{28l^2} \cdot \frac{2ly}{3I} = \frac{27E\delta_{\max} y}{7l^2} \ . \tag{E.4}$$

Calculation of stress levels is illustrated using an example. For a 35 μm thick silicon microcantilever E = 160 GPa, δ_{max} = 2 μm, y = 17 μm, and l = 3 mm, using Eq.(E.4) we find, σ_{max} = 2.4 MPa. The maximum tip displacement, δ_{max} can be manually controlled by varying the input voltage to the electromagnet to achieve matching stress levels.

Stress levels are calculated in liquids using Eq.(E.4), and matched by manually varying the input voltage of the electromagnet to obtain the desired value of δ_{max}. In liquids, $M_{net} = M_{mag} + M_m + M_v$, where M_{mag} is the applied magnetic moment, M_m is the moment due to acceleration of the cantilever and added liquid masses, and M_v is the moment due to viscous damping effects in the fluid. Instead of calculating the individual effects of each bending moment, the microcantilever is viewed as a spring structure subjected to magnetic, inertial, viscous, and restoring forces and moments. The resultant deflection of the cantilever was assumed to be a result of the net bending moment M_{net}. The bending stress can then be calculated from the tip displacement of the cantilever measured using the laser vibrometer. A practical observation was that for achieving equal tip displacements, a larger input voltage to the electromagnet was required in liquids compared to air to overcome the effects of viscous damping and added masses in liquid environments. For example, an input voltage of 15-18 V was sufficient to achieve δ_{max}= 2 μm in air, while an input voltage higher than 40 V was often required to achieve similar displacement in liquids. The maximum tip displacement, δ_{max} is determined experimentally, and maximum stress σ_{max} is calculated using Eq.(E.3). For a particular microcantilever tested in both air and liquid environments, this approximate method will lead to testing at equal values of δ_{max}. The only difference is that the input voltage to the electromagnet required in liquids will be significantly higher than that in air for obtaining similar values of δ_{max}.

Stress levels were matched for individual tests performed on the magnetic actuation setup. For tests performed on the experimental setup with piezoelectric actuation, stress

levels could not be matched for individual experiments. While the laser vibrometer was capable of measuring absolute displacements, the laser diode-PSD sensing scheme was not designed to measure displacements. However, the driving voltages required for the piezoelectric actuator to achieve stress levels comparable to the magnetic actuation setup were determined by measuring displacements for selected microcantilever samples with the laser vibrometer.

APPENDIX F

Resonant Frequency and Crack Growth Rate Calculations for Ti Coated Microcantilevers

In this appendix, the methods for calculating the resonant frequency of the Ti coated microcantilevers and the crack growth in the Ti coating are discussed. First, we focus on resonant frequency calculations. The minimum possible resonant frequency due to cracking of the Ti coating occurs when the Ti coating is cracked through its thickness and is indicated by dotted lines in Figure 5.10. Using the theory of composite beams, the cross section of the cantilever can be simplified as in Figure F.1 below. The Ti coating on both top and bottom surfaces of the microcantilever are replaced with silicon (Figure F.1b), with a reduced width corresponding to the modular ratio i.e E_{Ti}/ E_{Si} = 100/160= 0.625.

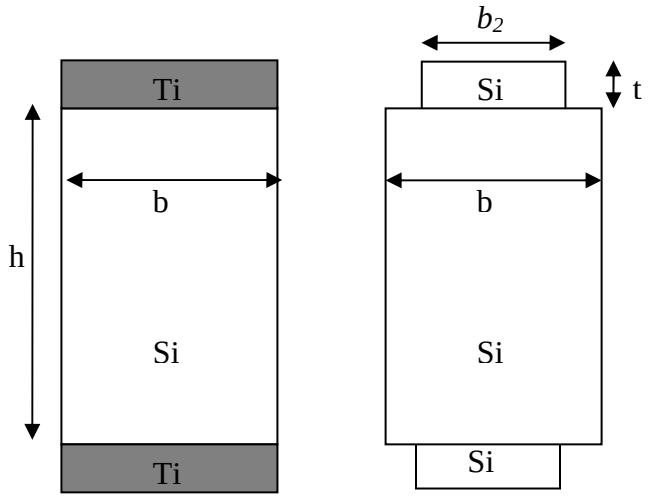

Figure F.1. Illustration showing cross-section of the Ti coated microcantilevers

Resonant frequency of a microcantilever in a vacuum is given by

$$f_n = \frac{\alpha_n^{\,2}}{2\pi}\sqrt{\frac{3EI}{ml^3}} \tag{F.1}$$

Consider two microcantilevers one with Ti coating, and the other without any Ti coating. The ratio of resonant frequencies of these coated and uncoated microcantilevers neglecting the small mass of Ti coating (so that mass *m* is same for both cantilevers) can be expressed as

$$\frac{f_{ctd}}{f_{unc}} = \sqrt{\frac{E_{ctd}I_{ctd}}{E_{unc}I_{unc}}} \tag{F.2}$$

where *f*, *E*, and *I* are resonant frequency, elastic modulus, and moment of inertia of the microcantilevers. The subscripts 'ctd' and 'unc' refer to the Ti coated and uncoated microcantilevers respectively. Since the Ti coating was replaced with equivalent silicon as in Figure F.1, $E_{unc}=E_{ctd}$. Further simplification of Eq.(F.2) leads to

$$\frac{f_{ctd}}{f_{unc}} = \sqrt{\frac{I_{ctd}}{I_{unc}}} \tag{F.3}$$

For the equivalent cross-section shown in Figure F.1b

$$I_{ctd} = \frac{bh^3}{12} + 2\left(\frac{b_2 t^3}{12}\right) + 2\left(\frac{(b_2 t)(h+t)^2}{4}\right) \tag{F.4}$$

where *b* is the width of the microcantilever in m, *t* is the thickness of the Ti coating in meters (10^{-7} m or 0.1 μm), and *h* is the thickness of the silicon structural layer in meters. The moment of inertia for the uncoated microcantilever is given by

$$I_{unc} = \frac{bh^3}{12} \tag{F.5}$$

Using Eqs. (F.3), (F.4), and (F.5), the ratio of the resonant frequencies in vacuum can be obtained. From Eq.(4.2), for equal thickness and widths, the ratio of resonant frequencies in vacuum is equal to the ratio of resonant frequencies of the microcantilevers in air. Hence, the ratio of resonant frequencies in air can be determined using Eq.(F.3)

$$\frac{f_{ctd,air}}{f_{unc,air}} = \sqrt{\frac{I_{ctd}}{I_{unc}}}, \tag{F.6}$$

where $f_{ctd,air}$ and $f_{unc,air}$ are the resonant frequencies in air for the coated and uncoated microcantilevers respectively. The resonant frequency in air for the coated microcantilevers, $f_{ctd,air}$ was determined experimentally. The resonant frequency in air without any coating was calculated using Eqs. (F.4), (F.5), and (F.6). The difference in resonant frequencies in air was calculated using

$$\Delta f_{air} = f_{ctd,air} - f_{unc,air}. \tag{F.7}$$

During the long-term tests a decrease in resonant frequencies of the Ti coated specimens is experimentally observed in saline solution. For comparison of experimentally observed and calculated values of resonant frequency, the decrease in saline solution corresponding to the decrease in resonant frequency in air (Δf_{air}) is determined. We assume that that the ratio of the decrease in resonant frequency in saline, Δf_{saline} to that in air, Δf_{air}, is equal to the ratio of the experimentally observed resonant frequencies of the Ti coated microcantilever measured in saline to that in air i.e

$$\frac{\Delta f_{saline}}{\Delta f_{air}} = \frac{f_{ctd,saline}}{f_{ctd,air}}, \tag{F.8}$$

where $f_{ctd,saline}$ is the experimentally determined initial resonant frequency in saline. The difference in resonant frequencies in saline was then estimated using

$$\Delta f_{saline} = \Delta f_{air} \cdot \frac{f_{ctd,saline}}{f_{ctd,air}}. \quad \text{(F.9)}$$

Applying Eq.(F.9), if Δf_{air} =12 to 16 Hz, then Δf_{saline}= 6.7 to 9.8 Hz. Experimentally, resonant frequency decreases in saline were observed to be between 4 to 8 Hz, which is within the maximum limits calculated above (Δf_{saline}).

Next, we discuss the method used to calculate the crack growth in the Ti coating. Crack growth in the Ti coating leads to a decrease in the moment of inertia (I_{ctd}) since only the remaining un-cracked Ti coating contributes to the moment of inertia. The thickness of the remaining un-cracked Ti coating (t') was determined by trial and error so as to match the experimentally observed values of Δf_{saline}. The crack growth in the Ti coating, a expressed in meters is calculated using

$$a = t - t'. \quad \text{(F.10)}$$

The average crack growth rate in meters per second for an experiment performed over T seconds is given by a/T. The average crack growth rate per cycle, expressed in meters per cycle is given by a/N, where N is the total number of cycles experienced by the Ti coated microcantilever in saline during an experiment.

APPENDIX G

Design and Fabrication of a MEMS Test Specimen for Study of Heterogeneous Liquid Flows

In this appendix, we discuss the design and fabrication of a MEMS test structure developed to study the interaction with bubbly and liquid flows. Microstructures described in this study were tested in stationary liquid environments. Environmental interaction between the liquid and the microstructures, and to a smaller extent vibration-induced effects were the major factors affecting reliability and performance of these test structures. Complex conditions such as flowing liquids, two-phase flows, liquids with bubbles and particles are frequently encountered in several microfluidic and biological applications of MEMS. It is important to understand the effect of these complex flows on sensor performance and vice-versa. For instance, Sparks et al. [28] discuss that presence of gas bubbles and solid particles result in a resonant frequency shift and signal damping of resonating micro-tubes tested in two-phase fluids. Naik et al. [18] have observed an increase in effective viscosity of liquids with increasing number density of particles in liquid-solid suspensions. Bubbles often form in fluids due to dissolved gases or are deliberately introduced for driving microscale flows [77, 78]. While bubbles seldom pose a serious problem in macroscale pipes, a single 50 μm bubble can clog a microchannel. Microstructures have been designed into microchannels to deflate bubbles that obstruct flows. Stegmeir et al. [79] have investigated the impact of bubbles with stationary microcantilever obstacles in a confined channel.

We discuss the design and fabrication of a MEMS test structure developed to study interaction of bubbly and particulate flows, and flowing liquids with vibrating microstructures. The proposed test structure is a micromachined silicon microcantilever with integrated magnetic actuation, and strain gage sensing. These microcantilever test structures are similar to the uncoated silicon microcantilevers described in Chapter 4, except for piezoresistive strain gages patterned near the root of the cantilever for vibration sensing. Piezoresistive strain gages are made of doped semiconductors such as polysilicon, and are characterized by higher sensitivity compared to metallic strain gages. The presence of bubbles and particles pose challenges for optical techniques such as laser vibrometry for sensing motion in liquids. The strain gages are encapsulated under an insulating layer of silicon oxide to prevent shorting failures in conductive liquid environments.

G. 1. Design of the test structure

(These test specimens were developed in collaboration with Matthew J. Stegmeir, Graduate Student, Aerospace Engineering & Mechanics, University of Minnesota. Several design features were chosen to meet requirements and specifications provided by Matthew J. Stegmeir.)

Figure G.1 shows a schematic of the test specimens. The test specimens have a 25 μm thick Permalloy magnetic strip electroplated near the cantilever tip to enable actuation using an external electromagnet. This feature is similar to that described earlier for the uncoated silicon microcantilevers in Chapter 4. For sensing vibration, a LPCVD polysilicon piezoresistive strain gage is patterned near the root of the cantilevers. Doped polysilicon is chosen as the strain gage material due to higher gage

factors (80-200) [80]. Higher gage factors are desirable for high sensitivity to the relatively small strains occurring in MEMS. Metallic strain gages have a smaller gage factor of 1-5 compared to LPCVD polysilicon [80]. Phosphorus is used as the dopant for polysilicon, since only the phosphorus doped polysilicon process is offered by the Nanofabrication Center at the University of Minnesota. Figure G.2 shows an optical image of the microcantilever specimens with strain gages. Geometrical dimensions of the cantilevers were designed based on microcantilever samples used in Stegmeir et al. [79]. Key geometrical dimensions are summarized in Table G.1. Figure G.3 shows an illustration of the strain gages wires with important dimensions. Some considerations which influenced specimen dimensions are:

(i) Size of the rectangular channel in which the microcantilevers is immersed

(ii) Fluid velocities in the channel and velocity profile.

(iii) Requirements for the microscope to record images.

(iv) Size of bubbles being produced by the bubble generator.

(v) Limitations of the magnetic actuation technique at high frequencies

Figure G.4 shows an optical image of the strain gages (functional and dummy) on the wafer. Design of the strain gage wires were influenced by the following factors:

(i) desired strain to be measured

(ii) resistivity ρ of the polysilicon layer and

(iii) thickness t_{poly} of the polysilicon layer.

For a given strain gage, the desired strain to be measured is proportional to the fractional change in resistance of the strain gage

$$\varepsilon = \frac{1}{F}\frac{\Delta R_g}{R_g} \tag{G.1}$$

where F is the gage factor (a constant for a strain gage), ΔR_g is the change in resistance of the strain gage, and R_g is the resistance of the strain gage. The resistance of a conductor such as a strain gage wire is given by

$$R = \rho\frac{l}{A} \tag{G.2}$$

where l is the length, and A is the area of cross-section of the strain gage. For estimated stress levels of 5 MPa, the strain in silicon (E = 160 GPa) is 3.13 x 10^{-5}. Commercial strain gage readout devices consisting of Wheatstone bridge and signal conditioning stages are typically capable of measuring strains of the order of 1 x 10^{-6} (1 micro-strain) [62]. Hence, sensitivity of measuring strains is primarily limited by the electronic circuitry. Gage factors (F) for polysilicon strain gages fabricated using the LPCVD process at the Nanofabrication Center have been reported to range from 13 to 22 [81]. Assuming F= 12, the fractional change in resistance ($\Delta R_g/R_g$) for strain of 1 x 10^{-6} is 1.2 x 10^{-5}. The resistance of the strain gages was chosen to be in the range of 1000 to 2000 Ω. The expected change in resistance (ΔR_g) for F= 12, ε = 1 x 10^{-6}, R_g= 1000 Ω is calculated to be 0.012 Ω. The resistances of the MEMS strain gages are higher compared to that of metal-foil strain gages since semiconductors such as polysilicon are characterized by higher resistivity compared to metallic materials. Resistivity is a material property of the LPCVD polysilicon thin film and is measured after deposition at the Nanofabrication Center (section G.2). The thickness of the strain gage wires is limited to the thickness of the polysilicon deposited on the wafers during

processing. The dimensions of the microcantilevers influenced the choice of the length and width of the strain gage wires. The strain gages were positioned near the center of the width of the microcantilevers and near the root of the microcantilevers to ensure stress uniformity.

Since these microcantilevers are intended for operation in a conducting liquid environment such as water, insulating the strain gages is important to prevent shorting failures. A thin-film of insulating PECVD silicon oxide is deposited over the polysilicon strain gage wires (section G.2). Dummy strain gages are also fabricated on the same test chip for temperature compensation.

Significant levels of excitation voltage may be required for measurement of small strains and changes in resistance. For a Wheatstone bridge the required excitation voltage can be determined using [62]

$$\frac{\Delta e_0}{e_i} = \frac{\Delta R_g / R_g}{4 + 2(\Delta R_g / R_g)} \tag{G.3}$$

where Δe_0 is the voltage output due to strain, and e_i is the excitation voltage.

G. 2. Microfabrication process

The fabrication process for these specimens is summarized in Figure G.5. The 5-mask fabrication process is described below:

(i) 500 μm thick double-side-polished (DSP) 4-inch p-type (Boron doped) silicon wafers with orientation (100) (Silicon Quest International) were used as the substrate. A 1.0 μm thick layer of LPCVD low-stress silicon nitride was deposited on the wafers as the isolation layer.

(ii) A 1600-1700 Å thick LPCVD phosphorus-doped polysilicon layer was deposited over the silicon nitride layer. The strain gages are patterned on this polysilicon layer. The slice resistivity (ρ), of this as-deposited polysilicon was measured using a four-point probe (Veeco Instruments FPP 5000) and was observed to be 9.5×10^{-3} ohm-cm. Annealing the wafers for an hour at 900° C in the Tylan furnace decreased the slice resistivity to $\sim 0.95 \times 10^{-3}$ ohm-cm. The resulting sheet resistivity was approximately 55 ohm/square which was satisfactory for fabricating polysilicon strain gages.

(iii) The wafers were subjected to a 30-second rinse in a 49% HF solution to remove the superficial layer of SiO_2. Removal of this layer ensures improved electrical contact between the polysilicon layer and the gold contacts.

(iv) Polysilicon strain gages are patterned on the frontside of the wafer using reactive ion etching (RIE) with the STS etcher. Shipley SPR-220-7.0 photoresist was used as the etch mask. The four-point probe was used to monitor the sheet resistivity of the wafers to ensure that unwanted polysilicon had been etched completely. Compete removal of the polysilicon layer exposed the underlying silicon nitride layer, which is characterized by significantly higher sheet resistivity compared to polysilicon (indicated by E 30 error code on the four point probe).

(v) Next, a 1 μm thick PECVD (plasma-enhanced chemical vapor deposition) SiO_2 (at temperature of 150°C) was deposited on the frontside of the wafers to encapsulate and isolate the polysilicon strain gages.

(vi) The backside of the wafer is now coated with Shipley SPR-220-7.0 photoresist, aligned to frontside features, and patterned to form the backside etch mask. The

backside of the wafer is subjected to a timed etch with DRIE so as leave only a thin 20-40 μm of silicon remaining as shown in Figure G.5.

(vii) The wafer is cleaned with solvents, and Piranha solution. The frontside of the wafers are coated with Cr-Cu seedlayer (200 Å of Cr followed by 1800 Å of Cu) in the AJA sputterer. Permalloy is electroplated on the wafers using a process similar to that described in Appendix B.

(viii) Holes are opened in the PECVD SiO_2 layer so that gold contacts may be deposited over polysilicon. These through holes are patterned using RIE in the STS etcher, and photoresist as the etch mask. The wafers are then cleaned by successive solvent rinses.

(ix) The gold contacts are patterned using the lift-off process (Appendix B). After the photoresist has been patterned, the wafers are subjected to a 15-20s HF (49%) etch. This step ensures proper electrical contact between polysilicon and gold contact pads by removing any residual SiO_2 covering the polysilicon contact pads. Gold contact pads are deposited by successively sputtering 300 Å of Cr followed by 1000-2000 Å of gold (Au) in the AJA sputterer. The chromium layer promotes adhesion between polysilicon and gold layers. The gold coated layers are then immersed in acetone and placed in an ultrasonic bath until all unwanted gold has been removed.

(x) The final mask layer is patterned on the frontside of the wafer with Shipley SPR-220-7.0 photoresist. The frontside of the wafer is subjected to a timed etch in the DRIE so as to etch away silicon from selected areas, resulting in microcantilevers structures. A backing wafer is bonded to the backside of the

wafer using a thermal paste (Appendix B, Cool Grease®, CGR-7016 from AI Technology). The microcantilevers are cleaned in successive solvent rinses.

(xi) Resistances of individual stain gages were tested using probe station (Signatone H100 series) to test contact pads and identify defective strain gages. Microcantilevers with operational strain gages were separated from the wafer by breaking the silicon tethers with a diamond tipped scriber.

G. 3. Calibration

Calibration of the strain gages is necessary to determine the gage factor in order to calculate the strain from the measured value of change in resistance (ΔR_g). Since the microcantilevers will be vibrated during testing, dynamic calibration of the strain gages is preferable over static calibration. However, in this study preliminary static calibration was performed to estimate the gage factor. (Dynamic calibration of the strain gages will be performed by Matthew Stegmeir). A microcantilever specimen 6 mm long, 1 mm wide, 0.02 mm thick, and ΔR_g= 2004 Ω is subjected to known tip deflections with a probe tip attached to a micrometer. Change in resistance of the strain gage was recorded with a multimeter. The change in resistance was plotted against strain as shown in Figure G.6. The gage factor can be obtained by multiplying the slope of the curve ($\Delta R_g/\varepsilon$) with ($1/R_g$)

$$F = \left(\frac{\Delta R_g}{\varepsilon}\right)\left(\frac{1}{R_g}\right) = \left(\frac{10}{0.0025}\right)\left(\frac{1}{2004}\right) = 19.96 \qquad \text{(G.4)}$$

The gage factor of 19.96 was within the previously reported range of 13 to 22 [81].

Sources of error in calibration are attributed to errors in measuring ΔR_g with a multimeter (instead of Wheatstone bridge) and determination of strains. Strains were calculated assuming the probe tip deflects the free end of microcantilever. However, during calibration the probe tip was not exactly positioned at the free end but on the cantilever surface a finite distance away from the free end. Further, the applied strain during calibration was significantly higher than the strain expected during testing in liquids.

Table G.1. Dimensions of microcantilever specimens with strain gages

Design No.	Length (mm)	Width (mm)	a (μm)	b (μm)	c (μm)	d (μm)	Comments
1	3	0.5	60	100	550	210	
2	3	1	60	100	550	210	
3	6	0.5	60	100	550	210	
4	6	1	60	100	550	210	
5	6	2	60	100	550	200	2 loops

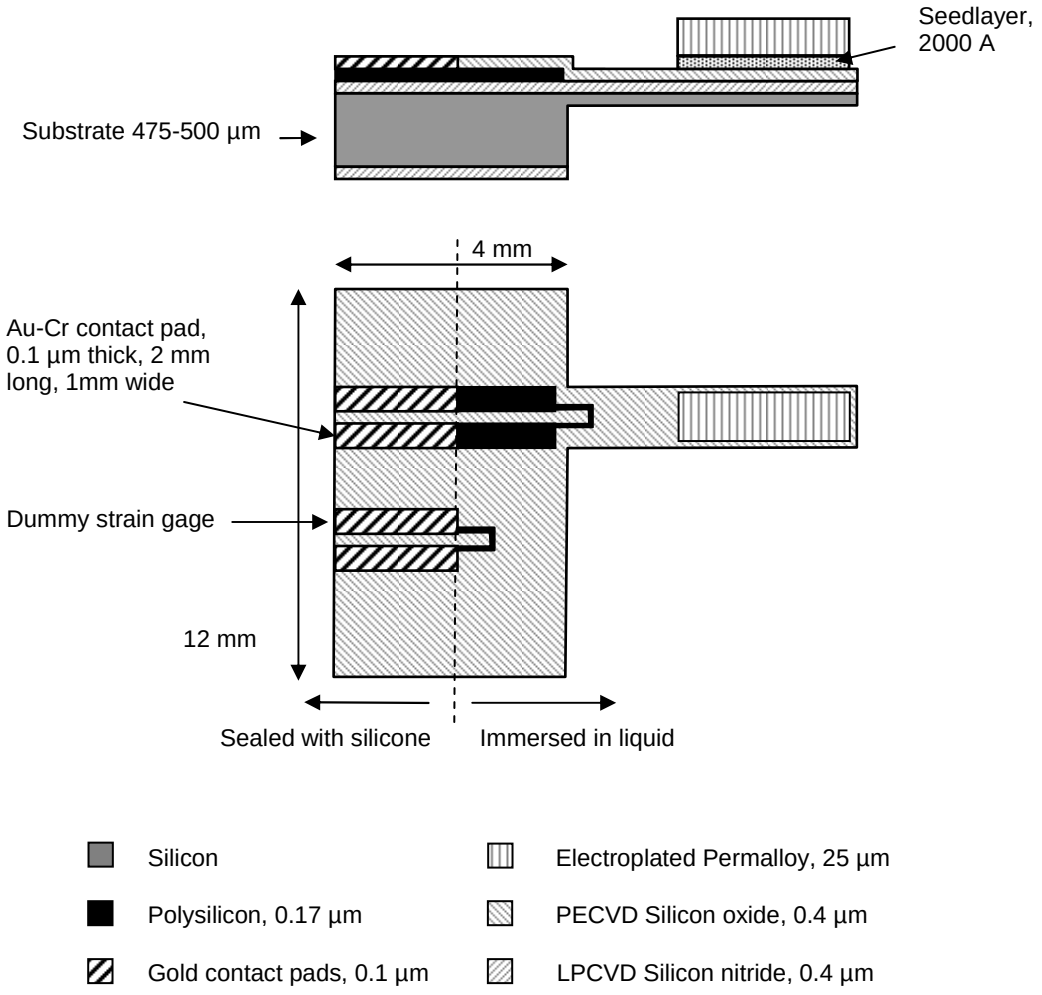

Figure G.1. Schematic of microcantilevers with strain gages

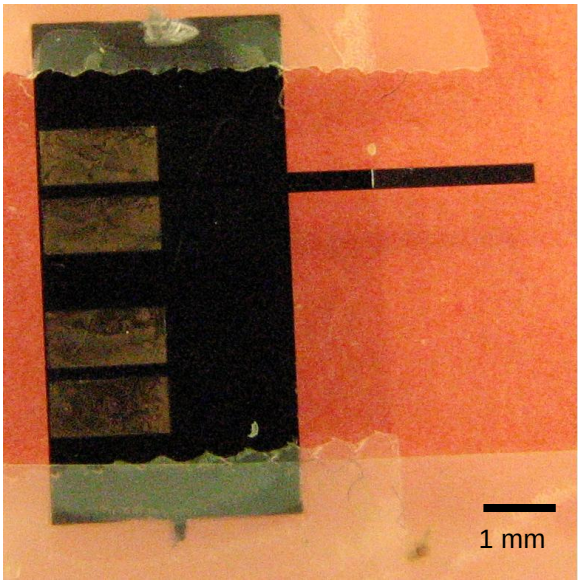

Figure G.2. Optical image of a microcantilever with piezoresistive strain gages

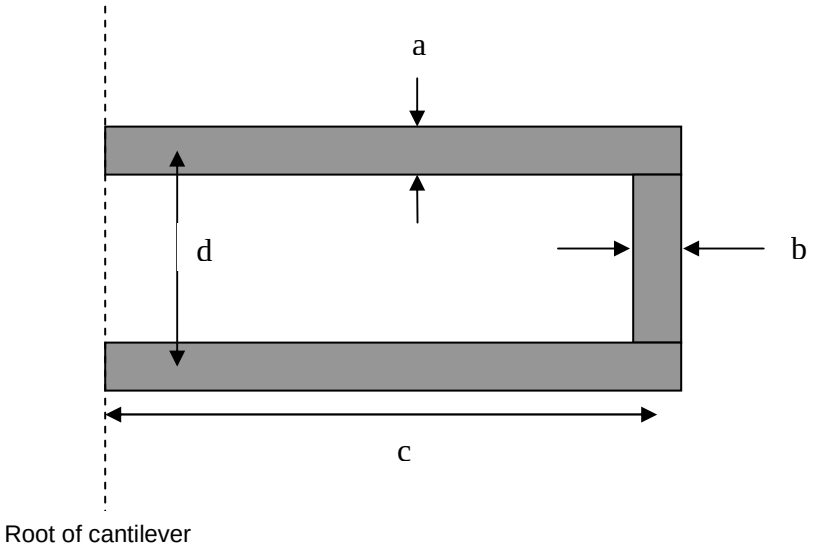

Figure G.3. Illustration of the strain gage wires showing important dimensions

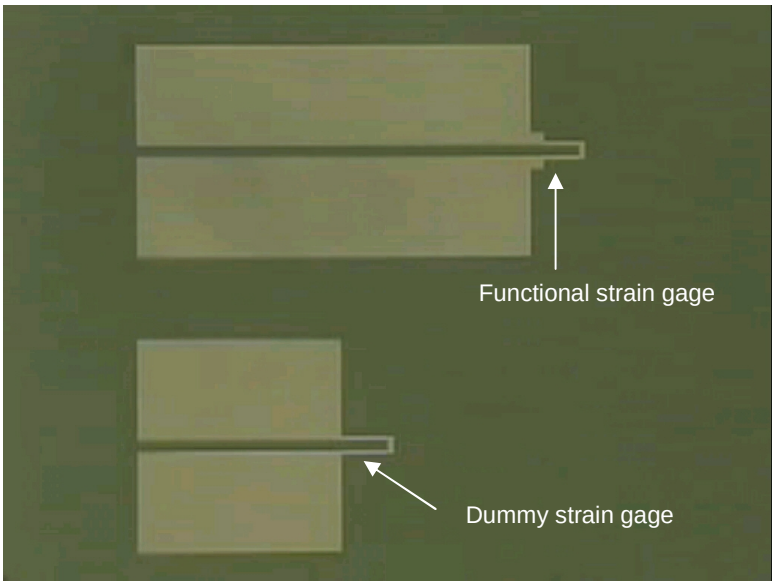

Figure G.4. Optical image showing functional and dummy strain gages patterned on the wafer

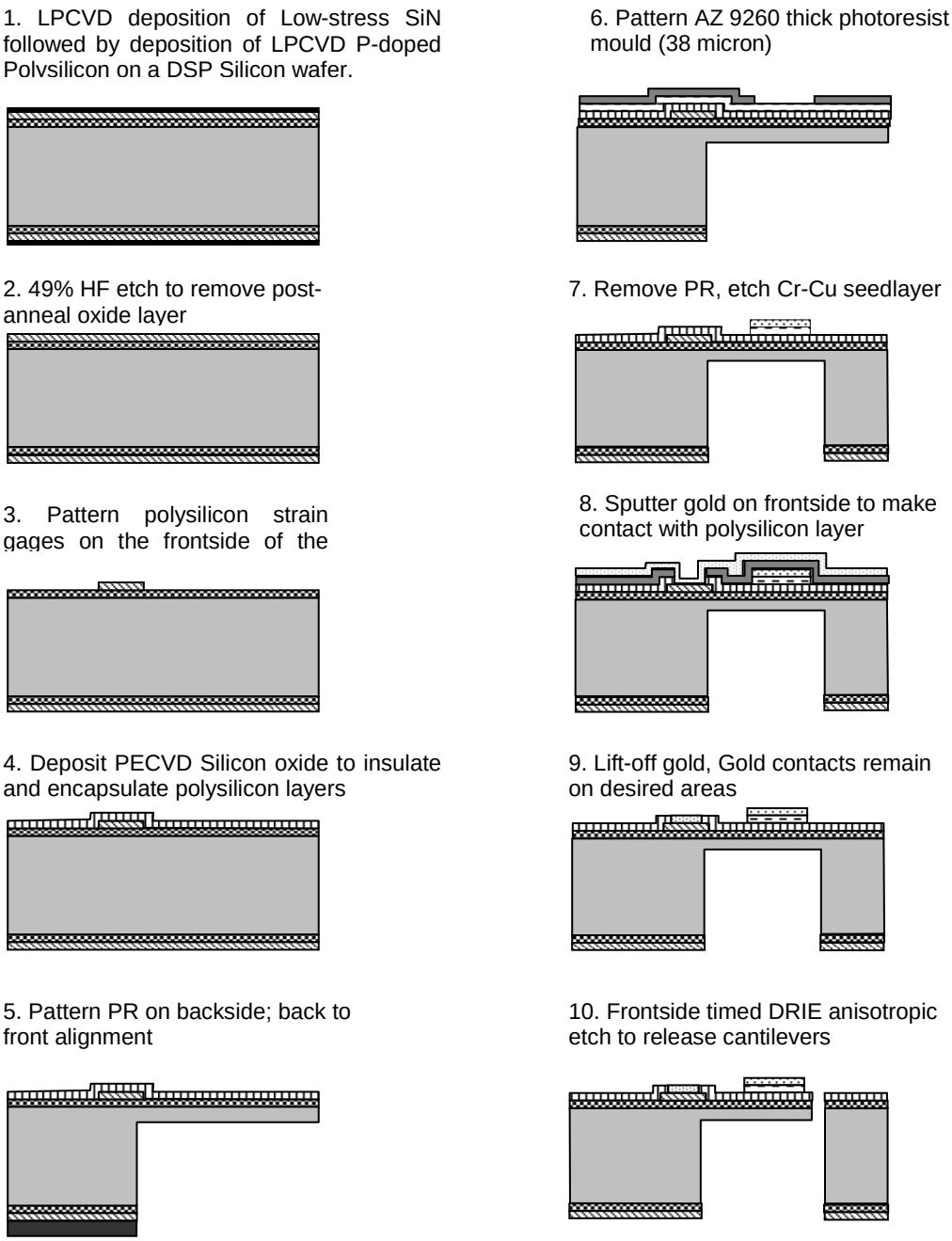

Figure G.5. Fabrication process for microcantilever specimen with strain gages

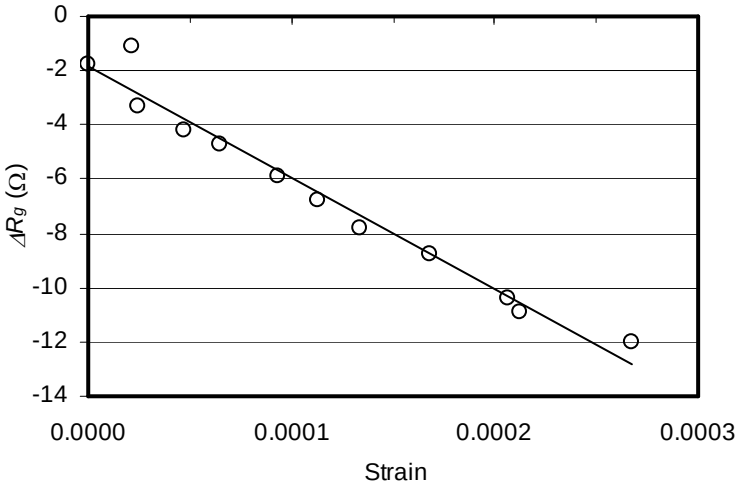

Figure G.6. Strain gage calibration: Plot of ΔR_g versus strain